

Microwave Processing in Additive Manufacturing



Samuel John Hefford

School of Engineering
Cardiff University

A thesis submitted to Cardiff University
for the degree of Doctor of Philosophy

DECLARATION

This work has not previously been accepted in substance for any degree and is not concurrently submitted in candidature for any degree.

Signed: Date:

STATEMENT 1

This thesis is being submitted in partial fulfilment of the requirements for the degree of PhD.

Signed: Date:

STATEMENT 2

This thesis is the result of my own independent work/investigation, except where otherwise stated. Other sources are acknowledged by explicit references. The views expressed are my own.

Signed: Date:

STATEMENT 3

I confirm that the electronic copy is identical to the bound copy of the thesis.

Signed: Date:

STATEMENT 4

I hereby give consent for my thesis, if accepted, to be available for photocopying and for inter-library loan, and for the title and summary to be made available to outside organisations.

Signed: Date:

Abstract

In this thesis the applications of microwave processing and measurement techniques for additive manufacture of metals by powder bed fusion (PBF) are investigated.

This thesis presents an experimental setup developed for microwave heating and sintering of powder compacts using a cavity applicator. The setup uses directionally coupled power meters to achieve the functionality of a scalar network analyser, which allows the tracking of the resonant frequency during heating. Software is developed, which can be used to control the system and set the sample temperature using sensor measurements as feedback. Additionally, a cavity applicator is designed using a novel method for breaking frequency degeneracy of the excitation mode, TE_{011} .

This thesis shows that microwave sintering acts to reduce the microwave magnetic absorption of metal powder compacts. This is confirmed through experiment where various metal powders are sintered using microwave magnetic field. Measurements of the Q_0 during the process are used to monitor the change in microwave loss of the powder compacts. This is important as previous results focus mainly on the post-sintering properties, while there is very little data pertaining to in-process changes.

This thesis presents a technique for measuring the surface resistance using a dielectric resonator. The novelty of the technique lays in its ability to determine the system losses by calibration in situ. This is achieved using a lift-off design, where the dielectric can be moved vertically within the resonator. Theoretical accuracy of this technique is shown to be good and simulation is used to investigate the effect on accuracy of different measurement conditions. Two prototype designs are produced and measurement results are presented for PBF manufactured metal parts, as well as metallised plastic surfaces produced by selective laser sintering (SLS) and stereo lithography (SLA).

Acknowledgements

I would like to express my sincere gratitude towards my supervisor, *Prof. Adrian Porch* for his guidance and support, and for giving me the opportunity to pursue such an interesting avenue of research. I could not have asked for a better mentor.

I acknowledge the financial support of Renishaw Plc. and I would like to thank *Nick Jones, Andrew Wescott, Jenna Tong* and my fellow colleagues in the additive manufacture group at Renishaw for their assistance, support, and insight.

I am grateful to my fellow colleagues at the Centre of High Frequency Engineering without whom this work would not have been possible. I would especially like to thank *Nick Clark, Jerome Cuenca, Heungjae Choi, Nyle Parker, Mike Barter, and Sam Partridge*, whose daily jokes and antics, and stimulating conversation helped create such a warm and engaging work environment.

I wish to express my heartfelt thanks to my extended family of friends. Their (tough) love and support has been a constant source of strength for me, and I am humbled to know such an amazing collection of people. In particular I would like to thank *Elinor, Lloyd, Mike, Charles, and Jack* for their sympathetic ears and for keeping me sane during the final stages of writing.

Finally, I would like to thank my loving parents, *John and Sally*, for their constant, unwavering support and encouragement, and my wonderful sister, *Claire*, for all the pineapples.

Publications

JOURNALS AND CONFERENCES:

S. Hefford, N. Parker, J. Lees, and A. Porph, "*Monitoring changes in microwave absorption of Ti64 powder during microwave sintering*", in Microwave Conference (EuMC), 2017 47th European, 2017, pp. 927-929.

N. Clark, S. Hefford, and A. Porph, "*Effect of build orientation and surface finish on surface resistance in microwave components produced by Selective Laser Melting*", in Microwave Conference (EuMC), 2017 47th European, 2017, pp. 508-511.

UNDER REVIEW:

S. Hefford, N. Clark, and A. Porph, "*Lift-Off Calibration Method for Determining System Loss of a Dielectric Resonator*", IEEE Trans. Microw. Theory Tech., *Awaiting Submission*.

Table of contents

1	Introduction and Thesis Summary	1
1.1	Microwave Heating for PBF	2
1.1.1	Motivation	2
1.1.2	Research Goal	3
1.2	Microwave Performance of PBF Surfaces	3
1.2.1	Motivation	3
1.2.2	Research Goal	3
1.3	Thesis Summary	4
2	Literature Review	13
2.1	Powder Metallurgy	13
2.1.1	Introduction	13
2.1.2	Basic Principles of Sintering	14
2.1.3	Density and Porosity	16
2.1.4	Surface Area	18
2.1.5	Mechanical Properties of Sintered Materials	19
2.1.6	Solid-State Sintering	20
2.1.7	Summary	22
2.2	Microwave Metal Sintering	23
2.2.1	Introduction	23
2.2.2	Microwave Heating of Metal Powder Compacts	23
2.2.3	Comparisons with Conventional Sintering	25
2.2.4	Systems for Microwave Sintering	28
2.2.5	Temperature Measurement For Microwave Metal Sintering	31
2.2.6	Summary	33
2.3	Microwave Absorption of Conducting Particles	34
2.3.1	Introduction	34
2.3.2	Surface Resistance and the Skin-Effect	34

2.3.3	Electromagnetic Absorption of Conducting Spheres	36
2.3.4	Electric Field Interaction	36
2.3.5	Magnetic Field Interaction	39
2.3.6	Comparison of Electric and Magnetic Dipole Absorptions . . .	41
2.3.7	Summary	42
2.4	Series and Parallel Resonators	44
2.4.1	Introduction	44
2.4.2	Series RLC Circuit Model	44
2.4.3	Parallel RLC Circuit Model	48
2.5	Microwave Cavity Resonators	51
2.5.1	Introduction	51
2.5.2	Electromagnetic Modes of a Cavity Resonator	51
2.5.3	Equivalent Circuit Model Analysis	54
2.5.4	Evaluating Q_0 From Measurement	56
3	Microwave Resonators for Power Delivery and Heating	59
3.1	Introduction	59
3.2	Designing a Cavity for Magnetic Heating	60
3.2.1	Design Requirements	60
3.2.2	Operation Frequency	61
3.2.3	The TE_{011} Resonant Mode	61
3.2.4	Isolation of TE_{011} by Intermediate Cavity Shaping	63
3.2.5	Cavity Design and Construction	67
3.3	Experimental Setup for Microwave Heating	68
3.3.1	Hardware Configuration	69
3.3.2	Measurement Principle	70
3.3.3	Control Software	72
3.4	Health and Safety for High-Power Microwaves	73
3.4.1	Health Effects and Exposure Limits for HF Radiation	74
3.4.2	Safety Measures Employed	75
3.5	Conclusions	75
4	Microwave Sintering of Metal Powders in the Magnetic Field	77
4.1	Introduction	77
4.2	Microwave Heating/Sintering of Metal Powders	77
4.3	Observations of Microwave Sintering at Low Temperatures	79
4.3.1	Experimental	81

4.3.2	Results and Discussion	83
4.4	Observations of Microwave Sintering at High Temperatures	87
4.4.1	Experimental	88
4.4.2	Results and Discussion	90
4.5	Physical Properties of Microwave Sintered Metals	103
4.5.1	Parameter Selection	104
4.5.2	Experimental	104
4.5.3	Results and Discussion	107
4.6	Conclusions	122
5	Lift-Off Dielectric Resonator for Measuring Microwave Surface Resistance	125
5.1	Introduction	125
5.1.1	Dielectric Resonators for Measuring R_S	126
5.1.2	General Measurement Theory	127
5.1.3	Determining System Losses	128
5.2	A Novel Calibration Technique for Determining System Losses	130
5.2.1	Measurement Principle	130
5.2.2	Measurement Mode Selection	133
5.2.3	Eliminating Adjacent Mode Interference	135
5.3	Evaluation of Geometric and Energy-Filling Factors in COMSOL	138
5.4	Calibration and Measurement Using Matlab	140
5.4.1	GEO.m	140
5.4.2	CAL.m	140
5.5	Simulation: Accuracy of LODR Measurements	141
5.5.1	Aims	141
5.5.2	COMSOL Model Setup	142
5.5.3	Calibration Study Step	144
5.5.4	Measurement Study Step	144
5.5.5	Results	145
5.5.6	Discussion	155
5.6	Designs: Prototype LODR Systems	156
5.6.1	First Prototype "Boromir"	156
5.6.2	Second Prototype "Faramir"	160
5.7	Experiment: R_S of Full-Metal AM Surfaces	166
5.7.1	Methodology	166
5.7.2	Results	168

5.7.3	Discussion	171
5.8	Experiment: R_S of Metallised Plastic SLS and SLA Surfaces	172
5.8.1	Methodology	173
5.8.2	Results	175
5.8.3	Discussion	175
5.9	Conclusions	176
6	Conclusions and Further Work	179
6.1	Achievements and Contributions	179
6.2	Further Work	184
	References	187
	Appendix A Control Software Implementation	199
A.1	Program Operation	199
A.2	User Interface	202
A.2.1	Closed-Loop Temperature Control Using the Scripted Event Manager	204
	Appendix B Additional Sintering Experiment Data	207
B.1	Low Temperature Observations	207
B.2	High Temperature Observations	218
	Appendix C Matlab Code for LODR Method	237
C.1	GEO.m	238
C.2	CAL.m	239
	Appendix D Geometric and Energy-Filling Factors for LODRs	243
D.1	Simulation-Only Models	243
D.2	First Prototype Design "Boromir"	250
D.3	Second Prototype Design "Faramir"	252

Chapter 1

Introduction and Thesis Summary

The overall theme of this thesis is to explore the potential applications for microwave processing and measurement techniques suitable for the metal PBF process employed by the Renishaw AM250/500 series of additive manufacture machines. These systems are able to produce fully dense metal parts in a variety of different materials (e.g. Titanium, Steel, Cobalt-Chromium, Aluminium, etc.) using a process known as powder bed fusion or PBF.

In PBF parts are constructed in successive stages using a high-energy laser to fuse powder deposited in a thin layer. Once the layer is complete the build platform is lowered and a fresh layer of powder is deposited. Fusion by laser continues the cycle and the process repeats until the part is finished. The surrounding powder acts to provide some support to parts as they are formed. Where this is not enough, additional structures are included in the design to aid stability [1].

There are a number of challenges associated with the PBF technology to which microwave techniques could be applied as a potential solution. Within this thesis, two key areas are explored:

1. The use of microwave heating to aid the PBF process.
2. The microwave performance of PBF metal surfaces.

In the following sections we shall expand upon each of these points and establish the aims and objectives for this thesis.

1.1 Microwave Heating for PBF

1.1.1 Motivation

As has been mentioned, in PBF layers of metal powder are repeatedly melted using a laser. Currently the energy requirements of the system are high due to the inefficiencies associated with coupling of laser power to the powder bed. This is largely due to the reflectivity of the metal powders used and so high power lasers are employed to overcome the low energy transfer efficiency. Additionally for larger builds there are concerns over thermal stresses occurring as a result of temperature gradients between the base and the top layer. These stresses can be fatal to builds, often leading to cracking or warping of the piece [2].

Currently a heating element in the build plate is used to homogenise the temperature across the build volume. This approach is widely adopted and has been shown to be successful in reducing thermal stresses [2]. Due to the placement of the heating element however, the ability to maintain constant temperature is reduced as parts become taller. Microwaves offer an alternative solution due to the enhanced absorption of magnetic field for metal powders, where the particle size is comparable to the skin-depth [3–5]. Using microwaves to heat the powder volume could help prevent thermal stresses by minimising the temperature gradient across the part. Furthermore, with the entire powder bed being pre-heated the power of the laser could potentially be reduced.

In order for microwave heating to be employed in PBF, it is important to first know how the microwave absorption of the part and surrounding powder will change during the PBF process. Since it was first reported nearly 20 years ago [3], there has been a growing interest in the microwave heating and sintering of metal powders. Despite this very little has been commented on as to the changes in microwave absorption during sintering. Measurements obtained from interrupting the sintering process have been reported for effective permeability, and effective conductivity [6]. It is worth noting though that these measurements occurred after the sample was allowed to cool, and so additional changes may have occurred. In situ measurements indicating a reduction in internal temperature for higher part densities have been reported [7], however to the authors knowledge and at time of writing no measurements of the change to microwave absorption *during* sintering have been published.

1.1.2 Research Goal

In order to move towards a microwave heating solution for PBF, this thesis will aim to close the gaps in the literature by investigating the changes in microwave absorption of metal powders as a result of microwave heating *in situ*. To achieve this a novel microwave cavity system shall be developed able to deliver focused microwave magnetic field to metal powder samples. A method for monitoring the change in magnetic absorption *in situ* will also be developed and implemented through periodic measurement of the unloaded Q-factor. Finally an investigation into the effects of microwave sintering on the microwave absorption of metal powder compacts will be performed.

1.2 Microwave Performance of PBF Surfaces

1.2.1 Motivation

Another area of interest for additive manufacture is in the production of full-metal waveguides. Such structures are able to take advantage of the flexibility in design offered by additive technology to form new geometries [8]. Another useful feature is part consolidation where multiple separate components can be merged to reduce the weight and profile [9]. In these cases it is important to minimise the surface resistance (R_s) of the metal surfaces produced by PBF, as for a hollow waveguide the attenuation per unit length will be set by conductive losses.

Given the large number of process variables available in the PBF process, it is likely there will be an equally large range of surface qualities achievable which will have their own influence on R_s . In order to investigate the microwave performance it follows that microwave measurement techniques be employed. One approach could be to produce PBF waveguides and measure the microwave attenuation constant, however this is best suited for optimisation of a particular design as the attenuation constant is related to both the material and geometry. Additionally this method would quickly become costly in terms of resources and time as entire waveguide sections would need to be manufactured for each data point.

1.2.2 Research Goal

In order to enable investigation of the R_s of PBF surfaces this thesis will aim to develop a compact microwave test fixture able to measure the R_s of PBF surfaces directly. To achieve this a novel measurement technique will be developed based on an open-ended

dielectric resonator. The test fixture should be designed to operate at microwave frequencies and to accept small flat sections of material for measurement in order to keep the cost per data point small. Finally the measurement method will be verified using both simulation and through testing of PBF samples produced in a variety of materials and with varied build parameters.

1.3 Thesis Summary

With the motivation established this thesis can therefore be broken down into three primary topics, each of which shall be covered individually in their own chapter:

1. The development of a microwave cavity system able to deliver focused microwave energy to the metal powder samples.
2. The investigation of the effects of microwave sintering; both on the final properties of the materials and on the microwave absorption of the powder compact during sintering.
3. The development of post-process measurement techniques; specifically methods of measuring the microwave surface resistance of built components.

What follows now is a brief overview and summary of the goals and contributions for each of the main chapters.

Chapter 2: Literature Review

This chapter covers powder metallurgy theory and fundamentals, and presents a brief summary of the research efforts made in the field of microwave metal processing.

The chapter begins with an introduction to sintering theory fundamentals. The concept of surface energy is introduced and the various mass-transport mechanisms involved in sintering are discussed. The physical properties of sintered metals are discussed with reference to the classical stages of sintering (initial, intermediate, and final). The measurement method used to determine density for the samples produced later is described. Ideally an Archimedes measurement setup would have been employed. However due to the low mass of the samples, the precision of the available Archimedes balance was too low to produce reliable readings and so the mass-over-volume method described is used.

Finally an introduction to the discovery and initial development of metal microwave sintering is given. Analyses and models reported in the literature are examined. A more complete study of the mechanism for microwave absorption in a metal powder is given in Ch. 4, however and here only their main findings are summarised. The various advantages that microwave sintering possesses over conventional sintering are addressed, and findings from the literature reporting enhanced properties are examined. The two most common types of setup used for microwave sintering are discussed: single-mode and multi-mode cavities. The distinction between direct and hybrid heating is also discussed, as well as the advantages hybrid heating has demonstrated. In particular, the ability for single-mode heating to enable the live monitoring of microwave power loss of the powder compact is discussed.

Chapter 3: Microwave Resonators for Power Delivery and Heating

This chapter concerns itself with the development of a microwave heating and measurement system for the processing of samples by cavity or other resonant applicators. Surplus to the requirements of the author, the system was designed in such a way that other researchers within the group can make use of it without the need for excessive tutelage.

The chapter begins by first introducing basic resonator theory using the series and parallel RLC circuit models as examples before moving on to the microwave cavity resonator. Formulas for the resonant cavity modes are presented and an equivalent circuit model of a 2-port inductively coupled cavity resonator is used to derive equations for unloaded Q . Two methods for evaluating the Q_0 from transmission measurements are discussed, the highly-accurate Lorentzian fit method and the simple 3-dB method.

The design of a novel cavity applicator suitable for magnetic heating of the powder samples is presented. The metal powders will most efficiently heat in magnetic field and so the TE_{011} mode is selected for use which has a large magnetic field hotspot at the centre of the cavity. The drawback to the TE_{011} mode is the degeneracy it shares in frequency with the TM_{111} mode, which must be broken in order to use it in isolation. A technique for breaking this degeneracy is demonstrated in which the shape of the cavity is partially deformed from a cylinder to a quasi-sphere. As a sphere does not experience the degeneracy of these particular modes the effect of the quasi-spherical geometry is to separate out the two modes. Furthermore the Q_0 of the quasi-spherical TE_{011} mode benefits from the higher surface-area-to-volume ratio. This is a huge advantage over other more conventional techniques involving splits, holes or dielectric inserts as they normally act to lower the Q_0 .

A measurement system for performing simultaneous excitation and resonant measurements for microwave heating and sintering of metal powders is presented. The system hardware consists of the aforementioned cavity applicator coupled by a single port to the excitation line. Along the line power meters are coupled directionally so as to measure the forward and reverse power to the cavity. The temperature of the sample is also continuously measured using an infra-red pyrometer. Software written in LabVIEW is used to interpret these measurements and also to control the source. The method used to evaluate Q_0 and f_0 from single port reflection measurements using the power meters and signal generator is explained. This procedure is automated by the control software and is used to track changes in resonant frequency to ensure excitation occurs at the correct frequency.

Features of the control software are explained along with general program flow. One of the major strengths of this program and measurement setup is the ability to automate heating cycles. The program is able to automatically adjust the duty-cycle of the source based on the temperature measurement from the pyrometer in an attempt to maintain a target temperature. A simple scripting procedure is implemented where the target temperature is set based on a pre-determined temperature profile written by the user. This feature is later used in the final experiment presented in Chapter 4, and it enabled a series of 27 experiments averaging around 2 hours each to be largely automated.

Original Contributions from Chapter 3

- A novel microwave cavity applicator for use in magnetic heating of samples at ISM frequency 5.80 GHz is presented. The cavity makes use of a lesser known technique for breaking the mode degeneracy between TE_{0ml} and TM_{1ml} modes
- A measurement system for use in heating and sintering experiments using microwave cavity applicators is presented. The system is able to perform intermittent resonant sweeps in order to update the excitation frequency and also to evaluate the Q_0 of the resonator.
- Control software for running the measurement system is developed using NI LabVIEW. The software was designed to be as user friendly as possible so that other researchers could make use of it. Additionally the ability to automate the heating process means not only improved repeatability of experiments but also that the operator is not required to stand by the setup at all times. Providing

suitable safety measures are in place the experiments can be setup and left to run themselves.

Chapter 4: Microwave Sintering of Metal Powders in the Magnetic Field

This chapter concerns itself with the microwave sintering experiments undertaken using the system developed in Chapter 3. The main goals of these experiments was to observe the change in microwave absorption of the metal powder as a result of sintering, and also to relate that change to the properties of the resultant material.

The chapter begins with a discussion on the microwave absorption of conducting metal powders. Equations are presented for the electric and magnetic dipole absorption of conducting metal spheres following the analysis in [5]. It is shown that for the majority of metal powders used in additive manufacture, their conductivity and size distribution mean that the dominant loss mechanism will be the induced magnetic dipole absorption [5].

Next, the microwave sintering of metal powder compacts is discussed and experimental results are presented. Three primary investigations are undertaken: the change in loss at low temperatures, the change in loss at sintering temperatures, and a systematic study on the influence of different heating regimes.

It is shown that even at low temperatures where one would not normally expect to see sintering there is evidence for mass transport events as indicated by a reduction in the loss. This is largely attributed to the increase in particle size distribution and also the formation of weak particle interconnects.

High temperature sintering is performed using the setup and solid samples are produced. The reduction in loss due to sintering is once again confirmed and to a greater extent, this behaviour is observed in all three materials sintered. Scanning electron microscopy is used to investigate the micro-structure of the sintered bulk and it is concluded that the sintering occurring can be characterised by the initial stage, where up to 50% of surfaces are eliminated but only slight densification occurs. Measurements of sample density compared to the green density of the unsintered powder compacts confirms this and on average the density only increased by about 5% of the bulk density.

The final study makes use of the temperature control and automation which was developed for the measurement system in order to perform a wide survey of different heating profiles. In total 27 experiments were performed with the average run time for each being about 2 hours. Including hardware setup and sample preparation, the

entire experiment was able to be completed in just over 9 days largely thanks to the automation of the bulk of the work. Heating rate, sintering temperature, sintering time, and cooling rate were all investigated using a design of experiments/robust design approach. It is shown that for the values tested only sintering temperature had a significant impact on both the final density and flexural modulus of the samples. Comparing the final density and flexural modulus with the total change in loss showed excellent correlation, indicating that the reduction in microwave loss could be used as a metric to monitor the progress of sintering.

Original Contributions from Chapter 4

- Measurements showing the change in microwave absorption of a metal powder compact during microwave sintering are presented. It is shown that the action of sintering reduces the microwave loss presented by the sample. While arguably a predictable result, data directly indicating this has not been previously observed in the literature.
- Measurements showing a reduction in loss are shown for temperatures below which bulk sintering occurred indicating a either a change in powder size distribution or development of weak inter-particle bonds (or both). An explanation for the apparent low temperature mass-transport is provided based on the higher surface energies of the smaller particles present in the powder sample.
- Scanning Electron Micrograph (SEM) images are presented for the microwave sintered samples indicating that the sintering performed did not progress beyond initial stage despite the large reduction of loss (80-90%). It is reasoned that the large reduction in surface area experienced during initial stage sintering was responsible for the change in loss.
- An extended series of sintering experiments is performed to investigate the influence of heating rate, sintering temperature, sintering time, and cooling rate on the final density and mechanical properties of the sintered pieces. It is found that for the sintering performed by the system, sintering temperature was the main determining factor whilst results were found to be insensitive to the other variables investigated.
- Strong correlation between the reduction in loss and the final density as well as the flexural modulus is observed. Both of these qualities will improve as the part becomes more sintered and at later stages the density of the sample determines

the strength. Therefore measurements of the change in microwave loss could be useful as a non-destructive metric for monitoring the progress of sintering.

Chapter 5: Lift-Off Dielectric Resonator for Measuring Microwave Surface Resistance

In this chapter a measurement technique for evaluating the surface resistance (R_s) of fused metal surfaces is presented. The main goal for this technique was to produce a sensor with a simple and easy to perform calibration technique. This was achieved using a sapphire dielectric resonator method, working in the $TE_{01\delta}$ resonant mode around 7 and 5 GHz.

The chapter begins by discussing the emergent interest in producing microwave waveguides using PBF or similar additive techniques. The two main advantages of this technology are the inherent freedoms in design and geometry and also the ability to reduce weight and size through part consolidation, where sections which would normally be machined separately are merged in the design and fabricated as a single piece. The need for a qualitative survey of post-processing techniques and their effects on R_s is explained and it is decided to design a sensor based on a dielectric resonator to facilitate this.

Following a brief introduction to dielectric resonator measurement theory the unique design and measurement principle for the "Lift-Off Dielectric Resonator" (LODR) is presented. This design makes use of novel calibration step where the position of the dielectric is varied through manipulation of a support rod. It is shown that by fitting a characteristic equation to measurements of the loss at different positions, the constituent components of loss relating to the R_s of the walls and $\tan \delta$ of the dielectric and support rod can be found. This process is performed using an end plate made from the same material as the cavity. Once calibrated the measurement of any surface can be performed by replacing the end effector with the target. It is shown that due to the shape of the current paths in the $TE_{01\delta}$ mode used, the measurement is naturally insensitive to the split where the cavity meets the sample surface.

Simulation results are presented investigating the influence of support material on calibration accuracy. It is shown that where the contribution to loss of the support can be minimised the loss term can be eliminated from the curve fit without any change to the overall result. The accuracy of measurement is investigated for different sample conductivities and measurement positions. It is shown that where the contribution to loss from the sample is reduced, either by a high conductivity or by moving the dielectric further away, the accuracy is degraded. Therefore for optimal results it

is recommended to maximise the sensitivity of the fixture to the sample. For the room temperature fixtures produced machined from aluminium and using c-plane sapphire as the dielectric, the losses of the system would make the fixture unsuitable for measurement of low loss materials such as high temperature superconductors. However for the metal surfaces produced by PBF where R_s is generally higher than the fixture cavity walls to begin with, the accuracy of measurements can be considered good.

Two LODR prototypes are produced and the design process is commented upon. In particular the importance of avoiding mode crossover or adjacent interference is stressed. Calibration results for both fixtures is performed and presented. The first prototype was made using existing sapphire from a split-post dielectric resonator (SPDR) and used nylon for the support. The second prototype was made using a single-piece sapphire and based on the simulation results, used PTFE for the support material.

Finally measurement results for PBF metal surfaces and metallised SLS and SLA plastic surfaces are presented. The build orientation and effect of grit-blasting is investigated for the PBF samples. It is shown that while vertical surfaces performed poorer initially, following grit-blasting there was no discernible difference between the two orientations. This was confirmed for a variety of different materials and indicates that post-processing techniques can be employed to homogenise the performance of PBF surfaces in microwave components. The same dependence is not observed in the plastic surfaces however a significant difference is noted between the two manufacture methods.

Original Contributions from Chapter 5

- A technique for measuring the surface resistance using a dielectric resonator is presented where a novel calibration step is used to determine the system losses. The technique makes use of a unique resonator geometry in which the position of the dielectric is varied through manipulation of a low-loss, low-permittivity support rod. Calibration is performed through curve fitting to Q_0 measurement data at various positions.
- Simulation results are shown investigating the accuracy of the measurement technique for varying sample conductivities, measurement positions, and support rod materials. Subject to the quality of the fit measurement accuracy was shown to be good at conductivities typical of the materials used in additive waveguide manufacture.

- The designs of two prototype resonators are presented along with their calibration results. The original prototype uses Nylon for its support while the newer prototype uses PTFE. As predicted by the simulation results, the lower loss support material allowed for a better calibration accuracy. Despite this measurement results of PBF surfaces are seen to be consistent between the two devices. This is likely due to the already large R_s of the samples, minimising the influence of error.
- Measurement results of PBF metal parts built in both horizontal and vertical orientations and undergoing different post-processing are presented. It is shown that without post-processing the vertically built surfaces performed poorer however with grit-blasting the difference was not significant. This is a very positive conclusion for the additive manufactured waveguide industry as it indicates that through post-processing R_s can be made independent of build orientation.
- Measurement results of metallised plastic surfaces are presented comparing two plastic additive manufacturing techniques as well as the build orientation. Unlike the metal PBF samples, build orientation of the surface was not found to be a significant factor. In all cases the metallised SLA parts were shown to outperform the metallised SLS parts. This is attributed to differences in surface roughness characteristic of the processes.

Chapter 2

Literature Review

2.1 Powder Metallurgy

2.1.1 Introduction

The practice of producing parts from powder through near-net shape forming is known as *Powder Metallurgy*. A fine metal powder with a sufficiently low mean particle radius will exhibit fluid-like characteristics. The ability for the powder to flow means it will easily take the shape of any container. This property is advantageous as it allows the formation of complex and intricate part geometries which would be otherwise costly in terms of time and material to produce by traditional machining. There are various methods used to form the shape such as injection-moulding, die casting, extrusion, etc. Regardless of the forming technique used, in order to create a strong part the powder must first be fired to a temperature where it coalesces and becomes dense. This "firing" is the process known as sintering and occurs at temperatures above roughly one-half of the known melting point. In the same way that melting can occur over a wide range of temperatures sintering can occur under a range of different circumstances dependent on temperature and pressure [10, 11].

At a fundamental level, sintering relies on mass transportation mechanisms at the atomic level to create solid fully dense parts from powder. The driving force behind this is the lowering of the surface energy through formation of inter-particle bonds. The surface energy of a sphere is very high and so the energy required to form new bonds between surfaces is lower than that required to melt the bulk powder. This accounts for the lower sintering temperature as compared to the melting point [10, 11]. As the process continues these bonds continue to grow until pores begin to close as the part becomes dense. Due to the migration of material to the inter-particle voids

there is some shrinkage to the total volume which must be accounted for in the initial preparation [10–12].

2.1.2 Basic Principles of Sintering

Definition of Surface Energy

As mentioned, particles sinter as a result of atomic level events which act to reduce the surface energy. What then is surface energy? We define surface energy as the work done per unit area to create a surface by breaking intermolecular bonds. This can be difficult to understand without visualisation so as an example consider the structure shown in Fig. 2.1.

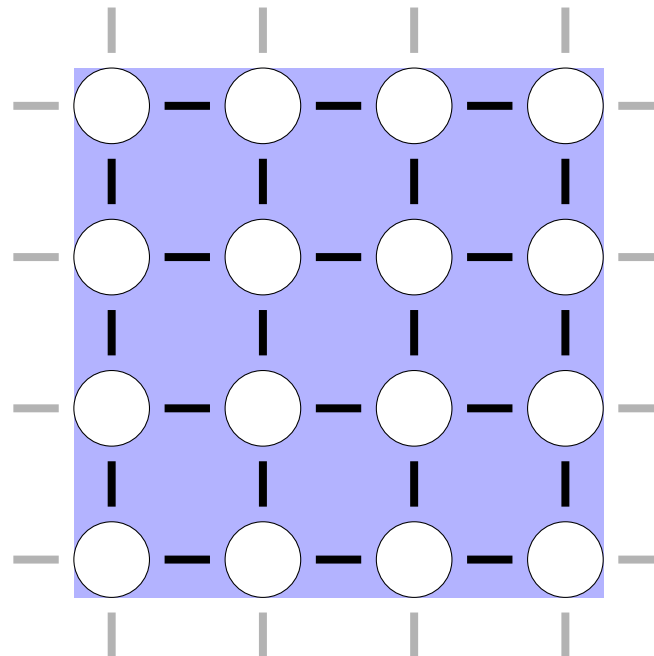


Fig. 2.1 Visualisation of the surface energy due to disrupted molecular bonds.

Here we have a solid formed of molecules which can make up to 4 bonds; solid mass is indicated in blue, the molecules are white and bonds are shown in black or grey depending if they have been made or not. Molecules within the solid exhibit complete while those at the surface have some bonds which are broken. The energy of the surface molecules is therefore higher than those in the bulk. We define surface energy classically as the excess energy associated with these broken bonds.

Another definition comes from the work done in creating a new surface. For the structure in Fig. 2.1, cutting it into two pieces would create a new surface. In doing

so the existing intermolecular bonds would need to be broken/disrupted and the work done per unit area to achieve this is equivalent to the increase in surface energy.

Driving Force Behind Mass Flow

Consider a spherical metal particle of radius r composed of n atoms with a finite volume Ω . If atoms are added to the sphere there will be a corresponding increase in volume, radius and surface area. The volume V can be defined in terms of n and r

$$V = \frac{4}{3}\pi r^3 = n\Omega \quad (2.1)$$

Differentiating the volume gives the expression relating changes in the volume dV and radius dr to a change in the number of atoms dn .

$$dV = 4\pi r^2 dr = \Omega dn \quad (2.2a)$$

$$dr = \frac{\Omega}{4\pi r^2} dn \quad (2.2b)$$

Consider the difference in surface energy between a sphere and a flat surface with infinite depth. Assuming a common surface energy density, there will be a chemical potential difference ΔU between the two surfaces due to the higher surface-area-to-volume ratio of the sphere [10]. With the addition of new atoms to the sphere the surface more and more approximates the flat one and so this potential difference can be related to the change in surface energy as new atoms are added. Defining γ as the energy density of the surface gives the expression

$$\Delta U = \gamma \frac{dA}{dn} = \gamma 8\pi r \frac{dr}{dn} = \frac{2\gamma\Omega}{r} \quad (2.3)$$

which indicates that excessive surface energy per atom is greater for smaller particles than larger ones.

There will also be an increase in total energy as atoms are added, which can be represented as a stress acting in opposition to growth and is given as [10]

$$\sigma = \frac{2\gamma}{r} \quad (2.4)$$

An important point is that this stress is zero for a flat surface as $r \rightarrow \text{inf}$.

The driving force for mass transport is the surface energy per unit volume of the powder, and is greater in smaller particles. For mass to flow the atomic mobility must

overcome the sintering stress and is normally increased through application of heat or pressure. Sintering stress is higher for smaller particles, however so too is the vapour pressure which acts to increase the mobility at the surface [10, 11]. The stress then acts to direct mass flow. With flat surfaces being energetically favourable, particles begin to merge and necking occurs at the interface to flatten them out, while pores occurring between particles become elongated.

Stages of Sintering

The process of sintering can be broken down into 4 stages, each categorised by a change in surface area, density, and coarsening. The progress of sintering is characterised by the degree to which pores are eliminated; densification, surface area, neck growth and shrinkage are all common indicators of pore elimination.

At the beginning of the sintering process is the adhesion stage. Before heat has been applied the powder is loosely compacted and initial contacts between particles are made. There is no surface area loss associated with this stage (unless compacted) and no densification occurs.

As heating begins we have the initial stage characterised by neck growth. In this stage there is significant surface area loss of up to 50%; some densification occurs but not a significant amount.

The intermediate stage is characterised by pore rounding and elongation. Mass transport acts to fill in the gaps between particles and open porosity is all but eliminated. Significant densification occurs as a result of this and the surface area is nearly completely reduced. Coarsening begins to occur as the distribution of pores and grain boundaries becomes more regular. In general most sintering does not progress past this stage [10]. As the reduction of surface energy drives the sintering process, the drive to reduce surface area to the point of full density becomes weaker as the process continues and the progress becomes slower [11].

The final stage is the logical conclusion as time approaches infinity. It is characterised by pore closure and a negligible degree to which the surface area can decrease further. Densification in this final stage is very slow and the distribution of pores and grain boundaries is highly regular [10, 13].

2.1.3 Density and Porosity

Density is one of the most common metrics used to describe sintering. For a bulk material this will normally be defined as mass per unit volume in grams per cubic-centimetre (g/cc). However for sintered material it is more common to express it

in terms of the fractional density as a percentage. This is useful as it allows for comparison between different materials and the degree of densification and is defined as follows

$$V_s = \frac{\rho_s}{\rho_0} \quad (2.5)$$

Porosity is another equally important factor and describes the fraction of the total volume that is either void or open to the environment. Porosity can be described in terms of number, shape, size, and distribution. They can either be open-surface or closed-surface and are formed as a result of inter-particle bonding.

Archimedes Method for Density Measurement

The Archimedes method for a porous material requires several measurements of weight to calculate density. Measurement setup requires a precision scale and a reference fluid of known density, typically water. A method of suspending the sample in the fluid is also required. The sample is weighed in air whilst dry W_1 , then again following impregnation by the fluid W_2 , finally it is measured whilst suspended in the fluid W_3 . If a wire was used to suspend the sample whilst in the fluid it too must be weighed in water W_0 . The density can then be calculated as follows

$$\rho_s = \rho_0 \frac{W_1}{W_2 - (W_3 - W_0)} \quad (2.6)$$

where ρ_0 is the density of the reference fluid, and ρ_s is the sample density.

The density of the reference fluid will often be temperature dependent so care must be taken to use the correct value.

The main advantage of this method is that it is able to account for open porosity and measures the density with respect to closed porosity only.

Mass/External-Volume Method for Density Measurement

The Mass/External-Volume method is by far the most simple method for calculating density. It relies on taking measurements of the external dimensions to calculate the volume, and as such it should only be used for simple geometries. It is also unable to account for open porosity. Density is calculated by dividing the mass measured by a precision scale by the calculated volume. For a cylindrical sample of length l and diameter D the density is calculated using the formula

$$\rho_s = 1000 \frac{4M}{\pi l D^2} \quad (2.7)$$

where ρ is the sample density in g/cc, M is the sample mass in g, and l and D are the length and diameter measured in mm.

For the samples produced later in Ch. 4 the Mass/External-Volume method had to be used. An Archimedes balance was available but the precision of the scales was not sufficient to accurately weigh the relatively low-mass samples.

A separate precision scale was used to weigh the samples, the length and diameter were measured using a micrometre. The measurement uncertainties for each were 0.005 g and 0.005 mm respectively and the uncertainty of the calculated density was found by taking the partial derivatives wrt. each measurement variable and then applying the well-known general formula for uncertainty

$$\delta\rho = 1000 \frac{4M}{\pi l d^2} \sqrt{\left(\frac{\delta M}{M}\right)^2 + \left(\frac{\delta l}{l}\right)^2 + \left(\frac{2\delta D}{D}\right)^2} \quad (2.8)$$

where δ indicates uncertainty in a specific variable, for example δM is the uncertainty in mass (0.005g).

Scanning Electron Microscopy (SEM)

SEM is often employed to evaluate porosity, normally by measurement of the pore size distribution. Sample preparation is often necessary and care must be taken not to prepare the samples in a way that might influence pore size. Recommended practice is repeated polishing and etching to expose the surface, impregnating with epoxy and then polishing the epoxy layer once cured. Impregnating with epoxy allows the pore structure to be preserved during the final polish. Image analysis can then be carried out with relative ease on the resulting micrographs.

2.1.4 Surface Area

Surface area is a good indication of early stage sintering. Even if there is little densification, the creation of interparticle bonds will act to greatly reduce the surface area by up to 50% without significantly increasing the density [10]. In the early stages of sintering the reduction in surface area can be closely correlated to the neck size ratio (X/D) by the relationship

$$\frac{\Delta S}{S_0} = -k_s \left(\frac{X}{D}\right)^M \quad (2.9)$$

where ΔS is the change in surface area, S_0 is the initial surface area, and k_s and M are constants. The value of M tends to fall between 1.8 and 2.0 depending on the transport mechanism [10]. The neck size ratio X/D is illustrated in Fig. 2.2 at the grain boundary interface of two particles undergoing necking.

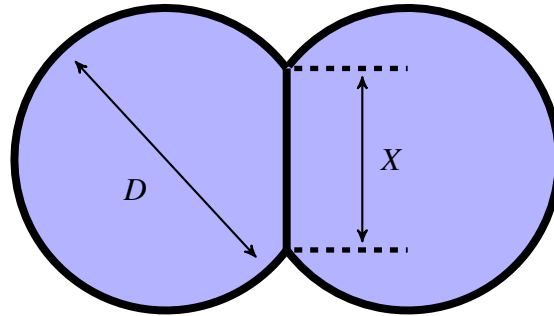


Fig. 2.2 Neck size ratio at the interface of two particles. X is neck width, D is the particle diameter. The neck size ratio is defined as X/D .

The main methods used to measure surface area currently are gas absorption and gas permeability. Both require open pore structures for admission of the test gas used limiting their usefulness [10]. Less commonly, surface area can also be assessed through SEM.

2.1.5 Mechanical Properties of Sintered Materials

The mechanical response of sintered material is often of high importance depending on its application. As properties such as strength will be greatly influenced by both the inter-particle bonds and the nature of the porosity, these are good parameters to use in the optimisation of sintering processes.

The effect of porosity, for instance, acts to reduce strength by both reducing average cross-sectional area and also by concentrating stress at the interparticle bonds. For low densities the strength is entirely dependent on the degree of necking and the strength of the interparticle bonds. At higher densities in later stages of sintering it is the pore shape and structure that determines strength [10].

The strength of a sintered sample is often correlated with the fractional density. Where there are no microstructural defects the sintered strength of a material as compared to its theoretical wrought strength can be expressed as [10]

$$\sigma = \sigma_0 K V_s^m \quad (2.10)$$

where K is a constant dependent on the geometry and processing representing stress concentration, m is another constant which typically ranges between 3 and 6 dependent on pore structure [10], and σ_0 is the wrought strength.

The flexural modulus of elasticity E_f can often be measured non-destructively using the 3-point bend test. It is also related to fractional density by a power law

$$E_f = E_{f0}V_s^z \quad (2.11)$$

where z is another constant and varies between 0.3 and 4 dependent on the pore structure [10], and E_{f0} is the equivalent flexural modulus for the wrought material. The importance of fractional density is therefore of great importance. As will be seen in Ch. 4 later on, samples produced by microwave sintering with a low fractional density of around 70% exhibited elastic moduli at a fraction of their bulk or wrought value.

2.1.6 Solid-State Sintering

In general most sintering is performed without application of pressure, and the major distinction between pressureless sintering is whether the process is a solid-state or liquid-phase one.

Liquid-phase sintering involves the use of an additive with a lower melt point. The presence of this liquid improves mass transportation and helps provide a capillary effect on particles equivalent to a large external pressure. The samples sintered in this chapter do not contain an additive and so we shall only discuss solid-state sintering in detail.

Solid-state sintering is the more common and classical type. It follows the same basic stages of sintering outlined previously and is illustrated in Fig. 2.3 between two particles. Neck growth defines the early stages and as more bonds grow the powder bulk is strengthened as a result of the interconnected network.

The two-sphere model shown indicates the gradual coalescence of the particles where conservation of volume gives rise to a single particle with a radius of 1.26 ($\sqrt[3]{2}$). In reality each particle is connected to a multitude of its neighbours and rather than forming a single particle, the gradual neck growth of the interconnects act to form closed pores [10, 11, 13]. The curvature of these pores decreases as sintering progresses, in addition to the reduced surface energy this causes the process to slow [10, 11].

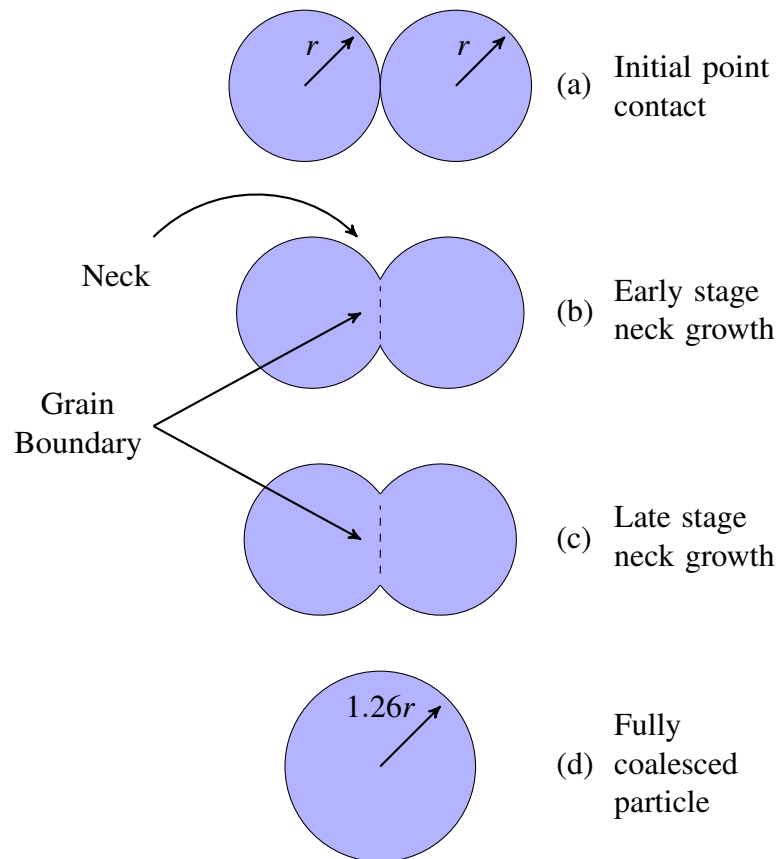


Fig. 2.3 Two-sphere sintering model showing the growth of inter-particle bond from point of contact by diffusion. Neck growth creates a grain boundary at the join. Given sufficient time the particles merge fully and the boundary disappears. The resultant particle has a radius 1.26 times the original particle.

A large number of mass-transport mechanisms occur in solid-state sintering, which can be broadly divided into either surface or bulk transport mechanisms.

Surface Transport

Surface transport is characterised by relocation of atoms from the surface to the neck, and is more prevalent at low temperatures. Surface transport mechanisms include surface-diffusion and evaporation-condensation (vapour-phase) transport. While surface transport does yield significant neck growth, the neck volume itself is low and so the size of the particles does not change significantly. Because of this very little shrinkage can occur in a compact where only surface transport is occurring as the distance between particles remains fixed [10–12].

Bulk Transport

Bulk transport is characterised by relocation of atoms from within the particle. As these atoms have a lower energy these mechanisms tend to occur at higher temperatures. Bulk transport mechanisms include volume diffusion, grain-boundary diffusion, plastic flow, and viscous flow. The action of bulk transport is to bring the particles closer together, thus it is the only class of transport mechanism able to promote shrinkage. The transport of atoms across the grain boundary in particular is critical for crystalline materials such as metals [10–12].

2.1.7 Summary

Sintering is a process whereby a powder compact is consolidated to increase its strength. It is a process both driven and characterised by surface energy and sintering stress. High temperatures are required to raise the atomic mobility so that sintering stress may be overcome, however due to the high surface energy per atom of small particles this temperature can be between 0.5 to 0.8 times the melting point [10–12].

Sintering is characterised by a rapid decrease in surface area followed by gradual densification. In its later stages pore closure begins to occur, however due to pressure exerted by the sinter stress they rarely completely disappear [10, 13]. Due to the rapid decrease in surface energy, further sintering is slowed due to reduced drive [10, 11].

Strength of sintered material is largely dependent on the density. At low densities the strength of the interparticle bonds determines the strength, at higher densities it is determined by a complex relationship with the pore structure [10]. The action of porosity is to decrease strength by decreasing cross-sectional area and also by focusing the stresses at the interparticle bonds. The effect of this is highly pronounced at lower densities due to the power law relationship between density and strength. As a result of this the Young's modulus of the sintered material can be a fraction of the wrought value for densities below 90% [10]

In solid state sintering surface and bulk transport mechanisms act to facilitate neck growth at interparticle bonds. Surface transport dominates at lower temperatures, however only bulk transport causes shrinkage [10–12]. Bulk transport occurs at higher temperatures than surface transport due to the lower energy of the internal atoms [10].

2.2 Microwave Metal Sintering

2.2.1 Introduction

Microwaves are a form of electromagnetic radiation with frequencies ranging between 0.3 and 300 GHz. They are used extensively in the communications industry, however they are probably more well-known for their ability to heat materials and, in particular, food thanks to the wide-spread adoption of the domestic microwave oven.

The industrial usage of microwaves for material processing has been widely popularised thanks to a number of advantages they possess over traditional approaches. Microwave heating is found to be more energy efficient, faster, safer, and more controllable than traditional approaches [14–20]. These qualities can be attributed to the way microwaves impart energy to materials. As the material is often fully penetrated by the microwave radiation, the heating occurring through dipole loss will be volumetric for an evenly applied field.

For a long time the application of microwave heating was thought to be impossible for metals and other highly conductive material. Magnetic field is able to penetrate slightly and induce eddy-currents, but these are confined to a thin layer at the surface known as the skin depth (again due to the high conductivity) [21]. A small amount of heating will occur at the surface of a metal due to the current density within the skin depth, and this is quantified by the surface resistance R_s , defined to be the power dissipated per m^2 for a unit surface magnetic field amplitude. However as the depth to which this induced current can penetrate is very low, the heat generated per unit volume is insufficient to cause significant temperature change in the bulk. The natural heat dissipation and high thermal conductivity of the metal will cause it to act as its own heat-sink, further reducing the effect of the generated heat.

The discovery that a metal powder will absorb microwaves began to be reported following the publication of results where conductive particles were added to refractory ceramics [22]. However it would be another decade before results were published reporting that pure metal powder compacts could be sintered by application of microwave field [3, 23].

2.2.2 Microwave Heating of Metal Powder Compacts

The rapid experimental heating observed by Roy et al. [3] has been investigated extensively. It is widely understood to occur due to an enhancement in magnetic absorption of small metal particles; where the volume fraction penetrated by the

magnetic field has become significant, and gives rise to noticeable temperature changes in the powder compact [24].

Porch et al. presented an analysis of the magnetic and electric dipole moment of conducting spheres [5]. They showed that the magnetic dipole absorption is the dominant mechanism for microwave loss over a wide range of particle radii, and that it was greatest when the particle radius was 2.41 times the skin-depth. Ignatenko et al. provide an alternative analysis [4] based on equations from Rybakov et al. [25] which also predict the same enhancement to magnetic absorption for particle radii at 2.4 times the skin-depth. At microwave frequencies this corresponds to no more than a few micrometers. Experimental results examining the electric and magnetic field heating have confirmed the analyses predictions and shown magnetic field heating to be vastly superior for a wide range of metal powders [3, 26, 27]. Experiments examining the influence of particle size to skin depth ratio have also been performed [28, 29].

The ability for microwave magnetic field to penetrate a metal powder compact has been studied experimentally by Buchelnikov et al. [30]. They found that microwaves were able to sinter samples of Sn powder shielded by Ti or Cu powders, while a thin layer of aluminium foil prevented any heating of the Sn powder. The penetration through the powder compacts was attributed to oxide layers naturally occurring on the particle surfaces. The comparatively weaker heating of Au also reported in [30] supported this conclusion, due to the absence of a native oxide shell.

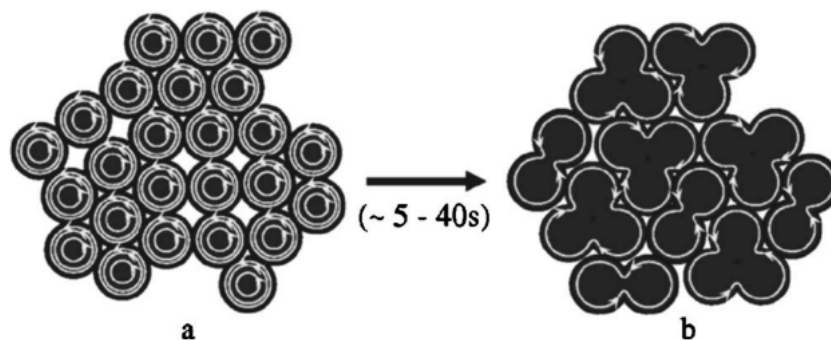


Fig. 2.4 Change in volume fraction subject to eddy current loss. a) Unsintered compact with intact oxide layers. b) Sintered compact. Eddy currents are indicated by arrows [6].

Mahmoud et al. also noted an improvement in microwave absorption for increased degrees of surface oxidation [31]. They proposed that the electrical insulation between particles due to the oxide layer is what allowed powder compacts to experience bulk penetration and heating. We would therefore expect to see a reduction in microwave magnetic loss as sintering progressed due to formation of electrical contacts between

particles, which would act to reduce the volume fraction where eddy current loss occurs. This is supported by the findings of Ma et al. in [6], where they noted that repeated heating of the same powder compact resulted in a lower process temperature than the first heating cycle. This is illustrated in Fig. 2.4. Takayama et al. [7] reported a gradual reduction in internal temperature of powder compacts compared to external temperature during sintering, which they also attributed to reduced penetration by the microwave field.

2.2.3 Comparisons with Conventional Sintering

The key distinction between the microwave and conventional methods of sintering is the mechanism by which the material is brought to temperature. In conventional sintering we rely on *energy transfer* of thermal energy. Commonly an electric furnace is used to bring the material to temperature. This is achieved through transfer of thermal energy by conduction/convection through an inert atmosphere, and the material is heated outside inwards. In microwave sintering however we rely on *energy conversion*, where thermal energy is generated inside the material by absorption of applied microwave energy, and the material heats inside outwards.

As is common in industrial heating, the microwave process tends to outperform the traditional convection/conduction methods for a number of reasons. Microwave heating tends to be comparatively much more uniform because the material itself is the heat source. The rate of heating is usually faster as the conversion of microwave energy into heat is not limited by the thermal conductivity of the material [32, 33] but instead is determined by the ability of the material itself to absorb microwaves. Finally microwave heating processes are often more energetically efficient, energy is not wasted heating the atmosphere but rather focused on the material itself [14, 33]. Indeed, many of these advantages have already been commented on for microwave sintering within the literature [19, 32, 34, 35].

Improvements to Mechanical Properties

The volumetric heating associated with microwave sintering has also been linked to improved mechanical properties when compared to parts produced by conventional sintering. Anklekar et al. noted that the more even heating gave rise to a highly uniform microstructure with minimal porosity in copper, copper-steel, and nickel-steel alloys. This was in contrast to the non-uniform microstructure and more porous core associated with conventional sintering [36, 37]. Gupta and Wong found that hybrid microwave sintering was able to improve the tensile strength of Al parts, which was

also attributed to the even temperature distribution and its effect on microstructure development [38].

Improvements to mechanical properties as a result of the rapid heating have also been reported [23, 37–39]. This is thought to be due to the rapid heating which slows coarsening, allowing for the development of rounder pores and more uniform grain structure [38, 40]. The resulting uniform microstructure is understood to have a positive influence on the mechanical performance and final density of the sintered product [13, 41].

Mondal et al. performed direct comparisons for materials sintered by microwave and conventional heating. They found a relative reduction in coarsening, with smaller and more evenly distributed grain sizes across a wide range of metal powders for microwave sintering [42]. Conversely, Luo et al. found that the microwave sintering of titanium powders gave increased grain sizes compared with conventional sintering [43]. Despite this the microwave parts were found to have shown enhanced hardness compared with the conventional titanium sintering.

Improvements to final part density over conventional sintering have been observed in a variety of materials such as tungsten [44, 45], copper-steel [36], and for iron, cobalt, nickel, copper and steel powders [40].

Disadvantages and Potential Limitations

Despite the many advantages to the microwave process, it is not without its drawbacks. Indeed, there are a number of limitations already apparent with regards to material compatibility and process scale-up.

A given conventional sintering furnace can process any material independent of that materials own properties, providing the furnace is capable of reaching the necessary temperatures. The microwave furnace on the other hand will not have such flexibility, as the ability to generate heat within the material is dependant on that materials own susceptance to microwave field. Given also that microwave loss, whether it be dielectric or eddy-current driven, is a frequency dependant property [46]; it should be clear that microwave sintering setups will be largely specialised to a particular group of materials.

Another challenge is the availability of high-power microwave sources which could potentially impose a limit on scale-up. The power output of a modern magnetron is limited by its operational frequency, where higher frequencies require much higher anode voltages there is a significant drop-off in output power. Available power outputs of up to 750 kW in the S-band reduce significantly to 300 kW in the C-band [47]. As

will be shown later, for the particle sizes typical of powder metallurgy most metals will fall within these two bands for optimum absorption. Techniques such as power-combining could be used to increase power output to an extent [48], however this still potentially imposes an upper limit for bulk processing of materials, even more so for materials which require higher sintering temperatures.

Table 2.1 Conventional versus Microwave Sintering

Parameter	Conventional	Microwave
Heating	Indirect, externally applied. Material independent.	Direct, internally applied. Material dependent.
Mechanism	Energy transfer. Conduction and convection heating using heating elements.	Energy conversion. Ohmic heating from induced eddy currents using microwave magnetic field.
Heating Rate	Slower - heat transfer limited by thermal conductivity of material and atmosphere/environment.	Faster - heat generated within material independent of thermal conductivity.
Compatible Materials	Any in principle.	Material dependant.
Coarsening [42, 43]	Inconclusive. Conflicting reports.	Inconclusive. Conflicting reports.
Pore Shape [37, 49, 50]	Sharper edges.	Rounder edges.
Hardness [36, 42, 43]	Lower. Assumed due to pore shape.	Higher. Assumed due to pore shape.
Ductility [37]	Lower. Assumed due to pore shape.	Higher. Assumed due to pore shape.
Density [42–45]	Marginally lower.	Marginally higher.

Summary

Overall, the main advantages of microwave sintering reported can be attributed to the more rapid and uniform heating achievable as compared to conventional sintering. This enables development of a more uniform distribution of pores with a rounder

more regular shape [36, 37], which has positive consequences on the final mechanical and structural properties of the material [13, 38, 40, 41]. The potential limitations for microwave sintering relate to industrial scale-up and material compatibility. Microwave sintering is a material dependant process, and so a single microwave furnace will not be able to process as wide a variety of materials as the conventional equivalent. Additionally there are potential upper-limits to bulk processing imposed by availability of high-power microwave sources at desirable frequencies. A summary of the potential advantages and disadvantages is presented in Tab. 2.1.

2.2.4 Systems for Microwave Sintering

Generally speaking microwave sintering of metal compacts can be classified by the type of applicator used, which will either be a single- or multi-mode cavity resonator. The main distinction between the two is whether the powder compact is exposed to purely microwave electric or magnetic field or both. Cavity resonators are discussed in detail later on in 2.5. Essentially they are a hollow metal chamber, which will form standing waves of microwave electric and magnetic field when excited at a resonant frequency.

Multi-mode Cavity

The majority of work on microwave sintering uses a multi-mode cavity system [28, 30, 31, 42–45, 51–62]. A multi-mode cavity is designed such that there are a multitude of resonant modes which can be excited close to the same frequency. This creates a more homogeneous distribution of microwave electric and magnetic field within the cavity, which results in more even exposure of the sample and therefore more even heating [33]. Magnetic stirrers and rotating tables can also be used to enhance this [14].

The main advantage of multi-mode applicators are their ability to process large volumes of material due to the more evenly distributed electric and magnetic fields. This makes multi-mode systems well suited for industrial scale-up of the microwave sintering process, and a number of patents for industrial implementations have appeared [51, 52]. A multi-mode hybrid system has also been presented, able to support industrial scale volumes up to 1 m³ [63].

Multi-mode systems are further classified based on whether or not a susceptor is used, which is a material to convert electromagnetic energy to heat. If a susceptor is used the heating is usually referred to as hybrid or two-directional, otherwise we refer to the method as direct heating.

Direct Heating

In direct heating only the powder compact itself is intended to convert microwave energy to heat. An example of a direct sintering setup using a multi-mode cavity is shown in Fig. 2.5 from [64]. As can be seen, the powder compact sits at the center of a multi-mode microwave oven. A low-loss, high-temperature insulator (typically mullite [45, 53, 55]) surrounds the powder. A [turn] table and reflector are used to homogenise the electromagnetic field distribution at the sample.

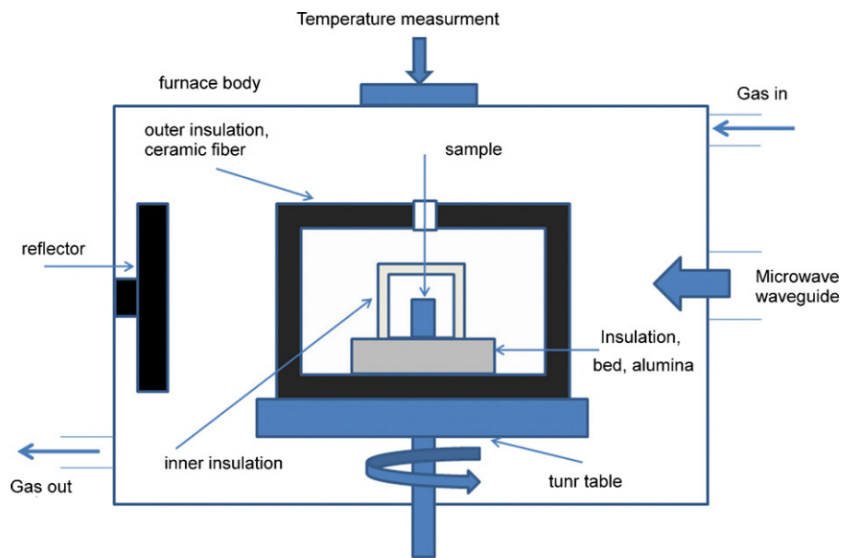


Fig. 2.5 Multi-mode sintering setup for direct heating [64].

This setup is often used to investigate the heating behaviour of the powder compact in isolation [7, 54]. In some cases however formation of an oxide layer during sintering has been shown to act as a local susceptor [34, 65]. This has mainly been reported for aluminium powders, however.

Hybrid or "Two-Directional" Heating

For hybrid heating the susceptor is placed near or around the powder compact in order to further homogenise the temperature. Materials which are lossy to the electric field are often used such as silicon carbide (SiC) [60–62], which allows both field components to be utilised in the heating process. An example of a hybrid (or two-directional) sintering setup using a multi-mode cavity is shown in Fig. 2.6 from [28].

The powder compact sits at the centre of a multi-mode microwave oven surrounded by a low microwave loss, high-temperature insulator (typically mullite [37]). As with the direct setup, the insulator provides an enhanced degree of temperature homogenisa-

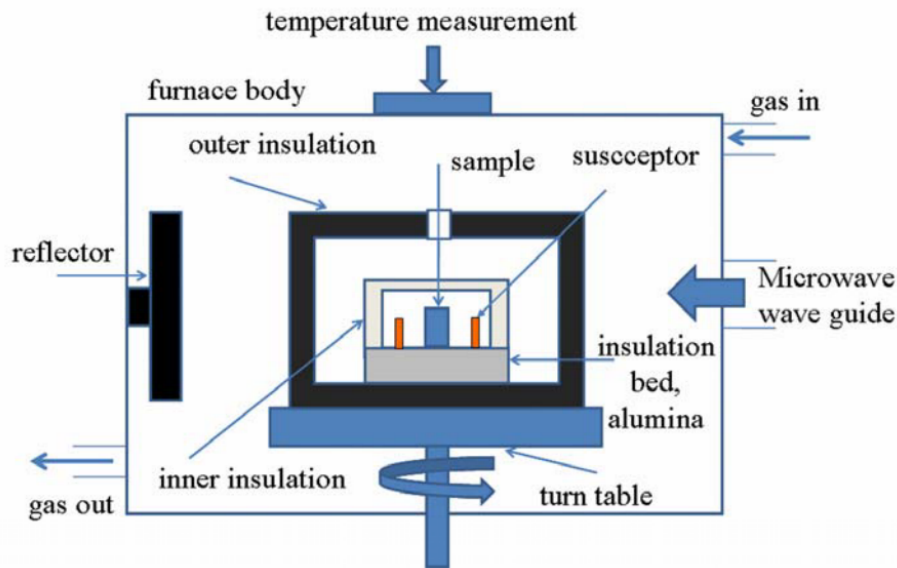


Fig. 2.6 Multi-mode sintering setup for hybrid/two-directional heating [28].

tion but does not participate in heat generation. Susceptor rods adjacent to the sample act to produce a secondary heat source through their own microwave power dissipation. A turn table and reflector are used to homogenise the electromagnetic field distribution.

Compared to direct heating, hybrid heating has been shown to achieve higher, more homogeneous temperatures [38, 43]. The increased homogeneity has been shown to yield improved material properties of the final product [28, 36, 66]. Hybrid heating has also enabled the casting of bulk metals by using the susceptor to initially heat the metal above its critical temperature, beyond this point the metal begins absorbing microwaves [65]. Another novel use of hybrid heating is in microwave joining, which was demonstrated for inconel-625 [59].

Single-mode Cavity

A single-mode cavity is designed so that only one resonant mode is excited at the operation frequency. As such, the electric and magnetic fields have a fixed distribution dependant on the mode excited and have their areas of maximum field strength at separate positions [46]. An example of a single-mode cavity sintering setup is shown in Fig. 2.7.

The disadvantage to these cavities is that they are difficult to scale-up for industrial size processing, as the frequency of the resonant cavity modes are dependant on cavity dimensions. The usefulness of these cavities goes beyond industrial processing, however, as the ability to spatially separate the electric and magnetic fields during

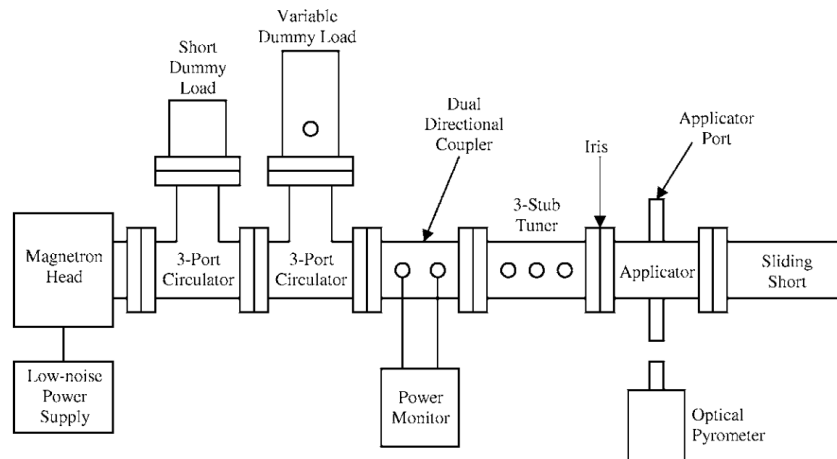


Fig. 2.7 Single-mode cavity sintering setup [6].

microwave sintering has enabled extensive study. This feature has been used to show experimentally that magnetic field is capable of heating metal powders far more than electric for the majority of metal powders [6, 26, 67, 68].

Another advantage of single-mode cavities is the ability to determine absorption or power loss of a sample through measurement of the resonant response and unloaded Q-factor. This could be measured in situ to monitor the evolution of the sintering, however at time of writing almost no work has been presented which takes advantage of this ability. Sato et al.[67] indicate the use of a vector network analyser (VNA) in their sintering system to measure initial insertion loss, but do not make any measurements during heating. The changes in effective permittivity and permeability during sintering were measured by Ma et al. [6]. These measurement were performed using a separate cavity resonator, however, by stopping the sintering process at different times. As such the sample temperature would not have been the same as it would have been during the sintering, which is known to enhance microwave absorption of metals [65]. There is therefore a need to close this gap in the research by performing these measurements in situ.

2.2.5 Temperature Measurement For Microwave Metal Sintering

Generally speaking, when comparing accuracy, a contact method for measuring temperature will usually be superior to a non-contact method. RTD sensors as an example, rely on the relationship between temperature and resistance of a resistive probe in contact with the measurement target. They are widely used in industrial and scientific applications as they are very accurate, can operate over a wide dynamic range, and ex-

perience minimal drift. Depending on the conditions of the measurement environment however, sometimes it is not practical or even possible to use a contact method.

In the case of microwave cavity resonators it is preferable to avoid using contact probes altogether as their presence in the cavity volume will cause an unwanted field perturbation. The reason for wanting to avoid this perturbation is twofold. Firstly there is the effect that the perturbation will have on the resonance of the cavity; any ingress into the cavity will cause both a shape and material perturbation. This will cause a shift in resonant frequency and system loss which must be accounted for in measurements, there is also the risk that the perturbation may suppress the resonant mode altogether [14, 33, 46]. Secondly is that in addition to perturbing the field the sensor may also interact with it and experience its own heating due to dielectric or magnetic loss (depending on material). This will ultimately lead to inaccuracies, as the sensor itself may be at an elevated temperature.

The requirement of avoiding ingress of a sensor into the cavity volume rules out many common contact measurement techniques. We therefore turn to infra-red pyrometer sensors for measurements of temperature inside our microwave resonators.

Infrared Pyrometry

Infra-red temperature measurement is a practice commonly used in industrial sintering and furnace applications, where target temperatures are too high for most contact probes to be used. The sensor head does not need to be in contact with the material, and requires only a clear line of sight to the target to perform the measurement. This makes them well-suited for our cavity resonators as the sensor will not need to enter the cavity, all that is needed is a small opening to allow the sensor to see the sample under test. This opening will need to be wide enough to allow sufficient focusing of the optics, but not so wide as to effect microwave resonance through disruption of current paths or to allow loss by radiation.

Infrared pyrometry calculates the target temperature by measuring the thermal infrared radiation given off by the target. This is achieved using an optical lens to focus the radiation to a detector sensitive to wavelengths of light in a particular portion of the EM spectrum. The measurement principle relies on treating the object as if it is a black-body radiator, and then performing a correction using the material emissivity and (if applicable) transmissivity. The emissivity of a material is measure of how well that material can emit radiation at a given temperature, as compared to a black-body radiator.

Incorrect setting of material emissivity is usually the greatest source of measurement error in infrared sensors, and so it is important to calibrate the material emissivity value using a secondary temperature sensor beforehand. This can be achieved by inserting a contact probe into the sample and placing the whole system in an oven and performing a temperature ramp, emissivity can then be adjusted so that measured temperature agrees with the more accurate contact probe. In practice the upper calibration temperature will be limited by either the maximum operating temperature of the contact probe or the maximum temperature of the oven, whichever is lower. This unfortunately means that the calibrated temperature range will not fully cover the process temperature achieved, and therefore some degree of error or drift in measurements above or below the calibrated range may occur.

Despite the need for calibration infrared temperature measurement remains a viable option for high-temperature measurements in microwave resonators, and so will be used in all such experiments presented in this thesis.

2.2.6 Summary

Microwave sintering of metal compacts differs from conventional sintering by the type of heating that occurs. In microwave sintering the microwave energy penetrates and is absorbed by the material where loss mechanisms convert the energy to heat. This results in volumetric heating of the sample. Additionally as the energy coupling is direct there can be faster heating rates and the overall energy cost is lower [32, 34, 35].

The dominant mechanism by which metal powders are heated by microwave energy is by induced eddy-current loss from the magnetic field [30]. This result has been explained by various analyses [4, 5, 25] and also confirmed by experiment [26, 67]. It has been observed in multiple studies that peak magnetic absorption occurs for particles with a radius 2.41 times the skin depth [5, 24, 25].

Numerous reports have been made citing improved mechanical properties of final samples for microwave sintering. This has included increases in hardness, strength, and density [23, 38] and has largely been attributed to enhancements to the micro-structure and pore rounding, due to the rapid and volumetric heating made possible [38, 58].

A large portion of the work in microwave sintering has used multi-mode cavity systems. This is likely due to their simpler operation, and ability to process larger sample sizes [63]. Single-mode cavities can be used to infer changes to microwave absorption during sintering, and measurements have been presented using this technique for samples sintered for increasing durations [6]. However no work has been

published which takes advantage of this ability to measure changes as they happen *in situ*.

Finally temperature measurements of samples within microwave cavities was discussed. As it is usually necessary to avoid ingress of a sensor head or probe into the cavity (to avoid unwanted interference through a material or volume perturbation), a non-contact method for measuring temperature is required. Infra-red temperature measurement is highly suited as the temperature can be read external to the cavity volume through a small opening. One drawback to this method is that it relies on knowing the target materials emissivity, this is further complicated by emissivity being a temperature dependant material property. This can be largely mitigated by performing a calibration with a secondary sensor beforehand, using an external heat source to bring the target to temperature as opposed to the microwave source.

2.3 Microwave Absorption of Conducting Particles

2.3.1 Introduction

In the previous section the topic of microwave sintering was discussed and the ability for microwaves to heat metal powders was briefly touched upon. In this section we will expand upon this heating ability of microwaves and examine the mechanisms for power loss of conducting powders in both the microwave electric, and magnetic field. The conditions for which these apply will be discussed with some reference to sintering theory, however an in-depth analysis is saved for Chapter 4, where the microwave absorption of metal powders is measured during microwave sintering.

As a large part of this analysis will refer to it, a useful starting point is to first discuss the skin-effect of an electric conductor.

2.3.2 Surface Resistance and the Skin-Effect

The skin-effect is the name used to describe the non-uniform current density of a conductor carrying (AC) alternating current which decays exponentially with increasing depth from the surface. This decay occurs as a result of the induced eddy-currents from the changing magnetic field within the conductor which act to minimise the total current at the centre in order to oppose the change in field. This allows the defining of current density J at a depth d in terms of its surface value J_S

$$J = J_S e^{-d/\delta} \quad (2.12)$$

where δ is the skin-depth, the depth from the surface at which current density has fallen to $1/e$ or 37% of the surface value and is defined as [21]

$$\delta = \sqrt{\frac{2\rho}{\omega\mu}} \quad (2.13)$$

where ω is the angular frequency (equal to $2\pi f$), and ρ and μ are the resistivity and permeability of the conductor. Most metals are non-magnetic at microwave frequencies and have a permeability equal to the free-space value ($\mu = \mu_0$).

The restriction of current to the surface implies that successive thickening of a layer will have an exponentially diminishing effect on the total resistance and will tend towards a lower limit. The value of the skin-depth for common conductors at 10 GHz typically falls below $1\mu\text{m}$, given also that a depth of 4δ accounts for 98% of the total current we can assume that in most cases conductor resistance is independent of dimensional thickness and is instead dependent on some arbitrary thickness due to the skin-effect. For this reason the surface resistance (sometimes *surface resistivity* or *sheet resistance*) is often used to describe the conductor power loss at microwave frequencies.

Surface resistance is defined as the resistance of a surface with uniform thickness and is distinct from the bulk resistance. In the classic definition DC resistance is defined by the resistivity, length and cross sectional area

$$R = \rho \frac{l}{A} = \rho \frac{l}{wt} \quad (2.14)$$

where l , w , and t are the length, width and thickness.

For a fixed t it is convenient to define $R_s = \rho t$ such that

$$R = R_s \frac{l}{w} \quad (2.15)$$

where R_s is the surface resistance.

An important consideration however is that while R and R_s will share the same SI unit of Ω they are not equivalent and R_s will only equal R for a 1:1 or square surface aspect ratio in the direction of current flow. The units of surface resistance are sometimes written as Ω/\square (ohms per square) to indicate this dependence. The power dissipated at the conductor surface can then be calculated from the tangential magnetic field component as

$$P_c = \frac{1}{2} R_s \int_s |\vec{H}_{tan}|^2 ds \quad (2.16)$$

2.3.3 Electromagnetic Absorption of Conducting Spheres

The remainder of this section follows the theoretical analysis provided in [5] for modelling the nature of loss of conducting spheres. In it the authors address the misconception that electric field is the main culprit for rapid heating of metal powders by microwave field excitation as explained by the nature of the high conductivity sphere to screen incident electric field. Instead the magnetic field is shown to be the dominant loss mechanism for high conductivity spheres and power absorption is maximised where $a \approx 2.41\delta$. This ratio has been arrived at repeatedly in the literature as in [4].

Consider an arrangement of spheres with radius uniform a in the presence of an electromagnetic field. Assuming the fields are transverse we relate the magnitudes of E_0 and H_0 by the free space wave impedance $\eta_0 = 376.7 \Omega$. Power loss is expressed per unit volume to allow comparison of different particle radii, and the individual particles are assumed to be dispersed evenly with a low filling fraction such that local field corrections can be omitted. This allows total power absorption to be computed as the sum of individual particles.

2.3.4 Electric Field Interaction

The electric dipole moment p of a conducting sphere of radius a in response to applied electric field of vector amplitude \vec{E}_0 is given by [5]

$$\vec{p} = 2\pi a^3 \epsilon_0 \vec{E}_0 \left(\frac{(2\epsilon_r + 1)(1 - ka \cot ka) - (ka)^2}{(\epsilon_r - 1)(1 - ka \cot ka) + (ka)^2} \right) \quad (2.17)$$

where k is the wave number *inside* the particle defined as

$$k = k_0 \sqrt{\epsilon_r \mu_r} = \frac{\omega}{c} \sqrt{\epsilon_r \mu_r} \quad (2.18)$$

and ϵ_r and μ_r are the relative permittivity and permeability which are complex

$$\epsilon_r = \epsilon_1 - j\epsilon_2 \quad (2.19a)$$

$$\mu_r = \mu_1 + j\mu_2 \quad (2.19b)$$

The time averaged power dissipated per unit volume can be found using (2.17) and is given as

$$\begin{aligned}\langle P_E \rangle &= -\frac{3\omega}{8\pi a^3} \Im \left(\vec{p} \cdot \vec{E}_0 \right) \\ &= -\frac{3}{4} \omega \epsilon_0 E_0^2 \Im \left(\frac{(2\epsilon_r + 1)(1 - ka \cot ka) - (ka)^2}{(\epsilon_r - 1)(1 - ka \cot ka) + (ka)^2} \right)\end{aligned}\quad (2.20)$$

where E_0 is the peak or maximum value of applied electric field.

At microwave frequencies non-magnetic metals with high conductivity will have $\epsilon_r = -j\sigma/\omega\epsilon_0$ and $\mu_r = 1$. The definition for ϵ is assumed to be valid over a wide range of σ , but in reality there will also be a real ϵ_1 term at low σ ; however this is ignored in this analysis. Substituting these values into (2.18) allows the wave number to be defined in terms of the skin-depth

$$k = \sqrt{-j\sigma\mu_0\omega} = \frac{1}{\delta} \sqrt{-2j}\quad (2.21)$$

In the large skin-depth limit ($a/\delta \ll 1$) (2.20) reduces to the quasi-static result for lossy dielectrics [5]

$$\lim_{a/\delta \rightarrow 0} \langle P_E \rangle = -\frac{3\omega\epsilon_0}{2} E_0^2 \Im \left(\frac{\epsilon - 1}{\epsilon + 2} \right)\quad (2.22)$$

which implies an internal electric field with a magnitude $E_i = 3E_0/(\epsilon_r + 2)$ that is independent of the skin-effect (the field is fully penetrating). The effect of this is that in the large skin-depth region the value of $\langle P_E \rangle$ is independent of particle size, and the power dissipated can be estimated from the total volume of conducting material. This can be seen in Fig. 2.8 where the value is constant up until the large skin-depth limit no longer applies. For particles of higher conductivity the skin-depth is much smaller and this limit ceases to apply sooner.

Within the large skin-depth limit there are a further two limits relating to the ratio $\sigma/\omega\epsilon_0$:

- $\sigma/\omega\epsilon_0 \ll 1$: The electric dipole absorption is proportional to conductivity and $\langle P_E \rangle \approx 9\sigma E_0^2/2$.
- $\sigma/\omega\epsilon_0 \gg 1$: The electric dipole absorption is inversely proportional to conductivity and $\langle P_E \rangle \approx 9\omega^2\epsilon_0^2 E_0^2/2\sigma$.

This can be seen in Fig. 2.9 where the effect of varying the conductivity between these limits is to reach a maximum value when $\sigma = 3\omega\epsilon_0$.

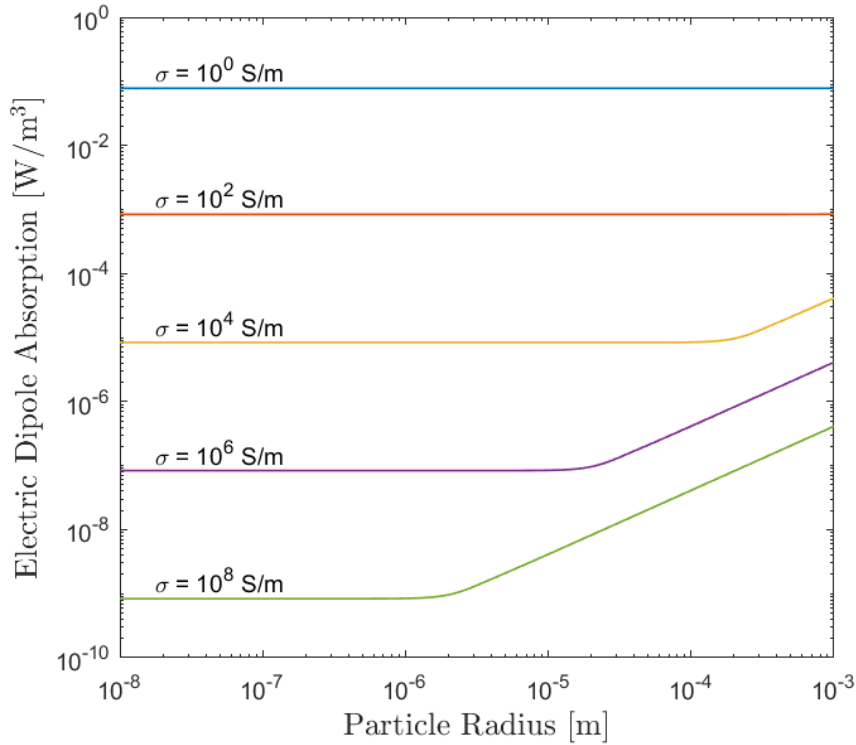


Fig. 2.8 Electric dipole absorption versus particle radius. Values obtained using a peak electric field of 1 V/m and a frequency of 2.45 GHz for various conductivities.

In the small skin-depth limit ($a/\delta \gg 1$) the electric field is no longer uniform and (2.20) reduces to [5]

$$\lim_{a/\delta \rightarrow \infty} \langle P_E \rangle = -\frac{9\omega^2 \epsilon_0^2 a}{4\sigma \delta} E_0^2 \propto a \sqrt{\frac{\omega^5}{\sigma}} \quad (2.23)$$

where the power loss has been increased however the effect of this is largely inconsequential. From Fig. 2.9 it should be clear that before the small-skin depth limit is reached the value of power loss will have become negligibly small [5]. Furthermore the size and/or conductivity of a particle necessary to achieve this limit at microwave frequencies is beyond what could be considered reasonable or even practical. Therefore the maximum achievable absorption should be considered as the value given in the large-skin depth limit when $\sigma = 3\omega\epsilon_0$.

$$\langle P_E \rangle_{max} = \frac{3\omega\epsilon_0}{4} E_0^2 \quad (2.24)$$

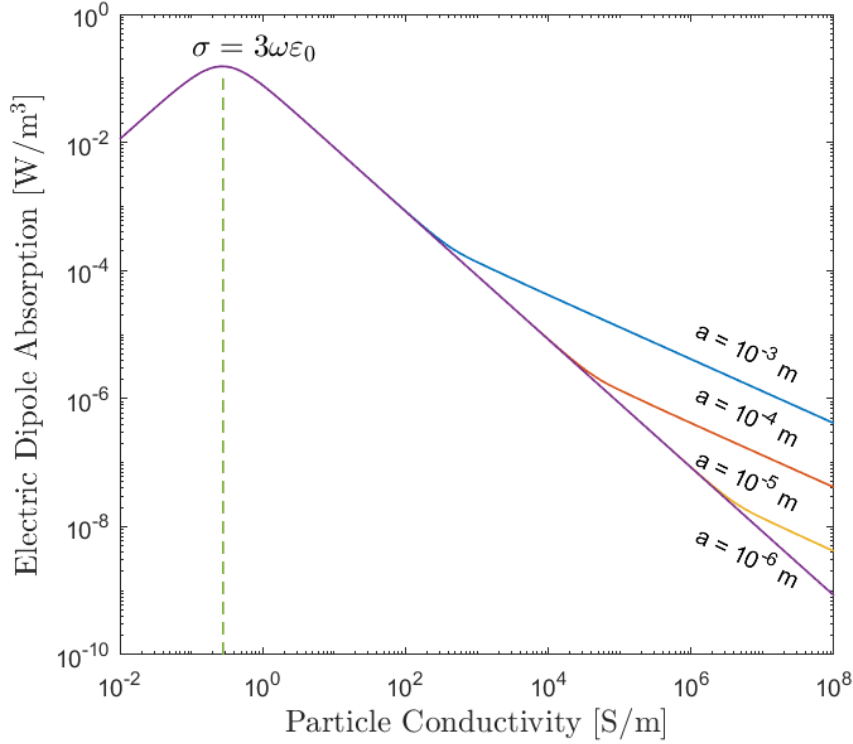


Fig. 2.9 Electric dipole absorption versus particle conductivity. Values obtained using a peak electric field of 1 V/m and a frequency of 2.45 GHz for various radii.

2.3.5 Magnetic Field Interaction

The magnetic dipole moment m of a conducting sphere of radius a in response to applied magnetic field \vec{H}_0 is given by [5]

$$\vec{m} = 2\pi a^3 \vec{H}_0 \left(\frac{(\mu + 2)(1 - ka \cot ka) - \mu (ka)^2}{(\mu - 1)(1 - ka \cot ka) - \mu (ka)^2} \right) \quad (2.25)$$

As with the electric dipole we define the time averaged power due to magnetic dipole absorption per unit volume for the sphere.

$$\begin{aligned} \langle P_M \rangle &= \frac{3\omega\mu_0}{8\pi a^3} \Im(\vec{m} \cdot \vec{H}_0) \\ &= \frac{3}{4} \omega\mu_0 H_0^2 \Im \left(\frac{(\mu_r + 2)(1 - ka \cot ka) - \mu_r (ka)^2}{(\mu_r - 1)(1 - ka \cot ka) - \mu_r (ka)^2} \right) \end{aligned} \quad (2.26)$$

where H_0 is the peak or maximum value of applied magnetic field.

As before we are considering a conductive non-magnetic particle and so the same definitions for ϵ_r and μ_r can be used. These serve to greatly simplify (2.26) which can be written as

$$\langle P_M \rangle = \frac{3\omega\mu_0}{4} H_0^2 \Im \left(1 + \frac{3 \cot ka}{ka} - \frac{3}{(ka)^2} \right) \quad (2.27)$$

Substituting in (2.21) allows us to define (2.26) in terms of the particle size to skin-depth ratio (a/δ), as before we define two limiting forms of the equation for the large skin-depth and small skin-depth limits.

In the large skin-depth limit ($a/\delta \ll 1$) the result in (2.27) reduces to [5]

$$\lim_{a/\delta \rightarrow 0} \langle P_M \rangle = \frac{\omega^2 \mu_0^2 a^2 \sigma}{20} H_0^2 \propto \omega^2 a^2 \sigma \quad (2.28)$$

which is the result for a uniform internal magnetic field, as we are considering non-magnetic material ($\mu_r = 1$) the value of internal field will be the same as the externally applied one. The effect of increasing either the conductivity or radius of a particle in this limit then would be to increase its magnetic dipole loss per unit volume.

In the small skin-depth limit ($a/\delta \gg 1$) the result in (2.27) reduces to [5]

$$\lim_{a/\delta \rightarrow \infty} \langle P_M \rangle = \frac{9R_s}{4a} H_0^2 \propto \frac{1}{a} \sqrt{\frac{\omega}{\sigma}} \quad (2.29)$$

where R_s is the surface resistance defined earlier. In this limit the effect of increasing the radius or conductivity is the opposite and will act to reduce the effects of magnetic dipole loss.

Examining the trends shown in Figs. 2.10 & 2.11 we can see that there the magnetic dipole loss approaches a maximum value. Unlike the electric dipole maximum these occur at a different conductivity for changing radius and it can be found from (2.27) that this occurs when $a \approx 2.41\delta$. As mentioned in the introduction this value is in agreement with values estimated in the literature [4]. At this point then the maximum magnetic dipole absorption is

$$\langle P_M \rangle_{max} \approx 0.266\omega\mu_0 H_0^2 \quad (2.30)$$

which is notably smaller than the maximum value for electric dipole absorption.

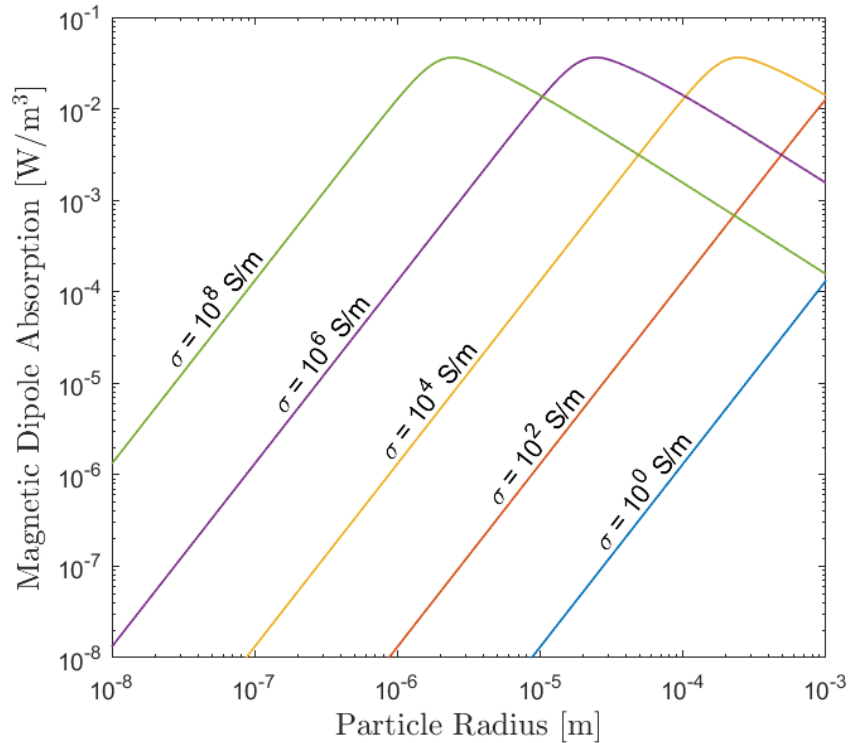


Fig. 2.10 Magnetic dipole absorption versus particle radius. Values obtained using a peak magnetic field of 2.654×10^{-3} A/m (corresponding to peak electric field of 1 V/m in free space) and a frequency of 2.45 GHz for various conductivities.

2.3.6 Comparison of Electric and Magnetic Dipole Absorptions

While it is true that the maximum electric dipole absorption is larger than the magnetic, it is important to recall that these values do not occur under the same conditions. The electric dipole absorption is maximum in the large skin-depth and minimised in the small skin-depth region, whereas the magnetic dipole absorption is maximum somewhere between the two extremes.

The ratio between the two dipole absorptions is plotted using $\log(P_M/P_E)$ for increasing particle radius in Fig. 2.12 and for increasing conductivity in Fig. 2.13. The dotted line is used to clarify the division, when the value of $\log(P_M/P_E)$ is above this line magnetic dipole absorption is dominant and vice versa. As can be seen in Fig. 2.12 for high values of conductivity magnetic dipole absorption is the main loss mechanism over a wide range of particle sizes. Where the conductivity becomes low however, the electric dipole absorption begins to dominate as shown in Fig. 2.13.

Metal powders used in sintering tend to have particle sizes in the order of μm . Common materials used include stainless steel, titanium, aluminium, etc. and their conductivities tend to fall in the region 10^6 to 10^8 S/m with alloys being on the lower

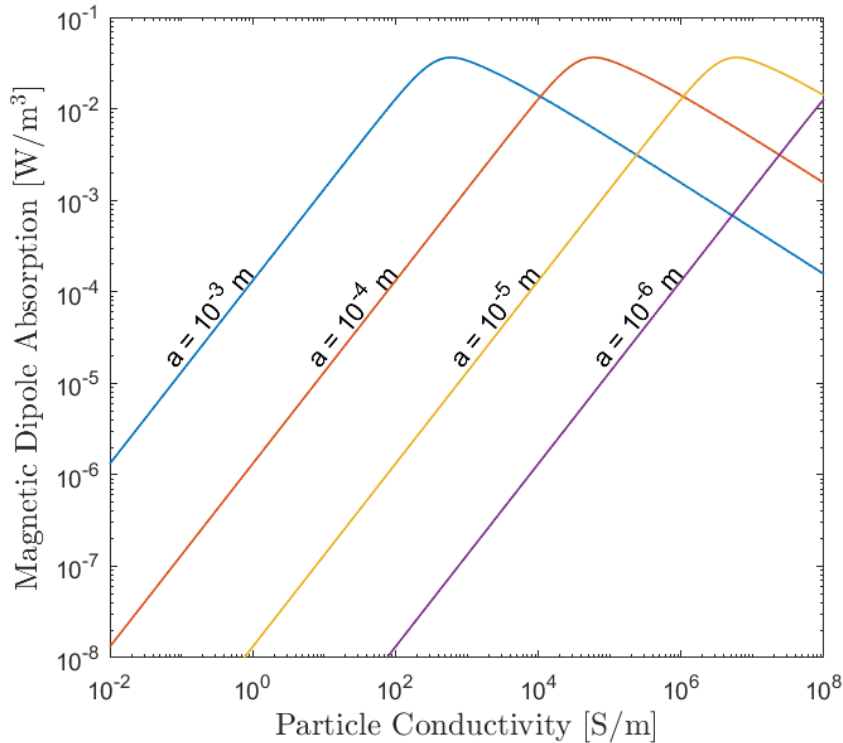


Fig. 2.11 Magnetic dipole absorption versus particle conductivity. Values obtained using a peak magnetic field of 2.654×10^{-3} A/m (corresponding to peak electric field of 1 V/m) and a frequency of 2.45 GHz for various radii.

end. Examining the plots then it is evident that under electric field no significant heating would occur, and that magnetic field must be employed.

2.3.7 Summary

Microwave heating of bulk metals in any volumetric capacity is difficult due to the limited field penetration due to the high conductivity of the material. The high conductivity means that electric field is screened at the surface while the magnetic field falls off exponentially due to the induced eddy currents. The nature of this field fall-off means that current is largely confined to a small depth beneath the surface with the current density being maximal at the surface. This is due to the skin effect, and the depth at which current density has fallen to $\approx 37\%$ of its maximum is referred to as the skin-depth, for metals at microwave frequencies this is typically a few μm .

The nature of the skin-depth means that power loss from conduction only occurs in a fraction of the total volume. For bulk metals where the total volume is high, the power absorption per unit volume is too low for any significant temperature rise to

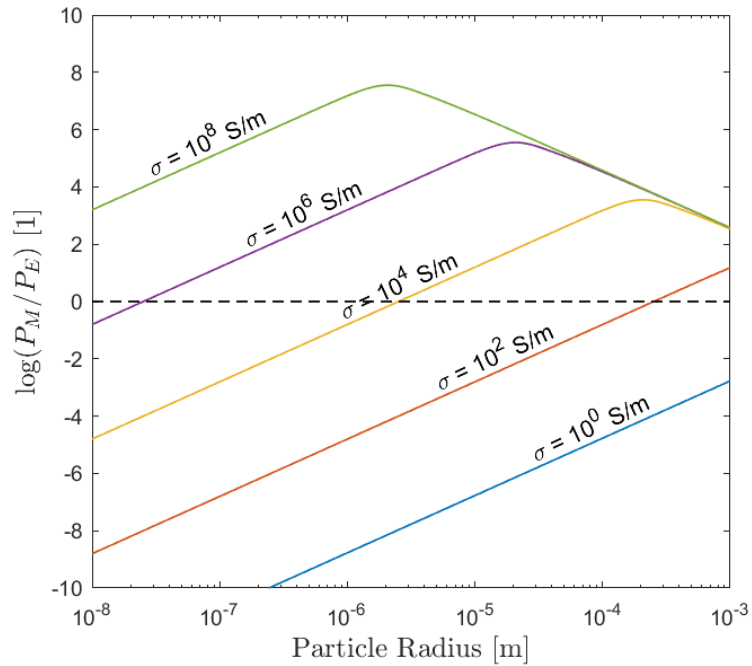


Fig. 2.12 Ratio of magnetic to electric dipole absorption of a conducting non-magnetic sphere for increasing radius. Applied fields were defined as $E_0 = \eta_0 H_0$ and a frequency of 2.45 GHz was used.

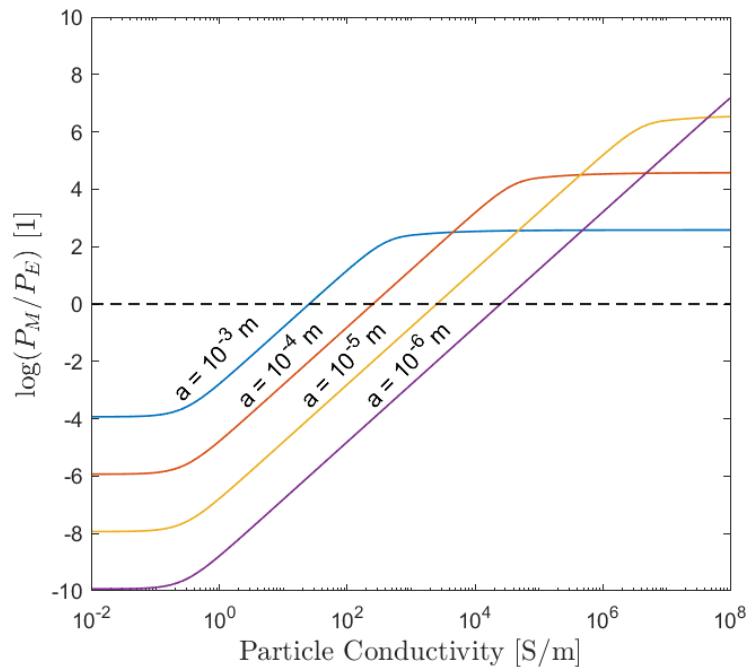


Fig. 2.13 Ratio of magnetic to electric dipole absorption of a conducting non-magnetic sphere for increasing conductivity. Applied fields were defined as $E_0 = \eta_0 H_0$ and a frequency of 2.45 GHz was used.

occur. If however the metal is in powder form where the average particle radius is comparable to the skin-depth then the per unit volume power absorbed will be high enough to cause significant volumetric heating of the bulk powder compact. This was first confirmed by Roy et al. experimentally in 1999 [3].

The interaction between the metal powder and the microwave electromagnetic field can be modelled assuming a distribution of conducting spheres. Exposure of the sphere to either electric or magnetic field will give rise to a dipole moment, as the sphere will have a finite conductivity there will be an associated power loss due to this moment. These dipole moments can be related to the particle radius to skin-depth ratio. Comparing the two at microwave frequencies it can be observed that electric dipole absorption dominates when the particle has a low conductivity, while for high conductivities magnetic dipole absorption dominates. For the majority of metals then which have their conductivities in the range $1 \times 10^6 - 1 \times 10^8$ S/m it will be the magnetic field component that drives the microwave heating.

2.4 Series and Parallel Resonators

2.4.1 Introduction

In this section general resonator concepts are covered using the series and parallel RLC circuit models as illustrative examples. This will form the basis for the proceeding section where the cylindrical microwave cavity is introduced.

A microwave resonant structure operating near or at the resonant frequency can be modelled using an equivalent RLC circuit. Such models are useful as they offer simple analytical solutions which help to aid understanding and in forming more complex models for analysis.

2.4.2 Series RLC Circuit Model

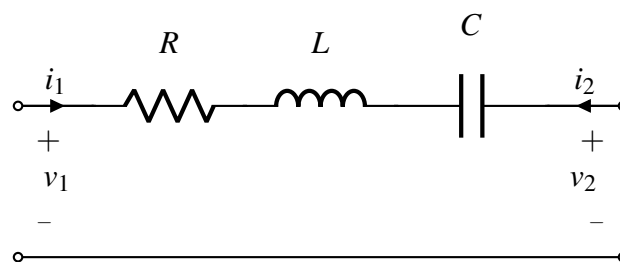


Fig. 2.14 Series RLC Circuit Model

The Series RLC resonator shown in Fig. 2.14 is presented in a two-port configuration. The resistance, R represents the real ohmic losses of the system while L and C relate to energy storage. It should be clear that the circuit can be represented by a single, complex, series impedance:

$$Z = R + j\omega L - j\frac{1}{\omega C} \quad (2.31)$$

Resonant frequency is defined as the frequency (ω_0) where the electric and magnetic stored energies become equal. This causes the reactive components of (2.31) to cancel out leaving a purely resistive impedance. Quality factor (or Q) relates the energy storage to the power loss. The equations for both are given as:

$$\omega_0 = \frac{1}{\sqrt{LC}} \quad (2.32)$$

$$Q_0 = \frac{\omega_0 L}{R} = \frac{1}{\omega_0 RC} \quad (2.33)$$

From (2.31) it is clear that the off-resonance impedance will tend to an open-circuit (LF behaviour of C , HF behaviour of L). This is illustrated for the general case in Fig. 2.15. The half-power bandwidth occurs where the impedance magnitude has risen to $R\sqrt{2}$.

Scattering parameters for transmission (S_{21}) and reflection (S_{11}) are obtained by first using the ABCD parameter identity for a series impedance:

$$\begin{bmatrix} A & B \\ C & D \end{bmatrix} = \begin{bmatrix} 1 & Z \\ 0 & 1 \end{bmatrix} \quad (2.34)$$

then by substituting the ABCD-matrix into well-known conversions, the S_{11} and S_{21} equations are found:

$$S_{11} = \frac{Z}{2Z_0 + Z} \quad (2.35a)$$

$$S_{21} = \frac{2}{Z/Z_0 + 2} \quad (2.35b)$$

These equations are plotted in both Log-Mag and in Polar/Smith form for a series RLC resonator with $f_0 = 2.45 \text{ GHz}$ and $Q_0 \approx 200$ in Fig. 2.16.

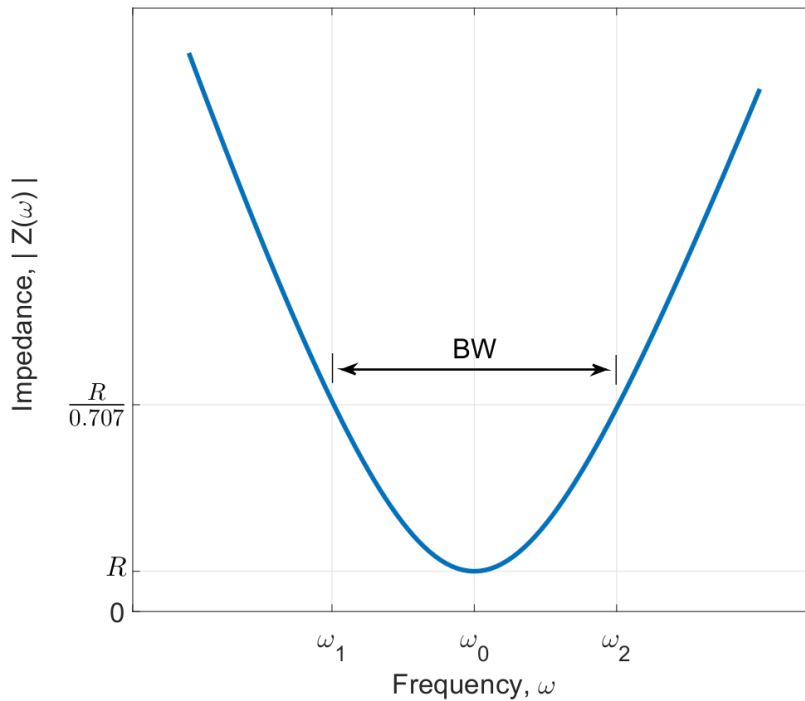


Fig. 2.15 Series RLC impedance response. Plot was obtained from simulation and normalised for illustrative purposes. Scales are arbitrary.

Reflection Response

The log-mag plot (Fig. 2.16a) shows total reflection when off-resonance moving to maximum absorption at the resonant frequency. The curve is almost parabolic in shape having a sharp response about f_0 .

The smith chart (Fig. 2.16c) shows that the resonance forms a circle. The two points of interest are f_0 and the "detuned point" being the off-resonance response. These points sit opposite each other on a circle centred on the real axis, with the detuned point being stuck to the edge of the smith chart indicating total-reflection as an open-circuit (consistent with (2.31)).

Transmission Response

The log-mag plot (Fig. 2.16b) shows zero transmission when off-resonance moving to a maximum at the resonant frequency. This curve is often compared to a Lorentzian in shape and has a much flatter response about f_0 when compared with S_{11} .

The polar plot (Fig. 2.16d) forms a circle. Similar to the reflection response this circle is centred on the real-axis, in this case however the detuned point lays at the

origin with f_0 opposite on the circle. It is worth noting that for the series RLC both the transmission and reflection responses are in-phase.

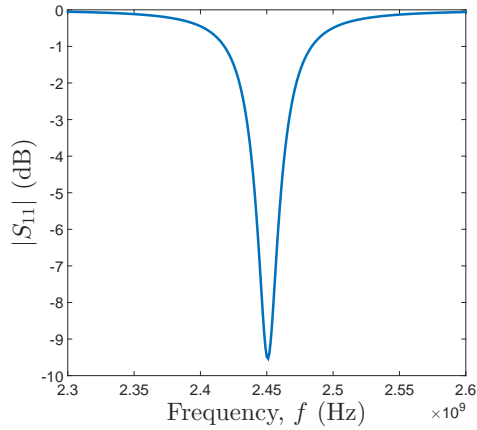
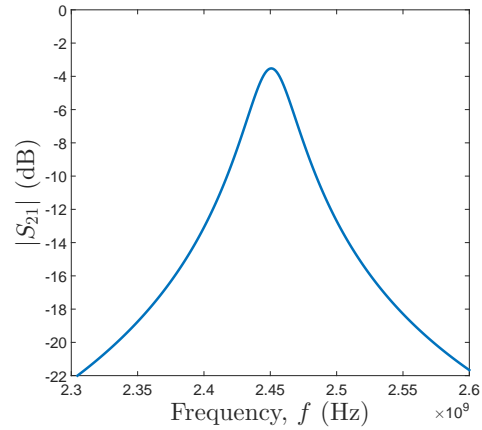
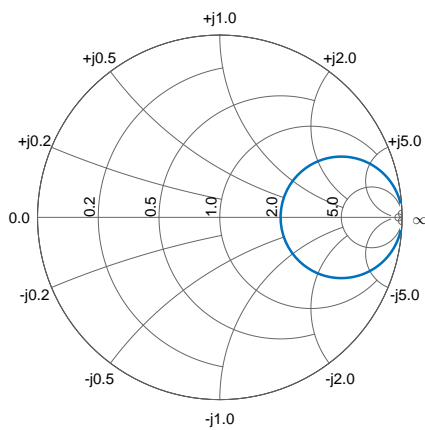
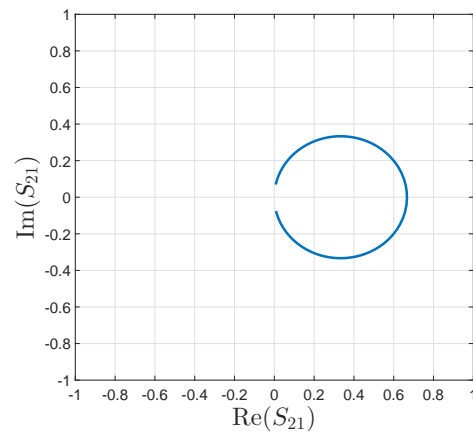
(a) S_{11} Log-Mag Plot(b) S_{21} Log-Mag Plot(c) S_{11} Smith Plot(d) S_{21} Polar Plot

Fig. 2.16 Reflection and Transmission characteristics of a series RLC resonator. Component values used were $R = 50\Omega$, $L = 660nH$, and $C = 6.39fF$. S-Parameters were obtained analytically and calculated in Matlab using $Z_0 = 50\Omega$.

2.4.3 Parallel RLC Circuit Model

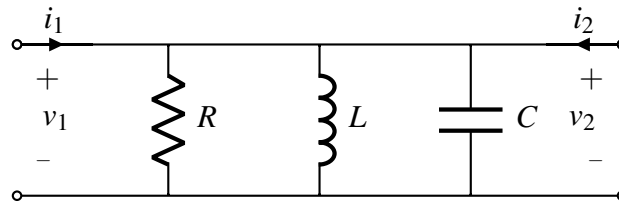


Fig. 2.17 Parallel RLC Circuit Model

The Parallel RLC resonator shown in 2.17 is presented in two-port configuration. As with the series resonator; R represents the real ohmic losses of the system while L and C relate to energy storage. This circuit can be represented by a single, complex, shunt impedance:

$$Z = \left(\frac{1}{R} + \frac{1}{j\omega L} + j\omega C \right)^{-1} \quad (2.36)$$

As with the series resonator; resonance occurs when the electric and magnetic stored energies are equal. This will also cause them to cancel out in 2.36 leaving a purely resistive impedance. Equations for ω_0 and Q_0 are given below, note that while the equation for ω_0 is the same as for the series case, the Q is proportional to R for the parallel case.

$$\omega_0 = \frac{1}{\sqrt{LC}} \quad (2.37)$$

$$Q_0 = \frac{R}{\omega_0 L} = \omega_0 RC \quad (2.38)$$

Examining (2.36) reveals that the off-resonance impedance will tend to a short circuit (LF behaviour of L , HF behaviour of C) and is illustrated in Fig. 2.18 for the general case. The half-power bandwidth occurs where the impedance has dropped to $R/\sqrt{2}$.

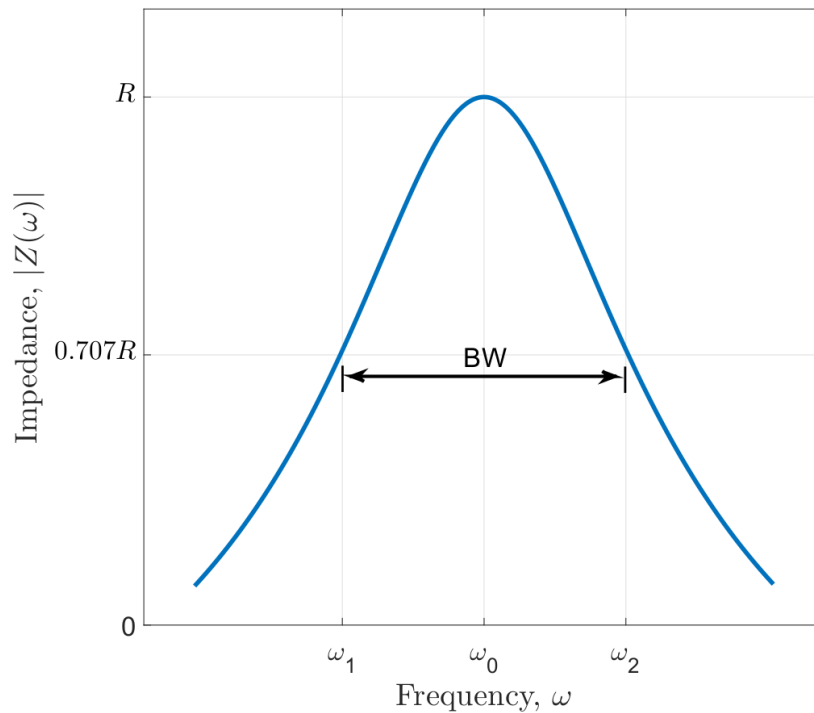


Fig. 2.18 Parallel RLC impedance response.

As with the series case the scattering parameters for transmission (S_{21}) and reflection (S_{11}) can be found using the ABCD parameter identity for a shunt admittance ($Y = 1/Z$):

$$\begin{bmatrix} A & B \\ C & D \end{bmatrix} = \begin{bmatrix} 1 & 0 \\ \frac{1}{Z} & 1 \end{bmatrix} \quad (2.39)$$

and then substituting into the well-known conversions:

$$S_{11} = \frac{-Z_0}{Z_0 + 2Z} \quad (2.40a)$$

$$S_{21} = \frac{2}{Z_0/Z + 2} \quad (2.40b)$$

These equations are then plotted in Log-Mag and Polar/Smith form for a Parallel RLC resonator with $f_0 = 2.45\text{GHz}$ and $Q_0 \approx 200$ in Fig. 2.19. The same values of f_0 and Q were used to aid in comparison.

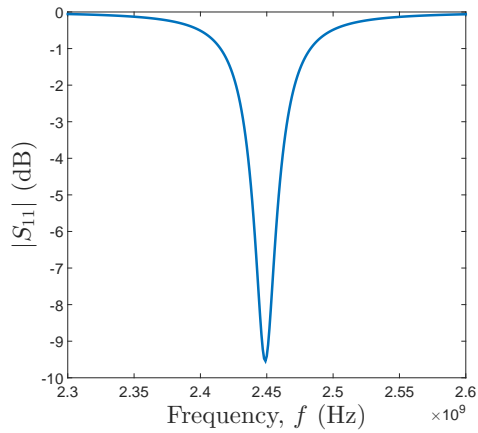
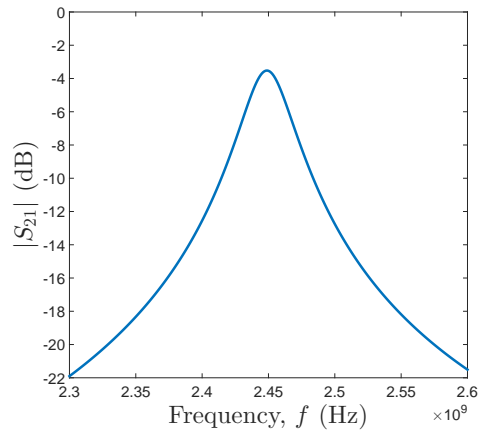
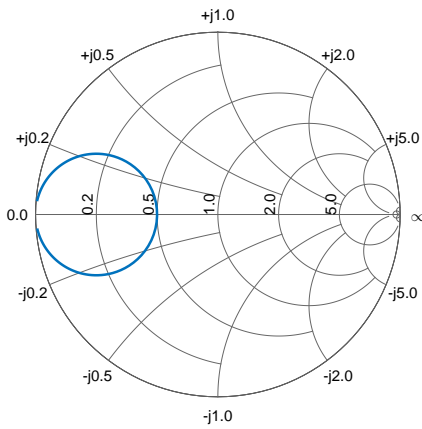
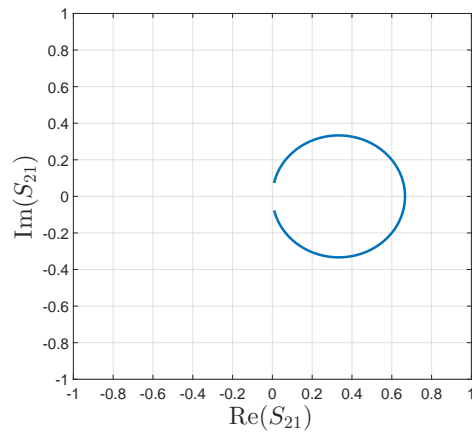
(a) S_{11} Log-Mag Plot(b) S_{21} Log-Mag Plot(c) S_{11} Smith Plot(d) S_{21} Polar Plot

Fig. 2.19 Reflection and Transmission characteristics of a parallel RLC resonator. Component values used were $R = 50\Omega$, $L = 16.5pH$, and $C = 256pF$. S-Parameters were obtained analytically and calculated in Matlab using $Z_0 = 50\Omega$.

Reflection Response

The reflection response is in many ways similar to that of the series case. There is almost total reflection in the off-resonance region with maximum absorption at f_0 as shown on Fig. 2.19a. The main difference can be seen on the smith plot in Fig. 2.19c where the response is still a circle centred on the real-axis however due to the off-resonance impedance illustrated in Fig. 2.18, the detuned point sits on the short-circuit position and thus will give a 180° phase shift.

Transmission Response

Transmission for the parallel case is identical to that of the series and possesses the same features of interest. A flatter response at f_0 in log-mag compared to the reflection response, and the complex plot having it's detuned point at the origin. Unlike reflection there is no phase shift for transmission.

2.5 Microwave Cavity Resonators

2.5.1 Introduction

In this section we discuss the microwave cavity resonator in more detail. Along with equations for resonant modes an equivalent circuit model is used to derive equations for the transmission and reflection response. Two common methods of obtaining values for resonant frequency (f_0) and unloaded Q-factor (Q_0) are shown.

A microwave cylindrical (or rectangular) cavity is a deceptively simple structure, being just a hollow conducting cylinder. They are commonly made from high conductivity metals such as aluminium or copper. In the same way that an RLC circuit facilitates a resonance through electric and magnetic energy storage of the capacitor and inductor, a microwave cavity resonator allows a resonance through storage of these same energies in the electric and magnetic fields. These fields exist as a result of standing electromagnetic waves in satisfaction of Maxwell's equations. The frequency of these electromagnetic modes is partially derived in the following subsection; for a full derivation including that of the field distribution see [46].

2.5.2 Electromagnetic Modes of a Cavity Resonator

In order to solve for the fields and resonant frequencies of a cylindrical resonator we start with the circular waveguide as depicted in Fig. 2.20 for a cylindrical coordinate

system. The space within the cavity is source free, so Maxwell's equations can be written as

$$\nabla \times \vec{E} = -j\omega\mu\vec{H} \quad (2.41)$$

$$\nabla \times \vec{H} = j\omega\varepsilon\vec{E} \quad (2.42)$$

where \vec{E} and \vec{H} are the vector electric and magnetic fields, ω is the angular frequency, and μ and ε are the permeability and permittivity respectively.

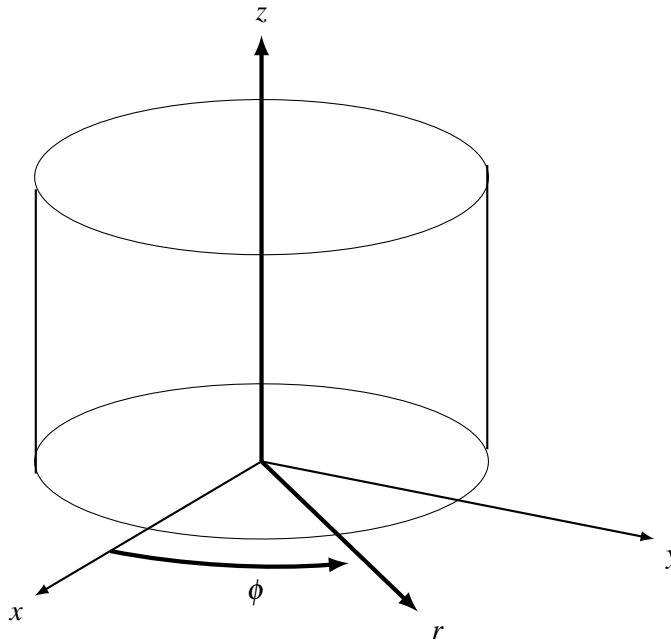


Fig. 2.20 Cylindrical coordinate system for cylindrical cavity waveguide.

Cylindrical waveguide modes are separated into either *Transverse Electric*, TE or *Transverse Magnetic*, TM modes depending on which field component is zero in the direction of propagation (z , by convention). Solving for the curl of \vec{E} and \vec{H} in the above equations for cylindrical coordinates, yields expressions for the transverse fields in terms of z . For TE modes $E_z = 0$ and so the wave equation can be solved for H_z

$$\nabla^2 H_z + k^2 H_z = 0 \quad (2.43)$$

where the wave number $k = \omega\sqrt{\mu\varepsilon}$.

The method of separation of variables is used and the solution found is of the form

$$h_z(\rho, \phi) = (A \sin n\phi + B \cos n\phi) J_n(k_c \rho) \quad (2.44)$$

where $k_c^2 = k^2 - \beta^2$ is the cut-off wave number and $e^{-j\beta z}$ is the phasor associated with propagation. The lower case h is used to indicate this is only the transverse variation.

In this solution A and B are arbitrary amplitude constants, n is an integer (as h_z must be periodic in ϕ), and J_n is a Bessel function of the first kind.

The azimuthal (ϕ) component of the H field is sinusoidal while the radial (ρ) component is a Bessel function. In order to find the cut-off wave number the boundary condition $E_{tan} = 0$ at the waveguide wall is used.

As $E_z = 0$ always for the TE mode we only need apply the condition to the azimuthal component such that $E_\phi(\rho, \phi) = 0$ when $\rho = a$. The general formula for $E_\phi(\rho, \phi, z)$ can be simplified using $E_z = 0$ and substituting in the formula for H_z , this yields the transverse variation

$$e_\phi(\rho, \phi) = \frac{j\omega\mu}{k_c}(A \sin n\phi + B \cos n\phi)J'_n(k_c\rho) \quad (2.45)$$

where $J'_n(k_c\rho)$ is the derivative of the first kind Bessel function. Therefore for E_ϕ to become 0 at the wall we require $J'_n(k_c a) = 0$, and so

$$k_c = \frac{P'_{nm}}{a} \quad (2.46)$$

where P'_{nm} denotes the m th root of the derivative of the first kind Bessel function $J'_n(x)$. This allows the writing of the propagation constant (β) as

$$\beta_{nm} = \sqrt{k^2 - k_c^2} = \sqrt{k^2 - \left(\frac{P'_{nm}}{a}\right)^2} \quad (2.47)$$

This is the result for a waveguide TE_{nm} mode. To find the result for a cavity we once again apply the $\hat{n} \times \vec{E} = 0$ boundary condition at the cavity end walls. This requires that $E_\phi = E_\rho = 0$ when $z = 0$ or d . As there will be transverse waves propagating in both directions we have

$$\vec{E}_t(\rho, \phi, z) = \vec{e}(\rho, \phi)(A^+ e^{-j\beta_{nm}z} + A^- e^{j\beta_{nm}z}) \quad (2.48)$$

To satisfy the boundary condition we first set $A^+ = -A^-$ and apply Euler's identity

$$\vec{E}_t(\rho, \phi, z) = \vec{e}(\rho, \phi)(-2A j \sin(\beta_{nm}z)) \quad (2.49)$$

For the sine term to equal zero at the end walls we must have $\beta_{nm}d = l\pi$ for $l = 0, 1, 2, 3, \dots$. Inserting this into the equation for propagation constant and solving for wave number gives

$$k = \omega\sqrt{\mu\varepsilon} = \sqrt{\left(\frac{P'_{nm}}{a}\right)^2 + \left(\frac{l\pi}{d}\right)^2} \quad (2.50)$$

Finally the resonant frequency of TE_{nml} cylindrical cavity modes is

$$f_{nml} = \frac{c}{2\pi\sqrt{\mu_r\varepsilon_r}} \sqrt{\left(\frac{P'_{nm}}{a}\right)^2 + \left(\frac{l\pi}{d}\right)^2} \quad (2.51)$$

The same analysis can be applied for TM_{nml} modes giving

$$f_{nml} = \frac{c}{2\pi\sqrt{\mu_r\varepsilon_r}} \sqrt{\left(\frac{P_{nm}}{a}\right)^2 + \left(\frac{l\pi}{d}\right)^2} \quad (2.52)$$

where P_{nm} is the m th root of the first kind Bessel function $J_n(x)$.

It should be evident then that the resonant frequencies of any mode in a cylindrical cavity are factors of the height (d), radius (a), and the relative permittivity/permeability of any spacer material present.

Another interesting facet is that for each the TE and TM modes there are an *infinite* number of theoretical modes at increasing frequency. In practice this merely serves to "clutter" the spectrum of resonances at higher frequencies, indeed as it is often preferred to excite one mode in isolation it is common practice for TM_{nm0} cavities to deliberately make the cavity as short as possible. As TM_{nm0} modes have no dependency on d and so they remain at the desired frequency, those modes that do however are shifted to higher frequencies. Unfortunately this is a merit available to TM modes only as the TE counterpart cannot exist due to the boundary conditions imposed at the cavity ends. This is all illustrated for the first few modes of a general cylindrical cavity in Fig. 2.21 where the response has been normalised to the geometry.

2.5.3 Equivalent Circuit Model Analysis

In a practical usage scenario a cavity by itself will do nothing unless coupled to by some external source. This can be achieved either capacitively to the electric field or

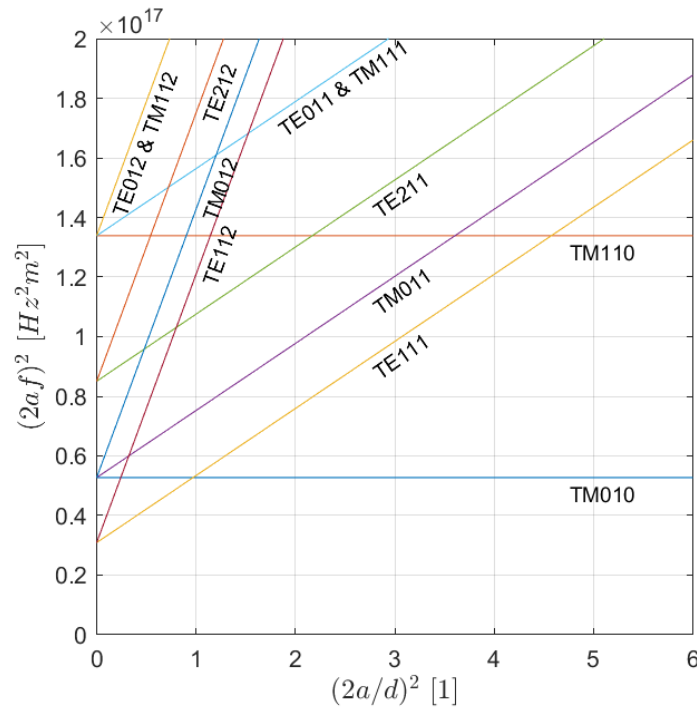


Fig. 2.21 Resonant mode chart of the cylindrical cavity. Data generated in Matlab using equations for frequency of TE and TM modes.

inductively to the magnetic field. The exact structures used to achieve this coupling in the work conducted here tend to be either probe or loop terminated transmission lines.

The microwave cavity system can be modelled as a lump impedance coupled to two transmission lines. The "2-port" configuration is primarily used for measurements due to the greater degree of accuracy when evaluating Q_0 . The equivalent circuit shown in Fig. 2.22 is of the inductively coupled resonator. Here the mutual inductances are used to represent coupling by loop terminated transmission lines.

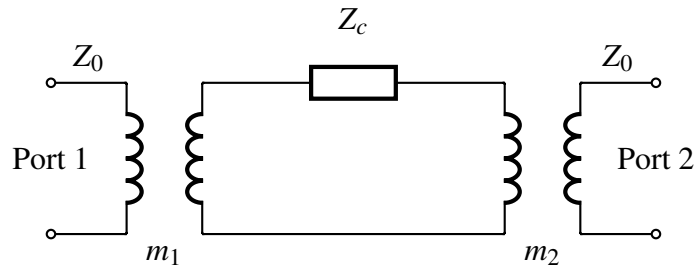


Fig. 2.22 Equivalent circuit model for 2-port cavity resonator. Z_c is the lumped impedance of the resonator, Z_0 is the characteristic impedance of transmission lines, and m_1 and m_2 are mutual inductances representing coupling.

In this case we apply the model of the series RLC circuit for the resonator lumped impedance. By combining the ABCD transfer matrices associated with the series RLC circuit and the coupling loops (which behave like transformers) the forward voltage transfer equation in the frequency domain is found as [69]

$$S_{21}(f) = \frac{2\sqrt{g_1 g_2}}{1 + g_1 + g_2 + 2jQ_0 \frac{f-f_0}{f_0}} \quad (2.53)$$

where g_1 and g_2 are dimensionless coupling coefficients defined by

$$g_n = \frac{\omega_0^2 m_n^2}{Z_0 R} = \frac{\omega_0 m_n^2 Q_0}{L} \quad (2.54)$$

where $n = 1$ or 2 .

The resultant power transmission coefficient is found from the forward voltage transfer as

$$P(f) = |S_{21}|^2 = \frac{4g_1 g_2}{(1 + g_1 + g_2)^2 + 4Q_0^2 \left(\frac{f-f_0}{f_0}\right)^2} \quad (2.55)$$

2.5.4 Evaluating Q_0 From Measurement

Accurate measurement of f_0 and Q_0 are fundamental for microwave measurements. To that end numerous methods exist and a large amount of effort has been put into developing them to be robust and precise methods. The 3 dB and Lorentzian fit methods will be discussed here, however other methods such as the circle fit and resonance curve area methods are also widely used [70–73]

The Lorentzian Fit Method

The power transmission equation (2.55) forms a Lorentzian line shape. Through use of curve fitting methods the value of the resonant parameters g , Q_0 , and f_0 can all be determined to a high degree of accuracy [70, 74] with relatively few measurements.

Assuming symmetric coupling such that $g_1 = g_2 = g$, at resonance where $f = f_0$ (2.55) can be reduced to give the peak transfer value

$$P_0 = \left(\frac{2g}{1 + 2g}\right)^2 \quad (2.56)$$

Next we define a loaded quality factor, Q_L to account for the coupling loss as so

$$Q_L = Q_0 \left(1 - \sqrt{P_0}\right) \quad (2.57)$$

The above two results allow the simplification of the power transfer to the Lorentzian form

$$P(f) = \frac{P_0}{1 + 4Q_L^2 \left(\frac{f-f_0}{f_0}\right)^2} \quad (2.58)$$

For the purposes of curve fitting it is useful to redefine (2.58) in terms of fitting parameters. This is achieved by first expanding the frequency term in the denominator to a quadratic

$$\left(\frac{f-f_0}{f_0}\right)^2 = \left(\frac{f}{f_0} - 1\right) \left(\frac{f}{f_0} - 1\right) = 1 - 2\left(\frac{f}{f_0}\right) + \left(\frac{f}{f_0}\right)^2 \quad (2.59)$$

This result can then be substituted back into the original equation, then by grouping powers of f allows the writing of the formula in terms of fitting parameters a_0 , a_1 , and a_2 . This generalised form is better suited for least squares curve fitting methods such as the Levenberg-Marquardt method.

$$P(f) = |S_{21}|^2 = \frac{P_0}{1 + 4Q_L^2 - 8Q_L^2 \left(\frac{f}{f_0}\right) + 4Q_L^2 \left(\frac{f}{f_0}\right)^2} = \frac{a_0}{1 + a_1 f + a_2 f^2} \quad (2.60)$$

In most cases solvers will attempt to do much of the work automatically but it is sometimes still necessary to inform the Jacobian matrix directly by finding the partial derivatives. In such cases the definitions given below will do fine for most solvers

$$\frac{\partial P}{\partial a_0} = \frac{1}{1 + a_1 f + a_2 f^2} \quad (2.61a)$$

$$\frac{\partial P}{\partial a_1} = \frac{-a_0 f}{(1 + a_1 f + a_2 f^2)^2} \quad (2.61b)$$

$$\frac{\partial P}{\partial a_2} = \frac{-a_0 f^2}{(1 + a_1 f + a_2 f^2)^2} \quad (2.61c)$$

Additional steps may be taken to normalise the data before passing it to the solver. This

is largely done so that the same optimisations can be used for multiple data sets. Once complete the returned values for fitting parameters can be used to calculate values for f_0 , Q_0 , and P_0 .

The three-point 3dB Method

Another even simpler method of attaining the value of Q_0 is the 3 dB method. Rather than perform a curve fit one simply measures the $|S_{21}|$ frequency response at the resonance, the value of f at maximum amplitude is used for f_0 and the bandwidth is determined from the half-power points either side at -3 dB relative. In this way Q_0 can be determined from only three measurement points using the well known formula

$$Q = \frac{f_0}{BW} \quad (2.62)$$

It is worth pointing out that in this case what is actually being calculated is not the true Q_0 but rather Q_L . Further by simply assuming the maximum value as the resonant peak we are risking inaccuracies from noise effects, the influence of which will be greater at the -3 dB points.

The assumptions made here may seem a bit haphazard and it is no wonder why the unofficial name of "the rough-and-dirty 3 dB method" has been coined [74]. It is worth noting however that for low coupling strengths the value of Q_L approaches Q_0 as shown in (2.57) and at an insertion loss of -40 dB the difference between the two is 1% [69]. In certain situations then it may be favourable to deliberately weaken the coupling to reduce the systematic error in converting Q_L to Q_0 due to lack of 2 port calibration.

Chapter 3

Microwave Resonators for Power Delivery and Heating

3.1 Introduction

In this chapter the development of a microwave cavity system for magnetic heating is discussed.

The TE_{011} resonant mode is introduced and its suitability for magnetic field heating is discussed. The issue of parasitic coupling to the degenerate TM_{111} mode is explained. The elimination of this parasitic coupling through a cavity shaping technique is shown, rather than using splits or holes this method has the advantage of not only avoiding a lowered Q but actually increases it due to the lower surface area to volume ratio. A so-called "quasi-spherical" cavity is designed and manufactured to operate in the TE_{011} mode at the ISM frequency 5.80 GHz.

Finally the experimental heating setup used to perform experiments in Ch. 4 is introduced. This particular setup utilises numerous pieces of equipment including signal generators, amplifiers, power sensors, and temperature probes for the purposes of microwave heating. The system uses a resonator as the applicator and so is able to track the resonance through periodic sweeping of the frequency over a narrow span. Aside from ensuring efficient power transfer to the sample, this also enables the extraction of resonant Q which can be used to monitor changes in microwave loss of the sample during heating. In addition to measuring the temperature of the sample the system is able to maintain the sample temperature to within 0.1°C of a target temperature. This is achieved through use of PID control by setting the source pulse-width based on the sample temperature. A simple scripting feature was added to allow specific temperature profiles to be set. While the experimental setup including

hardware itself is mentioned, precise detail on the control software implementation is not included here. For additional detail please see Appendix A.

3.2 Designing a Cavity for Magnetic Heating

3.2.1 Design Requirements

When designing a microwave cavity, as with any system we must first begin by deciding on the design requirements. The overall system will need to allow the heating of metal powders to near-sintering temperatures using microwave magnetic field. Whilst heating it will need to perform measurements of sample temperature and the unloaded Q-factor. The cavity itself is one part of a wider system, the complete measurement setup is covered later on in this chapter. Here we shall consider only the requirements of the cavity.

High-Temperature Heating

The main requirement of the cavity will be to facilitate efficient high-temperature heating using microwave magnetic field, this will inform our choice of operation frequency, and which resonant mode to use. The choice of frequency will need to be made to maximise magnetic dipole absorption for the range of particle sizes and sample conductivities which will be encountered. The resonant mode chosen will need to have a focused magnetic field maxima at the sample location, large enough to expose as much of the sample as possible. As the samples will be placed at the centre of the cavity in quartz tubing, the magnetic field maximum should also be on the axis.

Temperature Measurement

The measurement of temperature can be achieved through mounting of a suitable temperature sensor. With microwave cavities any ingress into the volume should be avoided as it can cause interference with the field distribution, for this reason an infra-red pyrometer would be most appropriate as discussed in Ch. 2. The only requirement for using these sensors is that the distance to sample must be within the focal range of the sensor.

Resonance Measurement

The measurement of resonant properties will be achieved using a 1-port measurement technique described later on. The accuracy of this measurement will depend on the

ratio of the unloaded cavity Q-factor when empty to its value when loaded by the sample. The cavity should therefore be designed to maximise Q-factor as much as possible.

3.2.2 Operation Frequency

As discussed in the design requirements the frequency used should maximise magnetic dipole absorption. The magnetic dipole absorption of small conducting particles has been introduced previously, and is related to the ratio between particle size and skin depth [4, 5], which for a given frequency is dependant on conductivity. Thus the optimal frequency will be determined by the particle size distribution and the conductivity or conductivities of the powders investigated. This can be expressed by substituting the optimal ratio into the skin depth equation and solving for frequency as shown below:

$$a = 2.41\delta \quad (3.1a)$$

$$\delta = \sqrt{\frac{2}{\omega\mu_0\sigma}} \quad (3.1b)$$

$$f = \frac{2.41^2}{\pi\mu_0} \frac{1}{a^2\sigma} \quad (3.1c)$$

The LPW powders used in this thesis were quoted as having particle radii normally distributed from 1 to 500 μm and typically had conductivities in the 5×10^5 to 1×10^6 S m^{-1} . This gives an upper and lower frequency bound of 6.29 THz and 1.10 kHz, taking the geometric mean gives a central frequency of 8.30 GHz. It is common practice to adjust a design so that resonance occurs at a frequency for which components are common and inexpensive such as an ISM band allocation. In this case the ISM allocation of 5.80 GHz is the closest and most obvious, while another option would be the 2.45 GHz band.

3.2.3 The TE₀₁₁ Resonant Mode

In order to meet the design requirements outlined previously the TE₀₁₁ cylindrical mode was selected. In this mode the magnetic field forms closed loops along \hat{z} with maximum field strength at the centre, and the electric field circulates in a region bound by the axis and the walls. Both field distributions are shown in Fig. 3.1 for cross sectional views from the front and the top.

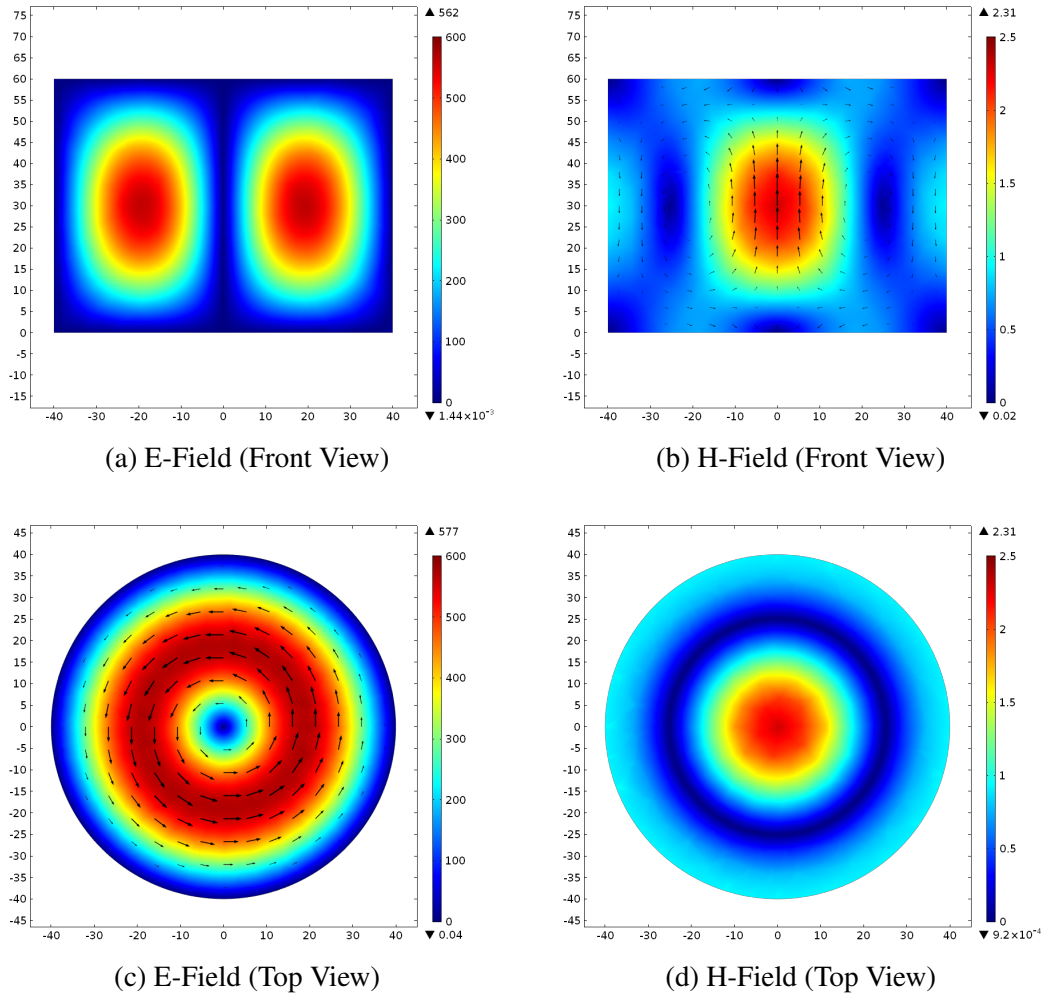


Fig. 3.1 The electric and magnetic field distributions of the TE_{011} cylindrical cavity resonant mode. Field Distributions obtained through eigenfrequency simulation in COMSOL. Physical dimensions are given in mm, field magnitudes are given in V/m and A/m for electric and magnetic fields.

Degeneracy of TE_{011} and TM_{111} Mode

Having established that the TE_{011} mode is a desirable mode to operate in, in order to excite this mode in isolation the issue of degeneracy with the TM_{111} mode must be addressed. Degeneracy of a mode refers to them sharing the same frequency. By definition a TE_{0ml} mode is said to be degenerate in frequency with the TM_{1ml} modes always. This becomes clear when comparing the equations for their resonant frequency, and so from (2.51) and (2.52) we have

$$TE, f_{0ml} = \frac{c}{2\pi\sqrt{\mu_r\epsilon_r}} \sqrt{\left(\frac{P'_{0m}}{a}\right)^2 + \left(\frac{l\pi}{d}\right)^2} \quad (3.2)$$

$$TM, f_{1ml} = \frac{c}{2\pi\sqrt{\mu_r\epsilon_r}} \sqrt{\left(\frac{P_{1m}}{a}\right)^2 + \left(\frac{l\pi}{d}\right)^2} \quad (3.3)$$

For the same cavity dimensions it should be clear that the only difference between the two will be the values of P_{1m} and P'_{0m} . These are the roots of the Bessel function of the 1st kind (J) and the derivative of the Bessel function of the 1st kind (J'). The values of these roots are the same for P_{1m} and P'_{0m} and so the frequency of any TE_{0ml} and TM_{1ml} will always be the same unless some action is taken to modify the cavity.

Failure to break the degeneracy will lead to uncertainty regarding the field distribution as either mode may be excited. Additionally if the modes are only separated by a small amount in the frequency domain they may still be parasitically coupled. This is explained in more detail in Ch. 5, where the effect is that the partial excitement of the adjacent mode interferes with the evaluation of the measurement mode from transmission measurements.

There are several common techniques for breaking the degeneracy. Almost always they involve some perturbation of the unwanted mode such as by dielectric insert, a small hole, or even by adding a split to the cavity walls [33]. These modifications are made in positions where there is strong field (dielectric inserts) or high current (splits/holes) in the unwanted mode (TM_{111}) but are minimal in the operational mode (TE_{011}). Despite this consideration the effect on the operational mode is not zero and there will always be some negative impact on the Q of the mode. This is non-ideal as for high measurement sensitivity the Q_0 of the unloaded cavity should be maximised. The same goes for cavities designed for heating.

3.2.4 Isolation of TE_{011} by Intermediate Cavity Shaping

Another technique for breaking mode degeneracy is the cavity shaping method. This method modifies the geometry of the cylindrical cavity to more closely approximate that of a sphere, and in doing so the quasi-spherical cavity has the degeneracy broken as its resonant mode distribution becomes intermediary of the two geometries. This can be understood by examining the equivalences between spherical and cylindrical resonant modes, as shown in Fig. 3.2 from [75].

A spherical cavity, as compared to a cylindrical cavity, has fewer resonant modes due to a higher degree of symmetry. However because of this there is also a higher degree of degeneracy of these modes. A cylindrical cavity on the other hand has less degeneracy and many more resonant modes. However in some cases these modes are at the same frequency despite having different electromagnetic fields. As can be seen

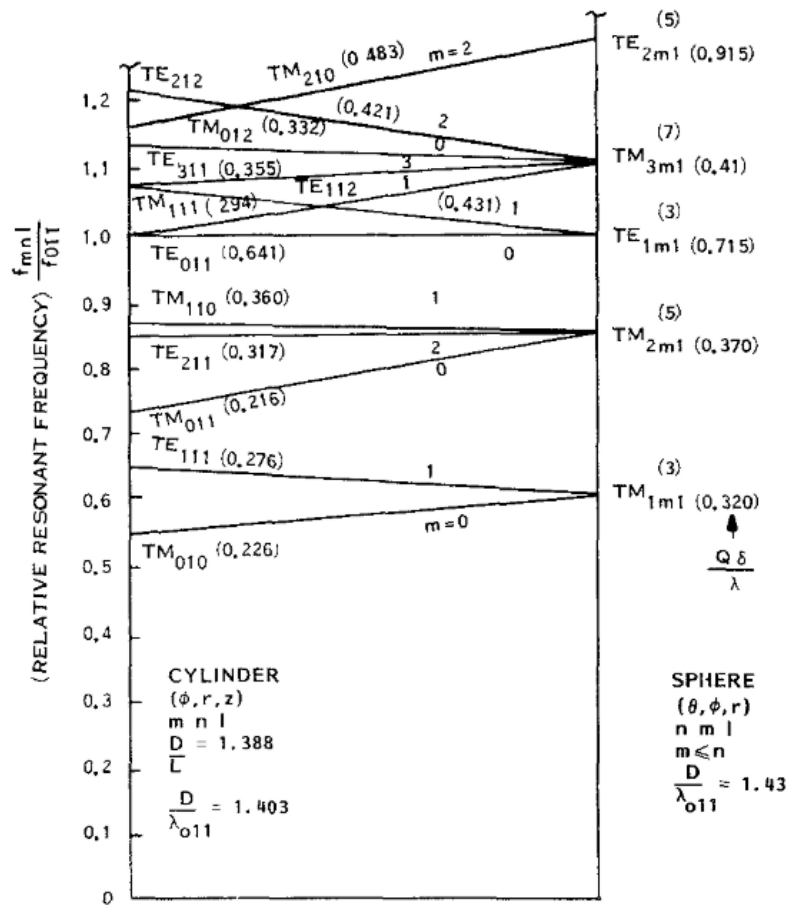


Fig. 3.2 Transition between cylindrical and spherical resonances from [75].

in Fig. 3.2 the equivalent spherical modes for TE_{011} and TM_{111} are separate but, as mentioned previously, they will be degenerate.

Instead of a completely spherical cavity, by modifying the shape of a cylinder to become quasi-spherical (intermediate of the two) it is possible to achieve mode separation whilst also avoiding introduction of additional degeneracy. These quasi-sphere shapes do not need to be particularly complicated and as will be shown a simple chamfered cylinder is sufficient to achieve the desired result. As a further benefit the Q of the quasi-spherical TE_{011} mode is slightly higher due to the increased surface-area-to-volume ratio as compared to its cylindrical counterpart.

Simulation: Mode Separation with Increasing "Sphericity"

As mentioned a revolved octagon (or chamfered cylinder) is sufficient to achieve the mode separation. In order to practically demonstrate this COMSOL was used to

simulate the increase in relative mode separation of the TE_{011} and TM_{111} modes as a cylinder is successively deformed into the revolved octagon "quasi-spherical" shape.

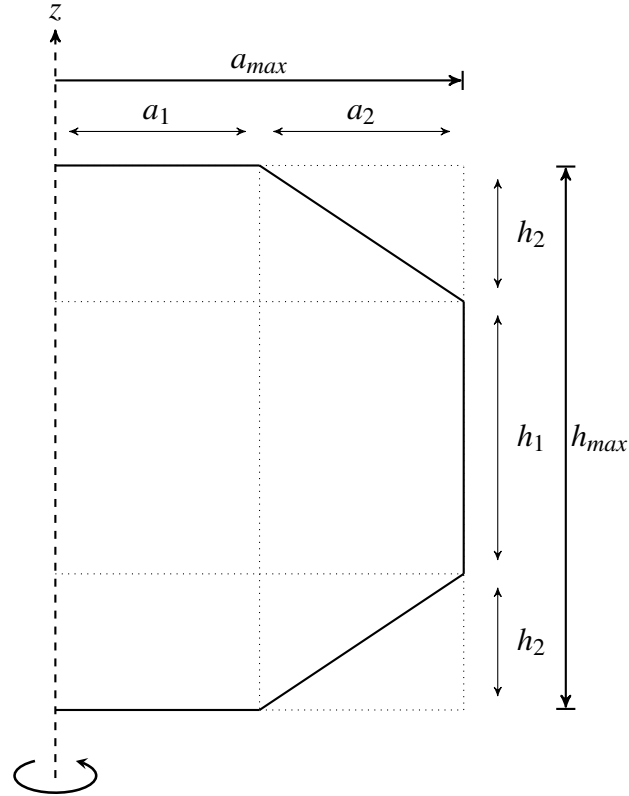


Fig. 3.3 Geometry used to investigate effect of increasing "sphericity" on the separation of TE_{011} and TM_{111} modes.

The cavity was setup using a revolved line shape as shown in Fig. 3.3 where the dimensions are defined in terms of their maximum values as well as a constant γ . The value of γ will determine the degree to which the volume is deformed from the regular cylinder shape to the more quasi-spherical form. Examining the definitions below one can see that when $\gamma = 0$ the cavity formed by the revolution will be a cylinder.

$$a_{max} = a_1 + a_2 \quad (3.4a)$$

$$a_1 = \frac{a_{max}}{\gamma + 1} \quad (3.4b)$$

$$a_2 = \gamma a_1 = \frac{\gamma a_{max}}{\gamma + 1} \quad (3.4c)$$

$$h_{max} = h_1 + h_2 \quad (3.4d)$$

$$h_1 = \frac{h_{max}}{\gamma + 1} \quad (3.4e)$$

$$h_2 = \gamma h_1 = \frac{\gamma h_{max}}{\gamma + 1} \quad (3.4f)$$

Values used in the simulation were $a_{max} = 40\text{mm}$ and $h_{max} = 60\text{mm}$, γ was swept parametrically from 0 to 1 in 0.2 steps. Electric and magnetic field distributions are shown for $\gamma = 0$ and $\gamma = 1$ in Fig. 3.5 and the change in resonant mode frequency is plotted relative to TE_{011} in Fig. 3.4.

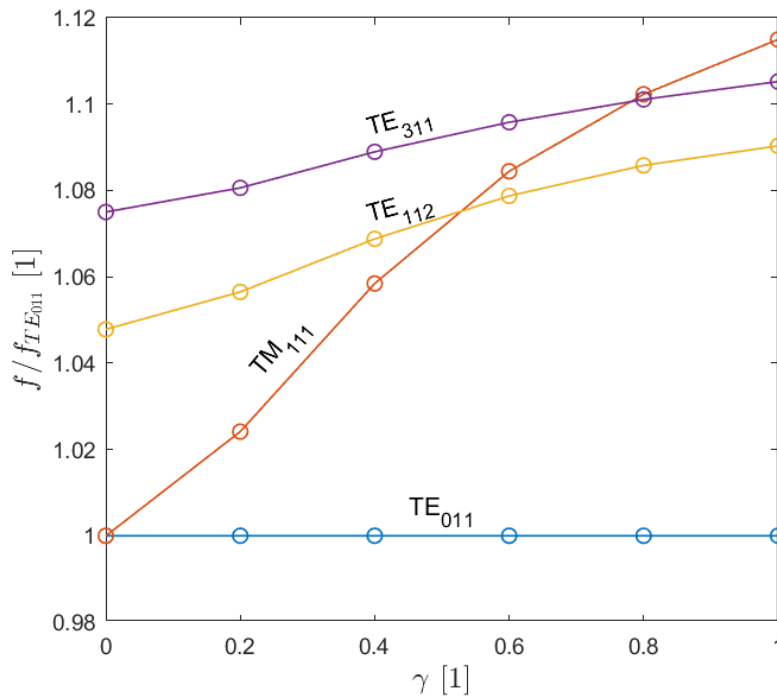
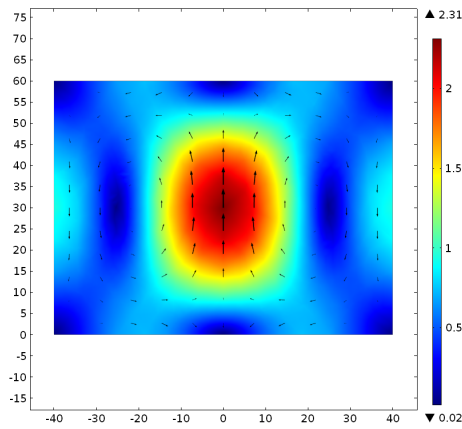


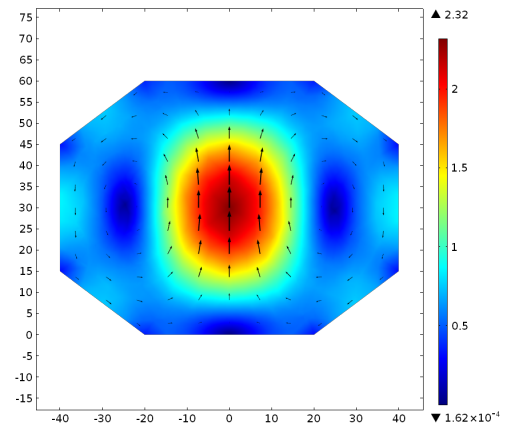
Fig. 3.4 Change in resonant frequency relative to TE_{011} with increasing chamfering of cylindrical resonator.

As can be seen the gradual change in the geometry is sufficient to cause separation of the modes. When $\gamma = 1$ the frequency of the TE_{011} mode was ≈ 5.46 GHz and the TM_{111} was shifted by about 630 MHz. From the plots in Fig. 3.5 it can also be seen the field distribution was not significantly altered.

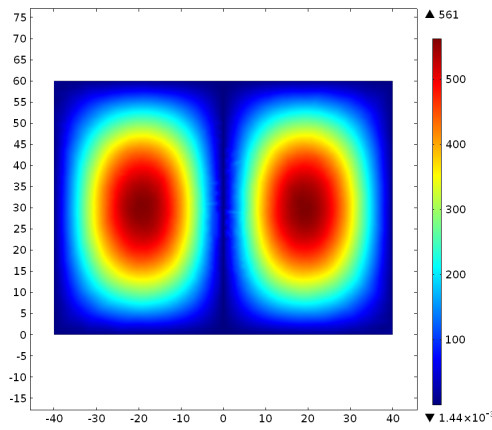
The intermediate shaping method as shown is an effective technique for breaking the $\text{TE}_{011}/\text{TM}_{111}$ degeneracy. Separation of the modes was possible with minimal modification to the cylindrical cavity. Additionally as the cavity still retained rotational symmetry it is still suited for machining on a lathe.



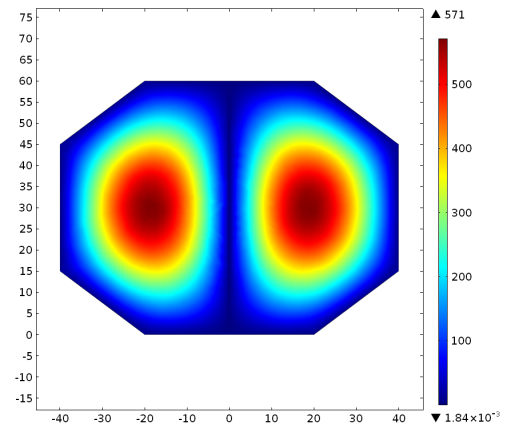
(a) Magnetic field of the TE_{011} mode for the cylindrical cavity.



(b) Magnetic field of the TE_{011} mode for the quasi-spherical cavity.



(c) Electric field of the TE_{011} mode for the cylindrical cavity.



(d) Electric field of the TE_{011} mode for the quasi-spherical cavity.

Fig. 3.5 Magnetic and electric field distribution of the TE_{011} mode for cylindrical and quasi-spherical cavity. Distributions were obtained through eigenfrequency simulation in COMSOL. Physical dimensions are given in mm, field magnitudes are given in V/m for electric field and A/m for magnetic field. Eigenmode frequency of TE_{011} was computed as 5.20 GHz for cylindrical, and 5.43 GHz for quasi-spherical cavity.

3.2.5 Cavity Design and Construction

Requirements of the final design were for a cavity designed to operate in the TE_{011} mode at a frequency near or at an ISM band such that availability of components would not be an issue. Samples would need to be able to be inserted at the axis and their temperature measured during excitation. As this cavity was designed for heating a single port would be needed for power delivery however as there may be a need for higher accuracy low-power measurements an additional two ports should be added for transmission measurements.

For sample temperature it was decided to use an infra-red (IR) pyrometer. This allowed accurate measurements of the temperature to be made without physical contact, meaning that high temperatures could be measured without risking damaging the device. To use this a small hole was required in the cavity wall to allow the pyrometer to see the sample. The focal length of the device also imposed a limit on the maximum cavity radius of 42.5 mm.

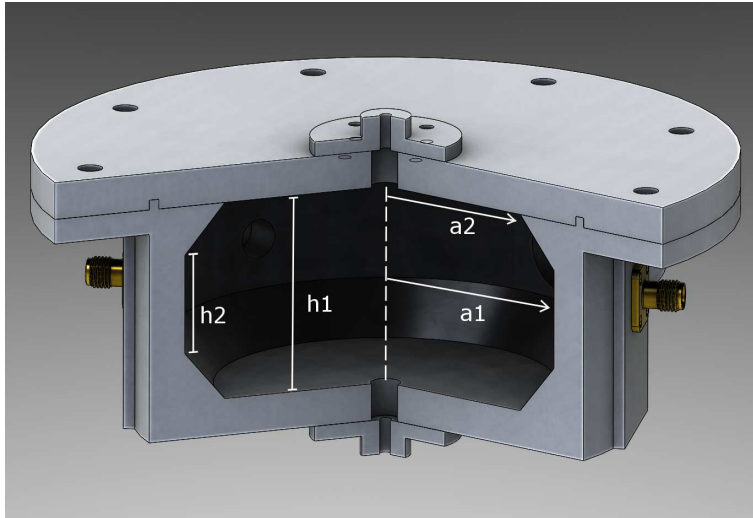


Fig. 3.6 Cutaway CAD image showing internal layout of cavity. The labelled dimensions are: $h_1 = 40$ mm, $h_2 = 20$ mm, $a_1 = 42.5$ mm, and $a_2 = 34$ mm.

Based on these requirements the cavity shown in Fig. 3.6 was designed to operate in the TE_{011} mode at the ISM frequency of 5.8 GHz. The final dimensions were found by first simulating a cylindrical cavity using the maximum radius of 42.5 mm, and then using the mode shaping technique to separate the degenerate modes. Once a sufficient separation had been achieved the cavity height was adjusted to correct for changes to the TE_{011} frequency.

The cavity was machined from 6082-T6 aluminium and its Q was measured as approximately 21,000 using a vector network analyser. Mode separation either side of TE_{011} was found to be excellent as shown in Fig. 3.7.

3.3 Experimental Setup for Microwave Heating

In this section the experimental setup and control software used for the heating and sintering experiments in Ch. 4 is discussed. This system (which was developed over a period of two years) enables the continuous excitation of resonators for the purposes of heating/sintering sample material. This is achieved largely through periodic frequency

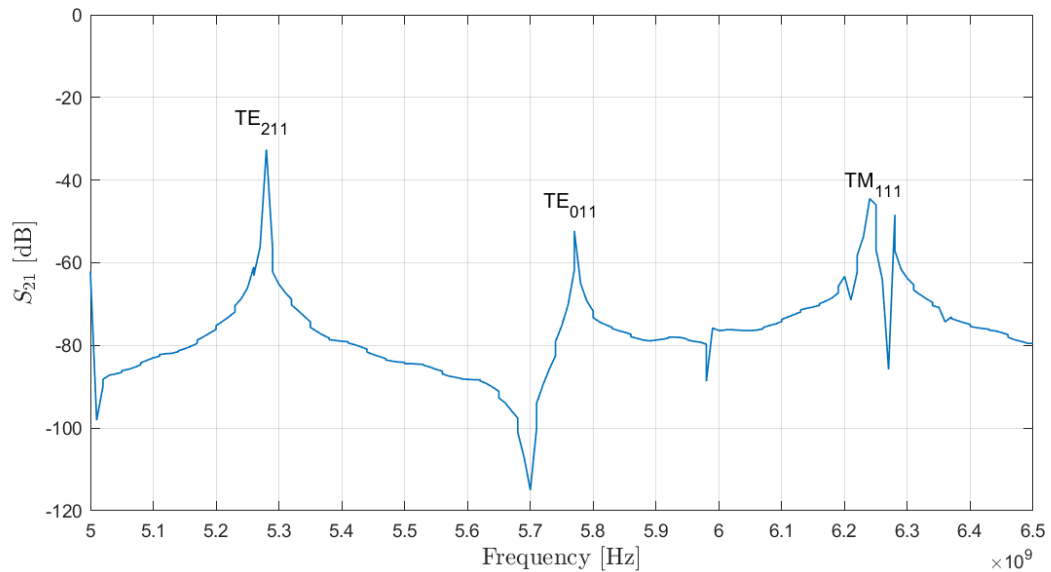


Fig. 3.7 Transmission measurement of Quasi-Sphere cavity showing isolation of TE₀₁₁ mode.

sweeps which allow the system to track changes in the resonant frequency. This ensures efficient power delivery and continuous excitation of the desired resonant mode throughout the entire process.

Additionally by manipulating the reflection response from the sweep and fitting a Lorentzian line shape, the unloaded Q of the resonator can be determined. While not as accurate as a transmission measurement, the values obtained in this way provide a useful indication of the changes related to the loss of the sample as they occur. As will be shown, if the empty resonator Q_0 is large the influence of error becomes negligible when plotting the change in loss due to the inverse proportionality between the two.

3.3.1 Hardware Configuration

The operation principle is quite simple and can easily be understood by considering the general hardware setup shown in Fig. 3.8.

As can be seen a programmable signal generator provides the excitation waveform which is then amplified by a fixed gain power amplifier. Different power levels are achieved by setting the amplitude of the input signal from the source. The signal passes through a circulator and directional coupler before reaching the resonant applicator. Typically this applicator will be a microwave resonant cavity and coupling is achieved (and adjusted) by a loop-terminated Type-N connector.

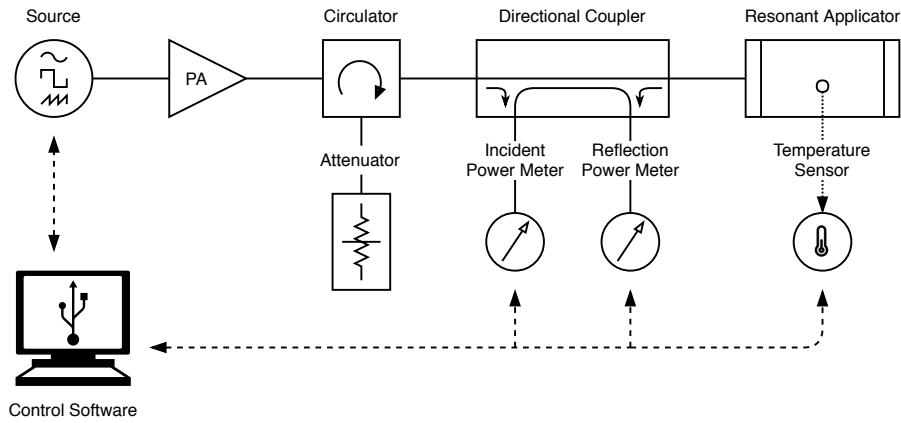


Fig. 3.8 General hardware configuration for microwave heating system.

There will be some reflection of the excitation signal at the cavity either as a result of coupling, incorrect excitation frequency, or both. This signal will travel back along the line, through the directional coupler and circulator, and into the attenuator. The directional coupler has two power meters connected which measure the forward (incident) and reverse (reflected) signals respectively. A line calibration is performed to move the reference plane for both power meters to the resonator port, which allows the reflection coefficient S_{11} to be calculated by subtracting the incident power from the reflected power. By configuring the signal generator to perform a frequency sweep, the S_{11} response of the resonator can be measured.

In this way the system is able to approximate the functionality of a scalar network analyser and by measuring the S_{11} response at regular intervals during high-power excitation, changes in resonant frequency can be tracked.

3.3.2 Measurement Principle

Consider the power loss experienced by a two-port system which is related to the transmission and reflection response as

$$P_0 = 1 - |S_{11}|^2 - |S_{21}|^2 \quad (3.5)$$

For a lossless system the value of $P_0 = 0$ and if symmetric coupling is assumed the transmission and reflection response will be related as

$$|S_{21}| = \sqrt{1 - |S_{11}|^2} \quad (3.6)$$

as discussed earlier the reflection response at resonance forms a Lorentzian line shape, which forms the basis for evaluating Q_0 from Lorentzian curve-fitting.

For a one-port system however there is no transmission, only reflection. It follows therefore that the power coupled to the resonator will be given by

$$P_0 = 1 - |S_{11}|^2 \quad (3.7)$$

It should be apparent that the curve of $\sqrt{P_0}$ will also share the same shape as the equivalent transmission response for the lossless two-port network. Lorentzian fitting strategies can therefore be applied to calculate the loaded bandwidth and centre frequency, and from these the loaded Q-factor can be calculated as

$$Q_L = \frac{f_0}{BW} \quad (3.8)$$

where BW is the loaded 3 dB bandwidth.

The advantage of determining f_0 from $\sqrt{P_0}$ as opposed to the reflection curve is that there is reduced sensitivity to missing data points near f_0 . This is especially important in the measurement setup used here as the low number of points measured mean that it is highly unlikely a point at f_0 will be measured in the first place. For a one-port network the loaded and unloaded Q factors are related by the coupling factor

$$Q_0 = Q_L(1 + g) \quad (3.9)$$

which for a single-port cavity is related to the mismatch between cavity and transmission line

$$g = \frac{Z_c}{Z_0} \quad (3.10)$$

where Z_c is the cavity lumped impedance including effects of coupling and Z_0 is the characteristic impedance of the transmission line [76].

When we talk about coupling we are actually referring to the match between the transmission line and the cavity. Depending on the ratio of Z_c to Z_0 there exist three possible coupling conditions for the one port network:

Under Coupled:	$g < 1$
Critically Coupled:	$g = 1$
Over Coupled:	$g > 1$

For critical coupling we have a perfect match and there will be zero reflection at f_0 , if the coupling were to move away from this critical value the match would be imperfect and there would be some reflection.

If phase information were available in the reflection measurements the value of g could be determined analytically, however as this is not the case with the scalar analyser setup g must be evaluated assuming both under (g_1) and over (g_2) coupling. These coefficients are evaluated from the value of the reflection at f_0 [77].

$$g_1 = \frac{1 - IL}{1 + IL} \quad (3.11a)$$

$$g_2 = \frac{1 + IL}{1 - IL} \quad (3.11b)$$

where IL is the insertion loss, which is the value of reflection at resonance ($S_{11}(f_0)$). It should be clear then that for critical coupling $IL = 0$ and $g_1 = g_2 = 1$.

In this way values for Q_0 can be determined assuming both under and over coupling.

3.3.3 Control Software

In order to coordinate the multiple devices used in the measurement setup a control program was developed and coded in NI LabVIEW. The program in its current state represents the culmination of over 2 years of development and is based on an early prototype written by Dr. Daniel Slocombe, a resident researcher and lecturer in the School of Engineering.

The original version used only a single power meter to provide a reflection reading and was written using the event-driven state-machine architecture. While useful for rapid prototyping, the event-driven state machine is ill-suited for more complex programs as operation is limited to a single execution loop. This means that if operation is waiting on a task to complete such as the resonant sweep, the user interface becomes unresponsive.

The task of improving the software was taken up and since its adoption the program has been completely overhauled, both in terms of architecture as well as available features. The overall goal for this software was to create an application which could be used by collaborators with minimal instruction and technical knowledge whilst still remaining a powerful and versatile tool for research. In the context of this work the system has largely been optimised for use in the microwave sintering of metal

compacts, to this end additional functionality such as closed-loop temperature control and a linear stage for moving the sample inside the applicator has been added.

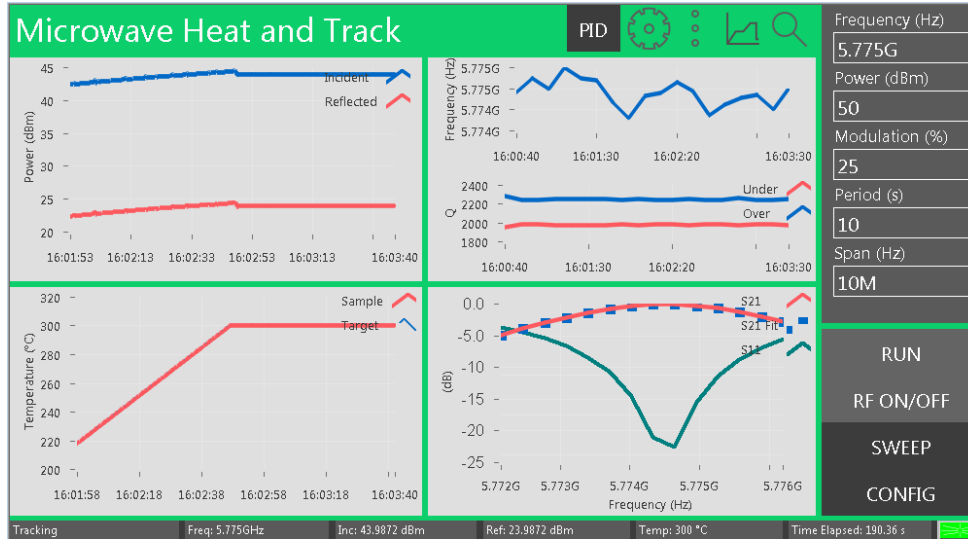


Fig. 3.9 Main user interface for the control program "Microwave Heat and Track"

The main user interface for the control software is shown in Fig. 3.9. The program performs periodic S_{11} frequency sweeps for purposes of tracking and measurement, autonomously at intervals set by the user. Additionally, closed-loop PID is utilised to perform temperature control using feedback from a connected infra-red temperature sensor (pyrometer). This enables the user to setup a desired temperature profile beforehand and the system will adjust the average power delivered to the sample accordingly to match this. As mentioned exact operation and implementation detail is not included here, however such information can be found in Appendix A.

3.4 Health and Safety for High-Power Microwaves

For the heating experiments performed in this thesis high-power microwaves are employed. Microwaves are electromagnetic waves with frequencies in the 300 MHz to 300 GHz range. Photons at these frequencies do not possess sufficient energy to ionise atoms, such radiation is therefore referred to as non-ionising radiation or NIR.

NIR can be divided into two categories: optical radiation (i.e. ultraviolet, visible, infra-red) and electromagnetic field or EMF (i.e. microwave, radio, power frequencies). For completeness we will consider the health effects of all High-Frequency (HF) EMF radiation; defined as frequencies between 100 kHz and 300 GHz by the ICNIRP [78].

3.4.1 Health Effects and Exposure Limits for HF Radiation

As HF radiation is non-ionising the primary effects of exposure relevant to health will be related to heating of exposed tissue. HF EMFs are able to penetrate the human body to a degree determined by the frequency, where a higher frequency gives a lower penetration depth. Molecules which are polar or charged will be excited by the applied fields causing them to vibrate, this results in heat generation.

The human body is able to self-regulate its internal temperature, and is able to deal with small increases in heat. Long-term exposure to HF fields at power levels low enough to not cause significant heating have not been linked to any health effects [78]. Exposure to HF radiation only becomes a problem when the heat generated is above a certain threshold, where the temperature increase can cause harm such as heatstroke or tissue damage.

Human bodies are composed of a number of different tissues, so heat generated by absorption of HF radiation will differ across the body. Different parts of the body are therefore more vulnerable to HF exposure, examples of these include the eyes and testis [78]. As such there are different recommendations for exposure limits for different parts of the body. These limits are given as specific absorption ratios (SAR) and are measured in Watts per Kilogram of body tissue (W kg^{-1}). In the UK we follow the ICNIRP 1998 and 2010 guidelines, and the SAR limits proposed by these guidelines are shown in Tab. 3.1. It is important to recognise that these are upper limits, and where possible exposure should be minimised as much as possible or entirely. As SAR is a calculation it is often more convenient to monitor power intensity when performing experiments, this is expressed in SI units of W m^{-2} .

Table 3.1 Basic SAR Limits for EMF Exposure from 100 kHz to 10 GHz

	Whole-body Avg. (W kg^{-1})	Head/Trunk (W kg^{-1})	Limbs (W kg^{-1})
Occupational	0.4	10	20
General Public	0.08	2	4

1. Values taken from ICNIRP 1998 [78].

2. SAR values are to be averaged over a 6 min period.

3.4.2 Safety Measures Employed

For the heating experiments performed in this thesis we can expect very little microwave EMF emission. No transmitting elements are used and so any emission will be due to leakage rather than design. The cables, circulator, couplers and resonant cavity are all self-shielding and designed to contain the field. There may be some emission at interconnects between cabling, or at small openings on the cavity such as the pyrometer sensor mount. These will be many times smaller than the wavelength of the microwaves however, which should act to minimise leakage much like a Faraday cage. During experiments an EMF/RF radiation sensor was used to monitor the field intensity of any EMF radiation. The ICNIRP recommend an upper limit of $5000 \mu\text{W cm}^{-2}$ for occupational exposure [78]. The sensor used measures up to $2500 \mu\text{W cm}^{-2}$ for frequencies 100 kHz - 10 GHz and so this was used as the upper limit instead.

3.5 Conclusions

Building on the basic resonator theory introduced previously, microwave resonant cavities were introduced. Equations for resonant frequency of the various TE and TM modes were given and equivalent circuit analysis was used to derive the behaviour of the two-port, inductively coupled cavity resonator. The concept of coupling was introduced and two methods of evaluating the unloaded Q were explained. The first method relied on fitting a Lorentzian curve to measured transmission data near the resonant frequency, and is widely acknowledged to provide excellent accuracy. The second method was much simpler and required a minimum of three measurements to determine the value of Q_L . This method is only accurate in the limit where the coupling strength is weak and $Q_0 \approx Q_L$, however due to its simplicity it is widely implemented on network analysers and is a useful estimate for fast/exploratory measurements.

The design of a novel microwave cavity applicator for magnetic field heating was explored. The desired attributes for resonant mode were stated and the choice to use TE_{011} was explained. The concept of frequency degeneracy between the TE_{011} and TM_{111} modes was introduced and the importance of separating the modes explained. It was shown that the intermediate shaping method can be used effectively to separate the modes without impacting the performance. In this method the cylindrical cavity is partially deformed into a quasi-spherical shape, in doing so the mode distribution becomes similar to that of a sphere and the degeneracy between TE_{0ml} and TM_{1ml} modes can be broken. The field distribution of the now quasi-spherical TE_{011} mode

was shown to be largely unaltered. A cavity design was presented based on these principles for use in magnetic microwave heating. The cavity was designed to operate in the TE_{011} mode at the ISM frequency of 5.8 GHz and the value of Q_0 was measured as around 21,000 when machined from aluminium.

Next a measurement setup for continuous excitation of resonant modes for heating was presented. The hardware configuration is able to loosely approximate the behaviour of a scalar network analyser using calibrated power meters directionally coupled to the transmission line setup. Measurement theory for determining the value of Q_0 in the single port configuration was introduced, due to the lack of phase information two values for Q_0 are evaluated assuming both under- and over-coupling. The control software used to perform and automate the experiments was introduced and the basics of operation were explained. Heating experiments are performed by using periodic sweeps to track the change in resonant frequency occurring as a result of material and temperature change. The control software can also be configured to perform closed-loop temperature control. This allows specific temperature profiles to be specified and by varying the excitation signal duty-cycle the PID controller is able to closely follow the set-point temperature.

Finally safe practices for working with high power microwaves were discussed. In the experiments performed in this thesis the fields were largely shielded and so the only concern was stray leakage, for example at interconnects. Field power meters were used to monitor any leakage to ensure exposure remained within acceptable safety limits.

Chapter 4

Microwave Sintering of Metal Powders in the Magnetic Field

4.1 Introduction

In this chapter microwave sintering of metal compacts is performed using the experimental setup described in Ch. 3. The general theories behind microwave absorption of conducting powders have been discussed in Ch. 2. In this chapter we will build on this and predictions for the changes to microwave absorption of a metal powder compact during sintering are presented and validated by experiment.

In total three experiments are performed investigating changes in microwave absorption during sintering. The first experiment investigates the changes in absorption at low temperatures where no significant sintering has occurred. The next experiment investigates the reduction in absorption at higher temperatures where solid-state sintering has occurred. Finally an in-depth study into the influence of process parameters is conducted. It is observed that the microwave absorption is highly sensitive to the changes in the powder morphology due to mass-transport even at sub-sintering temperatures where minute changes occur. The efficacy of using microwave absorption to monitor the progress of sintering non-destructively is discussed.

4.2 Microwave Heating/Sintering of Metal Powders

Already there has been much study in the field of microwave metal powder heating/sintering. Numerous reports in the literature have focused on the potential advantages over traditional furnace sintering. These studies have cited reductions in process time and sintering temperature as well as improvements in final density and strength

[32, 36, 37, 79]. These improvements are frequently attributed to the rapid heating that is experienced in microwave sintering which acts to minimise coarsening of the micro-structure [38].

The vast majority of published work involving microwave sintering uses either a multi-mode cavity or waveguide applicator to heat the green compact [36–38, 67, 80]. From a practical manufacturing perspective it is clear why this is preferred as there are few restrictions on powder compact geometry. The powder compact can be pressed and inserted into the oven, and insulators can be employed to contain the heat generated. In some cases a susceptor is used to further enhance the focused heat generation however it is worth pointing out that in this case the susceptor is generating the heat and not the sample itself. An example of this is shown in Fig. 4.1.

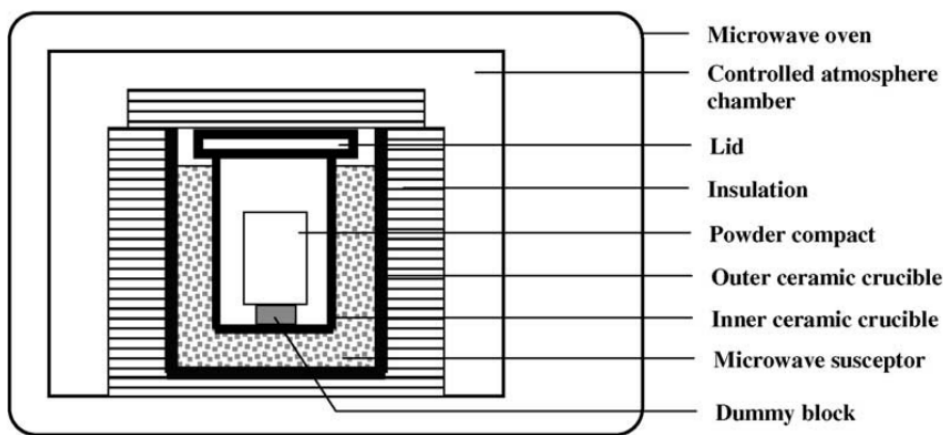


Fig. 4.1 Schematic diagram of the typical multi-mode setup used for microwave sintering [38].

One major drawback to these setups however is that they are forced to consider the electric and magnetic field interactions together rather than separately. As discussed previously for the majority of metal powder particle sizes used in sintering it will be the magnetic field effect that dominates [4, 5, 68]. In this section we are examining the changes to microwave absorption during sintering and so for purposes of study it is preferable to consider only microwave magnetic field effects.

Based on what we know of the microwave dipole loss the change in microwave absorption of a powder compact during sintering can be expected to be an overall reduction in loss. This prediction is based on the behaviour of mass transport during sintering where atoms will migrate to minimise surface free energy. This will occur in one of two ways. First there is the case where atoms will migrate from one particle into another to form a single larger particle by absorption. In this case the particle size to skin-depth ratio will have been modified and there will be a corresponding change

to the microwave magnetic dipole absorption per unit volume described by (2.26). The second case is where the atoms migrate to form particle interconnects. The action of this is to largely reduce the total surface area of the sample. As the skin-depth remains constant the effect of reducing the surface area is to decrease the volume of the sample experiencing eddy current loss. As a consequence the total power dissipated will decrease. As the growth of these interconnects continues and the sintering moves into intermediate stage there will be a further reduction in loss due to increased shielding as the sample becomes dense. The effect of shielding will be most pronounced at the centre of the sample, and initial studies where the green density has been varied indicate a noticeable reduction in internal temperature for increasing density [7].

In order to confirm this behaviour we turn to microwave cavity measurements using the experimental setup described in Ch. 3. Investigation into this behaviour is carried out through three main studies:

- First the low temperature behaviour is investigated where the sensitivity of the measurement setup is tested by observing low temperature modifications to the powder without forming a solid mass.
- Following this the high temperature behaviour is observed where sintering temperatures are achieved and the change in absorption during solid formation is observed. Scanning electron microscopy is used to confirm the micro-structure development due to sintering.
- Finally a systematic study is conducted investigating the effects of process variables. The significance of the total changes in absorption is also investigated with reference to final properties such as density and strength.

4.3 Observations of Microwave Sintering at Low Temperatures

While absolute sintering temperature is difficult to define, generally the formation of dense parts is said to occur at temperatures above half the apparent melting temperature [10–12]. Below this temperature then one would not expect to see any significant densification however that does not necessarily mean that the powder will be unmodified. As an example consider the recycling of powder in additive manufacture. Over repeated uses it has been shown that the particle size distribution gradually increases due to repeated exposure to elevated temperatures [81].

The elimination of small particles can be understood by recalling their higher surface energy per unit volume. While the relationship between the surface free energy and sintering temperature is complex and varies depending on the mass transport mechanisms in play [10], generally speaking a particle with a higher surface energy per unit volume can be expected to undergo mass transport at a lower temperature [10, 11]. The atoms undergoing mass transport will naturally migrate to a region of lower potential energy. This suggests that small particles will gradually be eliminated over repeated heating cycles as they are absorbed by larger ones or used to form weak particle interconnects.

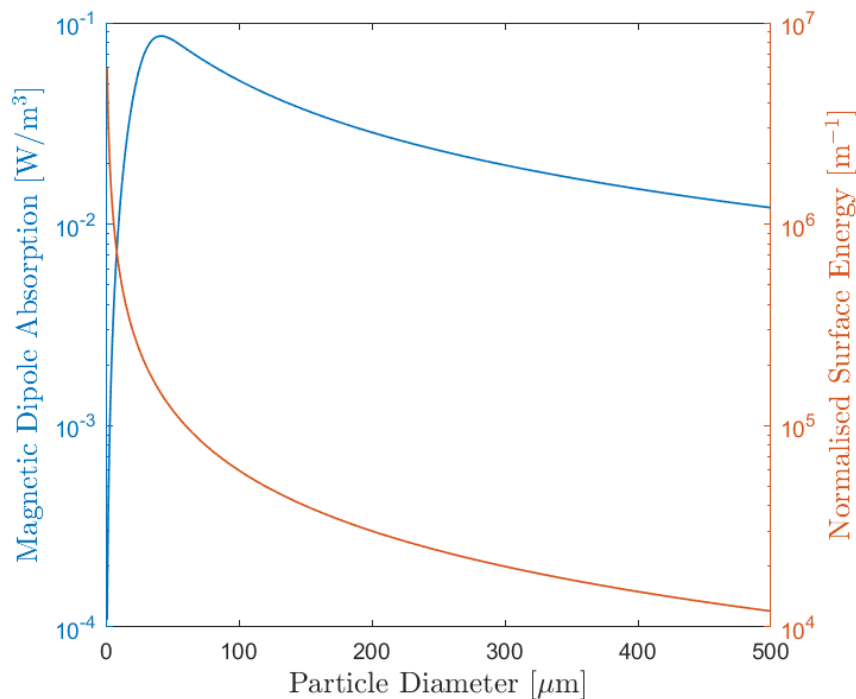


Fig. 4.2 Magnetic dipole absorption and normalised surface free energy as a function of particle radius for Ti6Al4V powder at 5.80 GHz. Plots were calculated for a magnetic field of 2.7×10^{-3} A/m. The value of σ used for Ti6Al4V was 5.88×10^5 S/m.

As discussed earlier microwave magnetic absorption will either increase or decrease with particle radius depending on whether the skin-depth is large or small with respect to the particle [5]. This is shown in Fig. 4.2 for Ti6Al4V powder at a frequency of 5.8 GHz. For the powders used in these experiments the particles are produced by gas-atomisation and their sizes typically range from 0 to 500 μm according to the manufacturer (LPW). Shown also in this plot is the normalised surface energy per unit volume which, when normalised to the surface energy density becomes the surface-area-to-volume ratio of a sphere ($3/r$).

It should be clear then by observing the plot in Fig. 4.2 that small particles in the distribution are targeted by the microwaves up to the absorption peak. Beyond this one might conclude that the small fraction of remaining particles will be unaffected due to the rapid decline in absorption. However the effect of the surface free energy acts counter to the decline in this limit. Considering also that the neighbouring particles of more absorbent radii will be acting to heat the small particles, there is precedent for mass-transport at sub-sintering temperatures albeit in small quantities.

There will be two main effects of this mass transport on the overall microwave loss of the sample powder. The atoms that undergo mass transport will tend to move to areas where their inclusion will lower the surface energy. This will either be through absorption by a larger particle or through the formation of an inter-particle bond.

The formation of weak particle interconnects will act to reduce the total surface area of the compact significantly. The microwave loss experienced by conductors is determined by the R_s and some geometric factor related to the available surface area. As surfaces are eliminated during the formation of these interconnects there will therefore be a corresponding reduction in microwave loss.

In the case where smaller particles are simply absorbed by larger ones there will be an increase in radius proportional to the cubed root of volume absorbed. This will result in either an enhancement or reduction in magnetic dipole loss of the powder, depending on the size of the particle formed for the given conditions (frequency, conductivity). If the particles formed are larger than the $a = 2.41\delta$ limit there will be a net reduction in microwave loss. Particles formed in the large skin-depth limit will see an enhancement to loss however if we assume a normal distribution of particle sizes, then for the powders used here their volume fraction will be small. Given also that small increase in radius per unit volume absorbed is small to begin with. The impact of any enhancement to dipole absorption will likely be negligible compared to the effect of surface elimination and larger particle formation in the small skin-depth limit.

Thus it is expected in general there will be a net reduction in loss for the Ti6Al4V powder supplied when sintered at 5.8 GHz in magnetic field. Given that there is enhanced absorption of small particles and also that surface energy per unit volume of such particles will be larger, the expectation for changes in absorption at lower sintering temperatures is not unfounded. We now confirm this hypothesis by experiment.

4.3.1 Experimental

Samples of Ti6Al4V titanium powder were prepared and sealed inside 100 mm long quartz capillary tubing. The tubes had an internal diameter of 2 mm, which gave a

typical sample volume of 300 μl . Two samples were sealed in air, while the remaining three were sealed in argon gas.

Before processing a Keysight N523A Vector Network Analyser was used to perform transmission measurements for each sample using the Quasi-Spherical cavity from Ch. 3. The Lorentzian curve fitting method was used to obtain the value of Q_0 .

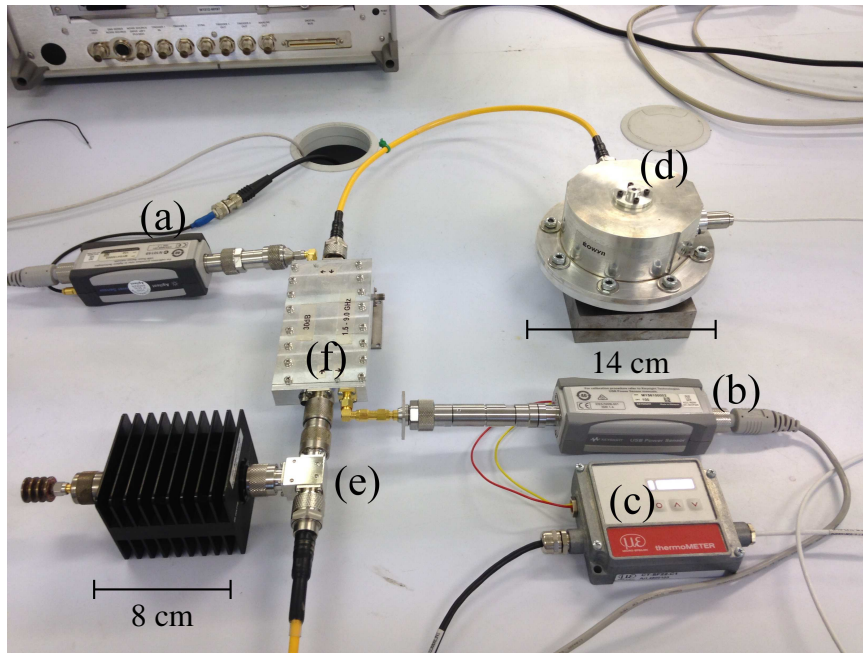


Fig. 4.3 Experimental setup. (a) Reverse power meter, (b) Forward power meter, (c) Pyrometer, (d) Cavity, (e) Circulator, and (f) Directional coupler.

The microwave heating system described in Ch. 3 was setup using the apparatus shown in Fig. 4.3. A complete list of hardware used is included in Tab. 4.1.

Table 4.1 Equipment Summary

Item	Model	Notes
Signal Generator	Keysight N5181B	
Power Amplifier	Milmega AS1860-100	
Forward Power Meter	Keysight U2000H	Average only
Reverse Power Meter	Keysight U2021XA	Peak and average
Circulator	AtlanTecRF AS7122	5.4 to 6.6 GHz
Directional Coupler	n/a [†]	1 to 18 GHz
IR Pyrometer	Micro-Epsilon CT-SF22	-30 to 975°C

[†] Bespoke unit made in-house, coupling was measured as part of setup calibration.

The source used was a Keysight MXG signal generator and power readings were taken using two Keysight USB power meters. For the frequency sweeps the power meters were triggered by the signal generator for each measurement point. A single Type-N connector with a loop termination was used to provide inductive coupling to the TE₀₁₁ resonant mode. The connector could be freely rotated and secured by a pin-screw, which allowed for manual adjustment of the coupling strength. As the loss of the sample was expected to decrease over the course of the experiment, the cavity was deliberately under-coupled to ensure acceptable power delivery throughout the experiment. Temperature was measured using a micro-epsilon USB IR Pyrometer. Emissivity was set to 0.5 which is the value given for solid titanium. It was assumed that the difference between powder and solid emissivity would not impact the results significantly. This was confirmed up to 100°C by calibrating to a contact temperature sensor, where the temperature difference between the two was found to be < 5°C.

The program was configured to perform a sweep measurement every 5 s. At the beginning of each experiment excitation was switched off for 20 s to establish a baseline measurement of Q_0 before heating. Once the 20 s had elapsed excitation was switched on for 2 min, and during this time power and temperature measurements were taken every 200 ms and resonant sweeps continued to occur every 5 s. Afterwards excitation was switched off and the sample was allowed to cool back to room temperature. During this time resonant sweeps continued to occur in order to confirm any changes in Q_0 were permanent and not a feature of the temperature.

4.3.2 Results and Discussion

A summary of the complete results series is given in Tab. 4.2. Power and temperature values given in Tab. 4.2 are the average values during "steady-state" heating (between temperature saturation and before cooling). The values for Q_0 are given before and after heating.

Comparing the measurements from VNA and the system there was close agreement in the pre-heating value. As Q_0 is reciprocal to loss the relative change in system loss can be calculated as

$$\Delta Loss = \frac{Q_{end}^{-1}}{Q_{start}^{-1}} - 1 \quad (4.1)$$

This was found to be higher for the argon sealed samples than those sealed in air.

Results for all samples have been plotted, however only results for sample A3 have been included here (as a representative sample) and are shown in Figs. 4.4, 4.5, 4.7, and 4.6. Plots for the remaining samples can be found in Appendix B.

Table 4.2 Summary of Results

Sample		Power [W]	Temp [°C]	Q_0 (Start)		Q_0 (End)	$\Delta Loss$ [%]
				VNA	System	System	
Air	A1	6.23	492	1824	1868	7415	-74.81
	A2	8.02	593	1931	2043	7453	-72.59
Argon	A3	8.05	544	1899	1954	9111	-78.56
	A4	8.04	553	1941	2056	9090	-77.38
	A5	8.00	590	1894	1460	8975	-78.90 [†]

[†]Calculated using VNA Q_0 start value.

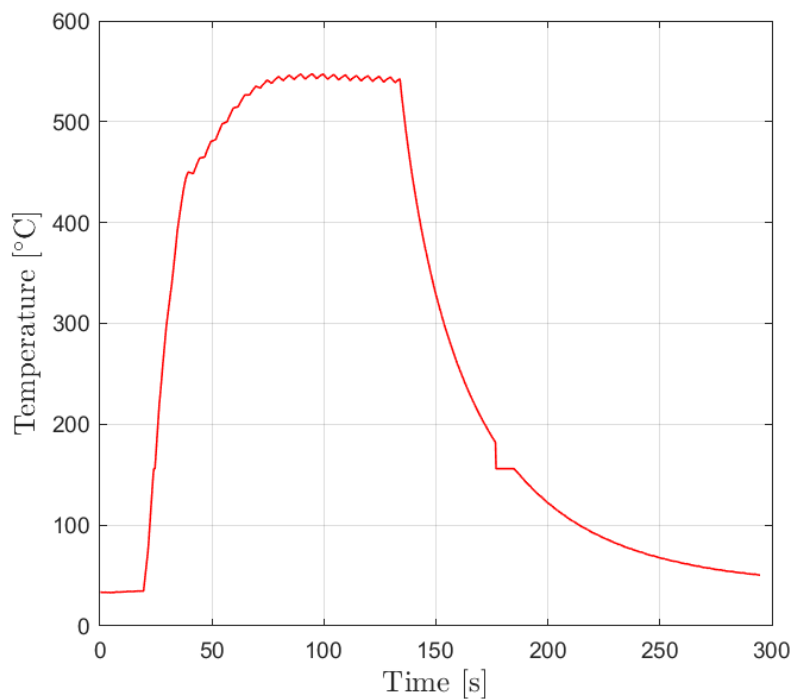


Fig. 4.4 Sample temperature during microwave excitation for sample A3 (Ti6Al4V in argon).

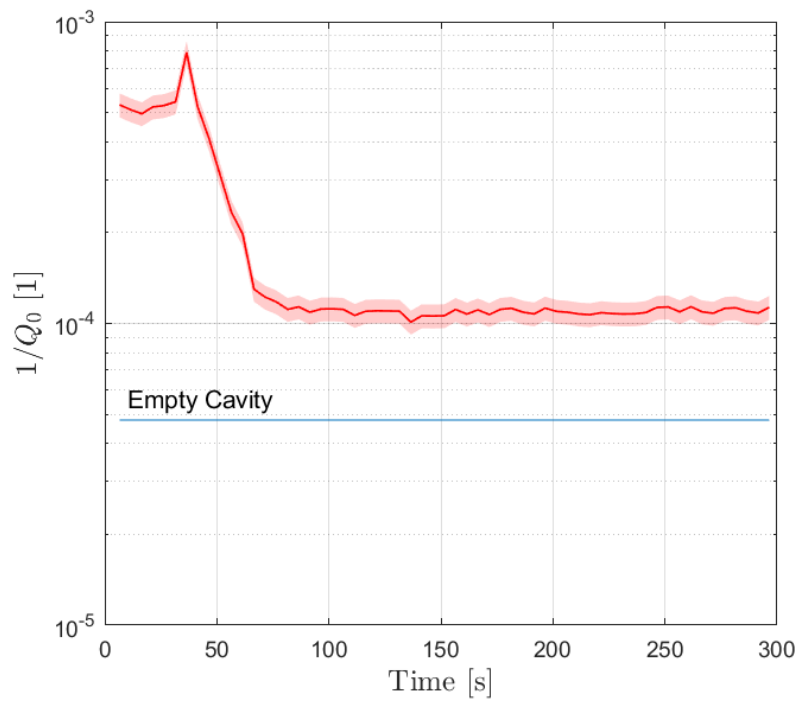


Fig. 4.5 Q_0 during microwave excitation for sample A3 (Ti6Al4V in argon).

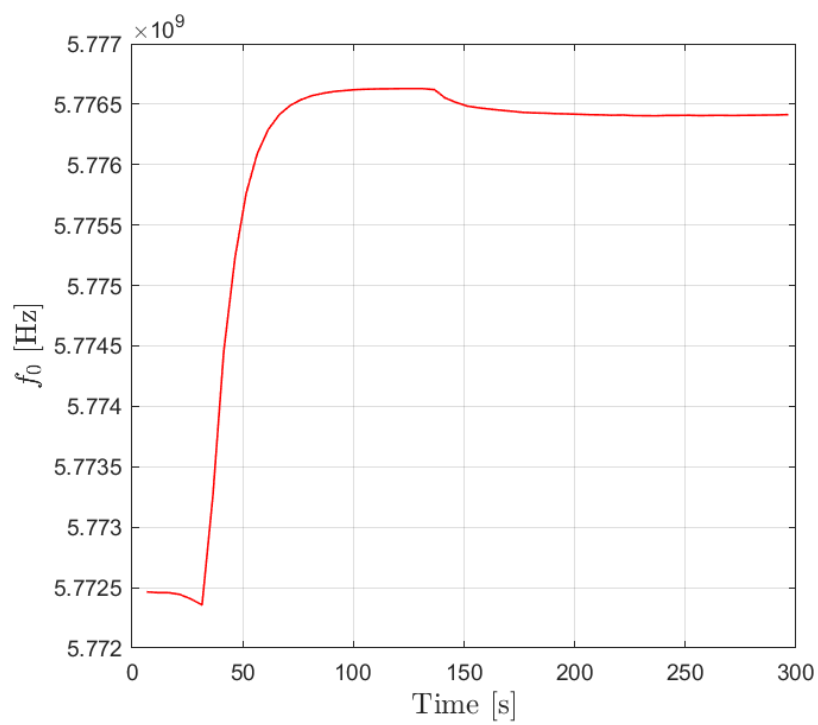


Fig. 4.6 Change in resonant frequency, f_0 during microwave excitation for sample A3 (Ti6Al4V in argon).

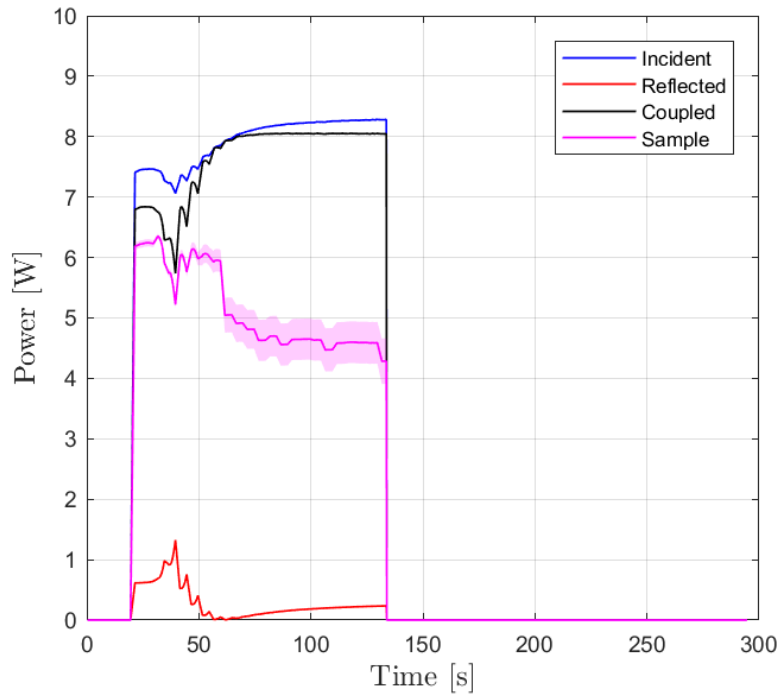


Fig. 4.7 Power absorbed by sample during microwave excitation for sample A3 (Ti6Al4V in argon).

In Fig. 4.4 the temperature of the sample as measured by IR pyrometer has been plotted. Around 175 seconds there is what resembles a notch in the series, which is due to self calibration of the sensor and is not representative of any physical phenomena.

In Fig. 4.5 the change in loss of the sample has been shown by plotting the reciprocal of Q_0 . An uncertainty of 10% in the system Q_0 measurements has been assumed and the effect of this is shown by the bounded region. For reference the value of Q_0^{-1} for the empty cavity has also been plotted, this represents the lower limit for loss of the system and was evaluated by reflection measurement using a VNA to account for the loading by the coupling loop. Change in resonant frequency has also been plotted and is shown in Fig. 4.6.

In Fig. 4.7 the power delivered to the sample has been approximated. In this plot the incident and reflected power represent actual measurement data from the sensors. Coupled power is the power absorbed by the cavity system including the sample and is calculated from the incident and reflected power readings. Sample power is the power absorbed by the sample itself and is calculated using the following formula:

$$P_{Sample} = P_{Coupled} \left(1 - \frac{Q_{Sample}}{Q_{Cavity}} \right) \quad (4.2)$$

where $P_{Coupled}$ is the coupled power, Q_{Sample} is the Q_0 value measured during heating, and Q_{Cavity} is the Q_0 of the empty cavity without the sample and was measured as 20,910 using a vector network analyser. As an uncertainty of 10% had been assumed in the Q_0 (sample) measurement, this has also been propagated to the sample power measurement.

Comparing before and after heating as expected all samples exhibited a significant and permanent increase in Q_0 indicating a reduction in microwave absorption. This was shown to be greater for argon than air sealed samples. Argon is typically used to flush nitrogen and oxygen out of the sintering environment to prevent (amongst other unwanted reactions) oxidation of the surfaces [1, 82] which is known to retard the sintering process [10–12].

Compared to the melting temperature of Ti6Al4V ($\approx 1,600$ °C) the process temperatures achieved were far below a level one would expect significant densification. Examining the powder samples after heating confirmed this and while the powder did exhibit clumping and a reduced ability to flow, no solid mass was found.

From these results we can conclude that even at low temperatures where mass transport will be small, the change in absorption due to particle interconnects is significant enough to cause noticeable a reduction in loss. This was less pronounced in samples sealed in air and was likely inhibited by oxide growth. The strength of low density sintered material is dependent on the strength of the particle interconnects [10], as the material was not able to hold its shape outside of the container we can conclude that these interconnects were very weak and likely small. This is in line with the expectation that mass flow would only be occurring for small particles. As the initial stage is characterised by the majority of surface elimination it should be clear that this reduction in absorption will continue to be enhanced.

4.4 Observations of Microwave Sintering at High Temperatures

With the changes to absorption at low temperature characterised we now move to the changes associated with high temperatures, where significant sintering can be seen to occur. As mentioned we expect to see a greater reduction in magnetic absorption of the samples due to formation of interconnects during necking.

It is expected that the power levels required to achieve the desired $>1,000$ °C temperatures will be increased due to the gradual reduction in absorption as the sample continues to sinter. Where previously excitation powers of <10 W were

sufficient to achieve temperatures of around 550°C we can expect this value to be disproportionately higher for the process temperatures desired, even considering the increase due to greater ambient loss.

The density of the produced samples will be a good indicator of the degree of sintering experienced. For initial stage sintering one can expect some increase in density, however not by a large amount. Should intermediate stage sintering begin there will be a much larger degree of densification accompanied by significant shrinkage.

4.4.1 Experimental

In this experiment three different metal powders commonly used in PBF were processed using the experimental microwave sintering setup described in Ch. 3. Samples of Ti6Al4V, 316L, and 247LC powder were prepared in quartz capillary tubing and sealed inside an inert argon atmosphere at slight positive pressure. The tube inner diameters were 3 mm and lengths were cut to 100 mm, which gave an approximate total sample volume of 700 μl when filled. Average sintering temperatures of around 1,000°C were targeted. However as the closed-loop temperature control described previously had not been implemented yet, this was set approximately by using power levels of about 130-140 W. Three samples of each material were prepared.

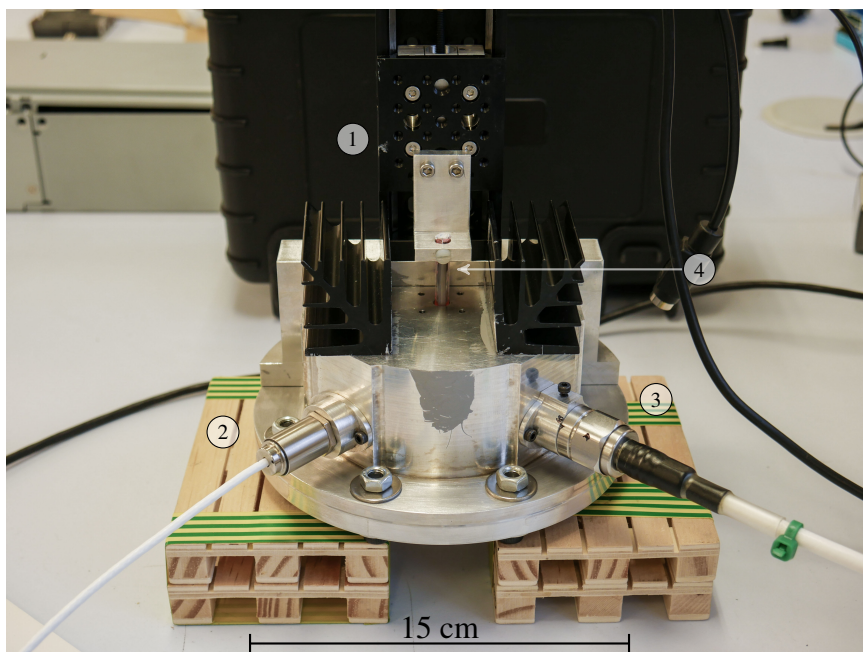


Fig. 4.8 Quasi-spherical cavity applicator setup. 1) Linear stage, 2) Pyrometer head, 3) Type-N coupler, 4) Sample holder.

As before the equipment setup featured a Keysight MXG signal generator and two USB peak-and-average power meters. Triggering of the power meters by the signal generator was used to synchronise the peak measurements during resonant sweeps. Temperature measurement was performed using a Micro-Epsilon IR pyrometer. The emissivity was calibrated for the powder sample using a contact temperature sensor up to 100°C. The focal length of the pyrometer when mounted to the cavity meant that a spot size of 1 mm diameter was measured over the sample surface. A linear stage was also included to move the sample through the magnetic field. This was done in an effort to extend the range over which the sample was sintered and so produce longer samples, this is shown in Fig. 4.8. A complete list of all equipment used along with model numbers is given in Tab. 4.3.

Table 4.3 Equipment Summary

Item	Model	Notes
Signal Generator	Keysight N5181B	
Power Amplifier	Milmega AS1860-100	
Forward Power Meter	Keysight U2042XA	Peak and Average
Reverse Power Meter	Keysight U2042XA	Peak and Average
Circulator	AtlanTecRF AS7122	5.4 to 6.6 GHz
Directional Coupler	n/a [†]	1 to 18 GHz
IR Pyrometer	Micro-Epsilon CTM-3CF75H3	250 to 1800°C
Linear Stage	Zaber T-LSM050A	

[†] Bespoke unit made in-house, coupling was measured as part of setup calibration.

Test samples were used to confirm power levels necessary to achieve temperature of $\approx 1,000^\circ\text{C}$, and in general this necessitated an excitation power of around 51 dBm (125 W). Excitation power was held at 30 dBm for 1 min to establish a baseline temperature before increasing to 51 dBm over 5 min. The increase was performed logarithmically by about 0.08 dBm/s. Excitation power was then held at 51 dBm for 5 min, following this the power was gradually ramped down to allow a more even cooling of the sample. Cooling was performed over 10 min for the 316L steel samples, and 20 min for the Ti6Al4V titanium and 247LC nickel samples.

Following processing, density measurements were taken using the method described in Sec. 2.1.3. Scanning Electron Microscopy was also performed on select samples with the assistance of Dr Jenna Tong at New Mills, Renishaw Plc.

4.4.2 Results and Discussion

Measurement results for all samples are shown in Tab. 4.4. For each sample the average excitation power and temperature was calculated as the mean value during steady state heating. The values of Q_0 for the system are given before and after the process as measured by the system through reflection frequency sweeps. The relative change in total system loss was calculated using the formula:

$$\Delta Loss = \frac{Q_{end}^{-1}}{Q_{start}^{-1}} - 1 \quad (4.3)$$

The delivered power, temperature, loss and resonant frequency were plotted against time. Plots for only a single sample of each material are included here to save space, and the complete results can be found in Appendix B.

Table 4.4 Percentage Change in System Loss Following Sintering

Sample	Power [W]	Temp [°C]	Q_{start} [1]	Q_{end} [1]	$\Delta Loss$ [%]	
Ti6Al4V	1	132.53	1148.21	462	4891	-90.56
	2	136.75	1140.90	435	5315	-91.81
	3	132.58	1130.38	392	5328	-92.65
316L	1	129.02	1032.62	471	5115	-91.57
	2	128.31	1027.64	438	5449	-92.56
	3	127.45	996.04	481	5788	-92.33
247LC	1	123.11	1062.70	508	3465	-87.21
	2	136.38	1226.88	415	3624	-89.73
	3	84.71	1070.26	477	4478	-90.38

As can be seen in Figs. 4.10, 4.14, and 4.18, all three materials showed a sharp decrease in the microwave loss which coincided with the rapid temperature increase following excitation. This was a significant decrease in loss as indicated by the apparent 90% average reduction in system loss shown in Tab. 4.4. As has been mentioned, initial stage sintering is largely characterised by elimination of up to 50% of the initial surface area [10]; some densification does occur but only a small amount.

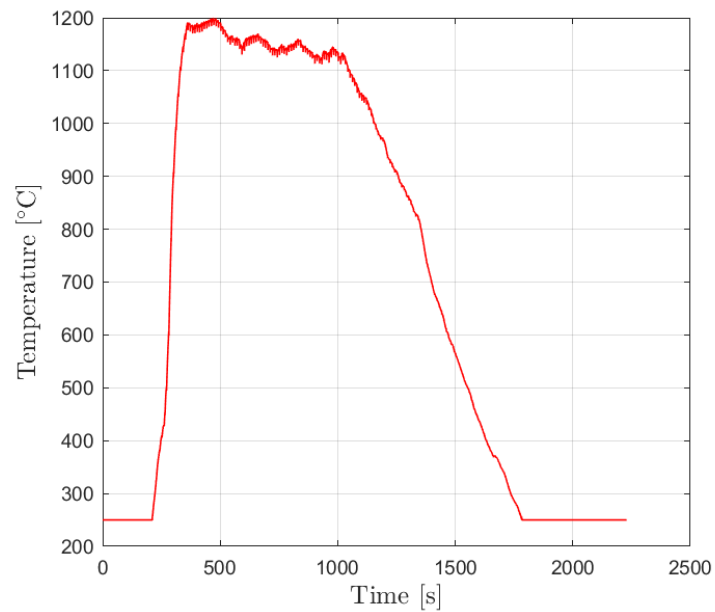


Fig. 4.9 Change in sample temperature during microwave sintering of Ti6Al4V. Data shown is for sample 1

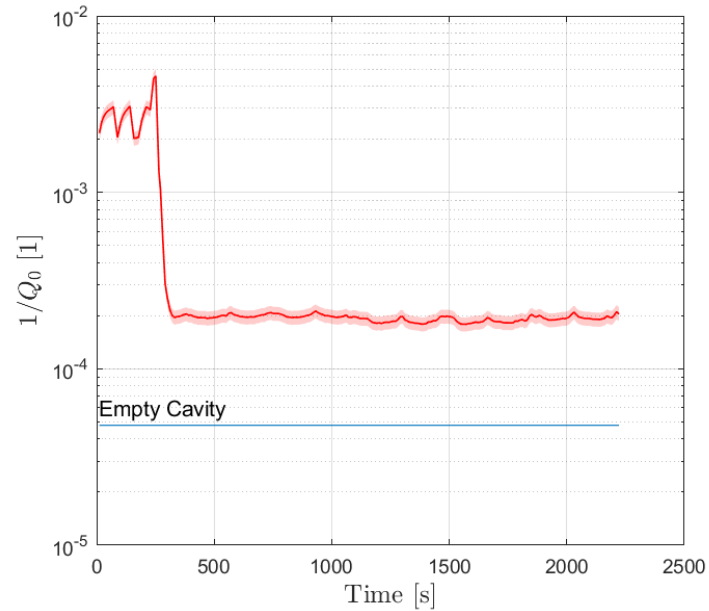


Fig. 4.10 Change in system loss during microwave sintering of Ti6Al4V. Data shown is for sample 1.

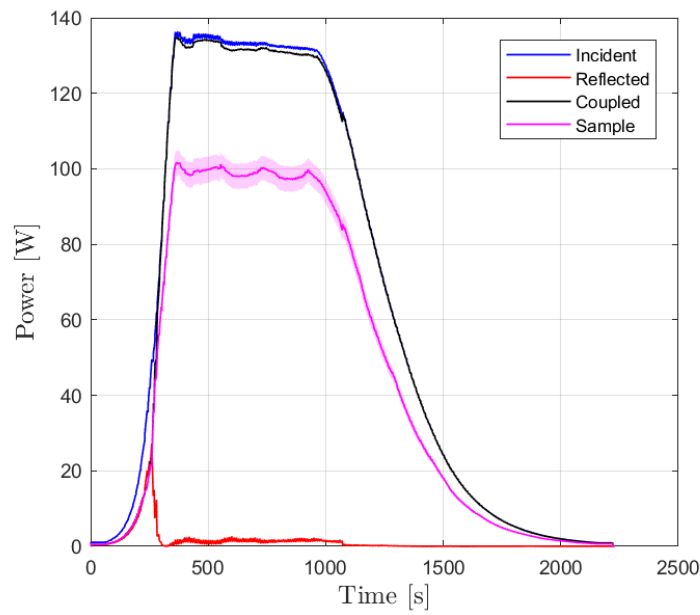


Fig. 4.11 Change in delivered power during microwave sintering of Ti6Al4V. Data show is for sample 1.

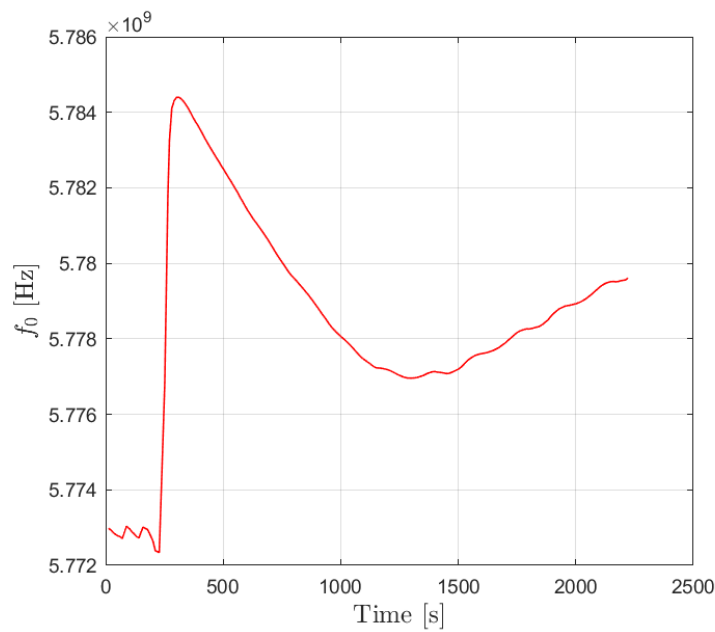


Fig. 4.12 Change in resonant frequency during microwave sintering of Ti6Al4V. Data show is for sample 1.

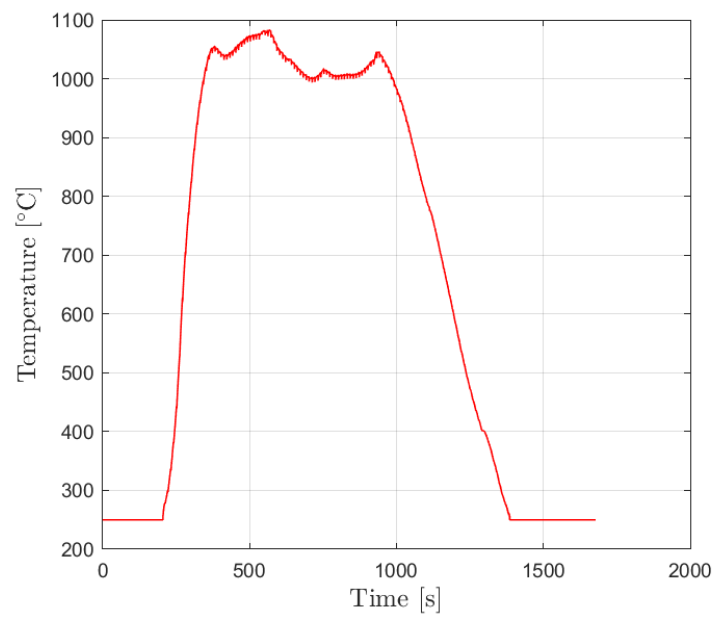


Fig. 4.13 Change in sample temperature during microwave sintering of 316L. Data shown is for sample 1

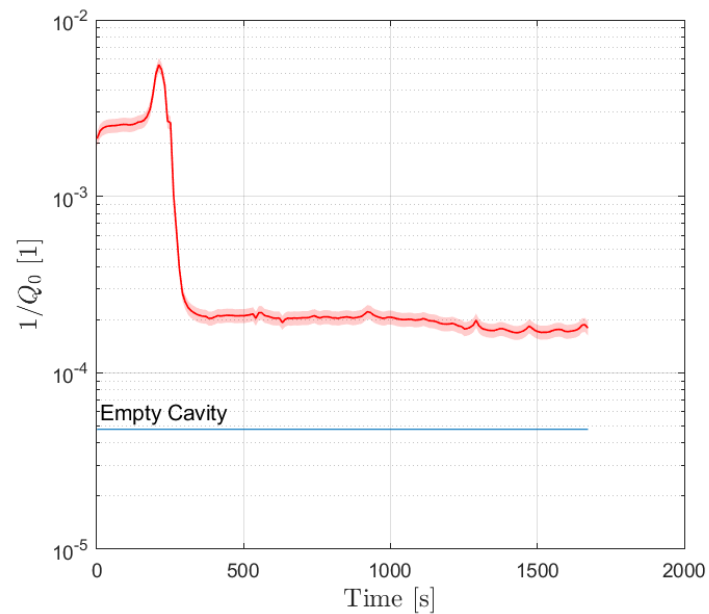


Fig. 4.14 Change in system loss during microwave sintering of 316L. Data shown is for sample 1.

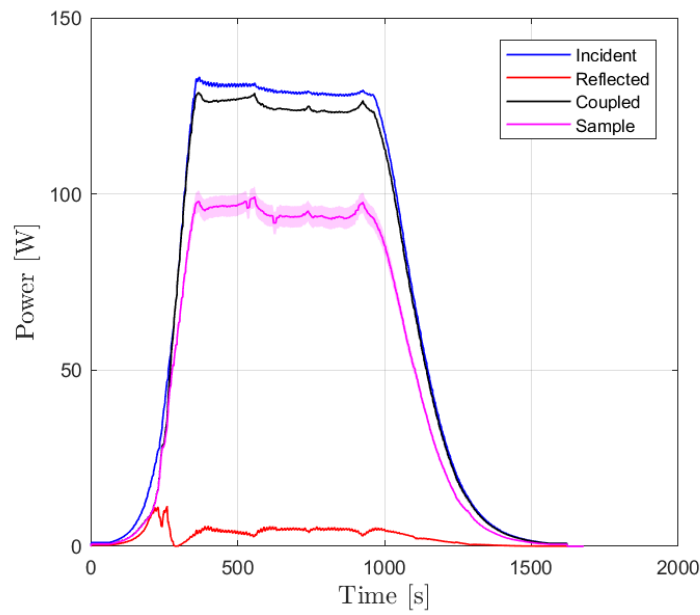


Fig. 4.15 Change in delivered power during microwave sintering of 316L. Data show is for sample 1.

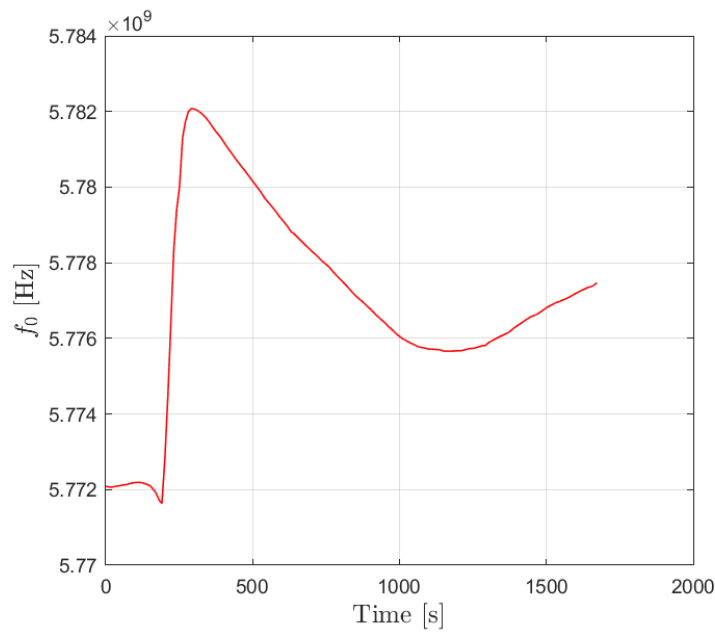


Fig. 4.16 Change in resonant frequency during microwave sintering of 316L. Data show is for sample 1.

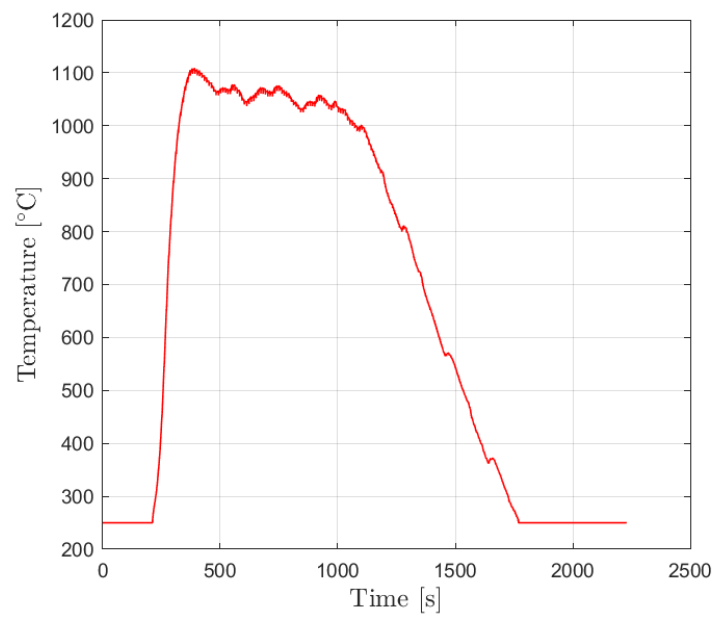


Fig. 4.17 Change in sample temperature during microwave sintering of 247LC. Data shown is for sample 1

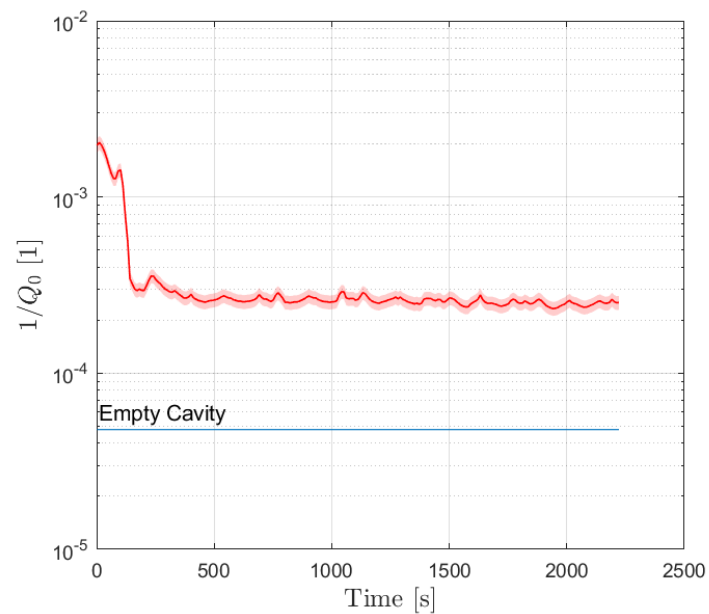


Fig. 4.18 Change in system loss during microwave sintering of 247LC. Data shown is for sample 1.

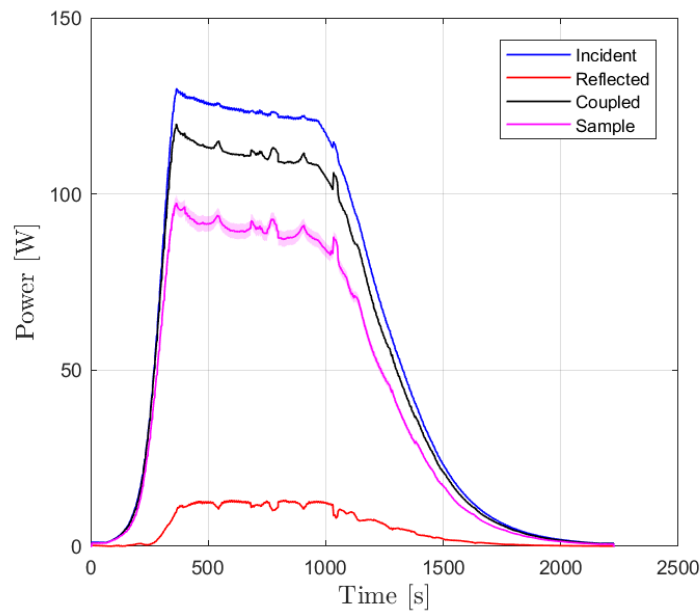


Fig. 4.19 Change in delivered power during microwave sintering of 247LC. Data show is for sample 1.

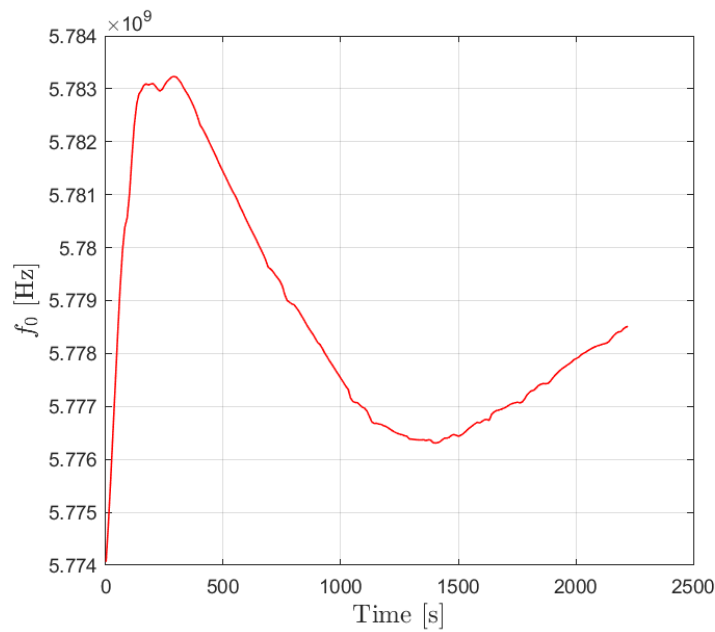


Fig. 4.20 Change in resonant frequency during microwave sintering of 247LC. Data show is for sample 1.

For the same approximate excitation power there was a noticeable difference in average equilibrium temperatures. Ti6Al4V on average was approximately 100°C hotter than both the 316L and 247LC powders. This is likely due to a difference in magnetic dipole absorption at this frequency and indeed by plotting them next to each other as in Fig. 4.21, we can see that Ti6Al4V does have a higher absorption on average compared to 316L for the particle size distribution quoted. Data for the conductivity of 247LC is difficult to obtain and so could not be plotted, however as a Nickel based alloy it is likely to have a higher conductivity than the Titanium based Ti6Al4V alloy. This would result in a similar reduction in absorption to 316L, which may also explain its lower process temperature.

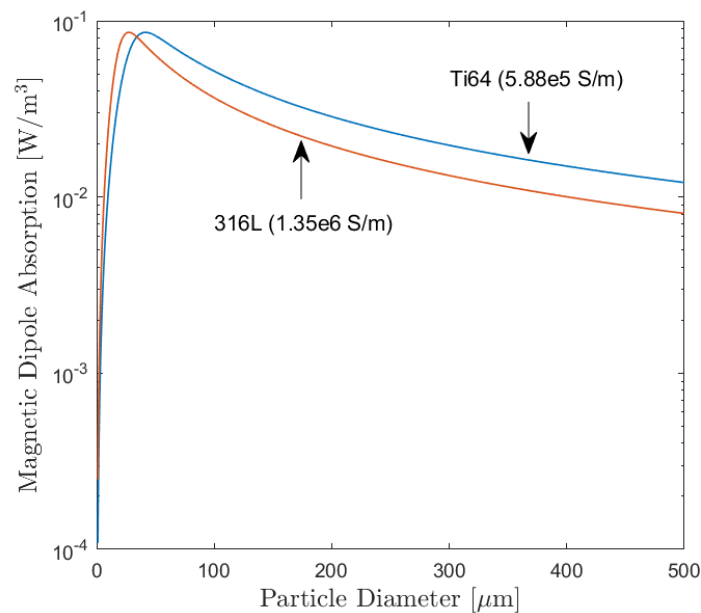


Fig. 4.21 Magnetic dipole absorption per unit volume at 5.8 GHz for Ti6Al4V and 316L powders. Conductivities used are labelled and a magnetic field strength of $2.7 \times 10^{-3} \text{ A m}^{-1}$ was used for calculation. Particle sizes shown are representative of those quoted by LPW for their gas-atomised powders.

Examining the changes in loss we see that when excitation is first switched on there is an initial increase in Fig. 4.14 for 316L powder. This can be explained by an increase in resistivity as temperature increases. However as shown in all cases once temperature reached a certain threshold value the loss quickly began to decrease due to the effects of sintering. This reduction in loss remained even after the samples had cooled indicating a permanent change. The actual loss of the samples post-sintering was higher than for the samples processed at low temperatures previously. This is due

to the difference in sample volume and examining the change in loss for both we see that high temperature sintering produced a greater percentage reduction in loss.

The overall shift in frequency can also be used to as evidence to support sintering. While the actual volume of the cavity is unchanged the formation of particle interconnects will act to reduce the depth of penetration by the microwave field. This results in a net reduction of effective cavity volume and can be thought of as a shape perturbation, the action of which will increase the resonant frequency. In the plots shown frequency does indeed increase however it then sharply decreases as excitation continues. This effect is of course due to thermal expansion of the cavity and it can be seen to reverse as the system cools.

Once removed from the sample tubes, the powder was seen to have formed a solid mass. A close-up photo of a Ti6Al4V sample is shown in Fig. 4.22, where it is apparent that individual particles are visible at the surface. The length of these samples exceeded the height of the cavity and so it can be concluded that the action of the stage to extend the exposure was a success. For Ti6Al4V and 316L these were unbroken but in all cases the 247LC samples had cracked and were split into small pieces.

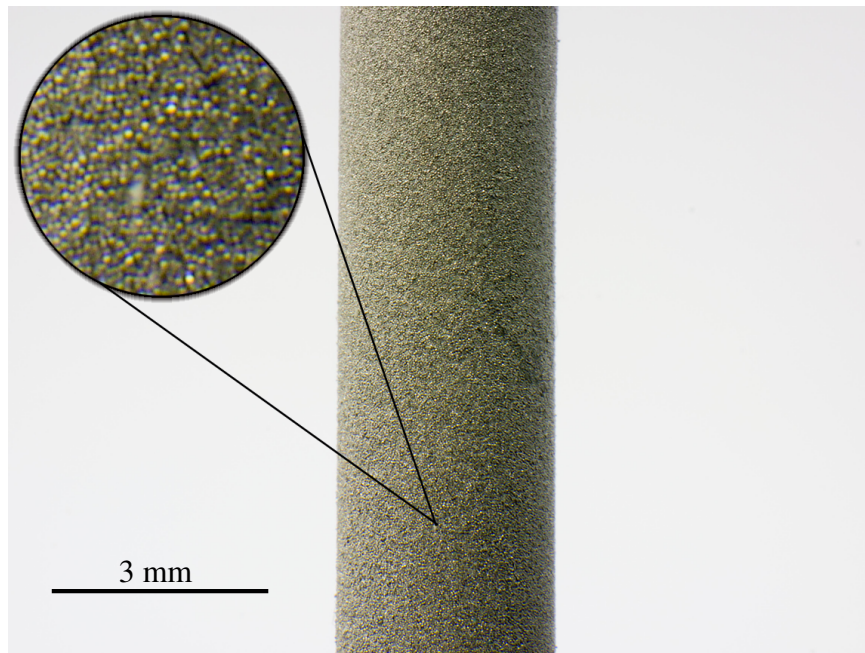


Fig. 4.22 Macro photograph of microwave sintered Ti6Al4V sample.

Density of the samples was calculated using the method in Sec. 2.1.3 and are given below in Tab. 4.5 for the Ti6Al4V and 316L samples. The 247LC samples were not measured as they were too brittle to handle easily, and would need to remain intact

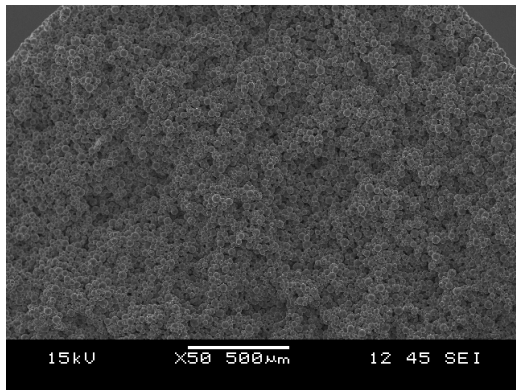
for SEM. Percentage density was calculated using values of 4.43 and 7.99 g/cc for Ti6Al4V and 316L, respectively, which were obtained from the supplier, LPW.

Table 4.5 Density of Microwave Sintered Samples

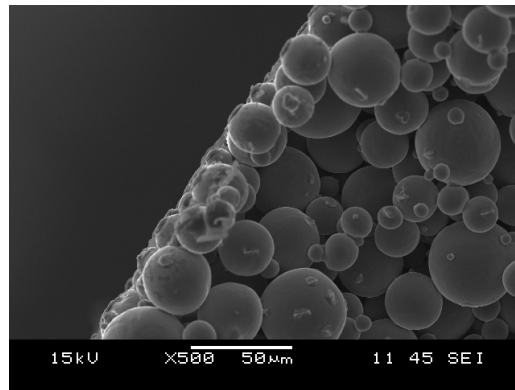
Sample	Weight [g]	Length [mm]	Diameter [mm]	Density [g/cc]	Density [%]	
Ti6Al4V	1	1.203	59	3.00	2.885 (± 0.029)	65.11 (± 0.65)
	2	1.220	59	3.01	2.906 (± 0.029)	65.60 (± 0.65)
	3	1.195	58	3.01	2.895 (± 0.029)	65.36 (± 0.66)
316L	1	1.947	52	2.98	5.368 (± 0.056)	67.10 (± 0.70)
	2	1.963	52	3.02	5.270 (± 0.055)	65.88 (± 0.69)
	3	1.976	53	2.96	5.418 (± 0.056)	67.72 (± 0.70)

Initial packing density of each material was calculated based on sample weight and inner dimensions. This gave an average value of about 61% before sintering for all three materials, and is consistent with expectations for the filling fraction associated with a random close pack of spheres one might achieve by hand [83]. Despite the large reduction in loss and high temperatures very little densification occurred. The 316L stainless experienced the largest increase on average but not by a significant margin. The small increase implies that intermediate stage sintering did not occur and so from the density data alone one would not expect to see significant merging of particles or pore elongation. Further the low density implies low mechanical strength as in this limit strength is determined by the inter-particle bonds [10, 11], as such the samples were brittle and easily snapped by hand. The 247LC samples behaved in a similar way and so it is likely their density was similar, if not less than the Ti6Al4V and 316L samples.

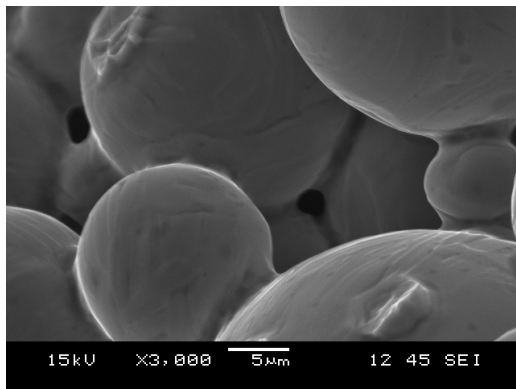
SEM was used to investigate the micro-structure for a selection of samples from each material. Samples were snapped in half to expose a clean cross-section for the microscope. Two modes of imaging were used: Secondary Electron Imaging (SEI/SE) and Backscattered Electron Contrast imaging (BEC/BSE). SE images rely on electrons emitted at the surface of the sample and thus possess the highest resolution of surface features. BSE images rely on backscattering of electrons and thus the energy is dependent on the nuclei atomic mass. This allows for differentiation of materials based on their contrast in the image, however this does not necessarily identify their composition.



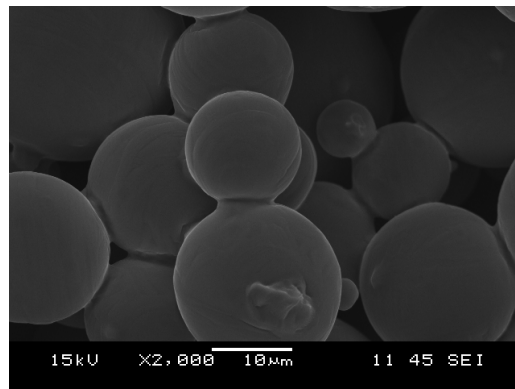
(a) Exposed cross-section and sample edges. Surface is visibly uneven.



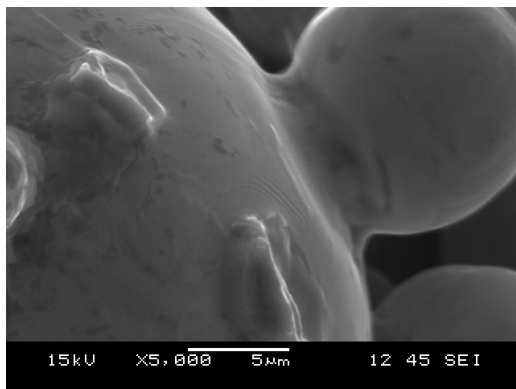
(b) Sample curvature at edge. Broken contact points visible on some particles.



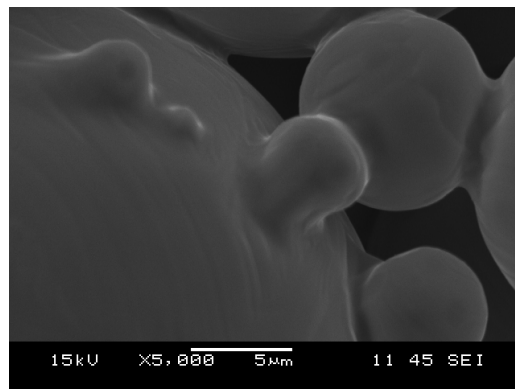
(c) Pore closures at intersection of three particles. Necking also visible.



(d) Particle necking and adhesion of multiple particles.

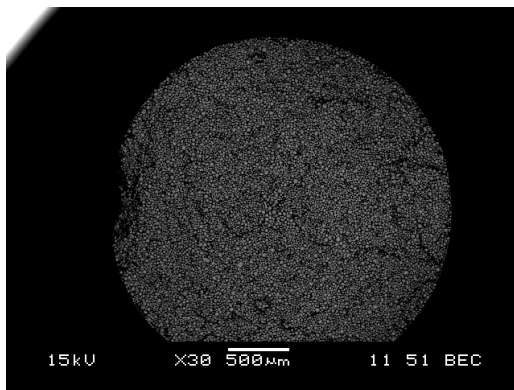


(e) Close-up view of necking. The larger particle also exhibits break points at surface.

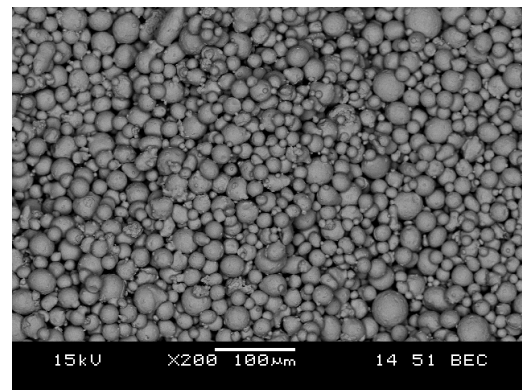


(f) Necking and examples of absorption of sub-species.

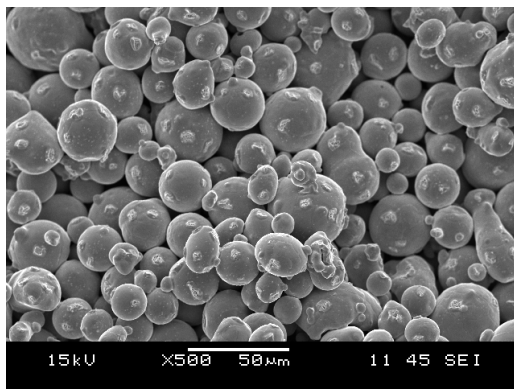
Fig. 4.23 SEM images of microwave sintered Ti6Al4V. Sample was snapped in half to provide a clean surface for imaging. Instances of necking, pore-closure and sub-species absorption are observed. Break points are also visible due to the snapping of the sample.



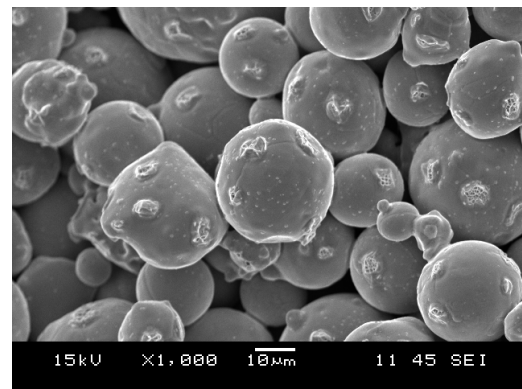
(a) Exposed sample cross-section showing outer edges of sample. Surface is visibly uneven.



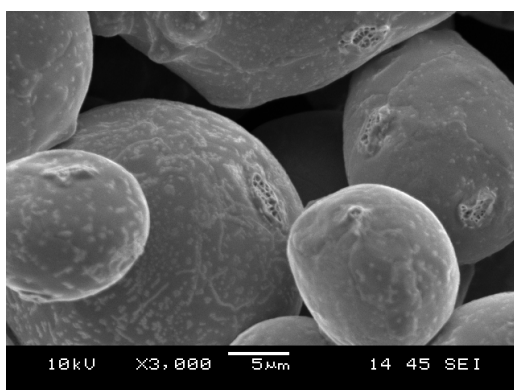
(b) Closer view of particle size distribution. Particles are primarily spherical and closely packed.



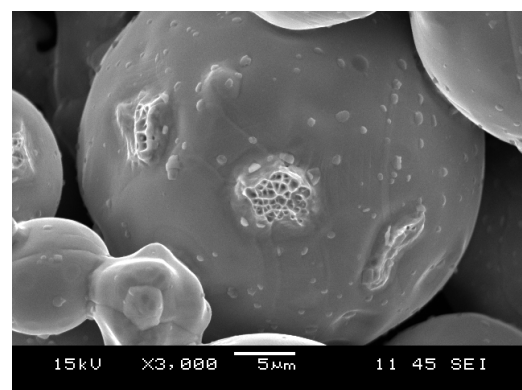
(c) Even and regular distribution of breakpoints visible. Example of two particles merging also seen.



(d) Zoomed in section of c. White "glow" at outer edge of particles due to charge build-up.

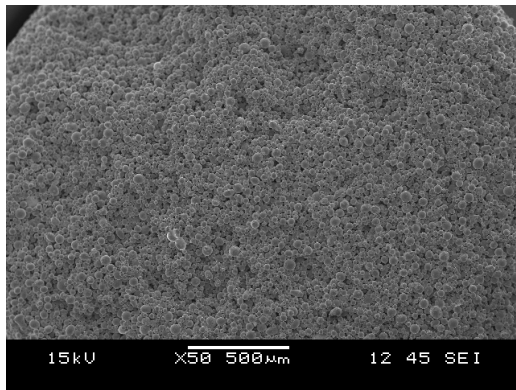


(e) The smaller particles tended to be less spherical. Beam energy was reduced to avoid charge build-up.

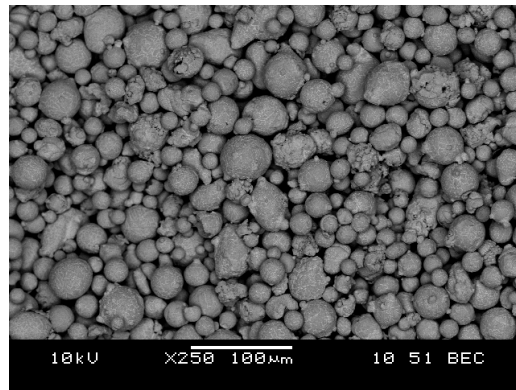


(f) Zoomed in view of single particle. Breakpoints appear to be pocketed like honeycomb.

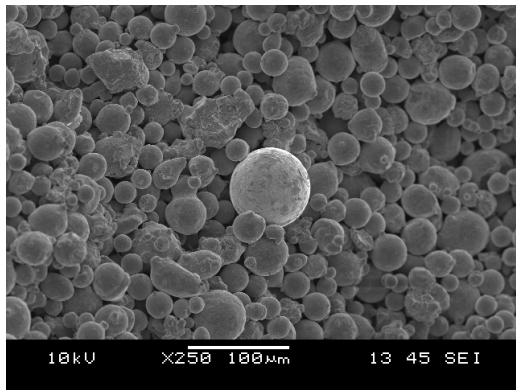
Fig. 4.24 SEM images of microwave sintered 316L Stainless Steel. Sample was snapped in half to provide a clean surface for imaging. Sintering evidenced by visible breakpoints on particle surfaces. Honeycomb-like structure of breakpoints indicates a strong mechanical bond between particles.



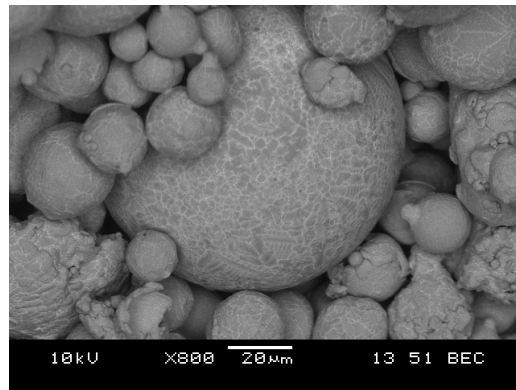
(a) Exposed sample cross-section showing outer edges of sample. Surface is visibly uneven.



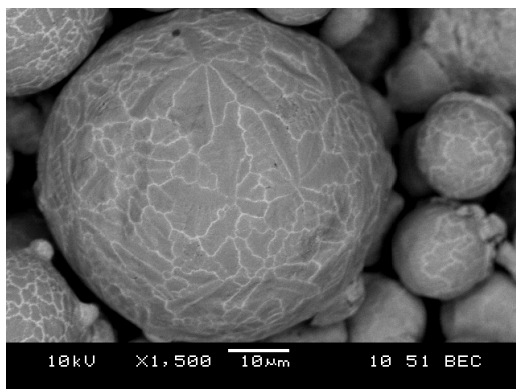
(b) Closer view of sample surface. Particle shape appears less regular and there is a wider size distribution.



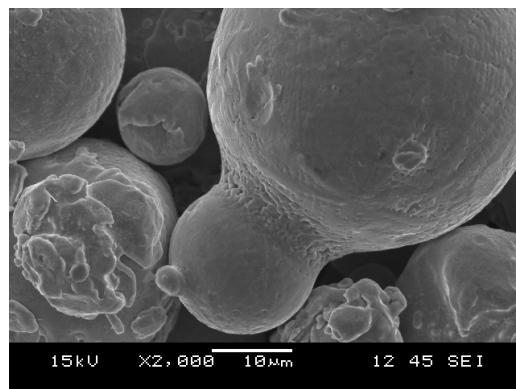
(c) Closer view of sample surface. The highlighted particle appears brighter due to charge build-up.



(d) Larger particle surrounded by smaller ones. Grain boundaries made visible due to BEC imaging.



(e) Carbide deposits at fractal grain boundaries. Some satellites also visible bottom left.



(f) Textbook example of necking between larger and smaller species.

Fig. 4.25 SEM images of microwave sintered 247LC Nickel. Sample was snapped in half to provide a clean surface for imaging. Particle size distribution largely uneven. Some examples of necking were found and the grain boundaries were highly visible in the backscattered (BEC) images.

As expected from the small change in density, the structures imaged do not show signs of intermediate stage sintering (pore elongation and rounding, coarsening and void filling). The images shown are typical of initial stage and good examples of necking can be seen for all three materials. For Ti6Al4V, shown in Fig. 4.23, there were almost textbook examples of neck growth noticeable across the sample surface, a good example is also seen in Fig. 4.25 for 247LC. For the 316L samples, shown in Fig. 4.24, visible neck growth was less commonly seen. However there is clear evidence from the numerous honey-comb like structures. These will have been formed where interconnects were broken when the samples were snapped. Therefore despite the larger reduction in overall microwave loss and solid mass formed, the sintering in this experiment was still initial stage.

4.5 Physical Properties of Microwave Sintered Metals

In this section we examine the influence of various control factors in the microwave sintering setup on the final properties of the sintered pieces. The aim of this study primarily was to produce optimised results for the system. In doing so there can be greater certainty that the results presented are representative of the type of microwave sintering performed, as opposed to incorrect or inefficient use of the experimental setup devised.

It has been demonstrated in previous work that important parameters of the sintering process are the heating rate, sintering time, sintering temperature, cooling rate, and atmosphere [82, 84–89]. These parameters have an influence on the final micro-structure formed, which in turn bears significance to the physical properties of the material (density, strength, hardness, etc.). With the inclusion of the closed-loop temperature control in the measurement setup, all of these parameters are common to the sintering setup used in this work and can therefore be investigated. The classical approach to such an investigation would be to vary each parameter individually. However this would necessitate a large number of experiments which, depending on the duration of each sintering cycle, could represent an overly-significant investment of time. By using a Design of Experiments (DoE) approach such as the Taguchi method, the total number of experiments can be minimised while still retaining statistical confidence [90, 91]. The Taguchi method has been proven successful in a variety of sintering studies [92–97] and so was selected to analyse the heating process.

4.5.1 Parameter Selection

The first stage in experiment design is the selection of parameters which shall be studied. As stated the main influencing factors common between conventional sintering and the system used here are the heating rate, sintering time, sintering temperature, cooling rate, and atmosphere [82, 84–89]. As the effect of the sintering atmosphere had been previously observed, it was decided to ignore varying this parameter and so all samples would be sealed in argon gas. This left four variables for testing, the ranges selected for each were: heating rate (10-20°C/min), sintering temperature (900-1000°C), sintering time (30-60 min), and cooling rate (20-60°C/min).

Three levels were chosen for each parameter and experiments were organised using an L9 orthogonal array as shown in Tab. 4.6. This practise allows for the minimising of experiments required whilst retaining statistical significance. An array is orthogonal where each individual parameter-level combination appears once.

In Taguchi's method we define signal-to-noise ratios to examine the repeatability or quality of a particular results set. Three forms are given depending on the objective of the optimisation [91].

Maximum is best:

$$SNR = -10 \log \left(\frac{1}{n} \sum x^{-2} \right) \quad (4.4a)$$

Nominal is best:

$$SNR = -10 \log (\sigma^2) \quad (4.4b)$$

Minimum is best:

$$SNR = -10 \log \left(\frac{1}{n} \sum x^2 \right) \quad (4.4c)$$

These are calculated from the output results for each row or experiment series. In the case of the experiments performed here this will be the final density and flexural modulus and so the "Maximum is best" definition is used. Once found the SNR for each parameter at each level is found from the mean of row results. As an example, the SNR for Heating Rate at 20°C/min would be the average of SNRs for profile 3, 6, and 9. Comparing the SNR at each level indicates the optimum combination of parameters. In this case it will mainly help identify which parameters influence the result most.

4.5.2 Experimental

Samples of Ti6Al4V powder were prepared and sealed in 100mm long, 3.00mm internal diameter quartz capillary tubing under an inert argon atmosphere. A minimum

Table 4.6 L9 Orthogonal Array of Heating Profiles

Profile No.	Heating Rate [°C/min]	Temperature [°C]	Hold Time [min]	Cooling Rate [°C/min]
1	10	900	30	20
2	15	900	45	40
3	20	900	60	60
4	10	950	45	60
5	15	950	60	20
6	20	950	30	40
7	10	1,000	60	40
8	15	1,000	30	60
9	20	1,000	45	20

of 3 repetitions was to be performed for each experiment so in total 27 samples were required as a minimum.

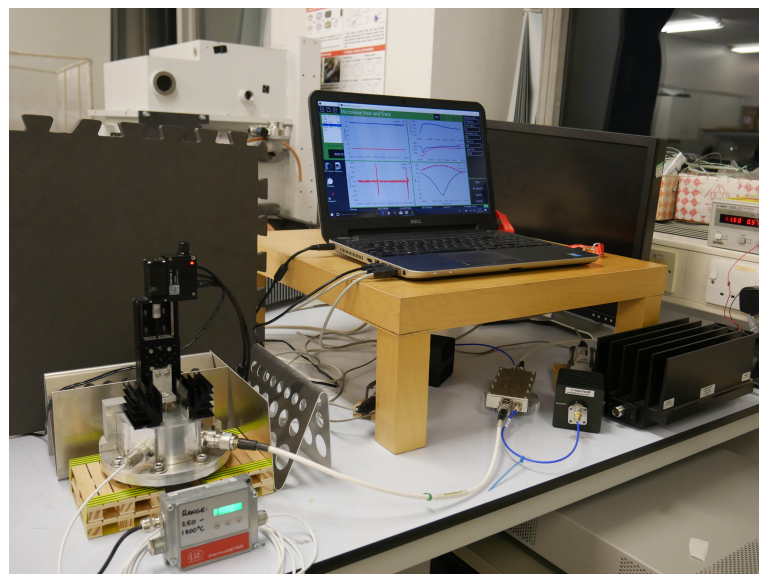


Fig. 4.26 Microwave sintering setup used. Pictured is the microwave cavity applicator with attached pyrometer and linear stage. Also shown is the laptop with control software loaded.

The measurement setup described in Ch. 3 was assembled using a Keysight MXG signal generator, two USB peak and average power meters, and a Milmega power amplifier. Temperature was monitored using a Micro-Epsilon infra-red pyrometer attached to the cavity, measurement range was 250-1,800°C. A linear stage was also

attached to the cavity to move the sample slowly back and forth through the magnetic field maximum. This allowed samples longer than the 40 mm cavity height to be produced, which was necessary for the universal testing machine used to perform the 3-point bend test later on. The stage was configured to complete one full cycle every 25 min moving 32 mm in total; including the length within the cavity at the start, this equated to exposure of 72 mm of the 100 mm sample length. A complete list of all hardware used along with model numbers can be found in Tab. 4.7.

Table 4.7 Equipment Summary

Item	Model	Notes
Signal Generator	Keysight N5181B	
Power Amplifier	Milmega AS1860-100	
Forward Power Meter	Keysight U2042XA	Peak and Average
Reverse Power Meter	Keysight U2042XA	Peak and Average
Circulator	AtlanTecRF AS7122	5.4 to 6.6 GHz
Directional Coupler	n/a [†]	1 to 18 GHz
IR Pyrometer	Micro-Epsilon CTM-3CF75H3	250 to 1800°C
Linear Stage	Zaber T-LSM050A	

[†] Bespoke unit made in-house, coupling was measured as part of setup calibration.

The control software described in Ch. 3 was used to run the measurement setup. Heating profiles from Tab. 4.6 were implemented using the closed-loop temperature control using the measured temperature as feedback. This was used to set the duty-cycle of the excitation signal which allowed the average power to be controlled through pulse-width modulation of the signal. Under normal operation the measured temperature was able to be kept within 0.1°C of the set-point, this value corresponding to the absolute precision of the pyrometer itself.

After sintering, transmission measurements of the Q_0 were carried out on each sample using a Keysight N5232A vector network analyser (VNA) at low input power. An unsintered control sample was also measured for comparison. Samples were then removed from tubing and loose powder was removed by sanding with a hand-file. Density was calculated from mass and external dimensions using the method described in Sec. 2.1.3. Finally the flexural modulus of each sample was found using the three-point bend test which was performed by Mr. Ian King in the School of Engineering.

4.5.3 Results and Discussion

The overall change in system loss for each sample is given in Tab. 4.8. Individual plots for each heating profile are given in Figs. 4.27 - 4.35. These show the change in loss and temperature over time during the sintering cycle. Each plot displays the results from all three repetitions for the specific heating profile used.

As can be seen the temperature profiles line up almost perfectly. Some variation can be observed where the resonant sweep occurs and temperature fluctuates before settling. The changes in loss also show good agreement between repetitions, albeit to a lesser extent. The final value of loss appeared to converge more for the higher sintering temperatures.

In some cases, notably Figs. 4.28, 4.30, 4.33, and 4.34, there are instances where the temperature control became temporarily unstable. However this was not found to cause significant issue and in all cases temperature control was able to re-stabilise without intervention.

Compared to previous experiments where the temperature was allowed to increase rapidly, the plots shown here where temperature is gradually increased give a clearer picture of the change in absorption. We note as before there is a slight enhancement to loss initially due to an increase in resistivity with temperature. Recalling the equation for skin-depth (2.13) there will be an increase proportional to the square-root of resistivity. Examining the plot for Ti6Al4V magnetic dipole absorption in Fig. 4.21 it should be clear that this increase is due to an enhancement in magnetic dipole loss. As temperature further increases the atomic mobility reaches the point where mass-transport can occur and sintering begins. The loss is shown to rapidly decrease between 400 and 500°C which corresponds with the results observed at "low" temperatures. Based on those results we can conclude that this rapid reduction is due to the initial formation of the inter-particle bonds. As these necking regions continue to grow and become stronger the loss is further reduced however by a successively smaller amount. This could be explained by the sintering process itself slowing down, or potentially, the increased screening from particle inter-connects making the measurement less sensitive to changes within the compact.

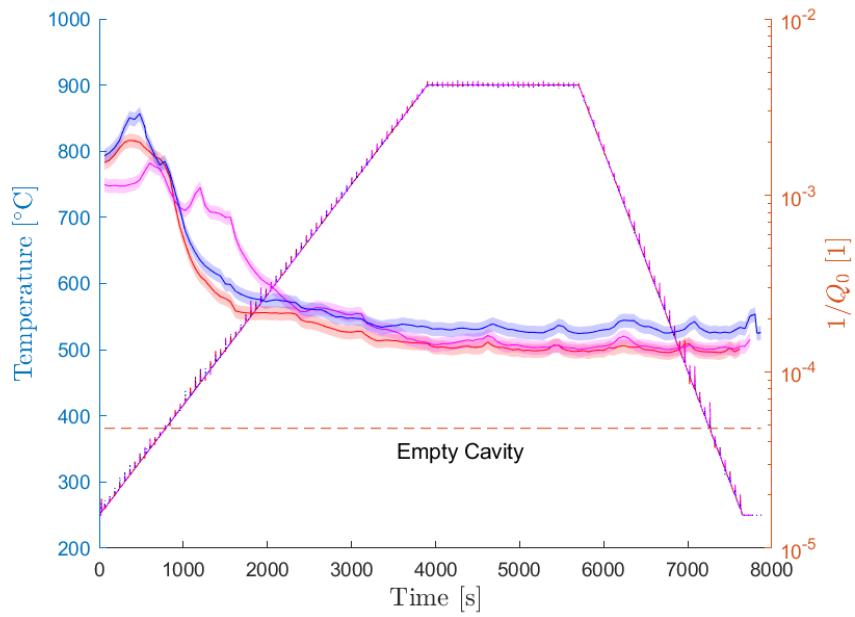


Fig. 4.27 Profile 1 - Change in temperature and system loss during sintering.

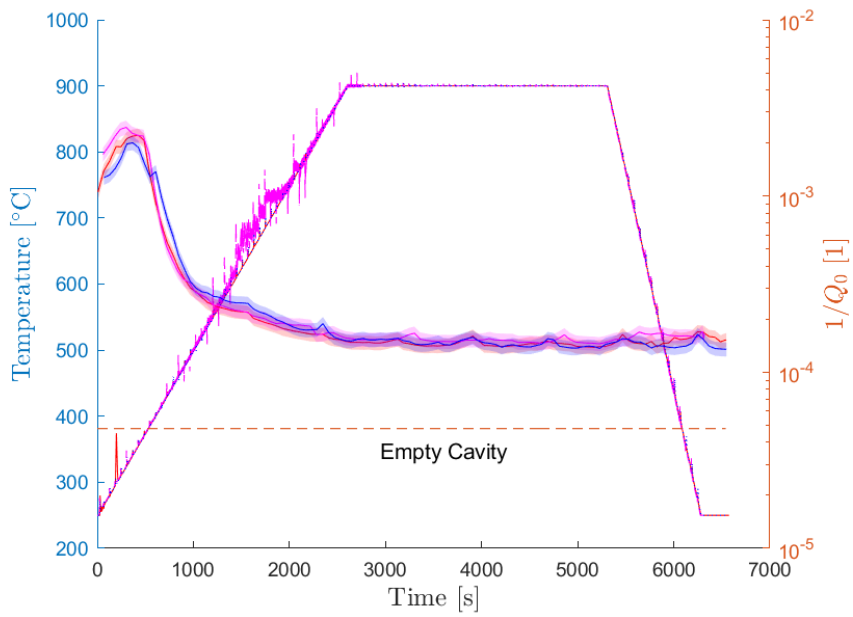


Fig. 4.28 Profile 2 - Change in temperature and system loss during sintering.

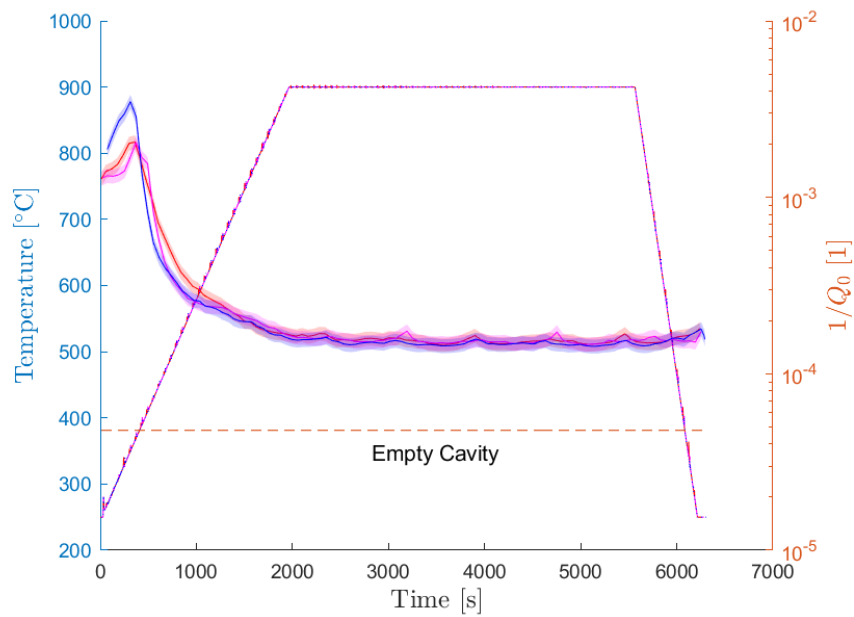


Fig. 4.29 Profile 3 - Change in temperature and system loss during sintering.

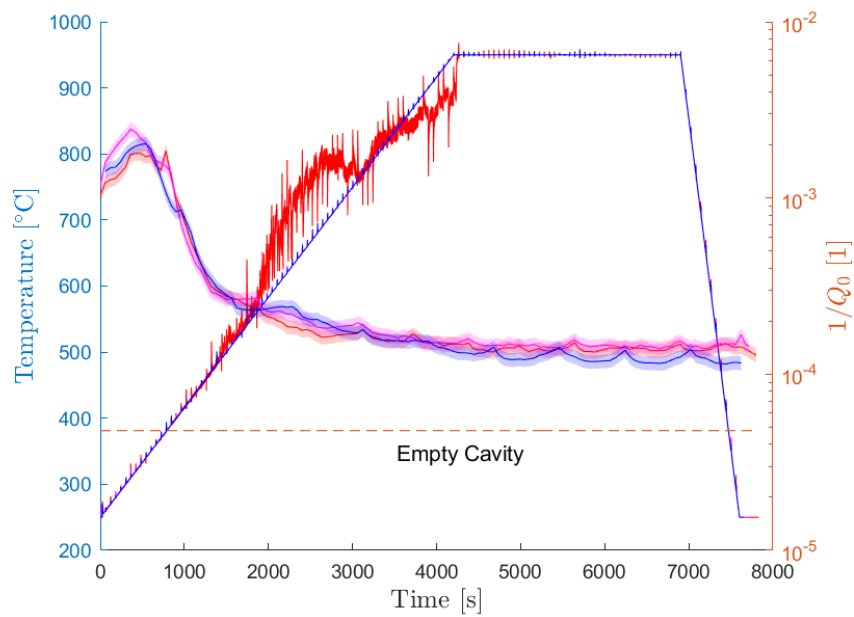


Fig. 4.30 Profile 4 - Change in temperature and system loss during sintering.

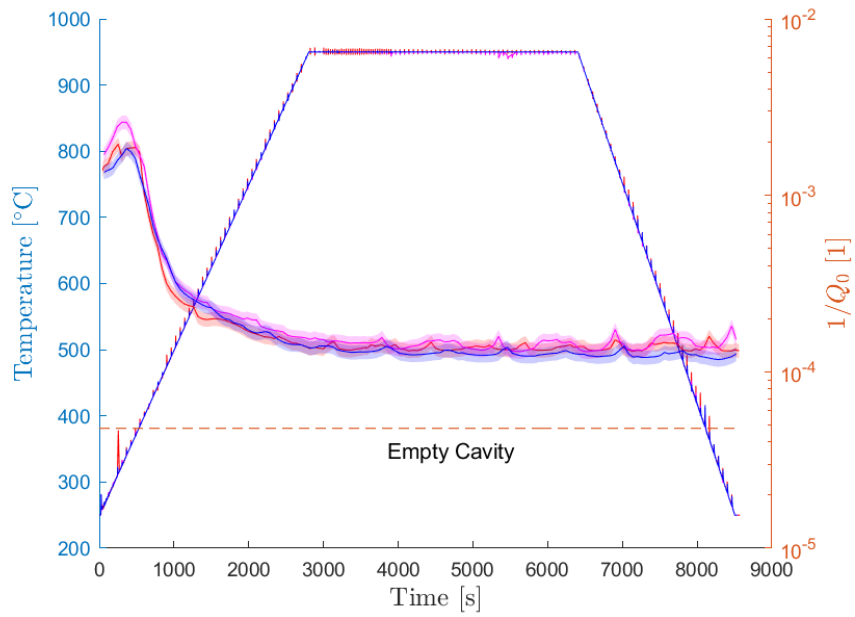


Fig. 4.31 Profile 5 - Change in temperature and system loss during sintering.

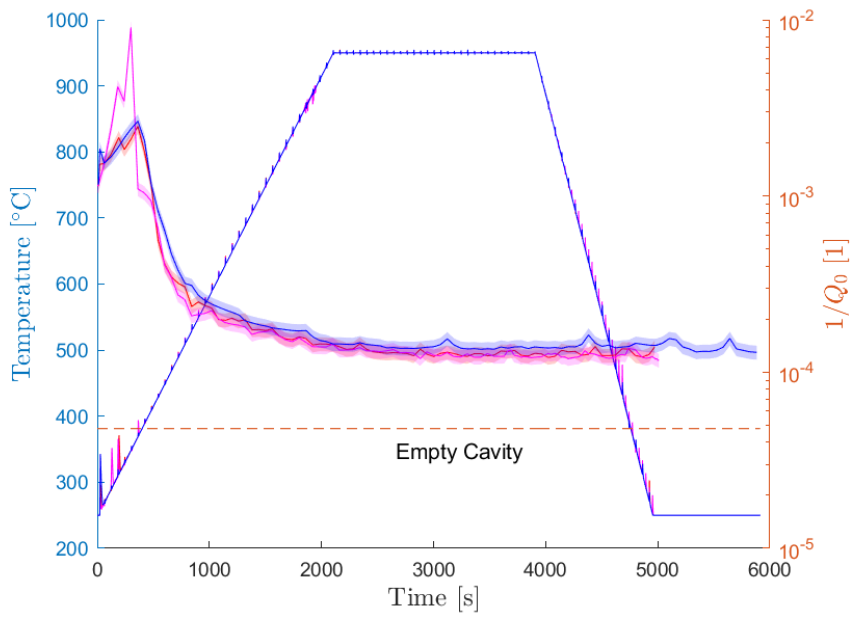


Fig. 4.32 Profile 6 - Change in temperature and system loss during sintering.

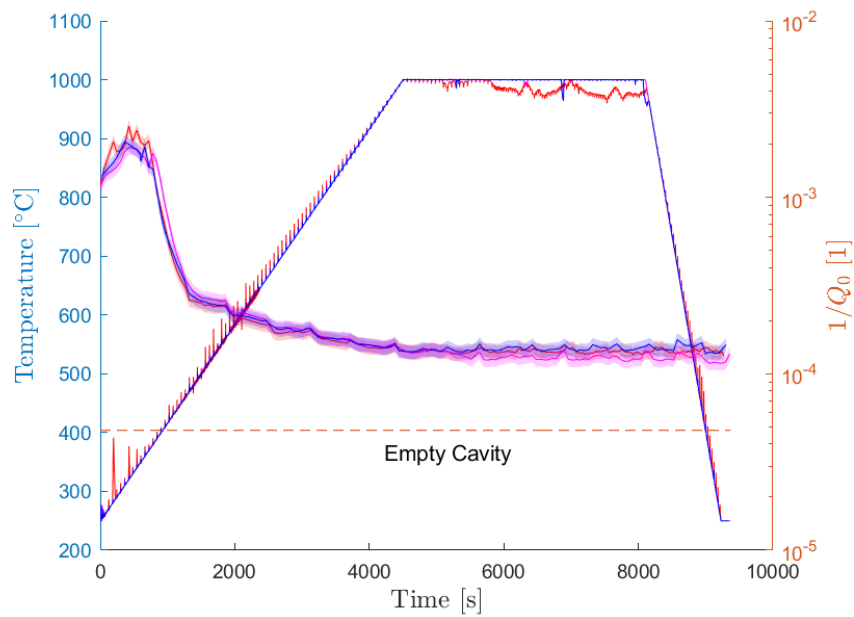


Fig. 4.33 Profile 7 - Change in temperature and system loss during sintering.

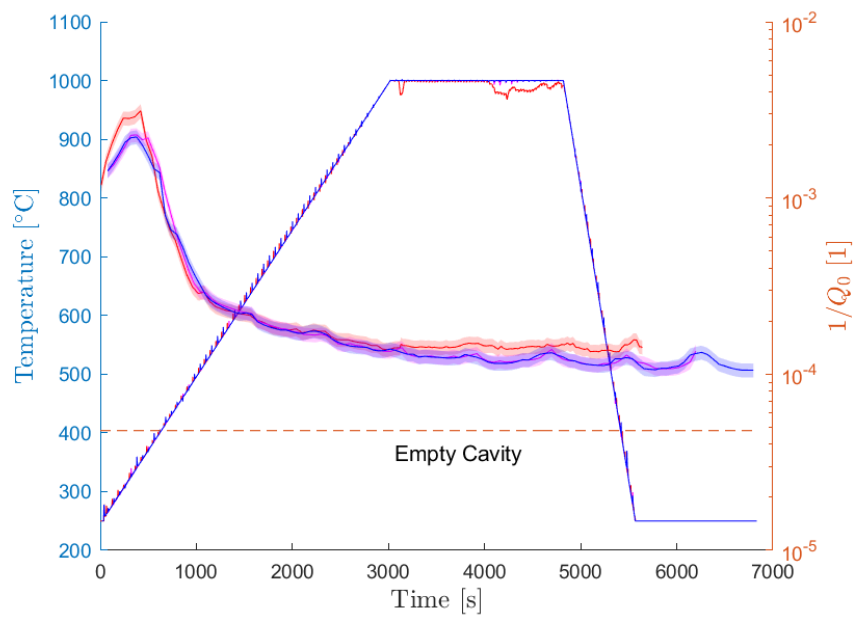


Fig. 4.34 Profile 8 - Change in temperature and system loss during sintering.

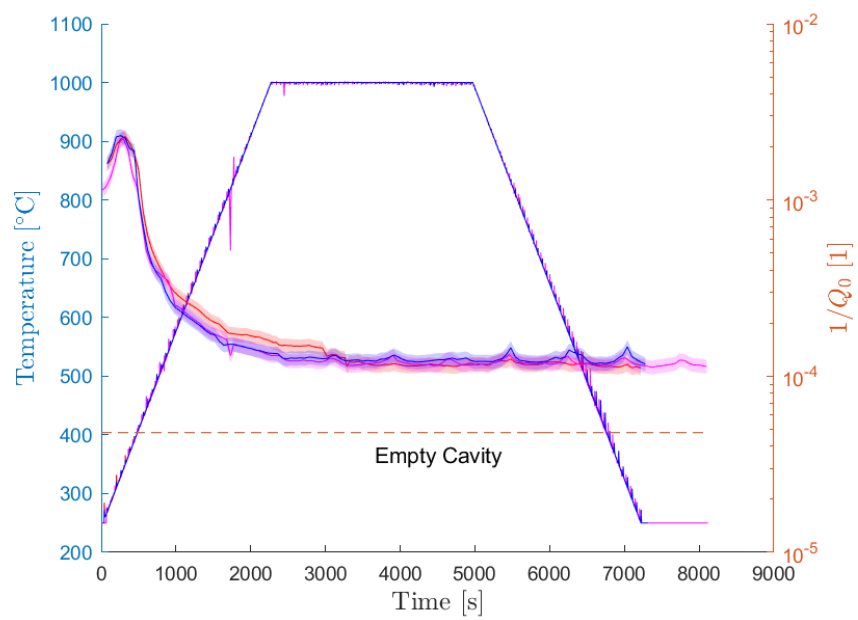


Fig. 4.35 Profile 9 - Change in temperature and system loss during sintering.

Table 4.8 Change in System Loss Following Sintering

Sample No.	Temp. [°C]	MHT System			Q_{Start}^{\dagger} [1]	VNA	
		Q_{Start} [1]	Q_{End} [1]	$\Delta Loss$ [%]		Q_{End} [1]	$\Delta Loss$ [%]
1-1	900	653	7794	-91.62	714	8912	-91.99
1-2	900	870	7471	-88.36	"	8604	-91.70
1-3	900	597	6012	-90.07	"	8975	-92.04
2-1	900	949	7180	-86.78	"	9407	-92.41
2-2	900	581	6907	-91.60	"	9298	-92.32
2-3	900	788	7413	-89.38	"	8868	-91.95
3-1	900	787	6684	-88.22	"	9061	-92.12
3-2	900	777	6621	-88.27	"	9201	-92.24
3-3	900	535	6378	-91.61	"	9423	-92.42
4-1	950	967	7803	-87.61	"	10791	-93.38
4-2	950	847	6937	-87.79	"	9335	-92.35
4-3	950	706	8651	-91.84	"	10590	-93.26
5-1	950	722	7598	-90.50	"	9718	-92.65
5-2	950	589	6570	-91.04	"	10662	-93.30
5-3	950	738	7914	-90.67	"	9637	-92.59
6-1	950	873	7204	-87.88	"	9756	-92.68
6-2	950	881	8591	-89.74	"	9951	-92.82
6-3	950	861	7718	-88.84	"	9245	-92.28
7-1	1000	870	7914	-89.00	"	10068	-92.91
7-2	1000	886	7711	-88.52	"	10506	-93.20
7-3	1000	760	6849	-88.91	"	10138	-92.96
8-1	1000	846	7067	-88.03	"	9932	-92.81
8-2	1000	703	7415	-90.51	"	10451	-93.17
8-3	1000	702	9491	-92.60	"	10431	-93.16
9-1	1000	625	8979	-93.04	"	9617	-92.58
9-2	1000	878	8815	-90.04	"	9866	-92.76
9-3	1000	623	8560	-92.72	"	9899	-92.79

[†]value for unsintered control sample.

The results from the density measurements for each sample are given in Tab. 4.9. As can be seen very little overall variation in density was observed, and values measured did not exceed 70%. This is not a surprising result however as the highest sintering temperature used was lower than the average value from previous experiments, the only difference being the improved stability of sintering temperature.

Table 4.9 Sample Densities Post-Sintering

Sample	Weight [g]	Length [mm]	Diameter [mm]	Density [g/cc]	Density [%]
1-1	1.070	50.430	3.014	2.974 (± 0.017)	67.13 (± 0.38)
1-2	0.902	42.820	2.996	2.988 (± 0.019)	67.45 (± 0.44)
1-3	0.996	46.220	3.038	2.973 (± 0.018)	67.11 (± 0.40)
2-1	1.111	52.930	2.998	2.973 (± 0.017)	67.12 (± 0.38)
2-2	1.164	53.680	3.044	2.980 (± 0.016)	67.26 (± 0.36)
2-3	0.956	45.550	3.000	2.969 (± 0.018)	67.02 (± 0.42)
3-1	1.059	50.350	3.018	2.940 (± 0.017)	66.37 (± 0.38)
3-2	1.113	52.030	3.018	2.990 (± 0.017)	67.50 (± 0.38)
3-3	1.138	52.640	3.026	3.006 (± 0.017)	67.86 (± 0.37)
4-1	1.092	52.090	2.960	3.046 (± 0.017)	68.77 (± 0.39)
4-2	1.120	53.000	2.992	3.006 (± 0.017)	67.85 (± 0.38)
4-3	1.100	52.080	2.962	3.065 (± 0.017)	69.19 (± 0.39)
5-1	1.120	52.960	3.000	2.992 (± 0.017)	67.54 (± 0.38)
5-2	1.087	51.090	2.956	3.100 (± 0.018)	69.98 (± 0.40)
5-3	1.125	53.370	3.002	2.978 (± 0.017)	67.23 (± 0.37)
6-1	1.186	54.820	3.010	3.040 (± 0.016)	68.63 (± 0.37)
6-2	1.116	52.490	2.986	3.036 (± 0.017)	68.54 (± 0.38)
6-3	1.095	51.080	3.006	3.021 (± 0.017)	68.19 (± 0.39)
7-1	1.218	56.520	3.020	3.008 (± 0.016)	67.91 (± 0.36)
7-2	1.189	56.440	2.966	3.049 (± 0.016)	68.83 (± 0.37)
7-3	1.195	56.150	2.986	3.039 (± 0.016)	68.60 (± 0.37)
8-1	1.100	51.810	3.008	2.988 (± 0.017)	67.44 (± 0.38)
8-2	1.114	52.700	2.954	3.084 (± 0.017)	69.62 (± 0.39)
8-3	1.065	51.290	2.924	3.092 (± 0.018)	69.80 (± 0.41)
9-1	1.069	50.640	3.016	2.955 (± 0.017)	66.70 (± 0.38)
9-2	0.972	45.870	2.978	3.042 (± 0.019)	68.67 (± 0.42)
9-3	1.141	53.430	3.026	2.969 (± 0.016)	67.03 (± 0.37)

The parameter SNR were calculated based on the values of density obtained and are shown in Fig.4.36. The mean of means plot showing the average measured density at each parameter level is also plotted in Fig. 4.37.

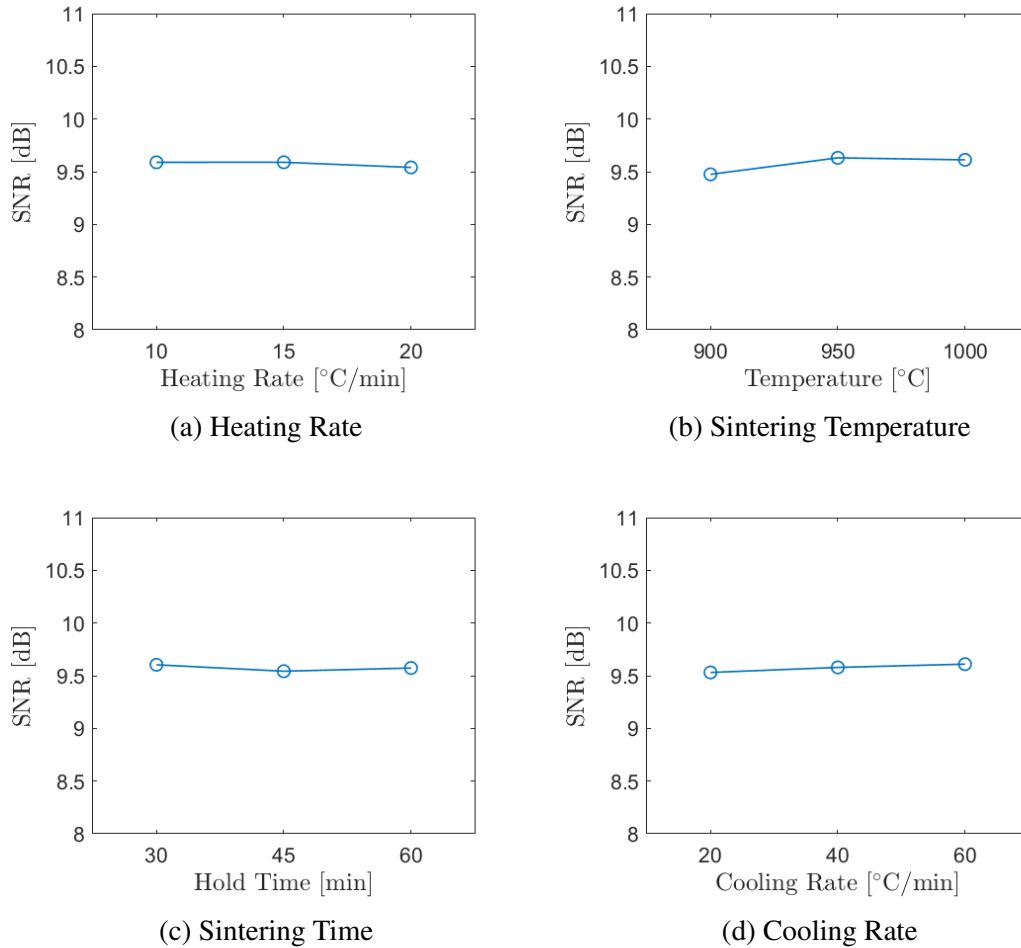


Fig. 4.36 Mean of means analysis indicating effect of each parameter level on the SNR for sample density

As can be seen there the parameters have very little impact on the SNR of the density, that is to say that changing a parameter has little statistical significance when considering the natural variation of a series due to noise.

At the risk of repeating previous statements, as the sintering is still believed to be initial stage there will be very little change in density to begin with. Taking into account the measurement uncertainty of about 0.02 g/cc, it should be clear that any trends observed in Fig. 4.37 can not be considered significant.

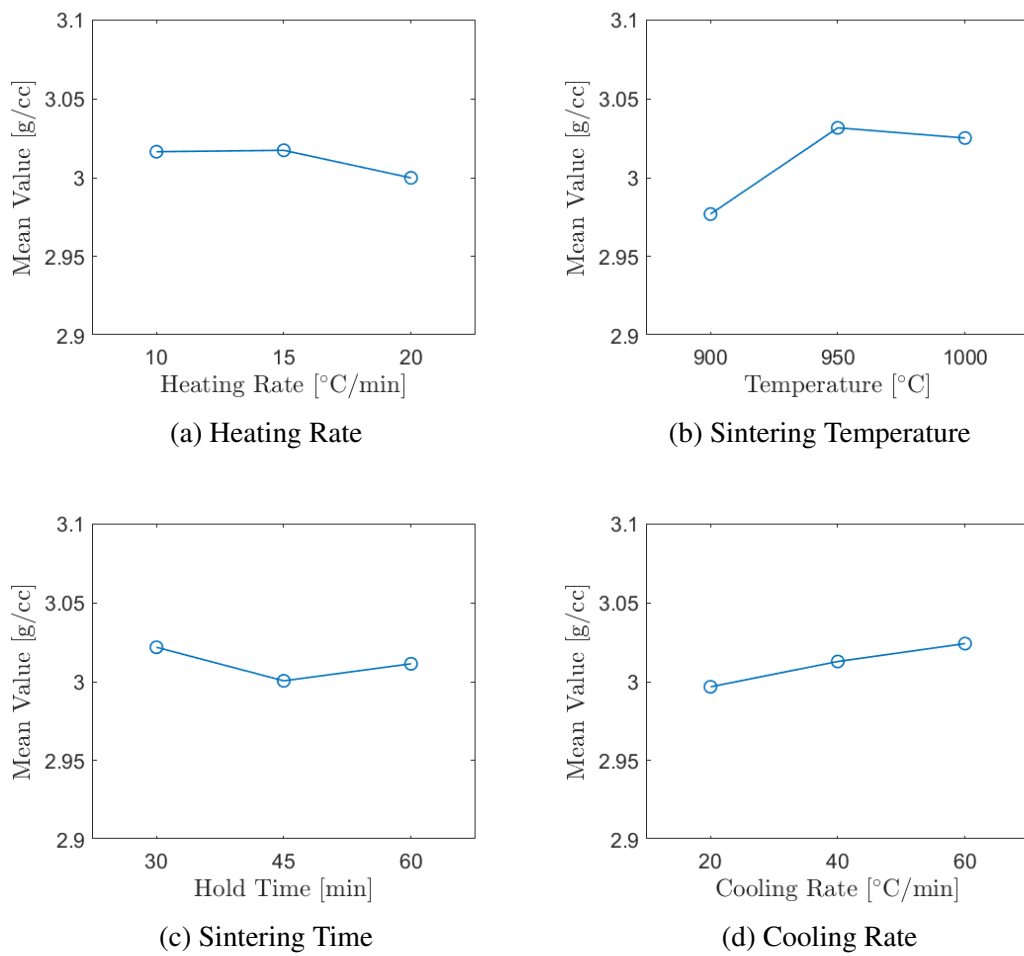


Fig. 4.37 Mean of means analysis indicating effect of each parameter level on the measured sample density.

The results from the 3-point bend tests are listed in Tab. 4.10, and an example plot showing the force applied for increasing deflection is shown in Fig. 4.38 for sample 5-2. In all cases the samples entered failure mode immediately after elastic deformation, with no obvious plastic deformation occurring.

Table 4.10 3-Point Bend Results

Sample	E_{mod} [GPa]	Sample	E_{mod} [GPa]	Sample	E_{mod} [GPa]
1-1	10.90	4-1	17.70	7-1	19.10
1-2	8.04	4-2	13.90	7-2	20.50
1-3	10.60	4-3	17.40	7-3	20.50
2-1	11.30	5-1	17.40	8-1	16.50
2-2	11.70	5-2	22.30	8-2	20.60
2-3	9.82	5-3	14.10	8-3	18.20
3-1	9.46	6-1	15.40	9-1	17.00
3-2	11.50	6-2	16.00	9-2	20.50
3-3	12.30	6-3	12.70	9-3	20.20

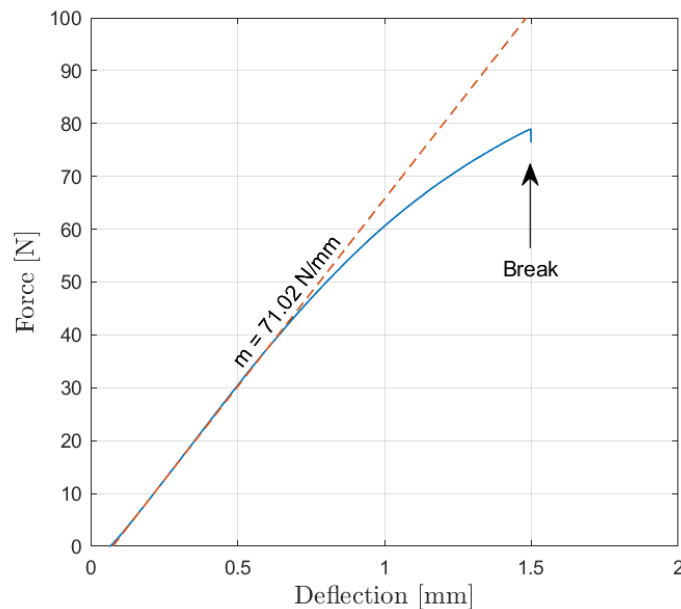


Fig. 4.38 Force/Displacement plot for 3-point flexural bend test (Sample 5-2). The dashed line shows the gradient of the linear response region.

The flexural modulus of elasticity (E_f) was measured using a ZwickRoell universal testing machine configured for a circular sample. The value of E_f can normally be considered equivalent to the Young's modulus for isotropic materials which is normally found to be 113.8 GPa for wrought Ti6Al4V [98]. The values shown for the sintered samples were found to be no more than 20% of the bulk value. As these samples may not necessarily be isotropic due to the low density, and also due to the small length tested, identically shaped samples were produced by PBF for comparison. In total 5 PBF samples were tested and the average E_f was found to be 71.4 GPa. As these samples were fused to near full density they behaved more like wrought titanium and were seen to undergo plastic deformation rather than break. The low mechanical strength of the microwave sintered samples can almost certainly be attributed to the low density.

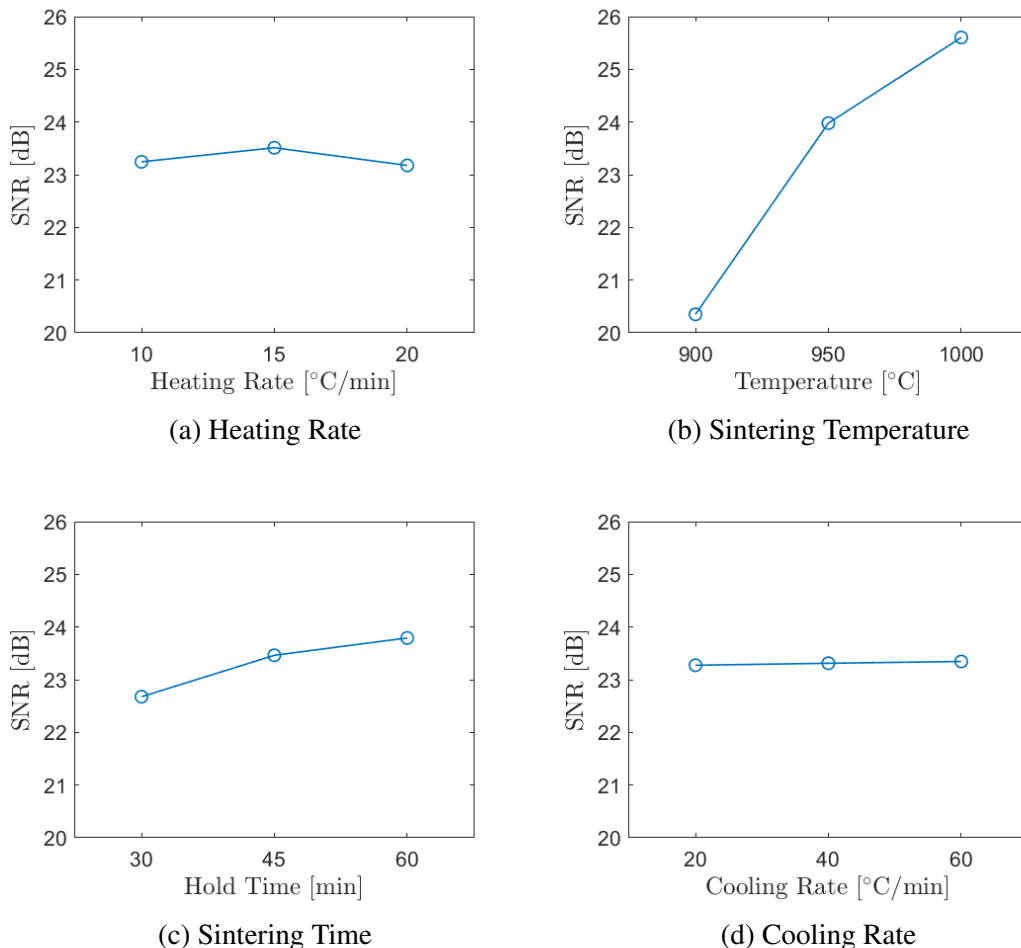


Fig. 4.39 Mean of SNR analysis indicating effect of each parameter level on the SNR for flexural modulus E_f .

The SNR plots for the flexural modulus are shown in Fig. 4.39 and the mean of means plots are given in Fig. 4.40. Unlike the density analysis, where there was no significant sensitivity, it can be seen that sintering temperature had a significant influence on the value of E_f . This is evidenced by its increasing SNR and also by the distinct change in average value at each given level.

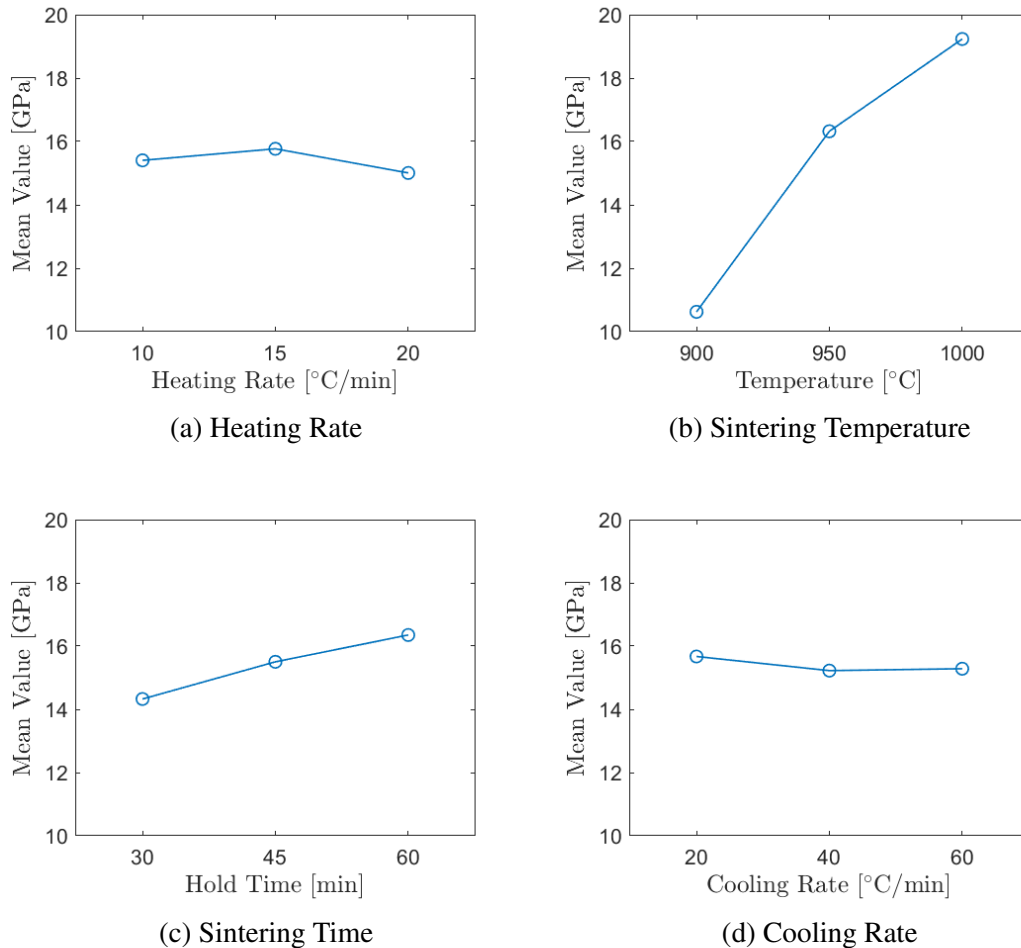


Fig. 4.40 Mean of means analysis indicating effect of each parameter level on the measured flexural modulus E_f .

The sintering time was also observed to have an effect, but at a reduced sensitivity compared to the sintering temperature. Heating rate was not shown to have a significant effect at the levels tested. In sintering the heating rate does in fact have a large influence on the final density due to its effect on coarsening [13, 92]. It has been shown that higher heating rates can act to slow grain growth in intermediate stage sintering[13]. This allows the slower moving pores to experience further shrinking at the boundaries where mass transport is higher [13, 92]. As the sintering here is largely observed to

be initial stage very little coarsening happens, and while heating rate may be highly impactful later on, here it will have limited effect.

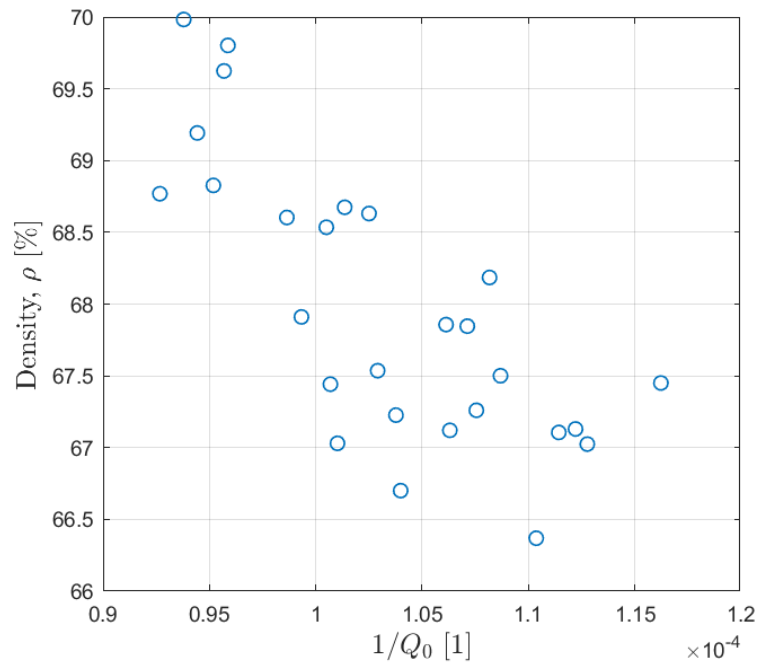


Fig. 4.41 Distribution of sample density and final loss

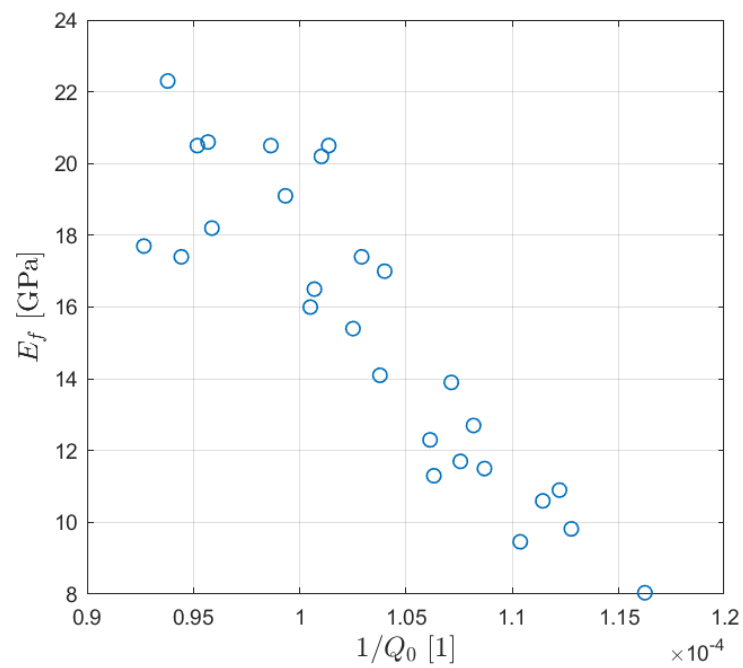


Fig. 4.42 Distribution of sample flexural modulus and final loss

The final loss as measured by VNA was plotted against the density and the flexural modulus for each sample in Figs. 4.41 and 4.42. As can be seen there is strong correlation for both plots, flexural modulus especially was shown to have excellent correlation with $1/Q_0$. The wider spread for the density plot is likely a factor of the measurement method and uncertainty.

4.6 Conclusions

Microwave sintering was performed on powder compacts using the magnetic field of the TE_{011} resonant cavity mode. The measurement setup described in Ch. 3 was used to perform the excitation while taking periodic measurements of the resonant reflection response. In addition to being used to track the changes to resonant frequency occurring as a result of heating/sintering, this allowed for the evaluation of the Q_0 which could be used to monitor the change in microwave absorption during the process.

It was shown that the action of mass-transport during sintering acts to lower the overall loss presented by the powder compact. We attribute this reduction in loss to two main effects:

1. The increase in particle size distribution due to absorption of smaller particles by larger ones.
2. The reduction in surface area due to formation of particle interconnects during necking.

An increase in particle size distribution would occur as a result of the reduction in surface free energy experienced when a smaller particle is absorbed by a larger one [10, 11]. The increase in particle size will have an associated sintering stress [10] and so it can be surmised that there will still be some activation energy required. The effect of this on microwave magnetic dipole loss will depend on the sizes of the particles involved in relation to the skin-depth: in the large skin-depth region the increase in particle size will enhance the magnetic dipole loss, while in the small skin-depth region there will be a reduction [5]. For the experiments performed in this work the majority of particle sizes will have been in the small skin-depth region and so a reduction in loss would have occurred. This mechanism does not involve the formation of particle interconnects and so powders would retain the ability to flow. Evidence for the change in particle sizes at sub-sintering temperatures has been reported previously for the continued recycling of powder in PBF [81].

The formation of particle interconnects act to reduce a significant amount of surface area during sintering [10, 11, 13]. Recalling the microwave power loss of a conductor is determined by R_s

$$P_{avg} = \frac{R_s}{2} \int_s |\vec{H}_t|^2 dS \quad (4.5)$$

where \vec{H}_t is the magnetic field tangential to that surface.

It should be clear therefore that a reduction in total surface area would lead to a reduction in power loss.

In all sintering experiments performed the same general behaviour was observed in the microwave loss. At the beginning of the cycle the unsintered powder presented a significant loss. As temperature began to increase there was an initial enhancement to the loss due to an increase in resistivity. This would act to increase the skin-depth by the square-root of temperature, assuming a linear variation of resistivity with temperature, and thus enhance the magnetic dipole absorption slightly.

At a certain temperature, however, the effects of mass-transport began to occur and as initial bonding between particles occurred there was a dramatic reduction in loss. For Ti6Al4V this was seen to occur as low as 300°C in the temperature controlled experiments. Interestingly, while the modification to the compact was sufficient to lower the loss significantly, samples processed up to 600°C remained in powder form. It was theorised that the particle interconnects formed must have been largely superficial in terms of mechanical bonding but gave good enough electrical contacts so as to reduce loss through surface elimination.

At higher temperatures the inter-particle bonds were shown to be strong enough to maintain a solid shape and the micro-structure was examined for samples of Ti6Al4V, 316L, and 247LC sintered powder. While evidence of sintering was identified such as necking, pore closure, and absorption of small particles, the overall structure was still observed to be largely porous. Calculations of the density before and after sintering indicated that very little densification had occurred. It was concluded that the sintering performed had not progressed beyond the initial stage.

Finally a large scale study was performed in order to investigate the influence of the heating rate, sintering temperature, sintering time, and cooling rate. To achieve this the closed-loop temperature control of the measurement system was developed and is described in Ch. 3. As a steady heating rate was employed in these experiments the overall change in loss with temperature could be observed. It was seen that following the initial rapid reduction in loss the value began to decrease less with increasing temperature before reaching a minimum once maximum sintering temperature had been reached. It was found that for the type of sintering being performed by the system

only sintering temperature had a significant influence. This again was attributed to the sintering not progressing beyond the initial stage. It was discussed that should further densification occur the heating rate would be seen to play a larger role.

In order to progress the sintering further then it is likely that higher temperatures would be required, and commonly reports in the literature for Ti6Al4V use temperatures between 1200°C and 1600°C [41, 79]. Higher temperatures could be achieved by switching to a higher power amplifier, or alternatively insulating material could be added to the sample applicator such as mullite, which is transparent to microwaves.

The final loss value of samples was found to have excellent correlation between the final mechanical properties of the sample. This is a logical result as the same developments in micro-structure during sintering which are associated with enhancing the mechanical properties of the powder compact will act to reduce the overall microwave loss of the sample. An interesting study to follow this work could therefore be an investigation of the ability for microwave measurements to detect differing degrees of open-surface porosity in sintered samples.

Chapter 5

Lift-Off Dielectric Resonator for Measuring Microwave Surface Resistance

5.1 Introduction

In recent years there has been a surge in activity surrounding the production of passive microwave components (in particular waveguides) using additive techniques [8, 9, 99, 100]. Additive manufacture can lead to increased flexibility in design and allows the realisation of complex geometries which would normally be difficult to produce. Additionally the overall weight and size of a design can be reduced by combining several sections (which would usually need to be machined separately) into a single piece suitable for additive manufacture. This process is known as part consolidation and eliminates the need for a large number of interconnects in the final assembly [101]. The advantages of part consolidation for waveguide antenna feed-chains in satellites alone has been commented upon, in particular the reduction in launch cost as a direct consequence of weight reduction [9].

For an empty metal waveguide/cavity the loss of the system is determined by the surface resistance (R_s). Thus to minimise loss in the system R_s should also be minimised. This can be done by increasing conductivity of the conducting walls or by reducing surface roughness [102–105].

Existing works on microwave performance of AM components tend to focus on the influence of the geometry used rather than the surfaces themselves [8, 9, 99]. There are a large number of process variables involved in any AM process, and when considering the options available for post-processing (annealing, shot-peening, grit

blasting, etc.) it should be quite clear that a variety of different surface finishes can be expected. It has been shown previously that simply measuring the RMS surface roughness is not sufficient to accurately predict the value of R_s [103] and so it is more convenient to measure the R_s directly when examining the effect of the build conditions or post-processing. In this chapter a microwave sensor using a dielectric resonator is proposed as a convenient way of measuring the R_s for flat conducting surfaces. The advantage of using a DR to make these measurements is that the device can be made much smaller than an air-filled cavity/waveguide for the same frequency [106] this reduces the size of the sample required, saving on both production time and cost.

5.1.1 Dielectric Resonators for Measuring R_s

Dielectric resonators are a special case of microwave resonator where the electric and magnetic fields are closely confined to a dielectric piece, often shielded by a conducting cavity. Due to their low-loss, high Q , and small profile they have been used extensively to measure R_s in a variety of applications including high-temperature superconductors, graphene sheets, semiconductors, and copper-clad laminates [107–114].

Hakki-Coleman and Open-Ended DRs

While there exist multiple variations on the basic design, DRs used to measure R_s will tend to fall into one of two categories, these being the 1-plate (or "Open-Ended") and 2-plate (or "Hakki-Coleman") configurations. The distinction between the two types is made depending on whether the dielectric is terminated on one end or both; this is illustrated in Fig. 5.1.

Hakki-Coleman resonators have the dielectric terminated on both ends and tend to be the favoured choice for measurements of high conductivity samples due to their higher accuracy (as compared to open-ended) owing to the reduction of systematic error. This is because the dual termination gives deterministic solutions to the field equations [110, 115], which enable accurate determination of geometric and energy-filling factors which are used to evaluate R_s . The downside to this however, is that two samples must be measured together and therefore the R_s measurement will be the average of the two values. In order to evaluate individual samples, multiple measurements must be taken looking at different combinations of samples [110], this "round-robin" approach can be both resource and time consuming. Open-ended resonators on the other hand only measure one sample at a time, greatly increasing the time taken to measure a group of samples. This comes at the potential cost of accuracy however as there are no deterministic field solutions [110]. This means the geometric

and energy-filling factors must be evaluated through simulation. Additionally as the dielectric is not sandwiched between two plates a support rod is normally necessary to keep everything in position, which introduces additional system losses and further complicates the analysis. It is worth noting however that the wide availability of finite-element modelling software suited for fields analysis makes these analyses almost trivial. Given also that the comparisons of accuracy and precision between the two types are almost always made in the context of superconductor measurements [108, 110], for a much lossier AM surface the open-ended structure may very well be "good-enough".

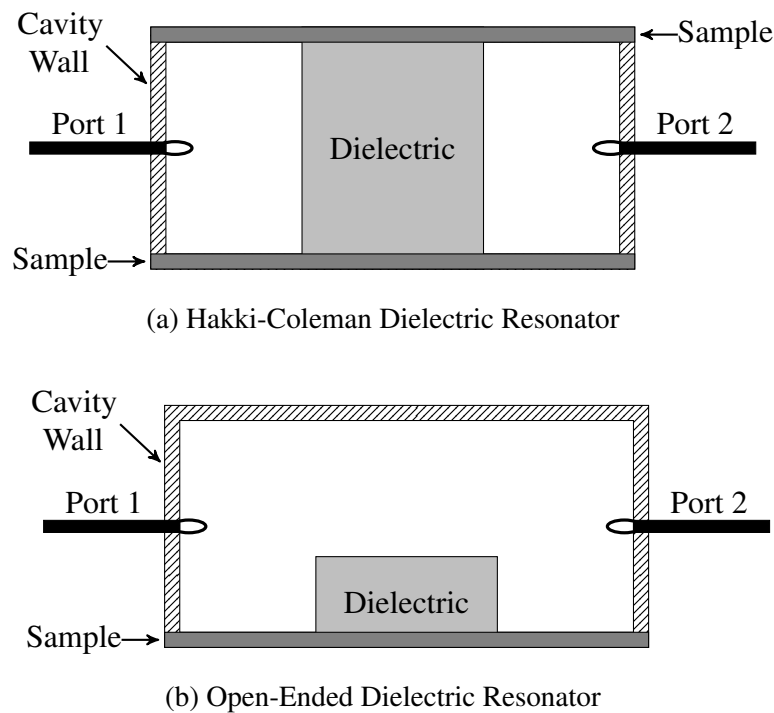


Fig. 5.1 General structure for (a) Hakki-Coleman and (b) Open-Ended resonators

5.1.2 General Measurement Theory

Regardless of the configuration used the basic measurement principle remains the same. For a given DR the value of Q_0 can be described as the inverse sum of Q_C and Q_D elements:

$$\frac{1}{Q} = \sum_{n=1}^i \frac{1}{Q_{C_n}} + \sum_{m=1}^j \frac{1}{Q_{D_m}} \quad (5.1)$$

where Q_C corresponds to a Q-factor for conductor elements and Q_D a Q-factor for dielectric elements.

Using the well-known derivations in [46] it is possible to define Q_C and Q_D in terms of R_s and $\tan \delta$:

$$\frac{1}{Q_C} = \frac{\iint_S H_t \cdot H_t^* ds}{\omega_0 \iiint_V \mu_0 H \cdot H^* dv} R_s = GR_s \quad (5.2)$$

$$\frac{1}{Q_D} = \frac{\iiint_V \epsilon E \cdot E^* dv}{\iiint_V \epsilon E \cdot E^* dv} \tan \delta = p \tan \delta \quad (5.3)$$

where G is a geometric factor (Ω^{-1}) and h is an energy-filling factor (unitless).

Providing the parasitic system losses are known (R_s of the walls, $\tan \delta$ of the dielectric) sample measurements are performed by measuring the unloaded Q and evaluating R_s by eliminating the known system losses.

$$R_{S(sample)} = \frac{\sum_{n=1}^i \{G_n R_{S_n}\} + \sum_{m=1}^j \{p_m \tan \delta_m\} - Q_0^{-1}}{G_{(sample)}} \quad (5.4)$$

5.1.3 Determining System Losses

The geometric and energy filling factors of dielectric resonators are easily calculated either by hand or through simulation software [116]. These factors are independent of loss and so are defined exclusively by the dimensions of the system, and the permeability/permittivity of the wave environment. Additionally most materials used in dielectric resonators have no magnetic properties, so one can omit the permeability leaving only the dimensions and permittivity. Conveniently these quantities are trivial to measure and calculate. Dimensions can be found through inspection by micrometer or similar while the permittivity can be found by measuring the frequency and adjusting the model successively to a desired accuracy.

The loss factors on the other hand (R_s , $\tan \delta$) are not as simply measured. Their accurate determination is crucial to the accuracy of any subsequent measurements [107, 108, 117] and so despite difficulty *great care must be taken to guarantee successful results.*

Determination of $\tan \delta$

Whispering gallery modes have been employed to determine $\tan \delta$ successfully [112]. The advantage of this technique is that the existing resonator can be used without modification. However, as these modes tend to be higher order it necessitates the use of high frequency vector network analysers which can be costly and harder to calibrate.

Another method is to measure the change in Q when using dielectrics of different apertures of the same material [107]. Since the operating mode is used to perform the measurement there is no additional need for equipment, but this does require the repeated assembly and disassembly of the resonator each time it requires calibration.

Determination of R_s

For R_s the design is often adjusted so that the contribution to loss from conductor elements is low to begin with. This is normally achieved by setting the cavity radius to be twice that of the dielectric [107]. A low contribution from conductor elements reduces the influence of error in R_s value used. This is sometimes considered sufficient enough to allow R_s to be calculated from material conductivity at the operation frequency, rather than measuring it directly [107, 108]. The issue in not measuring, however, is that at microwave frequencies surface defects including roughness can have a serious impact on the measured R_s [103, 104, 112]. Natural wear and tear over the system lifespan will likely result in a gradual drift in the accuracy of the assumed value.

In cases where the $\tan \delta$ has already been evaluated, R_s is often found through a measurement of the unloaded cavity. This is only valid for systems where there are only the two loss factors and will obviously carry the advantages or disadvantages of the method used to evaluate $\tan \delta$.

To summarise the current methods for determining loss factors require either expensive equipment or the disassembly and reassembly of the fixture. Results from previous measurements can be used however it is likely that through use the loss (mainly of conducting surfaces) will change over time. Another important consideration is temperature, requiring that the measurements of these factors be done at the same temperature as the sample measurement. If one wished to perform a measurement at a specific temperature, total recalibration would be necessary *each time*. In the next section the proposed calibration technique is introduced to address these issues. It is a calibration performed near the operation frequency and so no additional high frequency equipment is needed. It can be performed relatively quickly without need for modification to or disassembly of the resonator structure. Finally it determines the loss factors together in the same procedure.

5.2 A Novel Calibration Technique for Determining System Losses

In this section a variation of the open-ended dielectric resonator is presented where the dielectric can be moved vertically with respect to the sample or base as illustrated in Fig. 5.2. This vertical motion or "Lift-Off" enables a novel method for determining the parasitic system losses where the Q_0 is measured over a range of lift-off values (x). A characteristic equation is fitted to these values and the system losses are found through least-squares curve fitting. Once calibrated R_s of any sample can be found by replacing the end effector with the sample, measuring the Q_0 , and then eliminating in the conventional way as described previously. Additionally changing the position of the dielectric changes the frequency, enabling measurements to be performed over a range of frequencies with the same device.

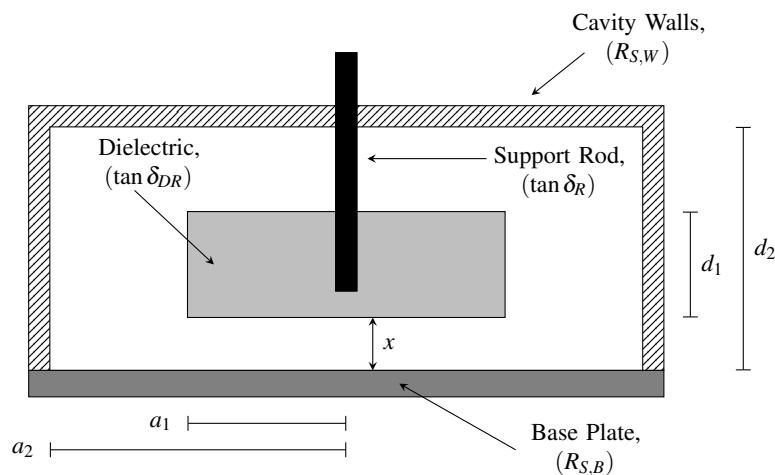


Fig. 5.2 Lift-Off Dielectric Resonator. Labelled dimensions a_1 , a_2 , d_1 , d_2 , and x represent the DR radius, cavity radius, DR height, cavity height, and lift-off position.

5.2.1 Measurement Principle

Static Equation for Q

In the last section it was shown that the Q-factor of a DR can be represented by an inverse sum of conductor and dielectric losses. Applying (5.1) to the structure shown in Fig. 5.2 gives conductive losses from the cavity walls and base, and dielectric losses from the dielectric and support rod. The cavity walls and bases are considered separately as the base can be removed.

$$\frac{1}{Q} = \frac{1}{Q_{(walls)}} + \frac{1}{Q_{(base)}} + \frac{1}{Q_{(DR)}} + \frac{1}{Q_{(rod)}} \quad (5.5)$$

These quantities are then related to R_s and $\tan \delta$ through geometric and energy-filling factors. For convenience in later steps the geometric factors for the LODR have been redefined to remove the frequency dependence. To avoid confusion with the definitions in (5.2) and (5.3) they are defined below:

$$G_w = \frac{\iint_{S(w)} H_t \cdot H_t^* ds}{2\pi \iiint_V \mu H \cdot H^* dv} \quad (5.6a)$$

$$G_b = \frac{\iint_{S(b)} H_t \cdot H_t^* ds}{2\pi \iiint_V \mu H \cdot H^* dv} \quad (5.6b)$$

$$p_d = \frac{\iiint_{V(d)} \epsilon E \cdot E^* dv}{\iiint_V \epsilon E \cdot E^* dv} \quad (5.6c)$$

$$p_r = \frac{\iiint_{V(r)} \epsilon E \cdot E^* dv}{\iiint_V \epsilon E \cdot E^* dv} \quad (5.6d)$$

Then following the earlier definition in (5.2) and (5.3) and using the newly defined geometric factors the general result for Q_0 is obtained.

$$\frac{1}{Q_0} = \frac{G_w R_{S,w}}{f} + \frac{G_b R_{S,b}}{f} + p_d \tan \delta_d + p_r \tan \delta_r \quad (5.7)$$

where $R_{S,w}$, $R_{S,b}$, $\tan \delta_d$ and $\tan \delta_r$ are the surface resistances of the walls and base, and the loss tangents for the dielectric and the support rod. This general definition considers the LODR in one fixed configuration, next the dependence on x will be considered.

Lift-Off Equation for Q

It is well known that dielectric resonant modes are largely confined to the immediate area around the dielectric itself [106]. It should be clear then that as the dielectric lift-off position, x is varied the field distributions in the cavity will be modified giving rise to a change in both Q and f .

Defining f_0 as the resonant frequency when the dielectric is at the measurement point (e.g. $x = 0$ mm) and recalling that both R_s and $\tan \delta$ vary with frequency gives the result shown below.

$$R_s(f) = R_{S_0} \sqrt{\frac{f}{f_0}} \quad (5.8)$$

$$\tan \delta(f) = \tan \delta_0 \frac{f}{f_0} \quad (5.9)$$

Letting $f(x)$ be the resonant frequency as a function of x these results allow rewriting (5.7) for any value of x as shown below.

$$\frac{1}{Q_0(x)} = \frac{G_w(x)R_{S_{w_0}}}{\sqrt{f(x)f_0}} + \frac{G_b(x)R_{S_{b_0}}}{\sqrt{f(x)f_0}} + \frac{p_d(x) \tan \delta_{d_0}}{f_0/f(x)} + \frac{p_r(x) \tan \delta_{r_0}}{f_0/f(x)} \quad (5.10)$$

This is the measurement equation and can be used to calculate the value of $R_{S_{b_0}}$ at any point providing the values of $R_{S_{w_0}}$, $\tan \delta_{d_0}$, and $\tan \delta_{r_0}$ ¹ are known. The geometric and energy-filling factors have also been given an x dependency to account for the changing field distributions.

The change in f will be independent to loss and can be used to increase the accuracy of supplied values for permittivity in the simulation model. This is done by adjusting their values parametrically and comparing to measured data. Once the values of ϵ_r for the dielectric and rod have been fixed, the geometric and energy-filling factors can be evaluated with confidence at discrete points using (5.6).

Calibration Equation

For calibration a base plate made from the same material as the cavity shield is used. As they are the same material they will have the same conductivity and it can be assumed that at a given frequency their values for R_s will also be the same.

$$R_{S_w} = R_{S_b} \quad (5.11)$$

This simplifies (5.10) yielding the calibration equation where a maximum of three unknown variables must be solved for.

$$\frac{1}{Q(x)} = \frac{G_w(x) + G_b(x)}{\sqrt{f(x)f_0}} R_{S_{w_0}} + \frac{p_d(x)}{f_0/f(x)} \tan \delta_{d_0} + \frac{p_r(x)}{f_0/f(x)} \tan \delta_{r_0} \quad (5.12)$$

¹It is later shown that the value of $\tan \delta$ for the rod can be ignored providing it's influence is minimal.

Calibration is then performed by least-squares curve fitting (5.12) to measured values of Q_0 over a range of x . Once calibration is done and the loss factors are known measurement can be performed at any value of x within the calibrated range by replacing the base with the sample under test, measuring Q_0 at that point and then solving for R_{sb_0} in (5.10).

An obvious point to consider is that if this fitting strategy could be employed to find the loss factors, why not skip calibration and use the fitting strategy to find all loss factors *including* the sample R_s ?

While certainly possible there are multiple reasons why this would be ill-advised. The reasoning behind the calibration as a separate step is three-fold:

Firstly there is the fact that least-squares fitting is a numeric procedure that only seeks to minimise error and does not involve the physical properties of the system at all. With a greater number of variables there will be an increased degree of freedom in the process which can make it more susceptible to over-fitting as a result of measurement or simulation error.

Secondly by performing the calibration separately to measurement, the quality of the calibration is not influenced by the sample loss. In the case of a high-loss sample the fit would be heavily weighted to the base which could result in over-fitting, the opposite is true of a low-loss sample where it might have such a low contribution that it may be below the tolerance level. This also has the advantage of sample measurements being comparable relative to each other regardless of absolute accuracy.

Finally there is the simple factor of time. It is more efficient to perform an extensive calibration and then multiple quick measurements than it is to perform multiple extensive measurements. There is also the fact that a good least-squares fit would require more data points for a 4-parameter fit than for a 3-parameter one.

5.2.2 Measurement Mode Selection

For the measurements and simulations shown in this work it was decided to use the $TE_{01\delta}$ dielectric resonator mode as the principal measurement mode. It is worth noting before proceeding however that this method holds true for any measurement mode and that the selection made here is dependent on the material chosen later on and the various suitabilities $TE_{01\delta}$ presents.

Shown in Fig. 5.3 is the electric and magnetic (normalised) field distributions for the $TE_{01\delta}$ resonant mode. From its designation 'TE' it is identified as a *transverse electric* mode, having no or zero \vec{E}_z component. This feature is useful as it naturally overcomes issues when using anisotropic dielectrics. sapphire is used frequently

in DRs owing to its extremely low loss tangent at microwave frequencies, but is anisotropic in that it has $\epsilon_r \approx 9.4$ in the c-plane but $\epsilon_r \approx 11.3$ along the c-axis. Orienting the c-plane so it is normal to the z-axis means the sapphire can be treated as isotropic when using $TE_{01\delta}$, this greatly simplifies analysis particularly when calculating the energy-filling factors.

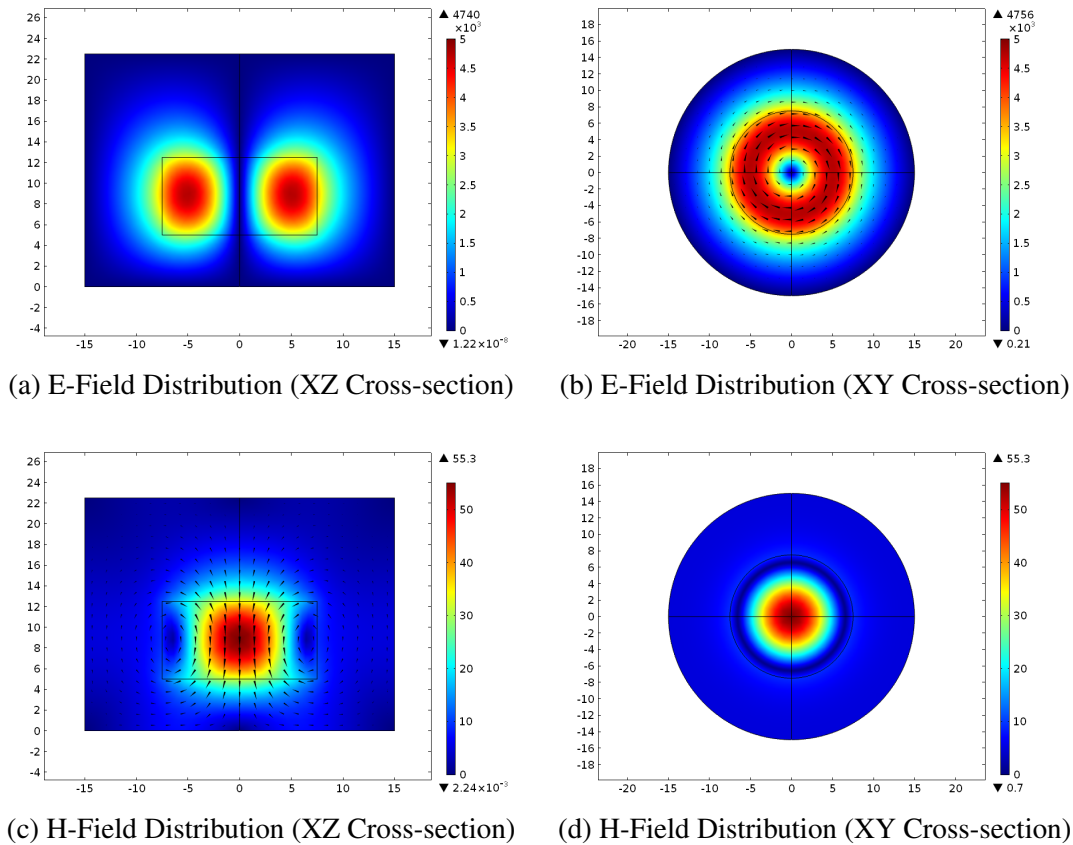


Fig. 5.3 Electric and Magnetic field distributions for $TE_{01\delta}$ dielectric resonator mode. Field Distributions obtained through eigenfrequency simulation in COMSOL. Physical dimensions are given in mm, field magnitudes are given in V/m and A/m for electric and magnetic fields.

The remaining identifiers '01 δ ' refer to the number of complete full-wave patterns along a given cylindrical-coordinate dimension. There is zero variation along the azimuth (angularly), which is useful as it eliminates degeneracy of having two superimposed modes. There is 1 full-wave pattern radially evidenced by the low E-field at the centre and edge of the dielectric, which is useful for supporting structures as they will have low energy-filling factors. Finally the "interesting" part is the δ variation along the z-axis. This naming convention arises from the use of δ in mathematics to represent a "small amount" and here simply means that there is slightly-less-than a full-wave pattern along the z-axis. This is very common among dielectric resonator

modes (including hybrid ones) which are tightly bound to the dielectric, for higher order modes this can increase to $1 + \delta$, $2 + \delta$ and so on.

As can be seen both the electric and magnetic fields are largely confined to the area immediately surrounding the dielectric. For the sapphire resonator simulated over 90% of the electric energy and 60% of the magnetic energy is confined to the dielectric, which can be even higher if high permittivity ceramics are used [106]. This is useful as it allows the magnetic field to be introduced to surfaces of interest through simple proximity whilst simultaneously, loss from the cavity walls can be minimised by increasing the distance between them and the dielectric. For the LODR method especially it means that the value of Q will be highly dependent on dielectric position, and the contribution to loss (weighting) for each parameter (R_s , $\tan \delta$) will also vary with position. This will help to prevent erroneous fits by reducing the number of possible solutions.

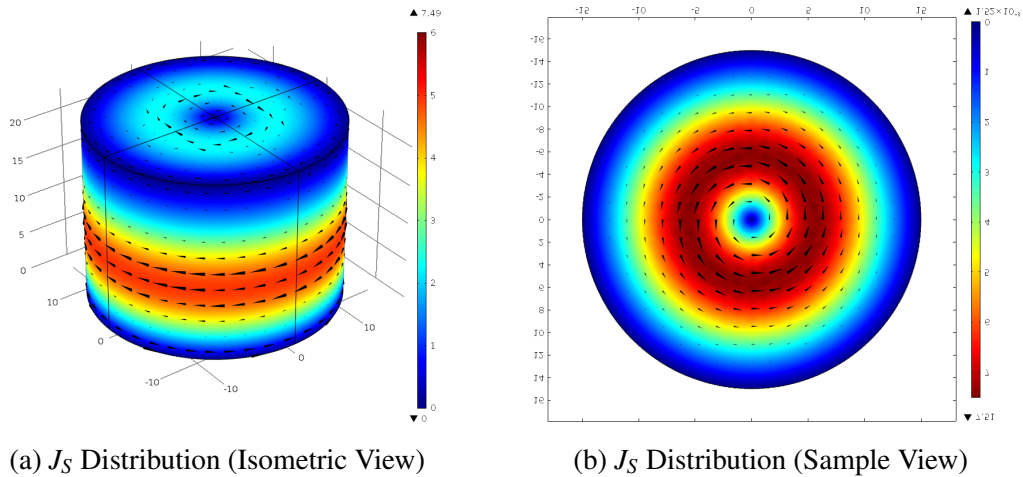


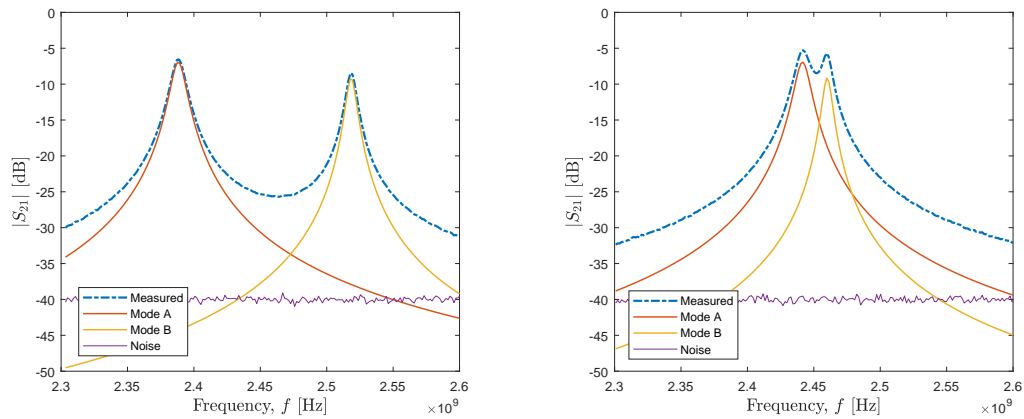
Fig. 5.4 Surface current density at cavity boundary for $TE_{01\delta}$ dielectric resonator mode. Field Distributions obtained through eigenfrequency simulation in COMSOL. Physical dimensions are given in mm, surface current density is given in A/m.

The magnetic field is oriented such that the surface currents form closed loops at the base. Fig. 5.4 shows the surface current density and paths for the $TE_{01\delta}$ mode. As the surface currents have purely azimuthal components the system is much less sensitive to any joins or gaps between the base and wall conductors [117]. This also means that there will be no orientation dependency for samples being measured.

5.2.3 Eliminating Adjacent Mode Interference

Once a measurement mode has been decided upon the design of the geometry aspect ratio can be considered. It is important to choose a geometry that maintains acceptable

separation of the measurement mode from adjacent modes over the calibration lift-off range. This is because the presence of interfering modes near or at the frequency of the measurement mode can significantly alter the measured Q-factor [118].



(a) Adjacent modes with acceptable separation. The measured response is largely unchanged at each resonant peak.

(b) Adjacent modes with unacceptable separation. The measured response at each resonant peak has become distorted

Fig. 5.5 Effect of interference from adjacent modes on transmission response. Measured represents the total transmission response, Mode A & B represent two adjacent modes, and Noise represents a -40dB noise floor. All data points were generated in Matlab using the Series RLC model developed in Ch. 3.

The effect of this is illustrated in Fig. 5.5. With the modes separated sufficiently the measured response is representative of the individual resonances. In this situation it would be simple enough to perform either a circle fit or Lorentzian fit to the data to extract resonant parameters. As the modes approach each other however, they become distorted. Even though it is clear from the measured response that there are still two modes, it would be difficult to achieve an accurate fit to this data for either mode. It is clear that as the spectral separation decreases, the fitted value of Q will become altered.

If during the LODR calibration there is a lift-off value for which the measurement mode is in close proximity to an adjacent mode, the extracted value of Q will be affected. If included in the fit it will introduce error proportional to the number of points affected as a percentage of the whole set. If detected it can be omitted from the fit. However, if this occurs too many times the quality of the fit will suffer. Additionally measurements cannot be performed at this point. These are all non-ideal factors and so it is preferable to avoid mode crossover through careful design.

Simplified K-matrix Approach

Analytic solutions for DR resonant modes are often only valid for specific geometries [119, 120], which makes an analytic approach to design impractical. We therefore turn to incremental design using FEM of electromagnetic fields. The following approach can be used as a starting point to find a geometry with no or minimal mode crossover. Once found it can then be altered and tuned to suit the requirements better.

It is well known that the normalised frequency distribution of a resonant cavity is determined by the ratio of dimensions to each other [46, 106], and this holds true for DRs also. The dimensions for the LODR shown in Fig. 5.2 can be defined relative to the dielectric radius a_1 as:

$$\begin{pmatrix} a_1 & d_1 \\ a_2 & d_2 \end{pmatrix} = a_1 \begin{pmatrix} K_1 & K_2 \\ K_3 & K_4 \end{pmatrix} \quad (5.13)$$

where a_1 , d_1 , a_2 , and d_2 , are the dielectric radius and height, and the cavity shield radius and height, respectively. The K-matrix is the ratio of each dimension to a_1 , and so $K_1 = a_1 : a_1 = 1$, always.

It is convenient to further define K_4 such that:

$$K_4 = kK_3 \quad (5.14)$$

where k is the aspect ratio of the cavity shield, $a_2 : d_2$.

The general procedure is to arbitrarily set a_1 and then choose generic values for the aspect ratios of the dielectric and cavity as a starting point. As shown in [107] setting the value of $a_2 > 2a_1$ minimised the loss from the walls significantly, so a useful starting point would be:

$$\begin{pmatrix} K_1 & K_2 \\ K_3 & K_4 \end{pmatrix} = \begin{pmatrix} 1 & K_2 \\ 2 & 2k \end{pmatrix}$$

Once an acceptable relative distribution has been achieved a_1 can be scaled up or down in size to achieve the desired frequency of operation for the measurement mode.

5.3 Evaluation of Geometric and Energy-Filling Factors in COMSOL

Rather than calculating analytically, the geometric and energy-filling factors can be evaluated in COMSOL using surface and volume integrals. For the structure described in Fig. 5.2 this can be achieved using just 6 integral evaluation operations following a parametric sweep of different lift-off positions¹.

The expressions used for the integrals are given in Tab. 5.1 and their domain/boundary selections are illustrated in Fig. 5.6.

Table 5.1 Volume and Surface Integral Expressions for COMSOL

Name	Type	Expression
g_int1	Volume	$2\pi\mu_0_{\text{const}}\text{emw.normH}^2$
g_int2	Surface	emw.normH^2
g_int3	Surface	$\text{emw.Hx}\cdot\text{conj}(\text{emw.Hx})+\text{emw.Hy}\cdot\text{conj}(\text{emw.Hy})$
p_int1	Volume	$\text{emw.normD}\cdot\text{emw.normE}$
p_int2	Volume	$\text{emw.normD}\cdot\text{emw.normE}$
p_int3	Volume	$\text{emw.normD}\cdot\text{emw.normE}$

Starting with the geometric factors G_w and G_b , from (5.6a) and (5.6b) it can be noted that they share the same general definition with the surface integral being over different surfaces (walls, base), thus the same volume integral can be used for both. g_{int1} is evaluated over all domains using the expression shown in Tab. 5.1. As the normalised H field is used there is no need to multiply by the complex conjugate as the field amplitudes are purely real and so it is simply squared, also since no materials were used with magnetic properties μ_0 was used. The two surface integrals g_{int2} and g_{int3} are then evaluated over the cavity wall and base boundaries respectively as shown in Fig. 5.6. It should be noted that while (5.6a) specifies tangential field, due to the lack of polar coordinates this proved difficult for the walls and normalised field had to be used. For the base, tangential H field is evaluated by omitting H_z from the

¹The setting up and simulation of the model for calibration is covered later on and so to avoid repetition this section shall cover the evaluation *following* the parametric study. For reference the model shown in the domain/boundary selections in Fig. 5.6 is for the second prototype LODR described later.

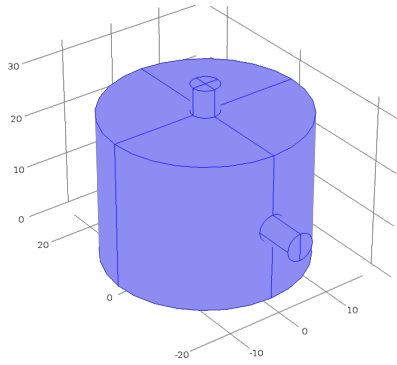
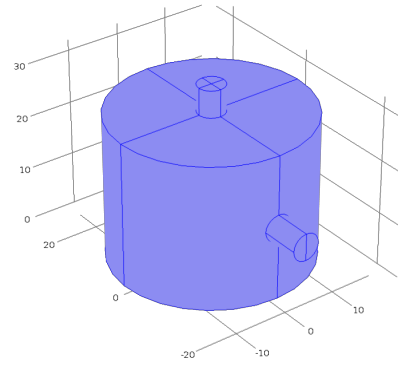
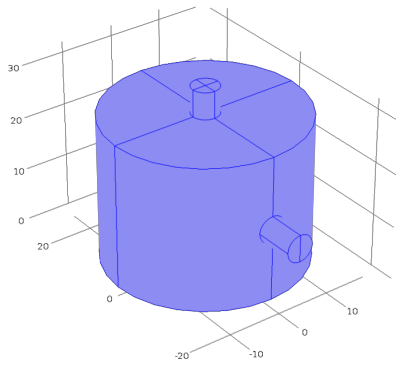
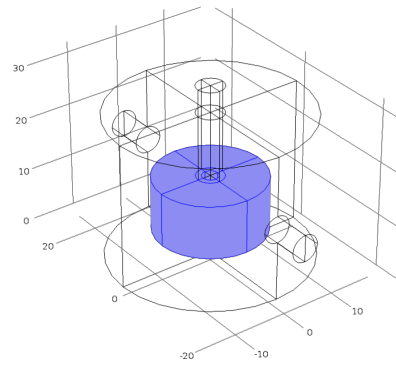
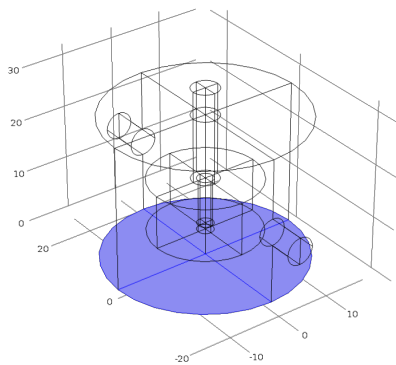
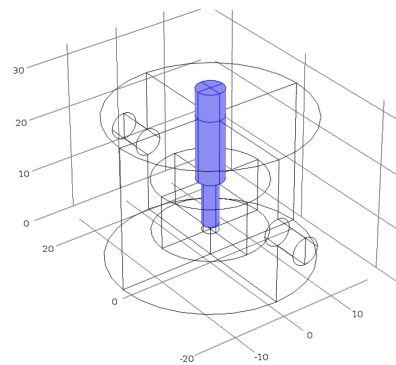
(a) g_int1 domain selection.(b) p_int1 domain selection.(c) g_int2 boundary selection.(d) p_int2 domain selection.(e) g_int3 boundary selection.(f) p_int3 domain selection.

Fig. 5.6 Domain and boundary selections for volume and surface integral operations. Dimensions shown on grid given in mm.

expression, since vector field quantities are used the complex conjugate function is required. G_w and G_b are then computed as:

$$G_w = g_{\text{int}2}/g_{\text{int}1} \quad (5.15a)$$

$$G_b = g_{\text{int}3}/g_{\text{int}1} \quad (5.15b)$$

The energy-filling factors are found in much the same way. From (5.6c) and (5.6d) it is noted that three volume integrals are needed over the total volume, and the dielectric and rod in isolation. The integrals $p_{\text{int}1}$, $p_{\text{int}2}$, and $p_{\text{int}3}$ share the same expression and are evaluated over their respective domains as illustrated in Fig. 5.6. In the expression ϵE is substituted for electric flux density, D to simplify evaluation. As before where the normalised fields are used complex conjugates are not necessary. p_d and p_r are then computed as:

$$p_d = p_{\text{int}2}/p_{\text{int}1} \quad (5.16a)$$

$$p_r = p_{\text{int}3}/p_{\text{int}1} \quad (5.16b)$$

5.4 Calibration and Measurement Using Matlab

This section presents the Matlab code written to perform the calibration and measurement operations for the LODR method.

5.4.1 GEO.m

"GEO.m" is a storage class for the geometric and energy filling factors. It is used simply to group the 5 variables together to make them more manageable. Currently it has no additional functionality. The full listing has been given in Appendix C to save space.

5.4.2 CAL.m

"CAL.m" is used to perform the calibration function and once complete, can be used to perform R_s measurements using Q_0 measurement data. The full listing has been given in Appendix C to save space, but the explanation is given here.

Calibration is performed automatically during construction taking calibration point (x_0), calibration measurement positions (x), frequencies (f), Q-factor (Q), and geometric factors (GEO) as inputs. An additional input is used to specify whether a full

fit (3-parameter) or a reduced fit (2-parameter) should be performed; the reason for doing so is covered in a later section.

The geometric factors are defined as functions of X and the "PCHIP" (piecewise cubic hermite interpolating polynomial) function is used to interpolate the factors for values of x not covered in the geometric factor evaluation. This data extension is only valid for x values within the evaluated range.

The least-squares curve fitting is setup to use the default options and settings for the algorithm. The calibration equation is defined as a function of the loss factors L and position X , depending on fit type L will either be a 3×1 or 2×1 array. The initial guess for each loss factor is set to 1, defined by $L0$. L_low is used to set the lower bounds so the loss factors cannot be negative; upper bounds are not imposed so L_upp is left empty. These settings were found to give a good result without over- or under-fitting. Calibration results are output to the terminal and the fit is displayed as a figure plot.

Following calibration measurement data can be processed using the class member function `Measure()`. Measurements taken at the calibration point can be performed using just Q . Optionally the position and frequency can also be defined to account for slight deviation. This also allows a calibration to be used to evaluate measurements taken at different lift-off positions.

5.5 Simulation: Accuracy of LODR Measurements

This study attempts to quantify the accuracy of the LODR method as well as factors influencing the accuracy that can be improved. This is achieved through simulation using COMSOL multi-physics. The advantage of using simulation is that the loss factors found through calibration can be compared to the actual values in the simulation model. This eliminates the need for secondary measurements and helps establish a theoretical accuracy.

5.5.1 Aims

To investigate accuracy of LODR method at different measurement points and for varying sample conductivities.

To assess the impact of the support rod material on calibration and measurement accuracy. This will be done by simulating the calibration procedure without the rod, with a nylon rod, and with a PTFE rod.

To determine whether or not the rod need be considered in the curve fitting equation. This will be done by comparing the calibration and measurement accuracy of a 2-parameter fit (R_{Sw} and $\tan \delta_d$) with a 3-parameter fit (R_{Sw} , $\tan \delta_d$, and $\tan \delta_r$).

5.5.2 COMSOL Model Setup

Two models were set up with the same dimensions, one with a support rod and one without. The dimensions for both are shown in Fig. 5.7. Material definitions are given in Tab. 5.2.

The cavity was setup as an air domain cylinder with aluminium boundaries. Loss from R_s was enabled by applying an impedance boundary condition to the walls. This told COMSOL to model the aluminium boundaries as if they were of sufficient thickness for the skin effect.

The dielectric was modelled as a sapphire domain cylinder inside the cavity. Displacement from the base was setup parametrically so that it could be swept during simulation, allowing the calibration step to be performed in a single study.

The rod was setup as two unioned cylinders; the material could be set as either nylon or PTFE. Its position and length was also controlled parametrically so that it would follow the dielectric during lift-off.

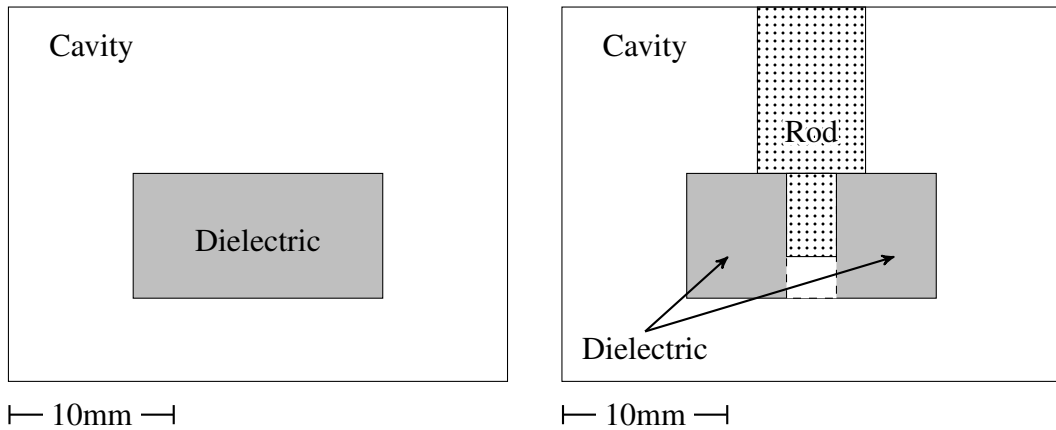
By default COMSOL does not scale $\tan \delta$ with frequency and so the material definition was modified to scale the value in agreement with (5.9).

Table 5.2 COMSOL Material Definitions

Material	ϵ_r [1]	$\tan \delta^\dagger$ [1]	μ_r [1]	σ [S/m]
Air	1.00	0.00	1.00	0.00
Aluminium	1.00	-	1.00	2.86×10^7
Nylon	2.90	1.20×10^{-2}	1.00	0.00
PTFE	2.10	1.50×10^{-4}	1.00	0.00
Sapphire	9.40	3.00×10^{-5}	1.00	0.00

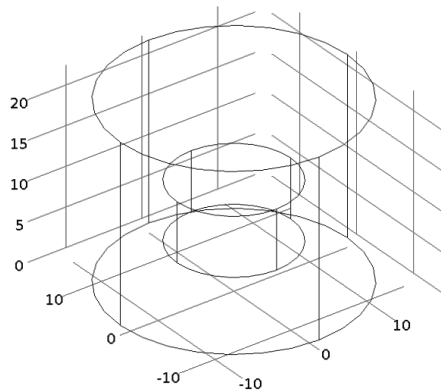
[†]Value at 10 GHz

For meshing the model geometry was sub-divided into four quadrants. As each quadrant shared rotational symmetry, only one quadrant needed to be meshed. This could then be copied onto the remaining three quadrants, helping to save time on re-meshing during the parametric sweep used in the study. Mesh elements were scaled

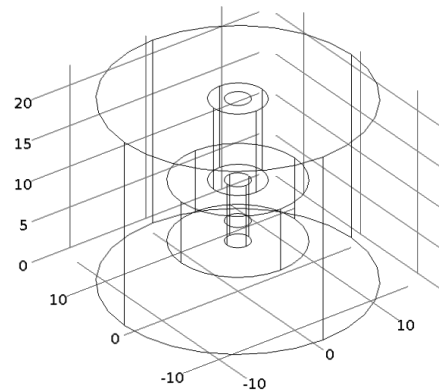


(a) Diagram of Simulation Model without Rod. Image is to scale.

(b) Diagram of Simulation Model with Rod. Image is to scale.



(c) Geometry of Model without Rod



(d) Geometry of Model with Rod

Fig. 5.7 LODR Simulation Model. Geometry and Dimensions. 5.7a and 5.7b show the dimensions in cross section. 5.7c and 5.7d show the geometry in COMSOL

according to frequency and were configured to be no larger than 5% of the wavelength (in air) to achieve good resolution. The mesh used is shown in Fig. 5.8.

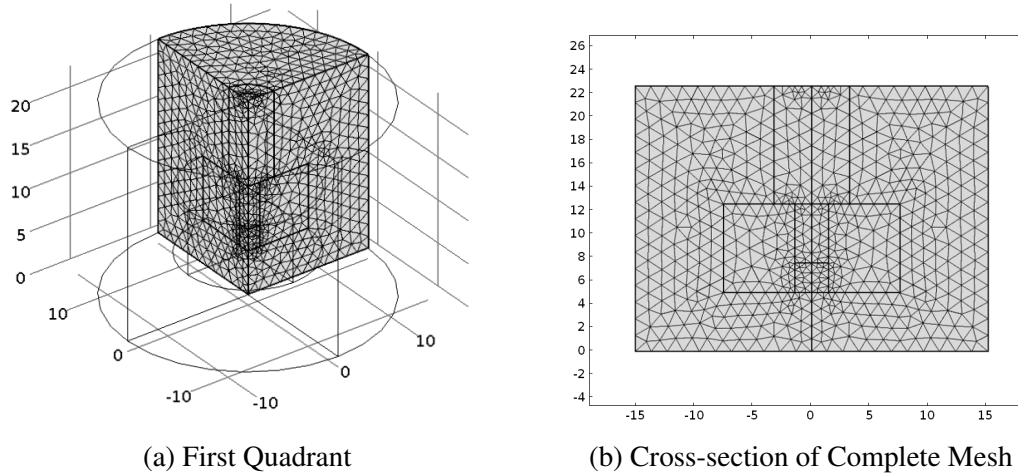


Fig. 5.8 Mesh used for the simple LODR simulation model. a) Meshing of the first quadrant. b) Cross-section showing copied mesh.

5.5.3 Calibration Study Step

Calibration was simulated using a parametric sweep which varied the lift-off value (x) from 0-5mm in 0.1mm steps. Between each step the geometry was modified and re-meshed before being simulated again. Thanks to the meshing strategy used, the time taken to perform the simulation was significantly reduced.

At each point, frequency, Q_0 and the loss tangents were evaluated for the $TE_{01\delta}$ resonant mode. Electric and Magnetic field integrals were also taken and the geometric and energy-filling factors were calculated using (5.6).

Calibration was performed in Matlab, fitting to the evaluated Q_0 from simulation. This was done using both a full 3-parameter fit and a 2-parameter fit which omitted the rod from the equation (for the no rod model only 2-parameter fit was used). Calibration was repeated multiple times using each value of x simulated as the reference point.

5.5.4 Measurement Study Step

Following the calibration study step the base material was modified so that the value of conductivity could be changed using a parametric sweep. Measurements of the base R_s were made by evaluating the Q_0 at a given lift-off position. Matlab was then used to calculate the value of R_s for the base using the calibration results and the measurement

equation (5.10). For comparison the actual value was calculated using the material conductivity and evaluated frequency.

Two sets of measurements were taken. One set had the dielectric fixed at a single measurement position (0.1mm) while the conductivity was swept from 1.0×10^7 S/m to 1.0×10^8 S/m. For the second set the conductivity of the base was fixed at 1.0×10^8 S/m and the measurement position was swept from 0.0mm to 5.0mm. This allowed the effect of changing the conductivity *and* the effect of changing the measurement position to be investigated separately.

5.5.5 Results

Calibration Accuracy

Geometric and energy-filling factors were evaluated using the method described in 5.3 for all three models. These can be found in Appendix D in Tables D.1, D.3, and D.2.

Calibration error was calculated as the absolute deviation of the fitted loss value from the true value used by the model as a percentage. Calibration values as well as error are given in Tables 5.3, 5.4, and 5.5 for reference point at 0.1mm. Calibration error was found to be constant for a given measurement regardless of reference point.

Table 5.3 Calibration Accuracy: R_{Sw0}

Rod	Fit Type	Model Value [Ω]	Fit Value [Ω]	Error [%]
None	2-Parameter	0.0324	0.0325	0.491
Nylon	3-Parameter	0.0323	0.0344	6.245
Nylon	2-Parameter	0.0323	0.0519	60.452
PTFE	3-Parameter	0.0324	0.0326	0.844
PTFE	2-Parameter	0.0324	0.0326	0.844

Reference point used (x_0) : 0.10mm

Calibration performed on the model without a rod was more accurate than for the PTFE model, and significantly more than for the nylon model. For the PTFE rod model the fitting results for R_{Sw0} and $\tan \delta_{d_0}$ were the same for the 2-parameter and 3-parameter fit. The value of $\tan \delta_{r_0}$ given by the 3-parameter fit for the PTFE model was drastically off, the low value returned indicates under-fitting of the parameter

Table 5.4 Calibration Accuracy: $\tan \delta_{d_0}$

Rod	Fit Type	Model Value [1]	Fit Value [1]	Error [%]
None	2-Parameter	2.270×10^{-5}	2.273×10^{-5}	0.089
Nylon	3-Parameter	2.270×10^{-5}	2.560×10^{-5}	12.457
Nylon	2-Parameter	2.270×10^{-5}	5.150×10^{-5}	126.285
PTFE	3-Parameter	2.280×10^{-5}	2.296×10^{-5}	0.867
PTFE	2-Parameter	2.280×10^{-5}	2.296×10^{-5}	0.867

Reference point used (x_0) : 0.10mmTable 5.5 Calibration Accuracy: $\tan \delta_{r_0}$

Rod	Fit Type	Model Value [1]	Fit Value [1]	Error [%]
None	2-Parameter	-	-	-
Nylon	3-Parameter	9.10×10^{-3}	8.21×10^{-3}	9.717
Nylon	2-Parameter	-	-	-
PTFE	3-Parameter	1.14×10^{-4}	1.45×10^{-10}	100.000
PTFE	2-Parameter	-	-	-

Reference point used (x_0) : 0.10mm

possibly due to its low impact on Q . For the nylon rod model there was a significant increase in error when performing a 2-parameter fit compared to a 3-parameter fit.

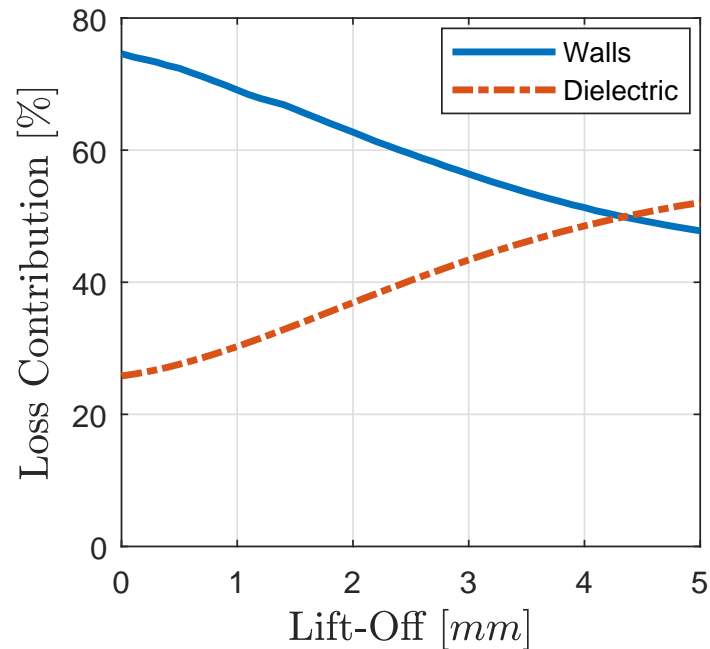


Fig. 5.9 Loss Contribution over Calibration Range (No Rod)

The contribution to system loss was calculated from the evaluated Q_0 and model values for R_{Sw} , $\tan \delta_d$, and $\tan \delta_r$ using the geometric and energy-filling factors. These are plotted in Figs. 5.9, 5.10, and 5.11 for all three models.

The PTFE model had negligible contribution from the rod. The contributions from the cavity and dielectric were comparable to the no rod model where the cavity loss dominated. In the nylon model the percentage loss contribution of the rod was significant and greater than the other elements across calibration range. This meant that there would be more even weighting of each parameter in the calibration curve fit.

Measurement Accuracy: Change in Conductivity

The measurement error was calculated by comparing the measured value of R_s for the base with the theoretical value calculated from the conductivity and frequency. The measurement error is plotted against conductivity for all three models in Figs. 5.12, 5.13, and 5.14.

For the nylon and PTFE Rod models measurement error was seen to increase with sample conductivity, however for the No-Rod model no such dependency was seen. The measurement error was much larger for the nylon than for the PTFE model

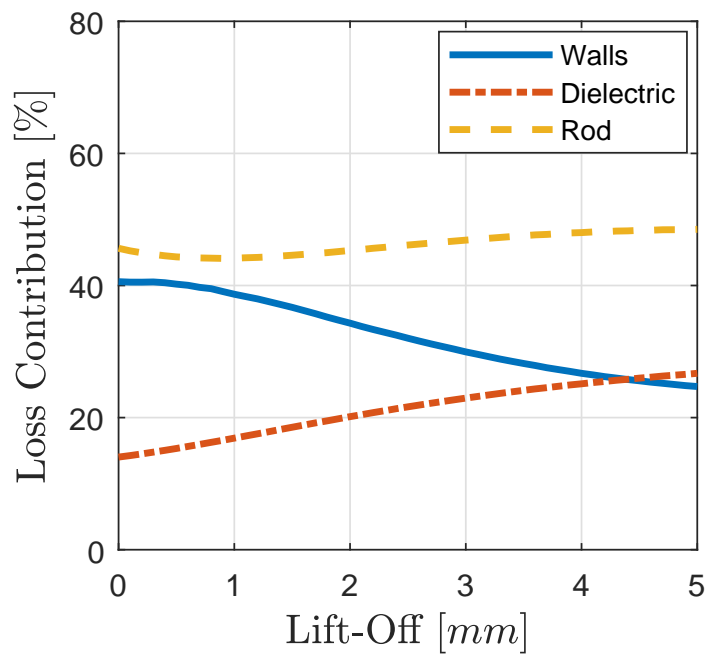


Fig. 5.10 Loss Contribution over Calibration Range (Nylon Rod)

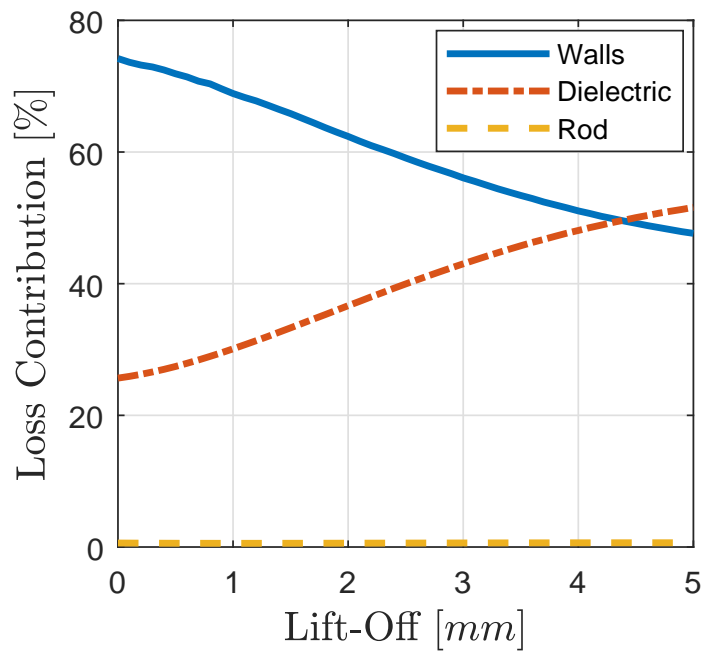


Fig. 5.11 Loss Contribution over Calibration Range (PTFE Rod)

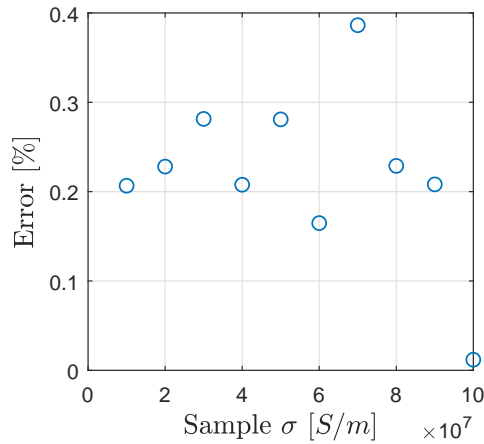


Fig. 5.12 Measurement Error vs. Sample Conductivity (No-Rod, $x_0 = 0.1\text{mm}$)

especially when using the simple CAL. For the PTFE model measurement error was virtually identical regardless of whether the full or simple CAL was used.

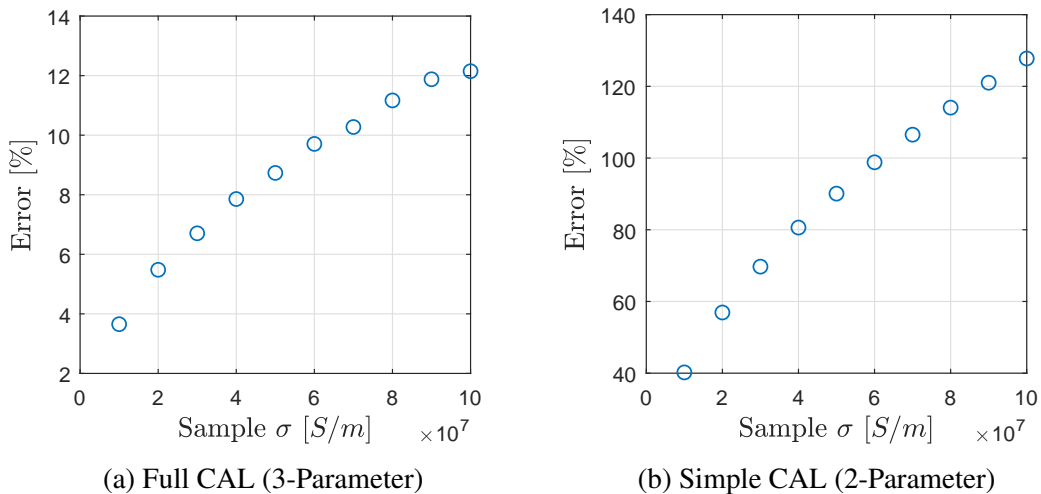


Fig. 5.13 Measurement Error vs. Sample Conductivity (Nylon Rod, $x_0 = 0.1\text{mm}$)

Using the values for loss components evaluated from the models themselves, loss contribution was plotted against the sample conductivity in Figs. 5.15, 5.16, and 5.17 for all three simulations. While the geometric factors were not changing (due to the measurement point being fixed) there was a change in loss contribution due to the increasing conductivity of the sample.

Loss contribution for the No-Rod and PTFE models were almost identical, with the contribution from the rod in the PTFE model being practically negligible. The extremely low contribution from the rod explains why a 2-parameter fit gave the same results as a 3-parameter fit. The nylon model on the other hand had a huge

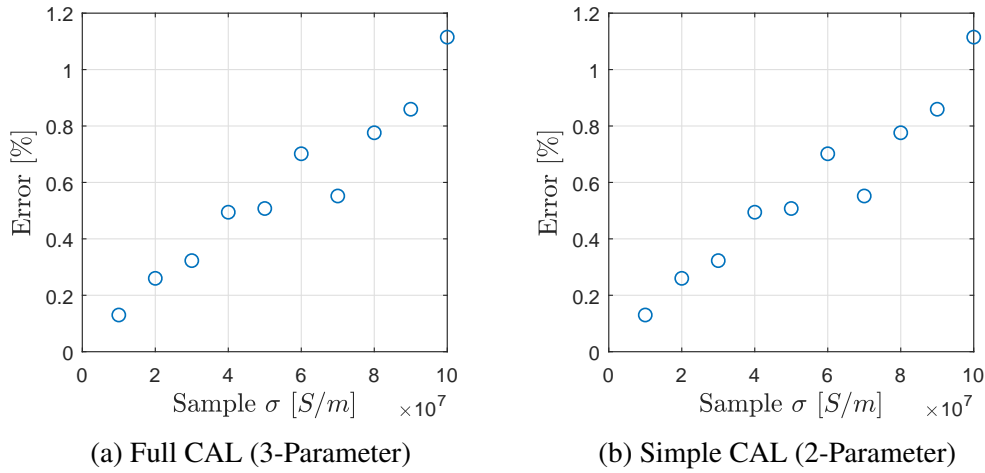


Fig. 5.14 Measurement Error vs. Sample Conductivity (PTFE Rod, $x_0 = 0.1\text{mm}$)

contribution from the rod and so a 2-parameter fit was not sufficient to describe the system accurately; this resulted in increased measurement error.

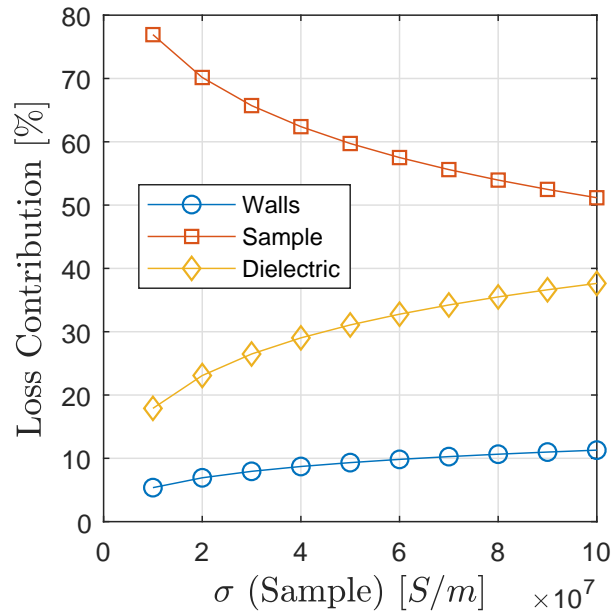
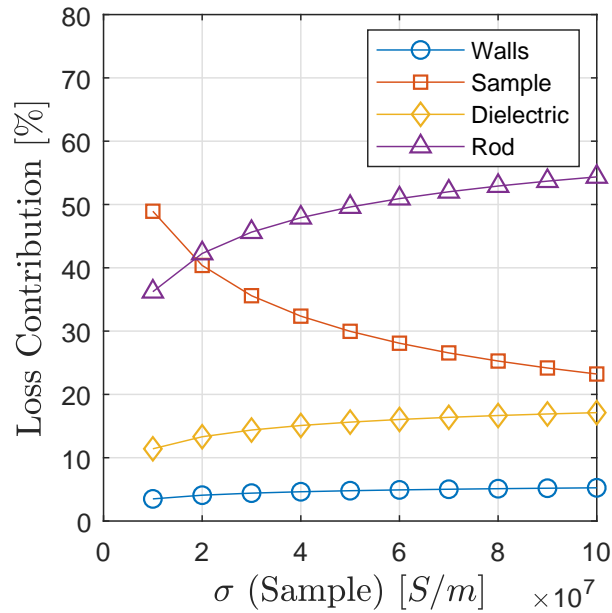
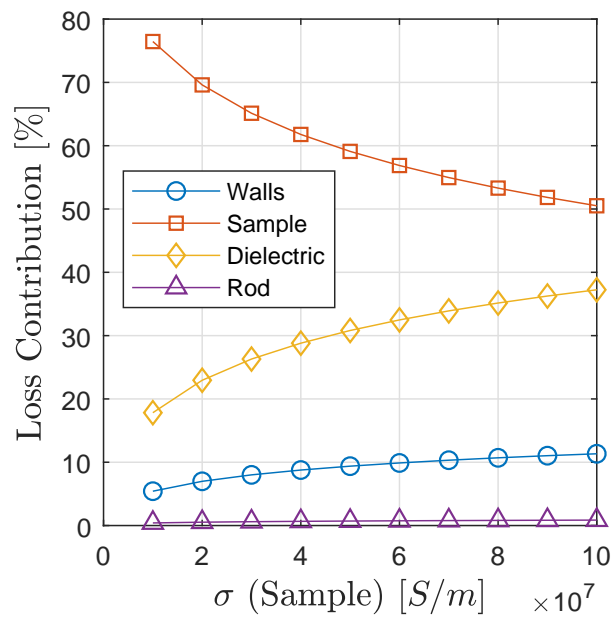


Fig. 5.15 Loss Contribution vs. Sample Conductivity (No Rod, $x_0 = 0.1\text{mm}$)

Measurement Accuracy: Change in Position

Measurement error was calculated in the same way as before; the value of R_s obtained from measurement was compared to the theoretical value calculated from the con-

Fig. 5.16 Loss Contribution vs. Sample Conductivity (Nylon Rod, $x_0 = 0.1\text{mm}$)Fig. 5.17 Loss Contribution vs. Sample Conductivity (PTFE Rod, $x_0 = 0.1\text{mm}$)

ductivity and frequency. Figs. 5.18, 5.19, and 5.20 show the measurement error at different lift-off positions.

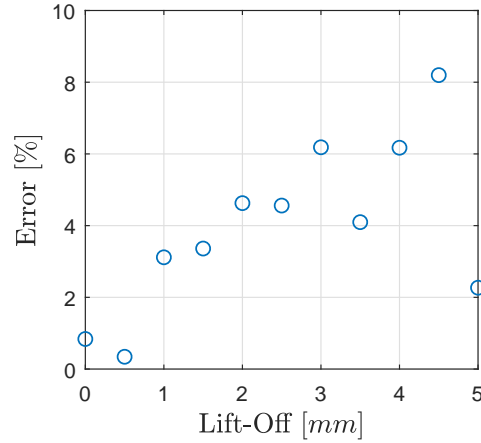


Fig. 5.18 Measurement Error vs. Measurement Position, x (No-Rod)

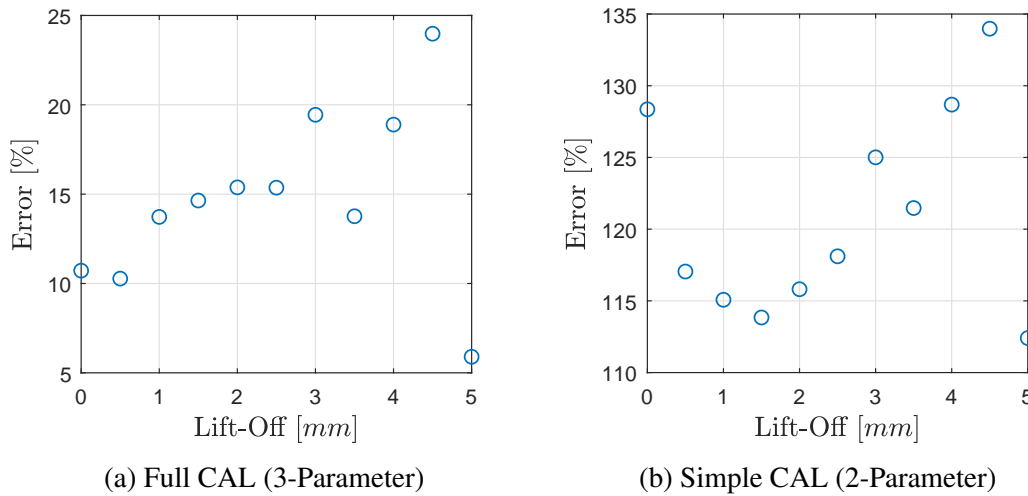
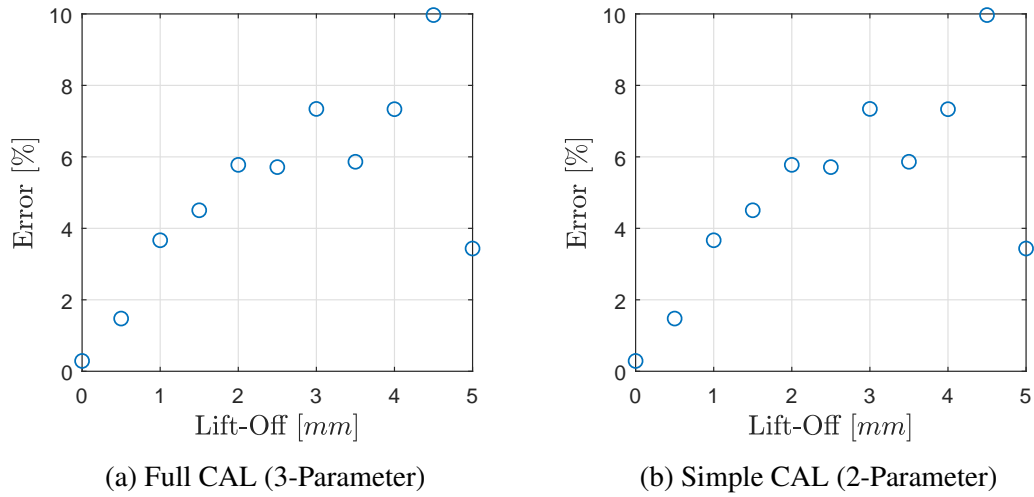
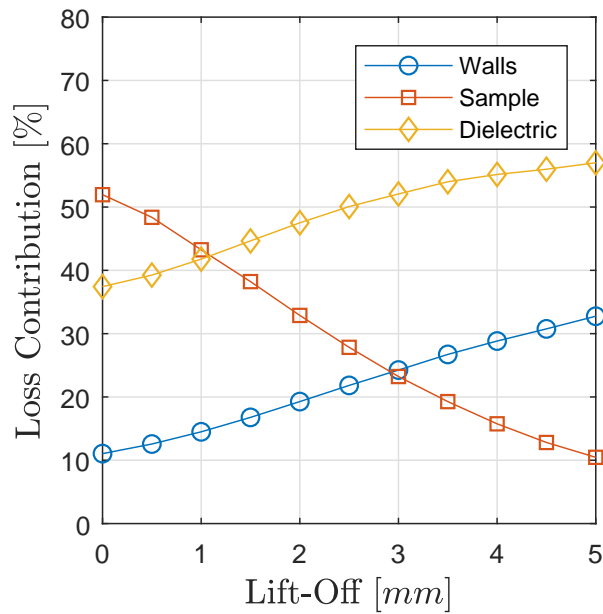


Fig. 5.19 Measurement Error vs. Measurement Position, x (Nylon Rod)

For all models the measurement error was shown to increase with lift-off. The No-Rod and PTFE models had similar measurement error and were both below 10% over the entire range. No difference was observed in error between the 3-parameter and 2-parameter CAL for PTFE. However, for the nylon there was a significant increase in error when the 2-parameter CAL was used.

Using the values for loss components evaluated from the models themselves, loss contribution was plotted against the lift-off in Figs. 5.21, 5.22, and 5.23 for all three simulations.

Fig. 5.20 Measurement Error vs. Measurement Position, x (PTFE Rod)Fig. 5.21 Loss Contribution vs. Measurement Position (No Rod, $x_0 = 0.1\text{mm}$)

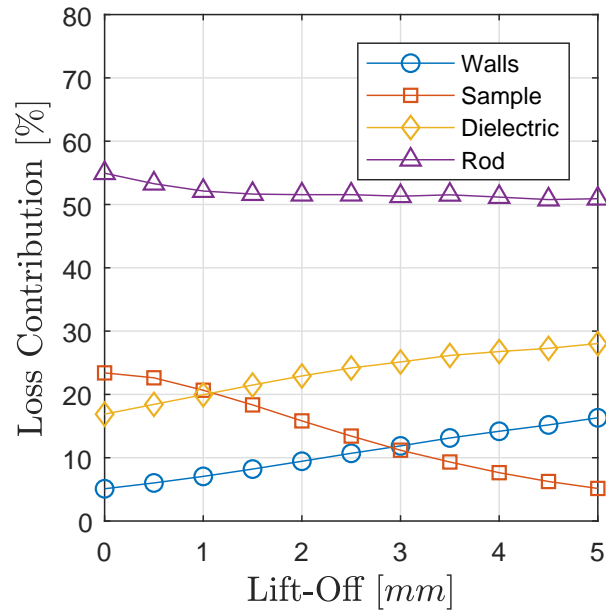


Fig. 5.22 Loss Contribution vs. Measurement Position (Nylon, $x_0 = 0.1\text{mm}$)

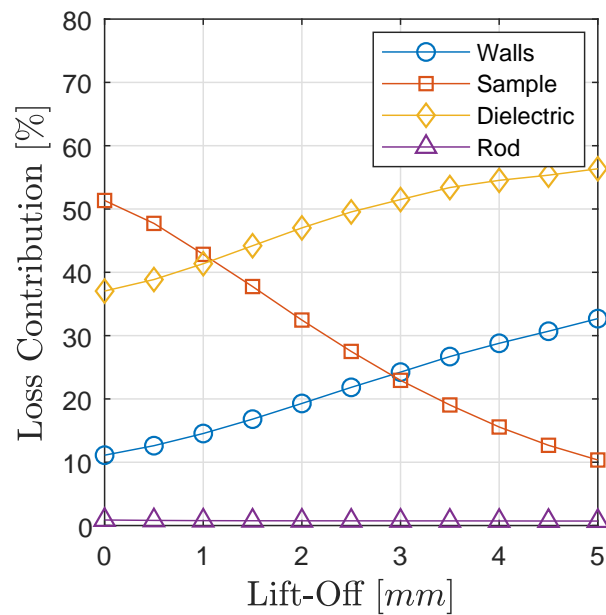


Fig. 5.23 Loss Contribution vs. Measurement Position (PTFE, $x_0 = 0.1\text{mm}$)

Similar to the results from varying conductivity; the No-Rod and PTFE models have an almost identical loss contribution, with the rod in the PTFE model having a negligible impact. The same observations can be made regarding 3 vs. 2 parameter fits; the insignificant contribution by the rod in the PTFE model means a 2-parameter fit gives the same result as a 3-parameter. The opposite is true for the nylon model; the dominant mechanism is the rod and attempting to simplify the fit does not yield an accurate enough description of the system.

5.5.6 Discussion

The aim of this study was to investigate the various influences on accuracy for both the calibration and measurement procedures.

It was found that the introduction of a lossy dielectric support rod (nylon) decreased the accuracy of calibration and subsequent measurements in all cases. Using a material with a lower $\tan \delta$ (PTFE) gave a significantly smaller reduction in accuracy. In this case the contribution to loss of the PTFE support was so low that it could be considered negligible, and a 2-parameter fit gave the same accuracy as a full 3-parameter one. In fact the contribution was so low that the 3-parameter fit could not arrive at a correct value for $\tan \delta_{r_0}$ due to the low weighting. In the case of nylon there *was* sufficient contribution to loss, and a 3-parameter fit was required. Higher accuracy for $\tan \delta_{r_0}$ was observed due to the even weighting of loss contribution, however there was lower overall accuracy as this increased the degree of freedom for the fit. Fitting error was shown to increase dramatically when using the reduced 2-parameter fit.

Practical implementation of the LODR structure requires some support rod, so its choice of material should be made to minimise its loss contribution. The most obvious way to achieve this is by choosing a material with low $\tan \delta$, however it is also possible to achieve this by minimising the energy-filling factor. The energy-filling factor will be determined by the total rod volume and value of ϵ_r , and both should be kept as low as is reasonable.

Increasing the conductivity of samples was seen to increase measurement error in all but the no-rod case. This is likely due to the sharp decline in loss contribution from the sample seen in all three cases. As the contribution becomes smaller the impact of calibration error becomes more pronounced. This is a well-known result, and so to maximise accuracy of measurements the loss term originating from the sample must dominate [117]. This is the reason for selecting low loss materials such as copper and sapphire/rutile when measuring high-conductivity samples (HTS, Graphene) [110, 111, 114, 121–123]. Therefore while accuracy will always be higher

when measuring low conductivity samples, reasonable accuracy of any conductivity could be achieved providing the sample loss term dominates.

The measurement position was also shown to influence error. Similar to the effect of increasing conductivity, as the lift-off value x was increased loss-contribution from the sample/base decreased rapidly resulting in increased measurement error, even for the no-rod case. In order to maximise accuracy of measurements the dielectric should be positioned as close to sample as possible. Practically this may need to be at a position near to the sample rather than touching it to avoid uncertainties regarding position due to compression of the support.

5.6 Designs: Prototype LODR Systems

5.6.1 First Prototype "Boromir"

The main goal for this design was to produce an LODR without crossover of adjacent modes to the measurement mode ($TE_{01\delta}$ in this case). A minimum separation of 100MHz around the measurement mode was specified to make tracking the resonant frequency easier during calibration. It was decided to use an existing piece of sapphire for the prototype, meaning its dimensions were fixed and only the cavity height and radius could be used to shape the mode distribution. Some flexibility remained in that the sapphire used was in two separate pieces, so there were two choices for aspect ratio (stacked or single). The dimensions for each sapphire disc were $a_1 = 10\text{mm}$, and $d_1 = 5\text{mm}$.

Internal Geometry and Mode Distribution

COMSOL multi-physics was used to simulate a variety of cavity aspect ratios for the two sapphire configurations using what is now referred to as the K-matrix approach described earlier. It was found necessary to use both pieces of sapphire in order to achieve a good mode distribution. The resulting dimensions are shown in Tab. 5.6 and the mode distribution in Fig. 5.24.

Modes shown include the measurement mode ($TE_{01\delta}$), two cavity modes (TM_{010} , TM_{011}), and three hybrid modes (HEM_{1-3}). The cavity modes appear as the normal cylindrical mode perturbed by the dielectric and are easy to identify, the hybrid modes however are very difficult to identify and so have been named in order of appearance at $x = 0\text{mm}$. As can be seen there was good spectral separation around the $TE_{01\delta}$ measurement mode.

Table 5.6 Boromir Internal Dimensions

Dimension	Value	Units	Description
a_1	10.00	mm	Dielectric radius.
d_1	10.00	mm	Dielectric height.
a_2	18.00	mm	Cavity radius.
d_2	27.00	mm	Cavity height.

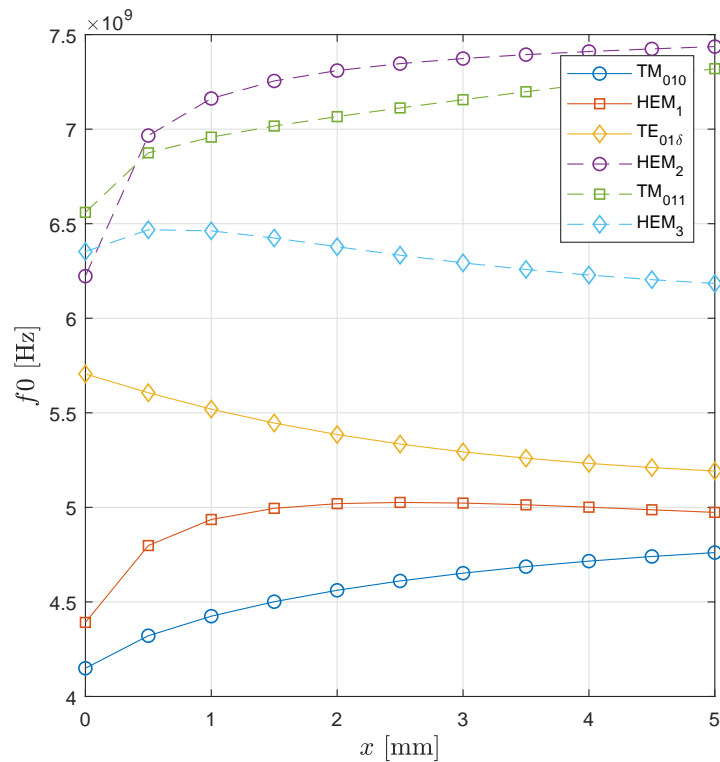


Fig. 5.24 Simulated Mode Distribution for First Prototype LODR

Cavity Manufacture and Model Refinement

With the inner cavity and sapphire dimensions known, the LODR shown in Fig. 5.25 was designed and manufactured. The cavity shield was made from aluminium and a support rod made of nylon was used to hold the sapphire dielectric in place. In order to control dielectric position accurately, a micrometer head was attached to the support rod. Once produced the dimensions were confirmed through inspection measurements, and these were used to update the COMSOL model in order to make the geometric and energy-filling factor evaluations more accurate. At this point additional detail was

added such as the SMA connectors and the hole where the support rod entered the cavity.

Frequency was measured with the dielectric at two extreme positions, which allowed the values of permittivity for the sapphire and the nylon in the model to be refined. This fixed the values at 9.47 and 3.1 respectively. Fig. 5.26 shows how the simulated and measured frequency of the $TE_{01\delta}$ mode compare. Note that there is still some error over the range, which was thought to be due to the slight separation of the sapphire disks which proved difficult to model.



Fig. 5.25 First Prototype LODR "Boromir". Image manipulation carried out to remove background.

Geometric/Energy-Filling Factors and Calibration

Geometric and energy-filling factors were evaluated and a calibration was performed. Measurements of Q_0 for the $TE_{01\delta}$ mode were taken for x from 0 to 2mm, and the Matlab scripts shown in 5.4 were used to fit to the data. The results of the calibration are shown in Fig. 5.27 and in Tab. 5.7, and the geometric and energy-filling factors are listed in Appendix D.

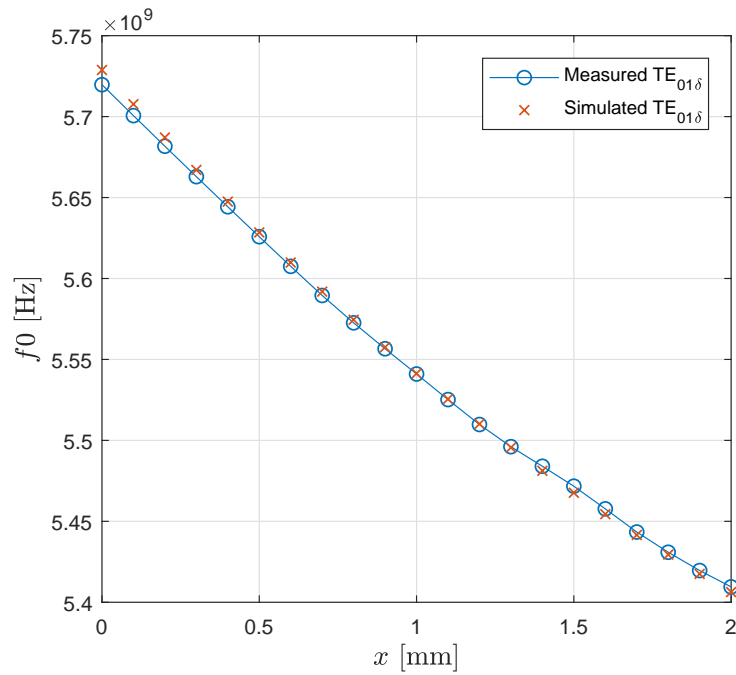
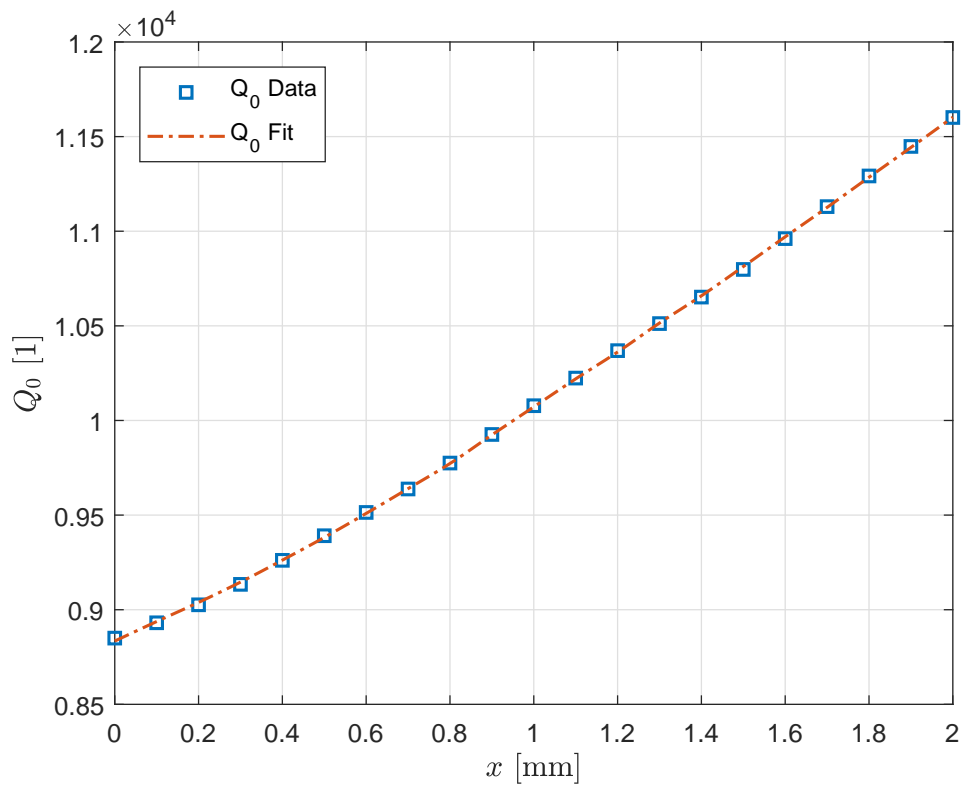
Fig. 5.26 Measured and Simulated Frequency of $TE_{01\delta}$ for First Prototype.

Fig. 5.27 Calibration Result for First Prototype LODR.

Table 5.7 Boromir Calibration Result

Loss Factor	Value	Units
R_{S_0}	0.0325	Ω
$\tan \delta_{d_0}$	3.4938×10^{-5}	1
$\tan \delta_{r_0}$	0.0124	1

$$(x_0 = 0.10\text{mm}, f_0 = 5.70\text{GHz})$$

Discussion

A prototype LODR cavity was designed and produced operating in the $TE_{01\delta}$ resonant mode. Through careful setting of the cavity aspect ratios interference from adjacent modes was prevented and sufficient separation was achieved. Following production the simulation model was refined and geometric and energy-filling factors evaluated. Calibration was performed and the resultant Q fit was shown to have high accuracy.

The accuracy of this cavity will likely be limited by the choice of support material (nylon) and the split dielectric. This could be improved by using a lower loss material for the support which would decrease system loss and by using a single piece sapphire for the dielectric which would help increase modelling accuracy for the geometric and energy-filling factors. Mechanical stability of the split dielectric was also found to be an issue and before use it was necessary to confirm it was fully in position.

The prototype was successfully used to measure the R_s of additively manufactured surfaces of various materials, build orientations, and post-processing techniques in collaboration with Dr. N. Clark. These results were published in [124] and were presented at the 2017 European Microwave Conference, Nuremberg.

5.6.2 Second Prototype "Faramir"

A second prototype LODR was produced with the aim of improving the calibration and measurement accuracy as compared to the previous design. Unlike the first prototype a new piece of sapphire would be ordered for the dielectric and so there was a greater degree of freedom in the design. As with the first prototype a minimum separation of 200MHz between the measurement mode ($TE_{01\delta}$) and any adjacent modes was specified for the first 5mm of lift-off.

Improvements to Design

Removing the split from the dielectric by using a single piece made the process of modelling (and by association the geometric and energy-filling factors) more accurate. Firstly, this was due to the absence of the split itself (which was difficult to model) but also due to the increased mechanical stability. Mechanical stability refers to the fact that in the previous version the lower disk would sometimes slip, requiring readjustment between measurements, and leading to uncertainty in the size of the split. With a single piece this uncertainty would not exist.

Perhaps the biggest improvement came from using PTFE for the support rod. As was confirmed through simulation, using a lower loss material for the support rod increased the accuracy of the calibration *and* subsequent measurements by decreasing the percentage contribution from the support [117].

Internal Geometry and Mode Distribution

The internal dimensions were found through successive iteration using the K-matrix approach described previously. These are listed in Tab. 5.8. The same aspect ratio for the dielectric was used as for the first prototype. The dielectric to cavity radius ratio was also kept as $a_2 = 2a_1$ to keep wall loss low [106, 107].

Table 5.8 Faramir Internal Dimensions

Dimension	Value	Units	Description
a_1	7.50	mm	Dielectric radius.
d_1	7.50	mm	Dielectric height.
a_2	15.00	mm	Cavity radius.
d_2	22.50	mm	Cavity height.

Mode distribution for the LODR geometry was found through simulation over a 5mm lift-off range and is shown in Fig. 5.28. As can be seen mode crossover was avoided and the minimum separation of 200MHz specified was achieved.

Cavity Manufacture and Model Refinement

With cavity internal dimensions specified the LODR could be designed and fabricated. As with the first prototype a micrometer head was used to manipulate the position of dielectric via the support rod.

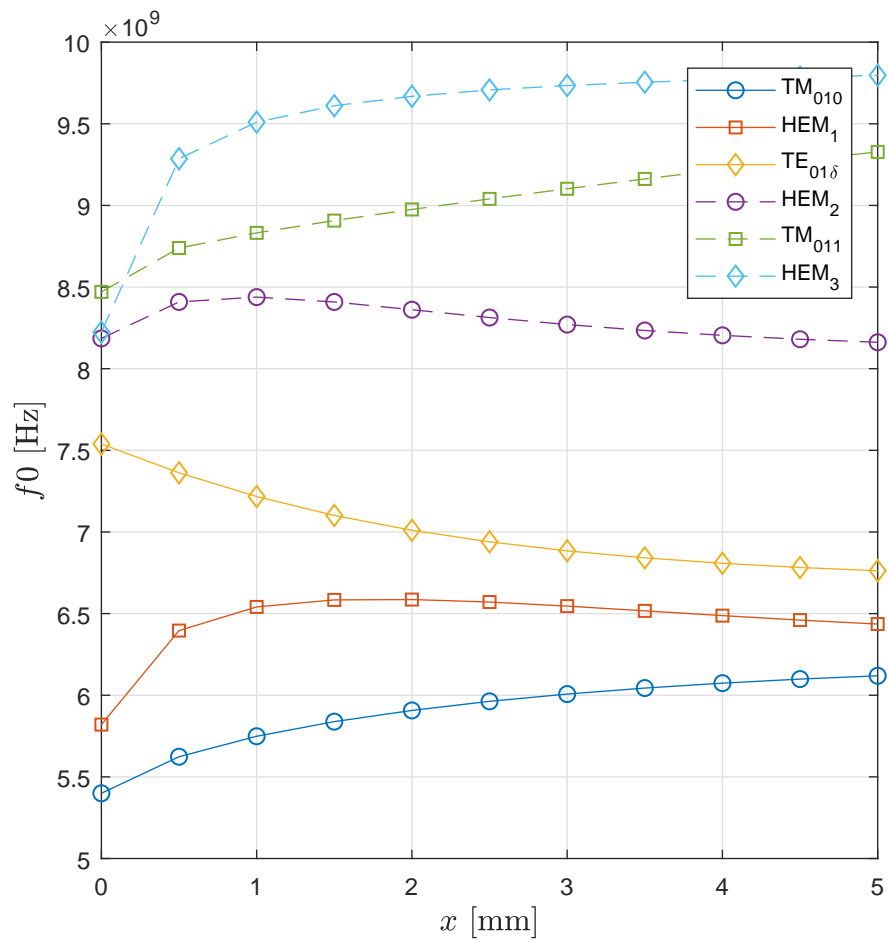


Fig. 5.28 Simulated Mode Distribution for Second Prototype LODR

While the first prototype was designed in CAD by the author and manufactured on site in the university workshop, the design and manufacture process for this LODR was outsourced to Renishaw Plc with the contribution of the author being the internal dimensions of the cavity, dielectric and support only.

The produced LODR was manufactured using aluminium for the cavity shield, C-plane sapphire for the dielectric, and PTFE for the support rod. SMA coupling loops were made and added once received. The prototype LODR is shown in Fig. 5.29.

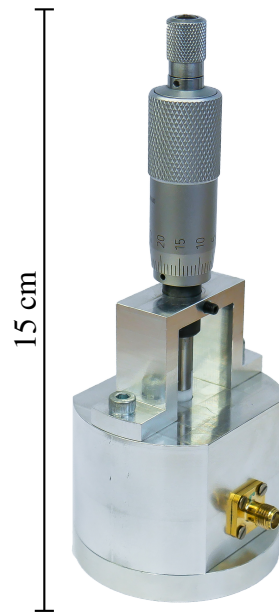


Fig. 5.29 Second Prototype LODR "Faramir". Image manipulation carried out to remove background.

The simulation model was updated using the dimension inspection report provided. Comparison between the measured and simulated frequency across a 2mm lift-off range shown in Fig. 5.30 shows good agreement between model and device.

Geometric/Energy-Filling Factors and Calibration

Following the update to the simulation model the geometric and energy-filling factors were evaluated and calibration was performed. The results from calibration are listed in Tab. 5.9 and shown in Fig. 5.31 for $x_0 = 0.10\text{mm}$, the geometric and energy-filling factors are listed in Appendix D.

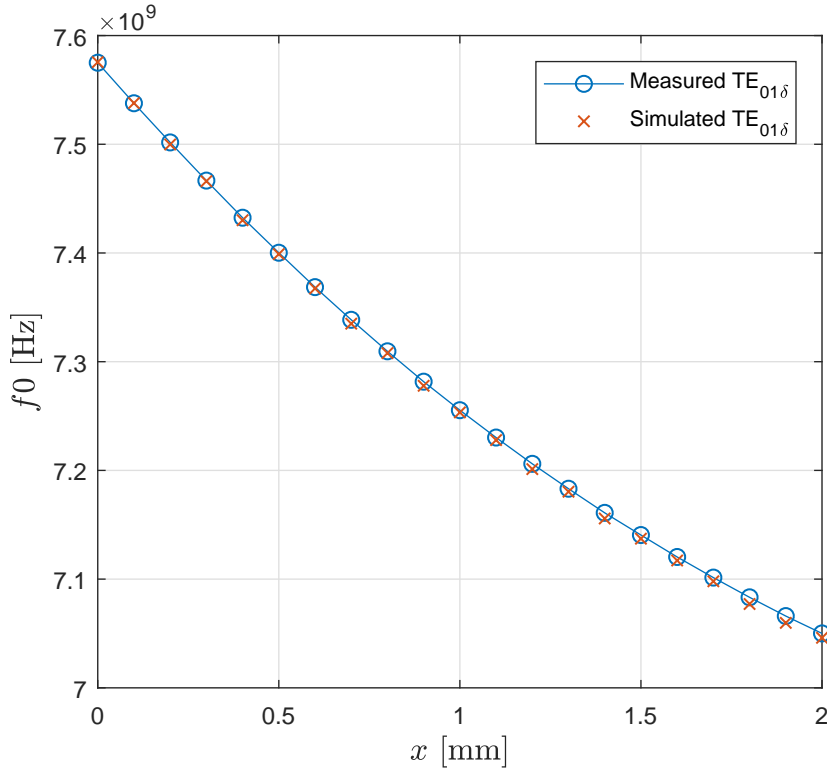


Fig. 5.30 Measured and Simulated Frequency of $TE_{01\delta}$ for Second Prototype.

Table 5.9 Faramir Calibration Result

Parameter	Value	Units
R_{S_0}	0.0304	Ω
$\tan \delta_{d_0}$	1.8926×10^{-5}	1
$\tan \delta_{r_0}$	0.0019	1

($x_0 = 0.10\text{mm}$, $f_0 = 7.54\text{GHz}$)

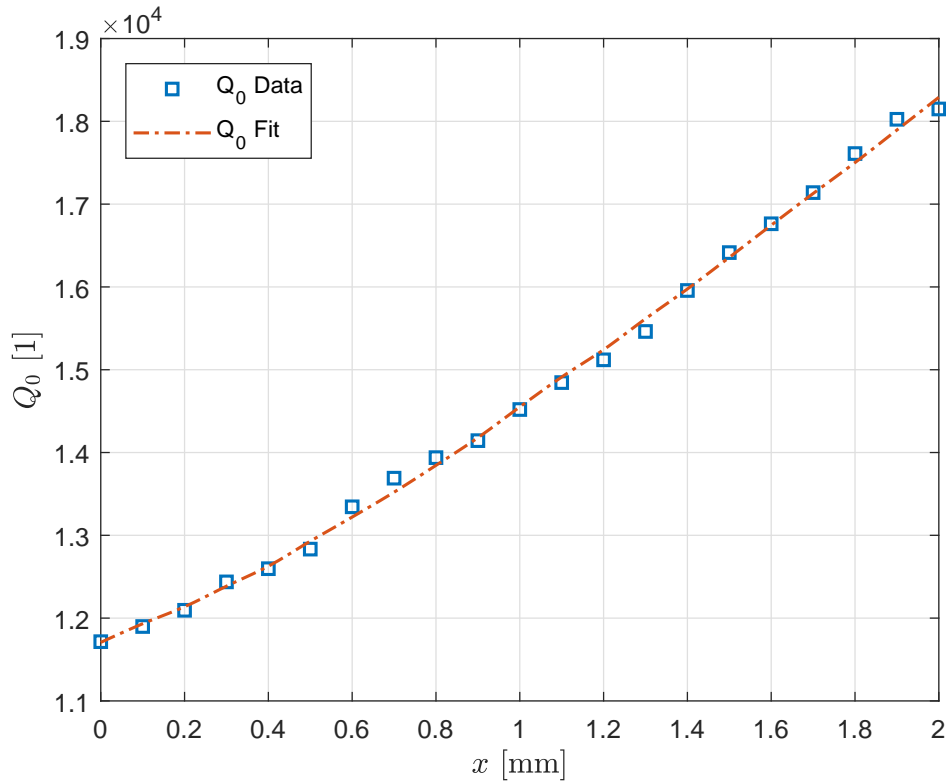


Fig. 5.31 Calibration Result for Second Prototype LODR.

Discussion

The results shown in Fig. 5.31 show a good fit of the calibration equation to measurement data. Some regular ripple is observable in the measured Q_0 , this was thought to be due to a slight bend in the support. As the dielectric is raised and lowered by micrometer it is also rotated, the small bend in the support meant that at regular intervals the dielectric was slightly closer to or further from the coupling structures. The change in proximity would affect the field pattern and so the value of Q_0 . This theory is supported by the fact that the micrometer would undergo one full revolution every 0.5mm which when examining the measured Q_0 in Fig. 5.31 appears to be similar to the period of maximum and minimum deviation from the fit curve.

Examining the values of calibration themselves gives a realistic value for R_s of the aluminium used. The value of $\tan \delta_{d_0}$ at 7.54 GHz is also close to the expected frequency scaled value from literature (2.262×10^{-5} at 7.54 GHz). The deviation from this could be due to inaccuracies in the fit or the quality of the material used, without a secondary measurement it is impossible to say for certain. It is worth noting that the calibration accuracy simulations performed earlier share the same dimensions for LODR as this prototype, and so one can infer a theoretical upper limit on accuracy

of 0.867%. True accuracy is likely to be slightly lower as one cannot guarantee the model is 100% representative of the system manufactured (in particular due to the slight bend in the support). However, it does give an idea as to its approximate magnitude. Again drawing comparisons to the simulation results from earlier, the value for $\tan \delta_{r_0}$ appears to be greater by an order of magnitude compared to literature values for PTFE (1×10^{-4} normally). Unlike the simulation, however, which drastically underestimated the value, here the value is given as higher. It is likely then that it is not the victim of under fitting due to low weighting. Two explanations seem obvious, one of course being that a lossier grade of PTFE was used in manufacture. The second is that it is worth noting that in order to secure the dielectric to the rod, PTFE tape was used to ensure a snug fit. The presence of additional PTFE in close proximity to the dielectric could be the cause. Secondary measurement of the material could be used to confirm this, potentially by the microwave cavity perturbation technique which is used frequently for dielectric measurement [125–127].

5.7 Experiment: R_s of Full-Metal AM Surfaces

The aim of this experiment was to investigate the microwave R_s of Full-metal AM surfaces as compared to theoretical performance, stock sheet metal performance and also as a product of different processing/build-configuration. Three materials were investigated: 316L stainless steel, AlSi10Mg aluminium, and CoCr Cobalt Chromium. All three materials are supported by the Renishaw's AM250 additive manufacture system.

In this experiment the second prototype LODR was used to perform the measurements with the aim of confirming some of the results published previously in [124]. To that end the same samples for AlSi10Mg and CoCr were used. Additionally samples of 316L steel were acquired in vertical configuration only. These and the aluminium vertical samples were compared with sheet metal counterparts which allowed for comparison with not only the theoretical R_s , but also the performance one can expect of a conventionally machined surface.

5.7.1 Methodology

Sample plates were produced by powder-bed fusion (PBF) in Renishaw's AM250 additive manufacture system. Holes for attachment to LODR fixture were included in the build file. Due to warping some plates had to undergo additional machining to round out the holes for attachment. In case of pre-existing samples used in [124],

additional holes were drilled due to the differences in fixture attachment method. Example of this patterning can be seen in Fig. 5.32.

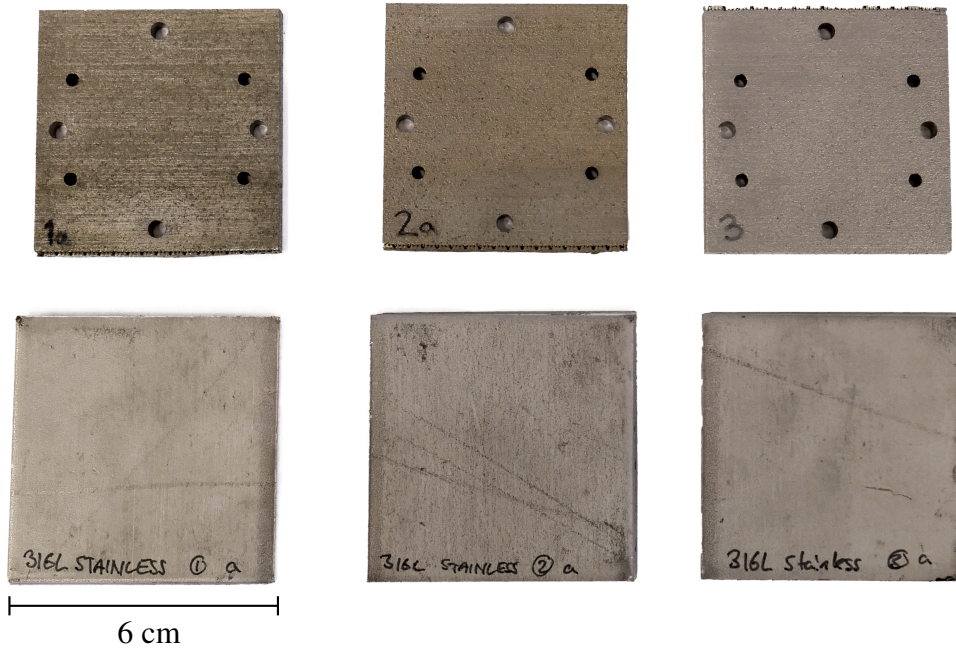


Fig. 5.32 316L Stainless Steel Samples. Top: PBF plates produced in vertical configuration. Bottom: Stock metal plates guillotine cut from same sheet. Image manipulation carried out to remove background.

The second prototype LODR was used to perform the R_S measurements using the calibration given in the previous section and the method described earlier. Calibration and measurement data were analysed using the Matlab scripts in Sec. 5.4. Measurements were performed at lift-off position $x_0 = 0.10\text{mm}$, $f_0 \approx 7.54\text{GHz}$. For stock plates the surface was smooth enough that attachment to the fixture was not deemed necessary, and in this case measurements were taken with fixture resting on top.

Each PBF sample was measured 3 times, and the average values were calculated as well as the sample standard deviation.

$$s = \sqrt{\frac{\sum_{i=1}^N (x_i - \bar{x})^2}{N - 1}} \quad (5.17)$$

where N is the number of measurements, 3 in this case.

For the stock samples only one measurement was taken as they were all identical pieces.

5.7.2 Results

In total 34 samples were measured, all of which are listed in Tab. 5.10 along with their measurement results given to 2 dp.

Fig. 5.33 shows the comparison of PBF/ALM and Sheet Stock plates with the theoretical value for R_s at the measurement frequency for 316L steel and AlSi10Mg aluminium. Values used for theoretical conductivity are 1.35×10^6 S/m for 316L and 2.17×10^7 S/m for AlSi10Mg. For 316L the sheet measurement is the average of 6 samples, and the ALM is the average of the 3 grit-blasted samples. For AlSi10Mg the sheet measurement is the average of 6 samples, and the ALM is the average of the 4 grit-blasted samples.

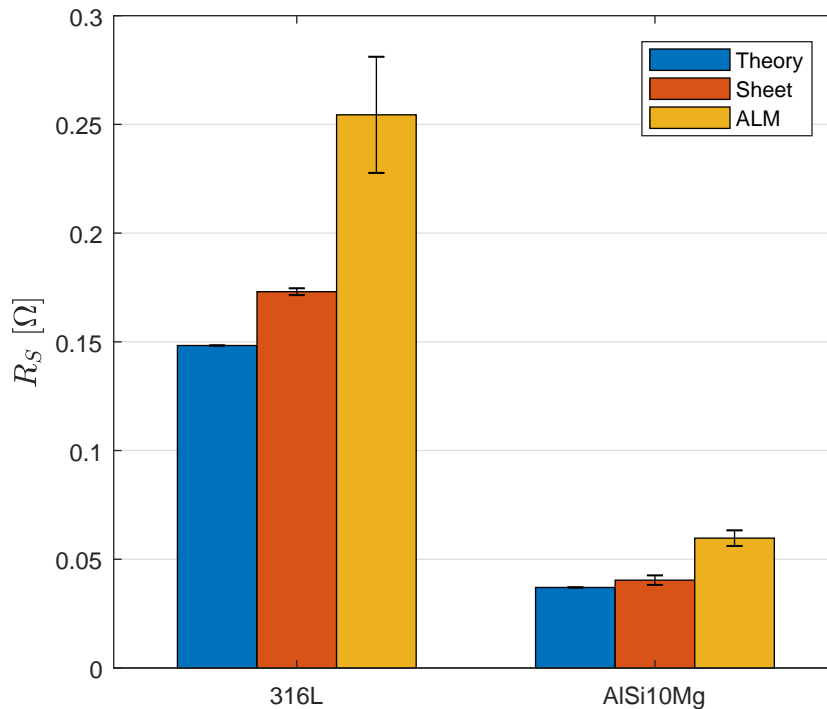


Fig. 5.33 Measured R_s of 316L stainless steel and AlSi10Mg aluminium. Error bars indicate the sample standard deviation.

Fig. 5.34 shows the measurement results of all ALM/PBF surfaces normalised to the expected theoretical value. Values of conductivity used for theoretical value were 2.17×10^7 , 1.10×10^6 , and 1.35×10^6 S/m for AlSi10Mg, CoCr, and 316L, respectively. Each sample was measured a total of 3 times, the value displayed is the average. Error bars are the sample standard deviation of each sample.

Table 5.10 List of All Samples Measured

ID	Material	Description	R_s [Ω]	Std. Dev.
PBF-Al-01	AlSi10Mg	H - Grit Blast	6.02×10^{-2}	3.00×10^{-4}
PBF-Al-02	AlSi10Mg	H - Grit Blast (EDM)	6.35×10^{-2}	3.50×10^{-4}
PBF-Al-03	AlSi10Mg	V - Grit Blast (1)	5.50×10^{-2}	3.00×10^{-4}
PBF-Al-04	AlSi10Mg	V - Grit Blast (2)	6.15×10^{-2}	3.50×10^{-4}
PBF-Al-05	AlSi10Mg	H - As Built	6.22×10^{-2}	3.00×10^{-4}
PBF-Al-06	AlSi10Mg	H - As Built (EDM)	7.28×10^{-2}	3.50×10^{-4}
PBF-Al-07	AlSi10Mg	V - As Built (1)	9.21×10^{-2}	3.50×10^{-4}
PBF-Al-08	AlSi10Mg	V - As Built (1)	1.08×10^{-1}	3.50×10^{-4}
SS-Al-01	AlSi10Mg	Stock, Guillotine Cut	4.02×10^{-2}	-
SS-Al-02	AlSi10Mg	Stock, Guillotine Cut	4.02×10^{-2}	-
SS-Al-03	AlSi10Mg	Stock, Guillotine Cut	4.14×10^{-2}	-
SS-Al-04	AlSi10Mg	Stock, Guillotine Cut	4.40×10^{-2}	-
SS-Al-05	AlSi10Mg	Stock, Guillotine Cut	3.88×10^{-2}	-
SS-Al-06	AlSi10Mg	Stock, Guillotine Cut	3.77×10^{-2}	-
PBF-CoCr-01	CoCr	H - Grit Blast	1.84×10^{-1}	3.50×10^{-4}
PBF-CoCr-02	CoCr	H - Grit Blast (EDM)	1.78×10^{-1}	3.50×10^{-4}
PBF-CoCr-03	CoCr	V - Grit Blast (1)	1.97×10^{-1}	4.00×10^{-4}
PBF-CoCr-04	CoCr	V - Grit Blast (2)	1.97×10^{-1}	3.50×10^{-4}
PBF-CoCr-05	CoCr	H - As Built	1.98×10^{-1}	3.50×10^{-4}
PBF-CoCr-06	CoCr	H - As Built (EDM)	2.09×10^{-1}	3.50×10^{-4}
PBF-CoCr-07	CoCr	V - As Built (1)	3.05×10^{-1}	4.00×10^{-4}
PBF-CoCr-08	CoCr	V - As Built (1)	3.28×10^{-1}	4.50×10^{-4}
PBF-316L-01	316L	V - Grit Blast (1)	2.46×10^{-1}	3.50×10^{-4}
PBF-316L-02	316L	V - Grit Blast (2)	2.85×10^{-1}	3.50×10^{-4}
PBF-316L-03	316L	V - Grit Blast (3)	2.34×10^{-1}	3.50×10^{-4}
PBF-316L-04	316L	V - As Built (1)	4.68×10^{-1}	4.00×10^{-4}
PBF-316L-05	316L	V - As Built (2)	4.14×10^{-1}	3.50×10^{-4}
PBF-316L-06	316L	V - As Built (3)	4.51×10^{-1}	3.50×10^{-4}
SS-316L-01	316L	Stock, Guillotine Cut	1.74×10^{-1}	-
SS-316L-02	316L	Stock, Guillotine Cut	1.73×10^{-1}	-
SS-316L-03	316L	Stock, Guillotine Cut	1.71×10^{-1}	-
SS-316L-04	316L	Stock, Guillotine Cut	1.73×10^{-1}	-
SS-316L-05	316L	Stock, Guillotine Cut	1.75×10^{-1}	-
SS-316L-06	316L	Stock, Guillotine Cut	1.73×10^{-1}	-

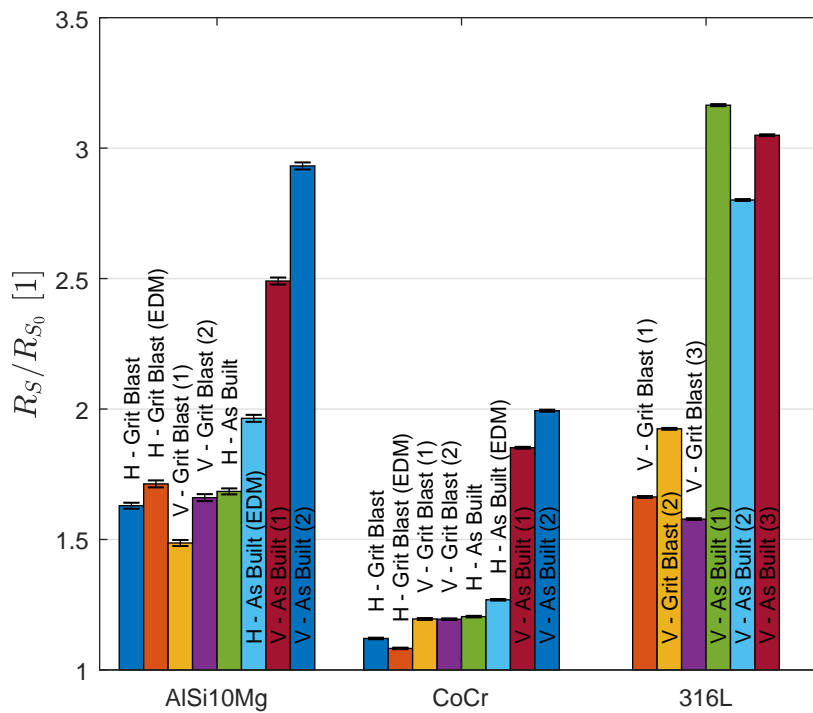


Fig. 5.34 Measured R_S of AlSi10Mg aluminium, 316L stainless steel, and CoCr cobalt chromium. Produced by various build conditions (shown). Error bars indicate the sample standard deviation.

5.7.3 Discussion

Starting with the Stock vs. ALM measurements of the 316L and AlSi10Mg, the sheet measurements for both materials were in close agreement to their theoretical values. Notably the aluminium was closer in value than the 316L, a possible explanation could be that while the aluminium stock plates were visibly shiny and potentially polished in some fashion, the 316L stock plates appeared tarnished somewhat, as can be seen in Fig. 5.32. As this is stainless steel it is unlikely to be surface oxidation, the more likely cause is roughness which as has been stated can be linked to increased R_s [103–105, 124]. Despite this the close agreement indicates that the measurements are measuring R_s to some accuracy. A comment on the exact level of accuracy is difficult without a standard, the existence of which would necessitate an extremely high-quality surface. If we assume the stock aluminium plates to be an acceptable standard surface then one could quote an accuracy to at least $5 \times 10^{-3} \Omega$ at that conductivity. It is important to stress however that accuracy will be inversely proportional to sample conductivity.

As might be expected the ALM samples performed poorer than the stock samples for both materials. There is a notably larger standard deviation on the 316L, despite the fact that all three samples measured were identical in build configuration (vertical and grit-blasted). The AlSi10Mg samples, on the other hand, were all grit-blasted but were 50/50 vertical and horizontal builds. One possible explanation for the discrepancy could be due to differences in the grit/sand-blasting processes.

Considering next the ALM measurements of all three materials and varying build conditions some patterns emerge. These are consistent with the results published in [124] for the same samples (AlSi10Mg, CoCr) measured using the first prototype LODR.

Overall grit-blasting was seen to improve R_s , with vertically built surfaces experiencing the greatest improvement across all three series. As the function of grit-blasting in this context is normally the removal of loose powder, this confirms previous observations that vertical surfaces are more prone to loose powder adhesion than the horizontal ones [128]. This is visible in the measurements when comparing the as-built surfaces; horizontal surfaces were seen to perform better in the absence of post-processing. It is worth noting that following the grit-blasting this performance gap disappeared and both orientations exhibited similar performance. This is good news for microwave component manufacture as it indicates that, regardless of orientation, post-processing techniques may be used to achieve consistent performance.

Comparing measurements of the same CoCr and AlSi10Mg samples from the new fixture with those reported in [124] from the old fixture show good agreement. As the results are normalised to theoretical R_s , the difference in frequency of measurement between the two fixtures can be largely ignored as it will cancel through during normalisation. Performance on a per sample basis was nearly identical between the two fixtures. This is an encouraging result and indicates a good accuracy for the original fixture. This is not so surprising when recalling the simulation results; as these samples exhibit high loss they will naturally dominate the other loss terms increasing the measurement accuracy. Therefore even though the new fixture has been designed to increase accuracy, with a lossy sample this will largely go unnoticed.

5.8 Experiment: R_s of Metallised Plastic SLS and SLA Surfaces

In the manufacture of microwave 3D-printed components it is a common practice to produce plastic parts which are then coated in a conducting metallic layer [129–133]. Providing this layer is of sufficient thickness (often 3-4 times the skin depth) the performance of these devices is equivalent to their bulk metal counterparts. The trade-off for this process is normally an upper limit on the operating power, as the plastics used tend to have low melting/degradation temperatures (compared to metals) any high-power applications risk destruction of the component. Despite this drawback they remain an economic way for components to access the freedoms of additive technologies.

The metallisation process patented by Jet Metal Technologies operates on the principle of jetting/spraying rather than the usual electro-plating/silver painting processes used. They are able to metallise any surface so long as it can be made wettable, which is normally achieved by plasma exposure. This process has been successfully employed in the metallisation of microwave antennas, attempting to improve on results achieved through conventional coating [132]; however, at time of writing no RF/MW performance data has been published.

This experiment attempts to investigate the performance of silver metallised plastic surfaces printed using Selective Laser Sintering (SLS) and Stereo-lithography (SLA) by measuring R_s using the LODR method. The advantage to measuring R_s directly as opposed to inferring performance through manufacture of a single component is that the result has wider, more general significance as it is not a factor of some particular design.

5.8.1 Methodology

In total 12 samples were prepared, each sample being one side of a produced plate for 6 plates total. Sample dimensions were the same for each plate, being designed to fit both LODR fixtures. Three of the plates were produced in nylon (PA 2200) using the SLS process, the other three were produced in epoxy (Somos GP Plus 14122) using an SLA process. For each material three build orientations were used: 45°, Horizontal, and Vertical. Following production the plates were sent to Jet Metal Tech. for metallisation in silver using their patented jetting process. Silver was deposited with a minimum layer thickness of 3 μ m. The samples post-metallisation can be seen in Fig. 5.35.

Measurements were carried out using the 7.54GHz LODR fixture "Faramir" using the same calibration from Sec. 5.6.2. Values of f_0 and Q_0 at the measurement point of $x_0 = 0.10$ mm were evaluated through Lorentzian curve fitting to transmission (S_{21}) data acquired using a vector network analyser (VNA). Measurement of the sample R_s were then evaluated out using the Matlab code described in Sec. 5.4.

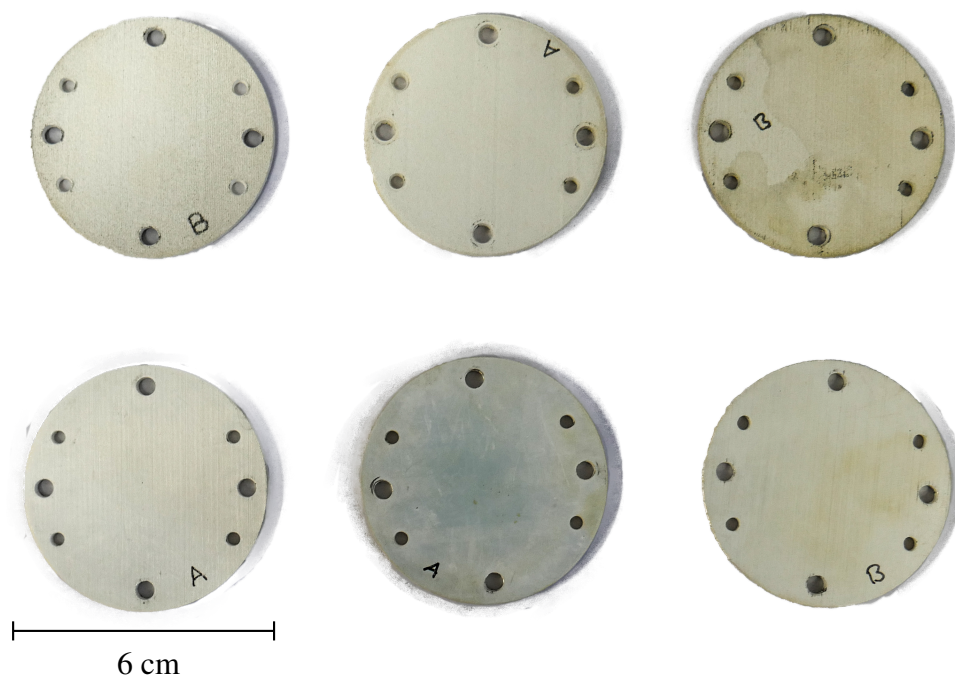


Fig. 5.35 Metallised SLS/SLA samples. Top: SLS (nylon) Plates. Bottom: SLA(Epoxy) Plates. Left to right the build orientations for both rows are 45°, Horizontal, Vertical. Image manipulation carried out to remove background.

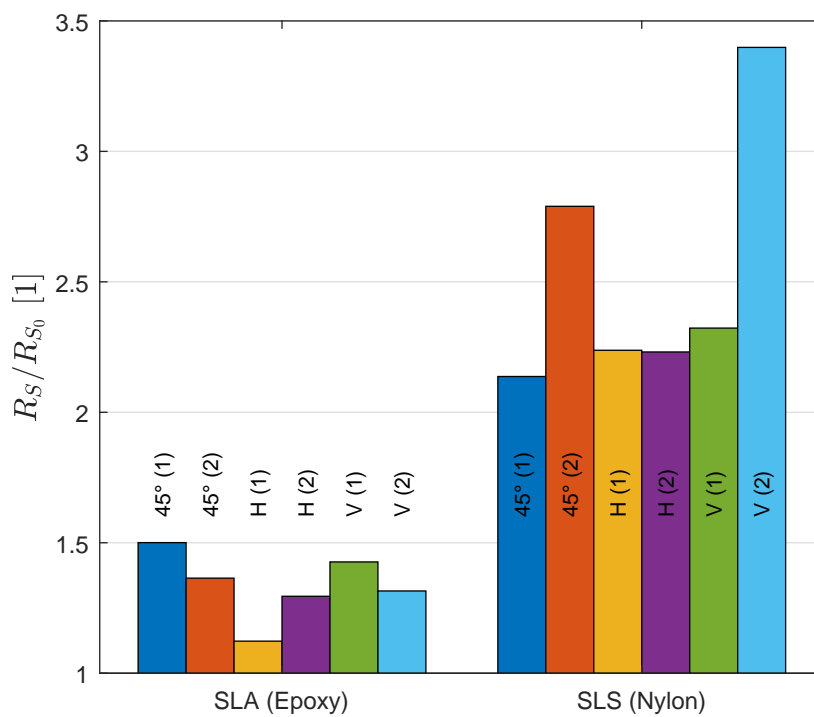


Fig. 5.36 Normalised R_S of Metallised SLS and SLA Plastic Surfaces. Various Orientations

5.8.2 Results

Measurement results for the R_s are plotted in Fig. 5.36 normalised to the theoretical value of R_s for silver at the measurement frequency (7.54GHz). The value used for conductivity of silver was $6.30 \times 10^7 \text{S/m}$.

5.8.3 Discussion

Despite the surface of the plates appearing matt white as opposed to metallic silver, the results clearly indicate that the surface has been successfully metallised.

The SLS surfaces as a whole performed noticeably poorer than the SLA surfaces. Since the same silver compound was used this is likely due to differences in surface morphology, rather than conductivity. The SLA process is known for producing smoother surfaces without need for post-processing. Additionally issues regarding metallisation adhesion to the PA2200 substrate used for the SLS have been reported [134]. However, it is worth pointing out that these plates were not under any mechanical load.

No clear bias towards a particular orientation was observed in either material. This falls in line with the findings reported for full-metal plates earlier and in [124] where it was proposed that loose powder as a secondary effect of orientation caused increased R_s rather than orientation itself.

Out of the two materials/manufacture methods there is a clear advantage to using the SLA process for microwave passive components. The SLA samples demonstrated a lower R_s than for the SLS samples, so they will exhibit less loss/attenuation. SLA as an optical curing process can produce parts at higher dimensional accuracy than the SLS process in general, this will generally lead to lower surface roughness. Silver coated plastic SLA waveguides have been shown to outperform SLS full-metal waveguides, where the superior performance has been attributed in part to reduced surface roughness [135].

Temperature handling should also be considered. For the SLS material used (PA 2200) the softening temperature is around 163°C . As a thermoplastic it will experience permanent deformation at this temperature and begin to melt beyond [136]. The Somos GP is a thermosetting plastic and so once cured it won't melt. However at temperatures past its glass transition temperature of 41°C , it will begin to degrade/decompose [136].

Further study could be carried out to investigate the efficacy of different finishing techniques. If the R_s performance of SLS parts could be improved to the level of the SLA ones, the superior temperature handling offered could make it the preferred material of the two for inexpensive passive microwave component manufacture. Another

point of interest would be the quality achievable on interior parts, and this could be investigated through metallisation of an enclosed surface which could later be cut open for measurement.

5.9 Conclusions

A new calibration technique has been introduced for determining parasitic system losses of a dielectric resonator. The technique utilises a novel structure which has been termed "Lift-Off Dielectric Resonator" (LODR) where dielectric position is manipulated in order to provide a characteristic change in Q to which the calibration equation may be fit to. As the lift-off procedure will generate a shift in resonant frequency it is important to avoid mode-crossover. However, this is easily achievable through careful setting of the LODR geometry.

Least-squares fitting of the calibration equation was shown to yield accurate results of the loss factors and a good quality fit. In cases where the contribution from the support rod were extremely low, however, the value for $\tan \delta_{r_0}$ was obscured by fitting error. This did not affect the quality of the fit and the term could be omitted. In the cases observed where the support term could be omitted, overall fit accuracy was higher. This is likely due to there being one fewer loss term influencing the value of Q , and so the curve fitting had fewer degrees of freedom and less uncertainty.

The accuracy of the technique was shown to be dependent on the loss contribution from the measurement sample. As is typical of dielectric resonator methods, the sample loss contribution must dominate [117]. Existing methods to sensitise the fixture to the sample may be used such as appropriately shaping the cavity aperture to reduce wall loss [107] and by using low loss materials to reduce unloaded system loss [106]. In the case of the LODR this may also be achieved by setting the measurement position as close to the sample as possible.

Two prototype LODRs were produced, both made from aluminium with a c-plane sapphire dielectric. Both fixtures were capable of accurately measuring the R_s of room temperature metals. Results from the new fixture of the same sample were in agreement with those from the old fixture.

The technique was successfully applied in the measurement of various conducting surfaces. Measurements were accurate with values of R_s measured for sheet aluminium and steel being in line with expected values from theory. Precision was also good, showing very low standard deviation on repeated measurements. Without a defined standard, exact accuracy is difficult to quantify and will be inversely proportional to

sample conductivity. Future work could attempt to quantitatively link sample loss contribution to measurement accuracy.

Experimental investigation into the effect of build orientation and surface finish of additive metal surfaces was carried out. In all cases there was no implicit bias towards orientation, and any change in loss was due to surface quality. As was shown, this is entirely correctable through post-processing, and future work could investigate different post-process treatments and their efficacy.

Finally, an experimental investigation into metallised additive plastic surfaces was also conducted. Two additive techniques were used: selective laser sintering (SLS) and stereo-lithography (SLA). Results indicated that the metallised SLA surface performed better than the SLS, which was attributed to differences in achievable surface quality without processing. The results also confirmed the non-dependency on build orientation for a given production method.

Chapter 6

Conclusions and Further Work

6.1 Achievements and Contributions

In this thesis the development of microwave processing and measurement techniques suitable for powder metallurgy have been explored. The ability for microwaves to couple power efficiently to a metal powder volume has previously been demonstrated in a number of publications [3, 32, 36]. More recent work has explored the change in absorption of metal powder volumes before and after sintering [6], however a lack of in process measurements limit our knowledge of the changes as they occur. Another area of intense activity is the development of microwave passive waveguide components produced using additive technologies [97, 130, 135, 137]; advances in this area are expected to bring about lighter, more space-efficient designs with significant impacts in both terrestrial and aero-space communications. Currently these designs are evaluated on a per-component basis and very little work has been done on the microwave performance of additive surface types themselves. The overall objective of this thesis was to investigate microwave processing applications to additive metal technologies. The knowledge gaps within these areas mentioned provided clear goals for the work; to investigate and observe the change in microwave absorption of a metal powder compact during sintering, and to develop a method for measuring the microwave performance of additive (in this case PBF) surfaces.

This chapter begins with a summary of the main achievements of this work. The new methods and findings and how they fit into the knowledge gaps are discussed along with any limitations of the individual studies. The chapter finishes with a brief overview of future work and also discusses possible applications for the thesis contributions.

Microwave Sintering Measurement Setup

A high-sensitivity microwave resonant cavity for use in magnetic heating was designed using the intermediate shaping technique. While this technique had been demonstrated as a method of separating the TE_{0ml} and TM_{1ml} cylindrical cavity mode degeneracy in filters previously [75], this was the first example of it being applied for high-power microwave heating applications. Additionally the original paper demonstrated the separation at the two extremes of the cylinder and sphere shape primitive, in this work FEM was performed in COMSOL to show the development of mode separation as the cylindrical cavity became more intermediate in shape. The produced cavity was able to operate in the equivalent TE_{011} resonant mode at ISM 5.8 GHz with an unloaded Q-factor of around 21,000, which is enhanced due to the SA:V ratio as compared to a cylindrical cavity; this increases the sensitivity for magnetic field measurements. The manufactured cavity will assist in future measurements involving magnetic field perturbations, while the work itself will assist in future cavity designs where greater sensitivity in magnetic field measurements are desired.

A methodology for evaluating unloaded Q-factor and resonant frequency (Q_0 , f_0) from reflection measurement using Lorentzian curve-fitting was developed. This method assumes the relationship between transmission, reflection and absorption of power in a two-port network can be applied to a single-port system. This is used to obtain an equivalent transmission response representative of the system, the advantage being that the response in this form can be used to fit a Lorentzian using least-squares methods. The advantage of this approach is that the resultant curve is less sensitive to disturbances at the resonant frequency due to noise.

A semi-automatic system for performing microwave resonance measurements during high-power heating was developed. Control software was written in LabVIEW to simplify use of the system, this included coordinating the various pieces of hardware such as the signal generator, power meters and temperature probes. The software was also able to adjust the delivered power to the sample in order to maintain desired temperatures. This could also be used to cycle samples through a specified temperature profile. Control was achieved by having the software adjust the duty-cycle of the excitation signal in response to the difference between target and sample temperatures, a software implemented PID module was used to determine the system response in real-time. This system enabled more robust analysis of the microwave sintering by examining specific heating profiles. The system will assist the future study of

microwave heating in the department and has already been used successfully in a number of ongoing collaborations.

Microwave Sintering of Metal Powders

The change in microwave absorption of some common AM metal powders during sintering was investigated. Using the developed measurement setup, samples of Ti6Al4V Titanium, CoCr Cobalt Chromium, 316L Steel and CM-247LC Nickel powders were all investigated for their change in microwave absorption over a range of temperatures. The change in microwave absorption was monitored by measuring the unloaded Q-factor, which is reciprocal to loss. In all cases it was observed that the microwave loss of the powder sample was greatly reduced after sintering. This reduction was consistent with expectations of a powder becoming more like a solid mass, and has been shown previously for samples removed at intermittent stages [6]. This was the first time measurements had been made in situ however, which allowed for the entire process to be observed without interruption. The greatest reduction to microwave loss occurred towards the beginning of the heating; it was proposed that this coincided with the initial formation of particle interconnects. An initial enhancement to loss was also observed at the beginning of each heating cycle, this was assumed to be due to an increase in resistivity due to temperature and was quickly overcome by the formation of particle interconnects however.

The first set of experiments investigated the changes to microwave loss at temperatures up to half the conventional sintering temperature, around 500°C. Despite the temperatures being so low a significant change in microwave loss was observed for samples of Ti6Al4V powder under both Argon and Air. This temperature range is important as commercial AM machines often attempt to hold the powder bed at some elevated temperature; this result indicates that there is some modification to the powder even at sub-sintering temperatures. These observations confirm the already established need for sieving and quality control of recycled powder [81, 101], and may need to be considered if a volumetric microwave heating system were to be developed.

The second set of experiments focused on heating of powder samples to sintering temperatures. In these experiments three materials were studied: Ti6Al4V, 316L, and CM-247LC. The Ti6Al4V and 316L powders were selected as they were commonly run powders in the AM250 PBF system. The CM-247LC powder was included as it was known to be prone to breakages, as an alloy of interest it was worth seeing

whether microwave sintering offered some advantage. As with the low temperature experiments it was shown that the reduction in loss occurred towards the beginning of the cycle, coming to a halt as the sample reached maximum temperature (1,000°C - 1,200°C). Measurements appeared to indicate that no further changes in loss occurred after reaching steady-state temperature. Scanning electron microscopy was carried out and confirmed that the samples had experienced sintering, however not to full density. This result is interesting as it appears to indicate that in microwave sintering densification occurs rapidly as temperature is increased to maximum, but that holding the sample at that temperature is unnecessary. It may be the case that insufficient final temperatures were simply limiting further sintering, due to limitations in system output power however, this could not be investigated at the time. The CM-247LC samples experienced cracking in all cases.

The final set of sintering experiments attempted to perform a study using Taguchi analysis. The aim of this study was to investigate the influence of various aspects of the heating profile on the final properties of microwave sintered material. This presented the challenging requirement of high repeatability in temperature profiles for each sample series, thanks to the automation of the control system this was achieved with minimal deviation between repetitions. Out of the four parameters tested (Final temperature, heating rate, hold time, cooling rate) only the final temperature had a significant impact, with both density and flexural modulus being enhanced at higher temperatures. For all samples tested the flexural modulus was found to be less than 20% of the value for PBF produced samples at full density. The final temperature being the most significant factor could indicate that the temperatures being used were too low, inhibiting further sintering. This may also explain why holding samples at temperature did not cause further change to microwave loss.

Lift-Off Dielectric Resonator for Measuring R_s

A measurement technique for measuring R_s was developed using a dielectric resonator. This technique made use of a unique calibration step where the system losses of the resonator could be determined by taking measurements of Q_0 as the dielectric was moved vertically. The resonator was designed to allow for manipulation of the dielectric position, which gave the value of Q_0 a characteristic shape over the range of motion. Curve-fitting could then be used to determine the system losses, having previously evaluated geometric and energy filling factors at each position measured. This technique made it simple to take multiple measurement in short succession,

and represents a convenient way to study the microwave performance of PBF parts. Two resonators were designed using this technique and their accuracy assessed by measuring sheet metal samples. These resonators will assist in future studies where accurate knowledge of R_s is required. Additionally the design process used can be employed to produce designs for any frequency, subject to practical limits on size.

A number of simulation studies were performed investigating the effect of measurement position and sample conductivity on the overall accuracy of the measurement. Three models were setup in order to test two candidate materials for the support rod (PTFE, Nylon) one of which was a control model and had no support rod. It was shown through simulation that for low loss support rods the loss term originating from the rod could be ignored without affecting the fit. In fact it was shown that even when included, due to the low contribution to loss the value given by calibration was largely distorted. This was due to the magnitude of the fit residual error being greater than the value of loss associated with the rod. Accuracy was shown to be dependent on sensitising the system to the sample base. For low conductivities and measurement positions near the sample, the system would be highly sensitised to the sample and accuracy was maximised. The opposite was also seen to hold true where desensitising the system to sample loss was sufficient to introduce significant errors. These simulation results will assist with future designs and also give an indicator of how best to maximise measurement accuracy for this method.

Surface Resistance Measurements of PBF Surfaces

Using the LODR method developed a number of PBF and other additive surfaces were measured and their R_s evaluated. The R_s of 316L steel and AlSi10Mg aluminium were measured for both PBF and sheet surfaces. The sheet metal was visibly more smooth and as expected had lower loss than its PBF counterparts in both cases. In this case the PBF surfaces had not received any post-processing and is a useful indicator of the base-line performance PBF waveguides can be expected to have relative to machining.

A study into the effect of build orientation and post-process grit-blasting on microwave R_s was conducted using the LODR method. This work was conducted in collaboration with Nick Clark, a fellow PhD student at the time. It was shown that there was a significant difference in performance between vertically and horizontally built surfaces however in all cases grit-blasting was seen to homogenise the performance. This is an important result for PBF waveguides as it implies that regardless of surface orientation

post-processing can be used to guarantee consistent performance. While measurements of PBF performance have been reported previously for waveguides, this is the first time to the authors knowledge that such results have been presented with regard to build parameters. This study laid the foundations for future investigations into suitable post-process treatments for microwave passive components manufactured by PBF, this work will hopefully help inform design considerations to maximise future performance of commercial parts.

Additional results were presented looking at the performance of metallised plastic surfaces. This is a common practise in the production of low-power microwave passive components. Samples were produced by selective laser sintering (SLS) and stereolithography (SLA) in three build orientations: vertical, horizontal, and 45°. These were sent off to Jet Metal Tech. for metallising in silver. Unlike with the PBF surfaces the build orientation did not seem to have a significant effect on the value of R_s after metallising. The SLS surfaces were observed to perform poorer than the SLA surfaces, however as noted the material used in the SLS process had superior thermal tolerances. Given the already low R_s of both materials when coated in silver, the thermal properties of the nylon used in the SLS process meant that it would likely have better power handling tolerances and would likely be a more reliable choice for passive component manufacture.

6.2 Further Work

The sintered samples produced using the microwave measurement system towards the end of this research were examined using the 3-point bend test and density measurements. These tests were chosen due to the limits of the samples able to be produced; in the current setup where samples are prepared in quartz tubes only cylinders can be produced. In future examinations it would be desirable to also measure other properties such as the tensile strength and hardness, however these measurements necessitate standard test shapes such as the "dog-bone" or simply rectangular flat surfaces which would likely require the use of a die for the powder compact.

The change in microwave loss of sintered samples was shown to be a good indicator as to the progress of sintering and was found to have excellent correlation with density and flexural strength, both of which are properties which improve as the sample sinters further. Unfortunately the sintering observed in the current work was unable to

progress beyond the initial stage and very little densifying occurred, this leaves a large part of the process unaccounted for and so the change in loss beyond the initial stage should be investigated. One of the main limiting factors identified was the process temperature, this could be increased through use of a higher power amplifier. Another possible method could be to compact the powder samples before sintering, this would require a different sample container than the quartz tubes used currently.

In the studies conducted only pure mixtures of the given powders were investigated, more and more common however is the use of liquid-phase sintering. The mass-transport mechanisms for liquid-phase sintering are different, mainly utilising the capillary action of the liquid additive [10]. The presence of a localised liquid phase has been theorised between at particle interconnects during microwave sintering, and has been suggested as one of the mechanisms by which microwaves are able to reduce sintering time [24]. What effect the presence of a liquid-phase would have on the microwave loss has yet to be investigated.

The potential applications for the porous, low density material produced in the sintering experiments could be examined. There is a growing interest in the production of porous titanium for use as scaffold in orthopaedic tissue engineering [86, 138–140]. Various methods for introducing porosity have been developed including conventional sintering with select particle sizes [139], solid-state foaming by expansion of argon-filled pores [138], selective electron beam melting [140], and through use of a sacrificial wax model [86]. The material produced in Ch. 4 did not require the use of any complex steps and was very quick to produce. Additionally the flexural modulus of the samples produced in Ch. 4 was around 20 GPa, which is similar to the value for cortical bone [139]. The porosity observed for the samples in the SEM images was much finer than that reported in [86] and less ordered. The effect on tissue compatibility would first need to be investigated, other bio-compatible metal alloys could also be examined.

The measurements of PBF surfaces by the LODR fixture indicated that post-processing could be used to overcome effects of the build process. The post-process treatments of the PBF surfaces measured however were limited to grit-blasting and wire erosion. This only represents a small portion of the surface treatments available to PBF parts, and a wider study should be conducted. Intention to perform this study has been made apparent by the next PhD student. Additionally the frequencies measured by the current test fixture are firmly in the C-band, while waveguides used in satellite communications tend to fall in the Ku-band [9]. In order to investigate the effect of

these treatments at typical communication frequencies, an LODR operating in the Ku-band could be developed potentially using a higher order mode such as $TE_{01,1+\delta}$ or $TE_{02\delta}$ to achieve the frequencies at a reasonable device size.

References

- [1] E. C. Santos, M. Shiomi, K. Osakada, and T. Laoui, "Rapid manufacturing of metal components by laser forming," *Int. J. Mach. Tools Manuf.*, vol. 46, pp. 1459–1468, Oct. 2006.
- [2] C. Li, Z. Liu, X. Fang, and Y. Guo, "Residual stress in metal additive manufacturing," *Procedia CIRP*, vol. 71, pp. 348–353, Jan. 2018.
- [3] R. Roy, D. Agrawal, J. Cheng, and S. Gedevarishvili, "Full sintering of powdered-metal bodies in a microwave field," *Nature*, vol. 399, pp. 668–670, June 1999.
- [4] M. Ignatenko, M. Tanaka, and M. Sato, "Absorption of microwave energy by a spherical nonmagnetic metal particle," *Jpn. J. Appl. Phys.*, vol. 48, June 2009.
- [5] A. Porch, D. Slocombe, and P. Edwards, "Microwave absorption in powders of small conducting particles for heating applications," *Phys Chem Chem Phys*, vol. 15, pp. 2757–2763, Feb. 2013.
- [6] J. Ma, J. F. Diehl, E. J. Johnson, K. R. Martin, N. M. Miskovsky, C. T. Smith, G. J. Weisel, B. L. Weiss, and D. T. Zimmerman, "Systematic study of microwave absorption, heating, and microstructure evolution of porous copper powder metal compacts," *J. Appl. Phys.*, vol. 101, Apr. 2007.
- [7] S. Takayama, G. Link, M. Sato, and M. Thumm, "Sintering of metal powder samples with millimeter wave technology," in *2004 Jt. 29th Int. Conf. Infrared Millim. Waves 12" Int. Conf. Terahertz Electron.*, pp. 729–730, Sept. 2004.
- [8] J. Lorente, M. Mendoza, Z. Petersson, L. Pambaguian, Melcon, and C. Ernst, "Single part microwave filters made from selective laser melting," in *Proc. 39th Eur. Microw. Conf.*, pp. 1421–1424, 2009.
- [9] O. A. Peverini, M. Lumia, F. Calignano, G. Addamo, M. Lorusso, E. P. Ambrosio, D. Manfredi, and G. Virone, "Selective laser melting manufacturing of microwave waveguide devices," *Proc. IEEE*, vol. 105, pp. 620–631, Apr. 2017.
- [10] R. M. German, *Sintering Theory and Practice*. Wiley, 1996.
- [11] J. Beddoes and M. J. Bibby, *Principles of Metal Manufacturing Processes*. Butterworth Heinemann, 1999.
- [12] S. Kalpakjian and S. Schmid, *Manufacturing Engineering and Technology*. Prentice Hall, 7th ed., 2014.

- [13] R. M. German, "Coarsening in sintering: Grain shape distribution, grain size distribution, and grain growth kinetics in solid-pore systems," *Crit. Rev. Solid State Mater. Sci.*, vol. 35, pp. 263–305, Nov. 2010.
- [14] A. C. Metaxas and R. J. Meredith, *Industrial Microwave Heating*, vol. 4. Peter Peregrinus Ltd., 1983.
- [15] D. E. Clark and W. H. Sutton, "Microwave processing of materials," *Annu. Rev. Mater. Sci.*, vol. 26, pp. 299–331, 1996.
- [16] S. W. Kingman and N. A. Rowson, "Microwave treatment of minerals—a review," *Miner. Eng.*, vol. 11, pp. 1081–1087, Nov. 1998.
- [17] E. Thostenson and T.-W. Chou, "Microwave processing: fundamentals and applications," *Compos. Part A Appl. Sci. Manuf.*, vol. 30, no. 9, pp. 1055–1071, 1999.
- [18] D. E. Clark, D. C. Folz, and J. K. West, "Processing materials with microwave energy," *Mater. Sci. Eng. A*, vol. 287, no. 2, pp. 153–158, 2000.
- [19] J. Kim, S. C. Mun, H.-U. Ko, K.-B. Kim, M. A. H. Khondoker, and L. Zhai, "Review of microwave assisted manufacturing technologies," *Int. J. Precis. Eng. Manuf.*, vol. 13, pp. 2263–2272, Dec. 2012.
- [20] S. Chandrasekaran, S. Ramanathan, and T. Basak, "Microwave material processing—a review," *AIChE J.*, vol. 58, pp. 330–363, Feb. 2012.
- [21] H. Wheeler, "Formulas for the skin effect," in *Proc. IRE*, vol. 30, pp. 412–424, 1942.
- [22] T. Nishitani, "Method for sintering refractories and an apparatus there for," 1979.
- [23] K. Rodiger, K. Dreyer, T. Gerdes, and M. Willert-Porada, "Microwave sintering of hardmetals," *Int. J. Refract. Met. Hard Mater.*, vol. 16, no. 4-6, pp. 409–416, 1998.
- [24] K. I. Rybakov, E. A. Olevsky, and E. V. Krikun, "Microwave sintering: Fundamentals and modeling," *J. Am. Ceram. Soc.*, vol. 96, no. 4, pp. 1003–1020, 2013.
- [25] K. I. Rybakov, V. E. Semenov, S. V. Egorov, A. G. Ereemeev, I. V. Plotnikov, and Y. V. Bykov, "Microwave heating of conductive powder materials," *J. Appl. Phys.*, vol. 99, Jan. 2006.
- [26] J. Cheng, R. Roy, and D. Agrawal, "Radically different effects on materials by separated microwave electric and magnetic fields," *Mater. Res. Innov.*, vol. 5, no. 3-4, pp. 170–177, 2002.
- [27] S. Das, A. K. Mukhopadhyay, S. Datta, and D. Basu, "Prospects of microwave processing: An overview," *Bull. Mater. Sci.*, vol. 32, pp. 1–13, Feb. 2009.
- [28] A. Mondal, A. Shukla, A. Upadhyaya, and D. Agrawal, "Effect of porosity and particle size on microwave heating of copper," *Sci. Sinter.*, vol. 42, no. 2, pp. 169–182, 2010.

- [29] C. Crane, M. Pantoya, B. Weeks, and M. Saed, "The effects of particle size on microwave heating of metal and metal oxide powders," *Powder Technol.*, vol. 256, pp. 113–117, Apr. 2014.
- [30] V. D. Buchelnikov, D. V. Louzguine-Luzgin, G. Xie, S. Li, N. Yoshikawa, M. Sato, A. P. Anzulevich, I. V. Bychkov, and A. Inoue, "Heating of metallic powders by microwaves: Experiment and theory," *J. Appl. Phys.*, vol. 104, no. 11, pp. 113–505, 2008.
- [31] M. M. Mahmoud, G. Link, and M. Thumm, "The role of the native oxide shell on the microwave sintering of copper metal powder compacts," *J. Alloys Compd.*, vol. 627, pp. 231–237, 2015.
- [32] D. Agrawal, "Microwave sintering of ceramics, composites and metallic materials, and melting of glasses," *Trans. Indian Ceram. Soc.*, vol. 65, pp. 129–144, July 2006.
- [33] M. Mehdizadeh, *Microwave/RF Applicators and Probes for Material Heating, Sensing, and Plasma Generation*. William Andrew, 2nd ed., 2015.
- [34] C. Leonelli, P. Veronesi, L. Denti, A. Gatto, and L. Iuliano, "Microwave assisted sintering of green metal parts," *J. Mater. Process. Technol.*, vol. 205, no. 1–3, pp. 489–496, 2008.
- [35] S. Singh, D. Gupta, V. Jain, and A. K. Sharma, "Microwave processing of materials and applications in manufacturing industries: A review," *Mater. Manuf. Process.*, vol. 30, pp. 1–29, Jan. 2015.
- [36] R. M. Anklekar, D. K. Agrawal, and R. Roy, "Microwave sintering and mechanical properties of pm copper steel," *Powder Metall.*, vol. 44, no. 4, pp. 355–362, 2001.
- [37] R. M. Anklekar, K. Bauer, D. K. Agrawal, and R. Roy, "Improved mechanical properties and microstructural development of microwave sintered copper and nickel steel pm parts," *Powder Metall.*, vol. 48, pp. 39–46, Mar. 2005.
- [38] M. Gupta and W. L. E. Wong, "Enhancing overall mechanical performance of metallic materials using two-directional microwave assisted rapid sintering," *Scr. Mater.*, vol. 52, no. 6, pp. 479–483, 2005.
- [39] M. Oghbaei and O. Mirzaee, "Microwave versus conventional sintering: A review of fundamentals, advantages and applications," *J. Alloys Compd.*, vol. 494, no. 1–2, pp. 175–189, 2010.
- [40] K. Saitou, "Microwave sintering of iron, cobalt, nickel, copper and stainless steel powders," *Scr. Mater.*, vol. 54, no. 5, pp. 875–879, 2006.
- [41] A. Amherd Hidalgo, R. Frykholm, T. Ebel, and F. Pyczak, "Powder metallurgy strategies to improve properties and processing of titanium alloys: A review," *Adv. Eng. Mater.*, vol. 19, no. 6, pp. 1–14, 2017.
- [42] A. Mondal, A. Upadhyaya, and D. Agrawal, "Effect of heating mode on sintering of tungsten," *Int. J. Refract. Met. Hard Mater.*, vol. 28, no. 5, pp. 597–600, 2010.

- [43] S. D. Luo, M. Yan, G. B. Schaffer, and M. Qian, "Sintering of titanium in vacuum by microwave radiation," *Metall. Mater. Trans. A - Phys. Metall. Mater. Sci.*, vol. 42A, pp. 2466–2474, Aug. 2011.
- [44] A. Mondal, A. Upadhyaya, and D. Agrawal, "Comparative study of densification and microstructural development in w-18cu composites using microwave and conventional heating," *Mater. Res. Innov.*, vol. 14, no. 5, pp. 355–360, 2010.
- [45] K. Wang, X. P. Wang, R. Liu, T. Hao, T. Zhang, C. S. Liu, and Q. F. Fang, "The study on the microwave sintering of tungsten at relatively low temperature," *J. Nucl. Mater.*, vol. 431, pp. 206–211, Dec. 2012.
- [46] D. M. Pozar, *Microwave Engineering*. Wiley, 4th ed., 2011.
- [47] New Japan Radio Co Ltd., "High power magnetrons," 2018.
- [48] C. Liu, H. Huang, Z. Liu, F. Huo, and K. Huang, "Experimental study on microwave power combining based on injection-locked 15-kw band continuous-wave magnetrons," *IEEE Trans. Plasma Sci.*, vol. 44, pp. 1291–1297, Aug. 2016.
- [49] S. M. L. Nai, J. V. M. Kuma, M. E. Alam, X. L. Zhong, P. Babaghorbani, and M. Gupta, "Using microwave-assisted powder metallurgy route and nano-size reinforcements to develop high-strength solder composites," *J. Mater. Eng. Perform.*, vol. 19, pp. 335–341, Apr. 2010.
- [50] R. Liu, T. Hao, K. Wang, T. Zhang, X. Wang, C. Liu, and Q. Fang, "Microwave sintering of w/cu functionally graded materials," *J. Nucl. Mater.*, vol. 431, pp. 196–201, Dec. 2012.
- [51] S. Gedevanishvili, D. K. Agrawal, R. Roy, and B. Vaidhyanathan, "Microwave processing using highly microwave absorbing powdered material layers," 2003.
- [52] R. Roy, D. K. Agrawal, and J. Cheng, "Process for sintering powder metal components," 2004.
- [53] D. Demirskyi, D. Agrawal, and A. Ragulya, "Neck growth kinetics during microwave sintering of copper," *Scr. Mater.*, vol. 62, no. 8, pp. 552–555, 2010.
- [54] D. Demirskyi, D. Agrawal, and A. Ragulya, "Neck growth kinetics during microwave sintering of nickel powder," *J. Alloys Compd.*, vol. 509, no. 5, pp. 1790–1795, 2011.
- [55] D. Demirskyi, D. Agrawal, and A. Ragulya, "A scaling law study of the initial stage of microwave sintering of iron spheres," *Scr. Mater.*, vol. 66, no. 6, pp. 323–326, 2012.
- [56] B. Warren, M. Awida, and A. Fathy, "Microwave heating of metals," *IET Microwaves, Antennas Propag.*, vol. 6, no. 2, p. 196, 2012.
- [57] R. Annamalai, A. Upadhyaya, and D. Agrawal, "An investigation on microwave sintering of fe, fe-cu and fe-cu-c alloys," *Bull. Mater. Sci.*, vol. 36, pp. 447–456, June 2013.

- [58] O. Ertugrul, H. S. Park, K. Onel, and M. Willert-Porada, "Effect of particle size and heating rate in microwave sintering of 316l stainless steel," *Powder Technol.*, vol. 253, pp. 703–709, Feb. 2014.
- [59] R. I. Badiger, S. Narendranath, and M. S. Srinath, "Joining of inconel-625 alloy through microwave hybrid heating and its characterization," *J. Manuf. Process.*, vol. 18, 2015.
- [60] F. Xu, Y. Li, X. Hu, Y. Niu, J. Zhao, and Z. Zhang, "In situ investigation of metal's microwave sintering," *Mater. Lett.*, vol. 67, no. 1, pp. 162–164, 2012.
- [61] F. Xu, Y. Xiao, X. Hu, B. Dong, W. Liu, and Y. Li, "In situ investigation of al-ti mixed metal system microwave sintering by synchrotron radiation computed tomography," *J. Instrum.*, vol. 11, no. 2, 2016.
- [62] Y. Xiao, F. Xu, X. Hu, Y. Li, W. Liu, and B. Dong, "In situ investigation of titanium powder microwave sintering by synchrotron radiation computed tomography," *Metals (Basel)*, vol. 6, no. 1, p. 9, 2016.
- [63] T. Gerdes, H. S. Park, A. Rosin, A. Schmidt, and M. Willert-Porada, "Microwave antenna array for high temperature material processing," 2010.
- [64] D. Demirskyi, D. Agrawal, and A. Ragulya, "Neck formation between copper spherical particles under single-mode and multimode microwave sintering," *Mater. Sci. Eng. A*, vol. 527, no. 7, pp. 2142–2145, 2010.
- [65] R. R. Mishra and A. K. Sharma, "On mechanism of in-situ microwave casting of aluminium alloy 7039 and cast microstructure," *Mater. Des.*, vol. 112, pp. 97–106, 2016.
- [66] A. K. Sharma and R. R. Mishra, "Role of particle size in microwave processing of metallic material systems," *Mater. Sci. Technol.*, vol. 34, no. 2, pp. 123–137, 2018.
- [67] M. Sato, H. Fukusima, F. Ozeki, T. Hayasi, Y. Saito, S. Takayama, and A. Jmr-gen, "Experimental investigation of mechanism of microwave heating in powder metals," *2004 Jt. 29th Int. Conf. Infrared Millim. Waves 12th Int. Conf. Terahertz Electron.*, vol. 50, pp. 831–832, 2004.
- [68] Y. Zhang, D. K. Agrawal, J. Cheng, and T. Slawecki, "Microwave power absorption mechanism of metallic powders," *IEEE Trans. Microw. Theory Tech.*, vol. 66, pp. 2107–2115, May 2018.
- [69] A. Porch, "Microwave resonator analysis and measurement," 2009.
- [70] P. J. Petersan and S. M. Anlage, "Measurement of resonant frequency and quality factor of microwave resonators: Comparison of methods," *J. Appl. Phys.*, vol. 84, no. 6, pp. 3392–3402, 1998.
- [71] D. Kajfez, "Linear fractional curve fitting for measurement of high q factors," *IEEE Trans. Microw. Theory Tech.*, vol. 42, pp. 1149–1153, July 1994.

- [72] M. V. Jacob, J. Mazierska, S. Member, K. Leong, and J. Krupka, "Simplified method for measurements and calculations of coupling coefficients and q_0 factor of high-temperature superconducting dielectric resonators," *IEEE Trans. Microw. Theory Tech.*, vol. 49, pp. 2401–2407, Dec. 2001.
- [73] K. Leong and J. Mazierska, "Precise measurements of the q factor of dielectric resonators in the transmission mode-accounting for noise, crosstalk, delay of uncalibrated lines, coupling loss, and coupling reactance," *IEEE Trans. Microw. Theory Tech.*, vol. 50, pp. 2115–2127, Sept. 2002.
- [74] N. Pompeo, K. Torokhtii, F. Leccese, A. Scorza, S. Sciuto, and E. Silva, "Fitting strategy of resonance curves from microwave resonators with non-idealities," in *I2MTC 2017 - 2017 IEEE Int. Instrum. Meas. Technol. Conf. Proc.*, vol. 21, 2017.
- [75] H. Thal, "Cylindrical te_{011}/tm_{111} mode control by cavity shaping," *IEEE Trans. Microw. Theory Tech.*, vol. 27, no. 12, pp. 982–986, 1979.
- [76] D. Kajfez, "Q factor measurements, analog and digital," 1999.
- [77] J. Knobloch, "Basic concepts of measurements made on superconducting rf cavities," 1991.
- [78] International Commission on Non-Ionizing Radiation Protection, "Guidelines for limiting exposure to time-varying electric, magnetic, and electromagnetic fields (up to 300 ghz)," *Health Phys.*, vol. 74, no. 4, pp. 494–522, 1998.
- [79] R. Mishra and A. Sharma, "A review of research trends in microwave processing of metal-based materials and opportunities in microwave metal casting," *Crit. Rev. Solid State Mater. Sci.*, vol. 41, pp. 217–255, May 2016.
- [80] E. Jerby, Y. Meir, A. Salzberg, E. Aharoni, A. Levy, J. Torralba, and B. Cavallini, "Incremental metal-powder solidification by localized microwave-heating and its potential for additive manufacturing," *Addit. Manuf.*, vol. 6, pp. 53–66, 2015.
- [81] J. A. Slotwinski, E. J. Garboczi, P. E. Stutzman, C. F. Ferraris, S. S. Watson, and M. A. Peltz, "Characterization of metal powders used for additive manufacturing," *J. Res. Natl. Inst. Stand. Technol.*, vol. 119, pp. 460–493, Sept. 2014.
- [82] G. B. Schaffer, B. J. Hall, S. J. Bonner, S. H. Huo, and T. B. Sercombe, "The effect of the atmosphere and the role of pore filling on the sintering of aluminium," *Acta Mater.*, vol. 54, no. 1, pp. 131–138, 2006.
- [83] F. A.L. Dullien, *Porous Media , Fluid transport and pore structure*. Academic Press, 2nd ed., 1992.
- [84] G. Lei, R. M. German, and H. S. Nayar, "Influence of sintering variables on the corrosion-resistance of 316l stainless-steel," *Powder Metall. Int.*, vol. 15, no. 2, pp. 70–76, 1983.
- [85] H. P. Büchkremer, E. El-Magd, D. Stöver, and G. Abouelmagd, "Mechanical properties of a TiAl6V4 alloy processed by powder metallurgy," *J. Mater. Process. Technol.*, vol. 37, no. 1-4, pp. 583–597, 1993.

- [86] G. E. Ryan, A. S. Pandit, and D. P. Apatsidis, "Porous titanium scaffolds fabricated using a rapid prototyping and powder metallurgy technique," *Biomaterials*, vol. 29, no. 27, pp. 3625–3635, 2008.
- [87] G. C. Obasi, O. M. Ferri, T. Ebel, and R. Bormann, "Influence of processing parameters on mechanical properties of ti-6al-4v alloy fabricated by mim," *Mater. Sci. Eng. A - Struct. Mater. Prop. Microstruct. Process.*, vol. 527, pp. 3929–3935, June 2010.
- [88] L. Bolzoni, P. G. Esteban, E. M. Ruiz-Navas, and E. Gordo, "Influence of powder characteristics on sintering behaviour and properties of pm ti alloys produced from prealloyed powder and master alloy," *Powder Metall.*, vol. 54, no. 4, pp. 543–550, 2011.
- [89] M. R. Raza, F. Ahmad, M. A. Omar, and R. M. German, "Effects of cooling rate on mechanical properties and corrosion resistance of vacuum sintered powder injection molded 316l stainless steel," *J. Mater. Process. Technol.*, vol. 212, no. 1, pp. 164–170, 2012.
- [90] G. Taguchi, "Quality engineering (taguchi methods) for the development of electronic circuit technology," *IEEE Trans. Reliab.*, vol. 44, pp. 225–229, June 1995.
- [91] H.-G. G. Beyer and B. Sendhoff, "Robust optimization – a comprehensive survey," *Comput. Methods Appl. Mech. Eng.*, vol. 196, no. 33, pp. 3190–3218, 2007.
- [92] C. H. Ji, N. H. Loh, K. A. Khor, and S. B. Tor, "Sintering study of 316l stainless steel metal injection molding parts using taguchi method: Final density," *Mater. Sci. Eng. A*, vol. 311, no. 1-2, pp. 74–82, 2001.
- [93] P. Sharma, A. Verma, R. K. Sidhu, and O. P. Pandey, "Process parameter selection for strontium ferrite sintered magnets using taguchi 19 orthogonal design," *J. Mater. Process. Technol.*, vol. 168, no. 1, pp. 147–151, 2005.
- [94] N. H. M. Nor, N. Muhamad, A. K. A. M. Ihsan, and K. R. Jamaludin, "Sintering parameter optimization of ti-6al-4v metal injection molding for highest strength using palm stearin binder," in *Int. Tribol. Conf. Malaysia 2013*, vol. 68, pp. 359–364, 2013.
- [95] M. Subasi and C. Karatas, "Investigation of molding and sintering parameters of feedstock prepared from ti-6al-4v alloy powder," *J. Fac. Eng. Archit. Gazi Univ.*, vol. 31, no. 2, pp. 473–483, 2016.
- [96] R. N. Ahmad, N. Muhammad, A. B. Sulong, and A. Wahi, "Parameter optimization of sintering ti-6al-7nb powder and palm stearin binder system for highest sintered density using taguchi method," in *Adv. Process. Syst. Manuf. (APSIM 2016)*, pp. 5–6, 2016.
- [97] F. Calignano, D. Manfredi, E. P. Ambrosio, S. Biamino, M. Lombardi, E. Atzeni, A. Salmi, P. Minetola, L. Iuliano, and P. Fino, "Overview on additive manufacturing technologies," *Proc. IEEE*, vol. 105, pp. 593–612, Apr. 2017.
- [98] AZoM, "Grade 23 Ti 6Al 4V ELI Alloy (UNS R56401)," 2013.

- [99] P. Booth, J. Gilmore, E. V. Lluch, and M. Harvey, "Enhancements to satellite feed chain performance, testing and lead-times using additive manufacturing," in *2016 10th Eur. Conf. Antennas Propag.*, pp. 1–5, Apr. 2016.
- [100] H. Yukawa, Y. Ushijima, M. Abe, N. Yoneda, and M. Miyazaki, "A metal 3d-printed t-junction omt with an offset stepped post," in *Proc. 47th Eur. Microw. Conf.*, pp. 444–447, 2017.
- [101] T. Duda and L. V. Raghavan, "3d metal printing technology: the need to reinvent design practice," *AI Soc.*, vol. 33, pp. 241–252, May 2018.
- [102] T. Y. Ootoshi and M. M. Franco, "The electrical conductivities of steel and other candidate materials for shrouds in a beam-waveguide antenna system," *IEEE Trans. Instrum. Meas.*, vol. 45, pp. 77–83, Feb. 1996.
- [103] B. Curran, I. Ndip, S. Guttowski, and H. Reichl, "On the quantification and improvement of the models for surface roughness," *2009 IEEE Work. Signal Propag. Interconnects*, 2009.
- [104] K. Pitt, C. Free, Z. Tian, and M. Jakubowska, "A method for the prediction of microwave properties of thick film conductors from physical measurements and d.c. conductivity," *J. Mater. Sci. Mater. Electron.*, vol. 12, no. 9, pp. 491–495, 2001.
- [105] E. Hammerstad and O. Jensen, "Accurate models for microstrip computer-aided design," *MTT-S Int. Microw. Symp. Dig.*, vol. 80, no. 1, pp. 407–409, 1980.
- [106] D. Kajfez and P. Guillon, *Dielectric Resonators*. Noble Publishing Classic Series, Noble Publishing Corporation, 2nd ed., 1998.
- [107] V. J. Krupka, M. Klinger, M. Kuhn, A. Baranyak, M. Stiller, J. Hinken, and J. Modelski, "Surface resistance measurements of hts films by means of sapphire dielectric resonators," *IEEE Trans. Appl. Supercond.*, vol. 3, no. 3, pp. 3043–3048, 1993.
- [108] J. Mazierska, "Dielectric resonator as a possible standard for characterization of high temperature superconducting films for microwave applications," *J. Supercond.*, vol. 10, pp. 73–84, Apr. 1997.
- [109] W. Diete, M. Getta, M. Hein, T. Kaiser, G. Muller, H. Piel, and H. Schlick, "Surface resistance and nonlinear dynamic microwave losses of epitaxial hts films," *IEEE Trans. Appl. Supercond.*, vol. 7, pp. 1236–1239, June 1997.
- [110] J. Mazierska and C. Wilker, "Accuracy issues in surface resistance measurements of high temperature superconductors using dielectric resonators (corrected)," *IEEE Trans. Appl. Supercond.*, vol. 11, pp. 4140–4147, Dec. 2001.
- [111] M. V. Jacob, J. Mazierska, K. Leong, D. Ledenyov, and J. Krupka, "Surface resistance measurements of hts thin films using slao dielectric resonator," *IEEE Trans. Appl. Supercond.*, vol. 13, pp. 2909–2912, June 2003.
- [112] J. Krupka, "Measurements of the surface resistance and the effective conductivity of copper clad laminates employing dielectric resonator technique," 2007.

- [113] J. Krupka and J. Mazierska, "Contactless measurements of resistivity of semiconductor wafers employing single-post and split-post dielectric-resonator techniques," *IEEE Trans. Instrum. Meas.*, vol. 56, pp. 1839–1844, Oct. 2007.
- [114] O. Shaforost, K. Wang, S. Goniszewski, M. Adabi, Z. Guo, S. Hanham, J. Gallop, L. Hao, and N. Klein, "Contact-free sheet resistance determination of large area graphene layers by an open dielectric loaded microwave cavity," *J. Appl. Phys.*, vol. 117, no. 2, p. 24501, 2015.
- [115] B. W. Hakki and P. D. Coleman, "A dielectric resonator method of measuring inductive capacities in the millimeter range," *IRE Trans. Microw. Theory Tech.*, vol. MTT-8, no. 4, pp. 402–410, 1960.
- [116] J. Krupka, Ł. Usydus, and H. Kołtuniak, "Sheet resistance and conductivity measurements of rough surfaces of metals on printed circuit boards and metalized ceramic substrates," 2012.
- [117] J. Krupka and J. Mazierska, "Improvement of accuracy in measurements of the surface resistance of superconductors using dielectric resonators," *IEEE Trans. Appl. Supercond.*, vol. 8, no. 4, pp. 164–167, 1998.
- [118] Z. Y. Shen, C. Wilker, P. Pang, W. L. Holstein, D. Face, and D. J. Kountz, "High tc superconductor-sapphire microwave resonator with extremely high q-values up to 90 k," 1992.
- [119] Y. Kobayashi and S. Tanaka, "Resonant modes of a dielectric rod resonator short-circuited at both ends by parallel conducting plates," *IEEE Trans. Microw. Theory Tech.*, vol. 28, no. 10, pp. 1077–1085, 1980.
- [120] Y. Kobayashi and T. Senju, "Resonant modes in shielded uniaxial-anisotropic dielectric rod resonators," *IEEE Trans. Microw. Theory Tech.*, vol. 41, no. 12, pp. 2198–2205, 1993.
- [121] T. Hashimoto and Y. Kobayashi, "A novel technique to measure frequency dependence of surface resistance of ybco films using some modes in a sapphire rod resonator," *2002 32nd Eur. Microw. Conf. EuMC 2002*, vol. 1, no. d, pp. 1–4, 2002.
- [122] T. Hashimoto and Y. Kobayashi, "Design of sapphire rod resonators to measure the surface resistance of high temperature superconductor films," *2002 IEEE MTT-S Int. Microw. Symp. Dig.*, vol. 3, pp. 1975–1978, 2002.
- [123] N. J. Parker, A. P. Kharel, J. R. Powell, P. A. Smith, P. D. Evans, and A. Porch, "Measurements and modeling of hts shielded dielectric resonators," *IEEE Trans. Appl. Supercond.*, vol. 9, no. 2, pp. 1928–1931, 1999.
- [124] N. Clark, S. Hefford, and A. Porch, "Effect of build orientation and surface finish on surface resistance in microwave components produced by selective laser melting," in *Proc. 47th Eur. Microw. Conf. Monit.*, pp. 2–5, 2017.
- [125] J. Sheen, "Amendment of cavity perturbation technique for loss tangent measurement at microwave frequencies," *J. Appl. Phys.*, vol. 102, no. 1, pp. 1–3, 2007.

- [126] M. Lin, Y. Wang, and M. N. Afsar, "Precision measurement of complex permittivity and permeability by microwave cavity perturbation technique," *2005 Jt. 30th Intl. Conf. Infrared Millim. Waves 13th Intl. Conf. Terahertz Electron.*, vol. 1, pp. 62–63, 2005.
- [127] R. A. Waldron, "Perturbation theory of resonant cavities," 1960.
- [128] G. Strano, L. Hao, R. M. Everson, and K. E. Evans, "Surface roughness analysis, modelling and prediction in selective laser melting," *J. Mater. Process. Technol.*, vol. 213, no. 4, pp. 589–597, 2013.
- [129] E. Laplanche, W. Feuray, J. Sence, A. Perigaud, O. Tantot, N. Delhote, C. Menudier, E. Arnaud, M. Thevenot, T. Monédière, D. Passerieux, S. Verdeyme, S. Bila, D. Baillargeat, and L. Carpentier, "Additive manufacturing of low cost and efficient proof of concepts for microwave passive components," *IET Microwaves, Antennas Propag.*, vol. 11, no. 14, pp. 1997–2004, 2017.
- [130] A. Genc, T. Goksu, and S. Helhel, "Fabrication of three-dimensional printed rectangular waveguide t-junction with in-phase and equal power division," *Microw. Opt. Technol. Lett.*, vol. 60, no. 8, pp. 2043–2048, 2018.
- [131] M. Pellaton, C. Affolderbach, A. K. Skrivervik, A. E. Ivanov, T. Debogovic, E. de Rijk, and G. Mileti, "3d printed microwave cavity for atomic clock applications: proof of concept," *Electron. Lett.*, vol. 54, no. 11, pp. 691–693, 2018.
- [132] C. Menudier, M. Thevenot, E. Arnaud, T. Monediere, O. Tantot, A. Perigaud, S. Bila, N. Delhote, and K. Staelens, "Additive manufacturing of microwave antennas up to 60 ghz," in *2017 Int. Conf. Electromagn. Adv. Appl.*, pp. 1551–1554, Sept. 2017.
- [133] M. Dionigi, C. Tomassoni, G. Venanzoni, and R. Sorrentino, "Simple high-performance metal-plating procedure for stereolithographically 3-d-printed waveguide components," *IEEE Microw. Wirel. Components Lett.*, vol. 27, pp. 953–955, Nov. 2017.
- [134] S. Brinkhues, A. Kanthamneni, A. Brose, S. Majcherek, and B. Schmidt, "Investigation of adhesion strength of metallization on thermoplastic and ceramic substrates," *2016 12th Int. Congr. Molded Interconnect Devices*, 2016.
- [135] S. Verploegh, M. Coffey, E. Grossman, and Z. Popovic, "Properties of 50-110-ghz waveguide components fabricated by metal additive manufacturing," *IEEE Trans. Microw. Theory Tech.*, vol. 65, pp. 5144–5153, Dec. 2017.
- [136] R. J. Crawford, *Plastics engineering*. Elsevier, 1998.
- [137] F. Calignano, D. Manfredi, E. P. Ambrosio, L. Iuliano, and P. Fino, "Influence of process parameters on surface roughness of aluminum parts produced by dmls," *Int. J. Adv. Manuf. Technol.*, vol. 67, no. 9-12, pp. 2743–2751, 2013.
- [138] N. G. Davis, J. Teisen, C. Schuh, and D. C. Dunand, "Solid-state foaming of titanium by superplastic expansion of argon-filled pores," *J. Mater. Res.*, vol. 16, pp. 1508–1519, May 2001.

-
- [139] I. H. Oh, N. Nomura, N. Masahashi, and S. Hanada, "Mechanical properties of porous titanium compacts prepared by powder sintering," *Scr. Mater.*, vol. 49, pp. 1197–1202, Dec. 2003.
- [140] P. Heintz, L. Mueller, C. Koerner, R. F. Singer, and F. A. Mueller, "Cellular ti-6al-4v structures with interconnected macro porosity for bone implants fabricated by selective electron beam melting," *Acta Biomater.*, vol. 4, pp. 1536–1544, Sept. 2008.

Appendix A

Control Software Implementation

A.1 Program Operation

The current software is written using NI LabVIEW and uses the "Queued Message Handler" (QMH) architecture. The QMH format consists of multiple parallel execution loops which communicate asynchronously via messages. The main advantage of this design is its scalability and additional functionality can easily be added without having to alter the core program significantly.

Main program flow is described in Fig. A.1 and is organised into multiple "states" of operation. These states are used to determine which controls and features are enabled/disabled and are described in Tab. A.1 The three main modes of operation "Standby", "Heat and Track", and "Continuous Sweep" are determined by these states. Once launched the program is locked in a safe do-nothing state until configuration is performed. Once complete, the user interface is unlocked and execution moves into the "Standby" mode. In this mode the sensors are polled and the data is displayed at the bottom of the user interface in the ribbon, however no data is written to file and the source power cannot be switched on.

By clicking "RUN" on the user interface the "Heat and Track" mode is initiated. In this mode the resonator is continuously excited at a fixed frequency, while periodic tracking sweeps are performed to ensure that the excitation frequency matches the resonant frequency. The power level used for the tracking sweep depends on whether or not the source power is switched on. If the source power is off the sweep is performed at the configured "low" power setting (Default: 20 dBm), if it is on the sweep is performed at the excitation power in order to minimise cooling of the sample. The user is prompted to create a save file at the start and data from the power meters and temperature sensor

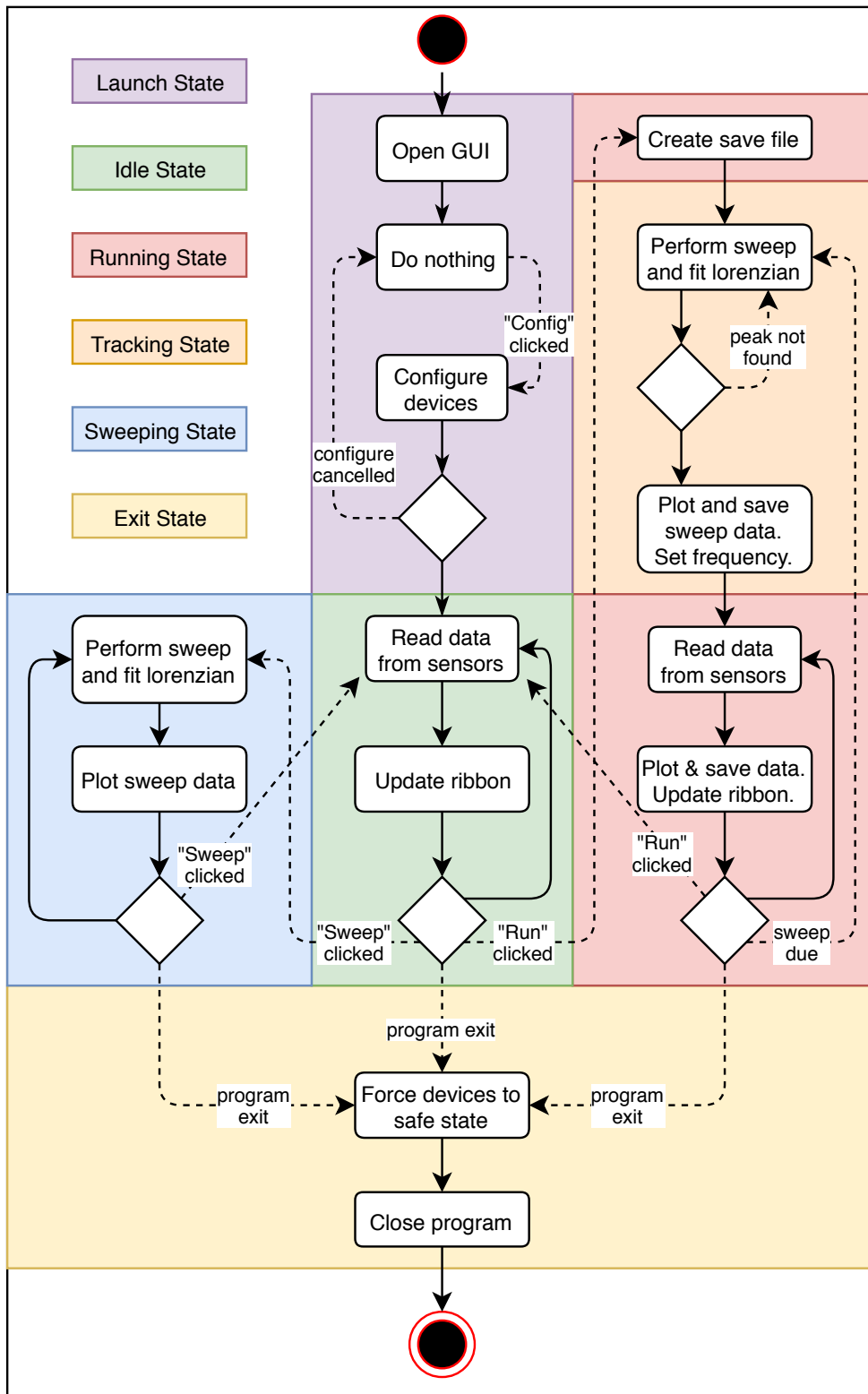


Fig. A.1 Control program flowchart.

is continuously sampled and saved to file along with the resonant sweep data as it occurs.

Clicking "SWEEP" on the user interface will initiate the "Continuous Sweep" mode. In this mode a resonant sweep is repeatedly performed, approximating the functionality of a scalar network analyser. This mode is usually used during setup when adjusting the coupling of the resonant cavity or other applicator.

Table A.1 Operation "States" and Definitions

State	Description
Launch	A "do nothing" state, on program launch all controls are disabled until configuration is performed.
Idle	A Standby or "safe mode" in between operation. Settings can be updated and are written to devices however the source cannot be switched on in this state.
Running	Part of the main "Heat and Track" mode. Source control is enabled in this state and power can be switched on and off. On entering this state the user is prompted to create a save file.
Tracking	Part of the main "Heat and Track" mode. In this state a resonant sweep is performed and a Lorentzian curve fit is performed. While in this state the linear stage is paused (if enabled)
Sweeping	Continuous sweep or scalar network analyser mode. Similar to Tracking in that a resonant sweep is performed, in this state however the sweep is performed repeatedly.
Exit	Exiting state, triggered by closing the program or by a non-recoverable error. Forces the devices to a safe state (source switched off) before terminating operation.

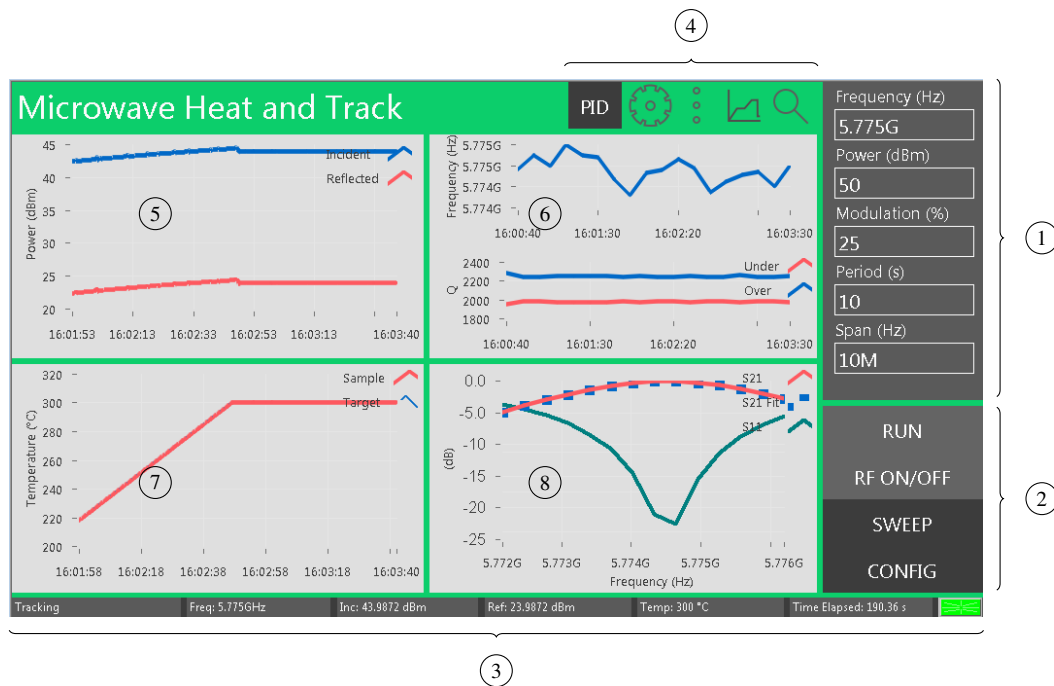


Fig. A.2 Main user interface for the control program "Microwave Heat and Track"

A.2 User Interface

The main user interface is shown in Fig. A.2. As can be seen the interface is largely dominated by the data plots, with minimalistic controls located to the right-hand side. Additional controls and options are available through various sub-menus. Labelled features are described below.

- ① The main user configurable settings used in both the normal "Heat and Track" excitation mode and the continuous sweep mode. They are described in Tab. A.2.
- ② These controls are used to move between the two main modes of operation, control the RF switch and open the configuration window.
- ③ Ribbon display. Displays information relating to the state of the system as well as power and temperature sensor readings even during idle operation.
- ④ Used to open and close various sub-menus and windows for more specialised functions. They are described in Tab. A.3
- ⑤ Power plot. During "Heat and Track" operation plots the change in measured incident and reflected power in real-time.

- ⑥ Tracking plot. During "Heat and Track" operation plots the change in resonant frequency and unloaded Q factor.
- ⑦ Temperature Plot. During "Heat and Track" operation plots the change in measured sample temperature over time. If a script is being run the target temperature is also displayed.
- ⑧ Sweep plot. Displays the results of the resonant sweep as well as the Lorentzian fit to the $\sqrt{P_0}$ plot.

Table A.2 Main Settings

Setting	Description
Frequency (Hz)	Initial excitation frequency for "Heat and Track" mode. For continuous sweep mode this becomes the center frequency.
Power (dBm)	Power of excitation signal in "Heat and Track" mode accounting for gain of PA. If gain has not been configured or no PA is used, this is the output power of the signal generator.
Modulation (%)	Duty cycle for excitation signal in "Heat and Track" mode.
Period (s)	Time between tracking sweeps in "Heat and Track" mode. If set to 0 tracking is disabled.
Span (Hz)	Initial span for tracking sweeps in "Heat and Track" mode. For continuous sweep mode this value is not updated.

Table A.3 Sub-Menu Controls

Control	Description
PID Settings	Opens the PID settings window.
Global Settings	Opens the global settings window.
Stage Settings	Opens the linear stage control window.
SEM Window	Opens the scripted events manager window.
Sweep Window	Used to open a separate window to view the resonant sweep plot.

A.2.1 Closed-Loop Temperature Control Using the Scripted Event Manager

Where temperature control is desired the scripted event manager (SEM) sub-system can be used to execute an automated heating profile during "Heat and Track" mode. The interface for this is shown in Fig. A.3 and allows the user to create, save, or load a comma separated value (.CSV) file containing basic instructions which are used to describe the heating profile.

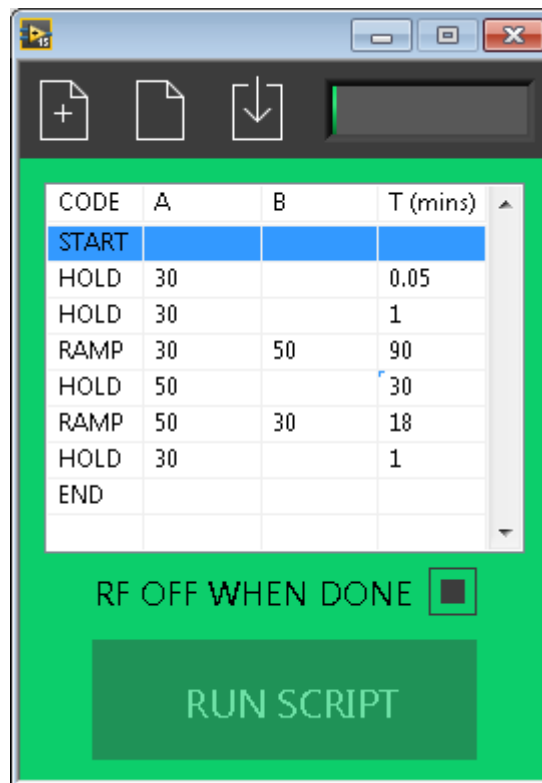


Fig. A.3 Scripted Event Manager window.

The scripting language used is very basic and consists of only four commands: *START*, *END*, *HOLD*, and *RAMP*. The *START* and *END* commands are only really used to inform the SEM which part of the file contains the code and so target temperature is controlled entirely by the *HOLD* and *RAMP* commands. *HOLD* is used when the temperature needs to be kept at a fixed value for a length of time, while *RAMP* is used to change the temperature linearly between two values over a period of time.

Temperature control is achieved using a PID controller embedded in the HaT (Heat and Track) sub-system. The PID controller uses the temperature measurement as its process variable and the target temperature as its set-point. Based on the difference between the two the controller adjusts the duty-cycle of the excitation signal. Duty-cycle is

adjusted rather than excitation power to avoid having to compensate for potentially non-linear amplifier gain.

Appendix B

Additional Sintering Experiment Data

B.1 Low Temperature Observations

Results for Sample A1

Ti6Al4V powder sealed in quartz capillary tubing in air. An oversight during the experiment meant the excitation power used was lower than intended.

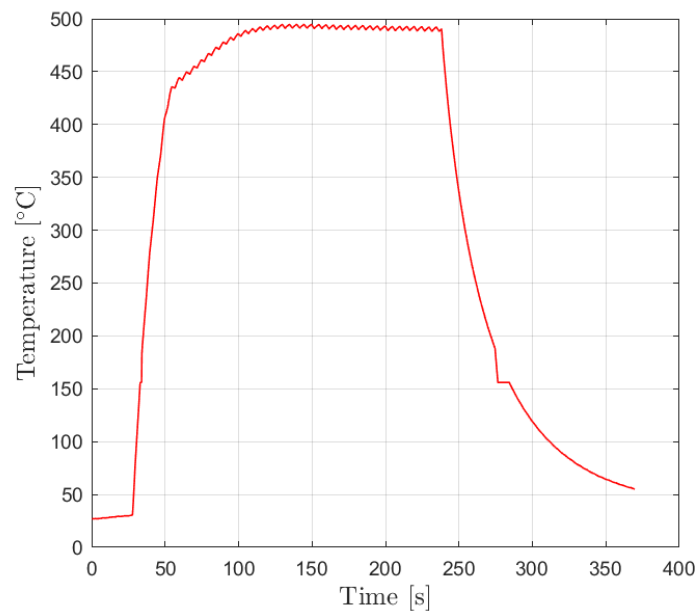


Fig. B.1 Sample temperature during microwave excitation.

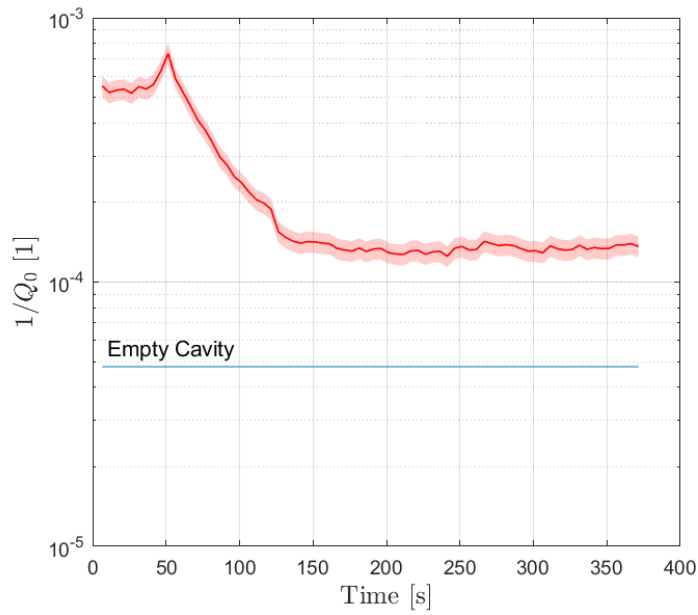
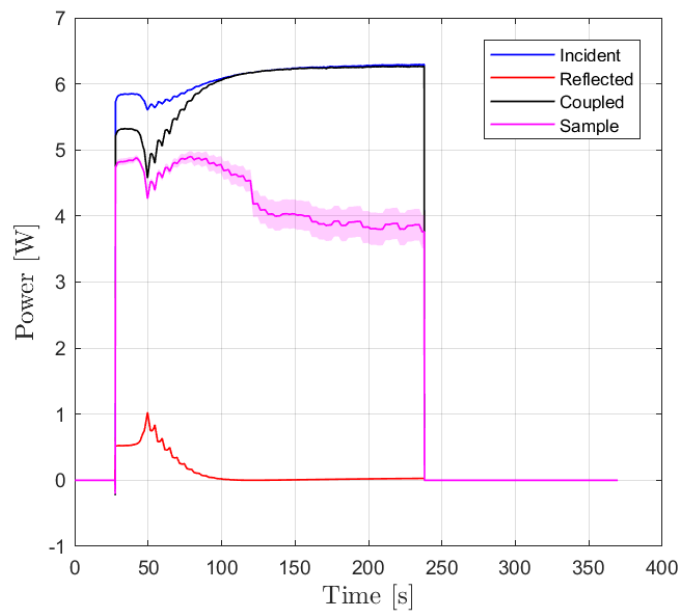
Fig. B.2 Q_0 during microwave excitation.

Fig. B.3 Power absorbed by sample during microwave excitation.

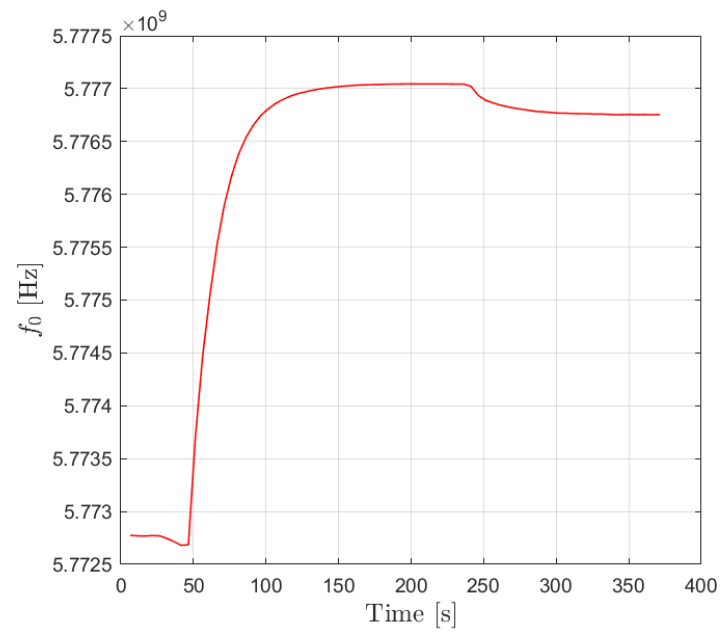


Fig. B.4 Change in resonant frequency, f_0 during microwave excitation.

Results for Sample A2

Ti6Al4V powder sealed in quartz capillary tubing in air. An oversight during the experiment meant the excitation power used was initially lower than intended.

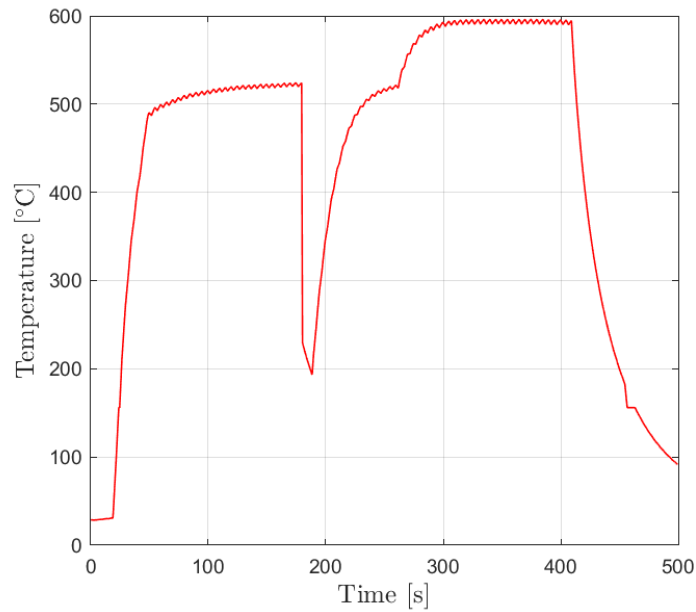


Fig. B.5 Sample temperature during microwave excitation.

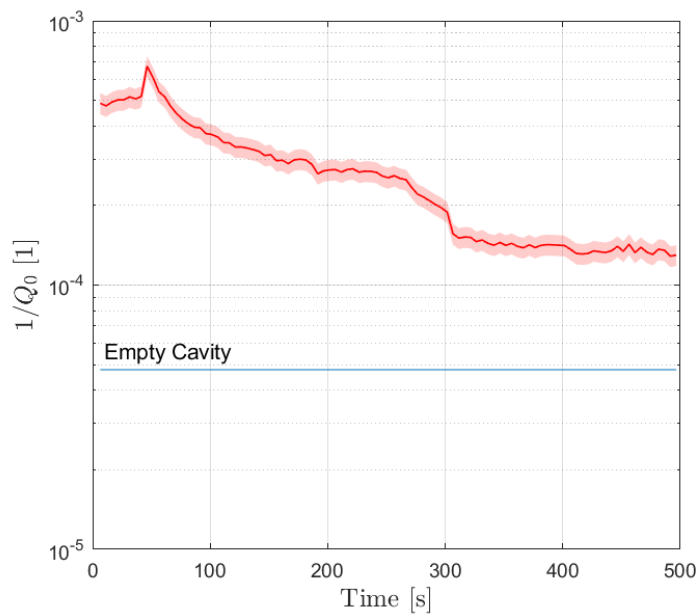


Fig. B.6 Q_0 during microwave excitation.

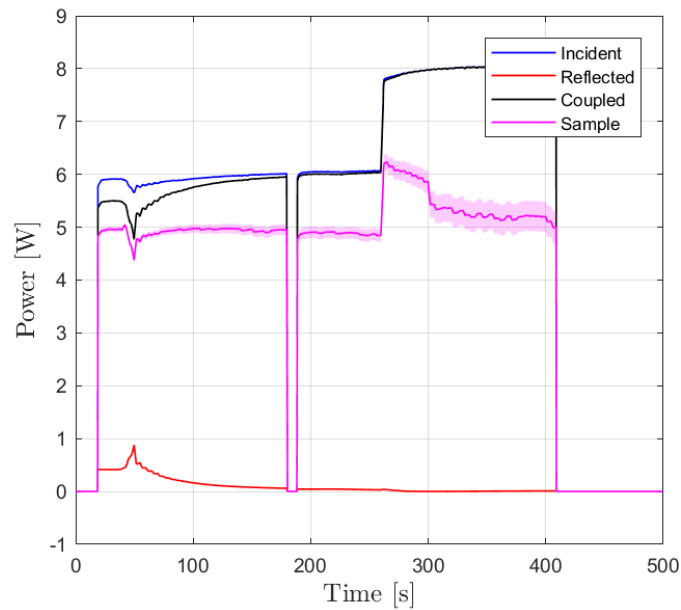


Fig. B.7 Power absorbed by sample during microwave excitation.

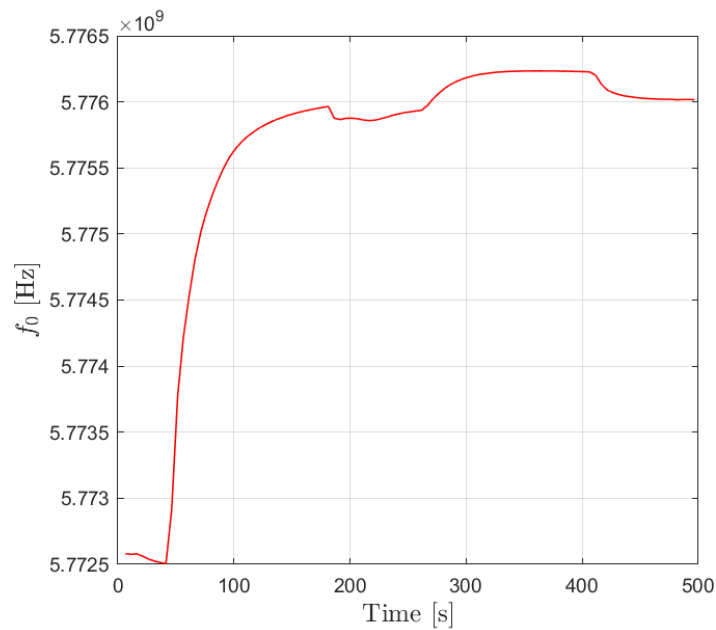


Fig. B.8 Change in resonant frequency, f_0 during microwave excitation.

Results for Sample A3

Ti6Al4V powder sealed in quartz capillary tubing in argon.

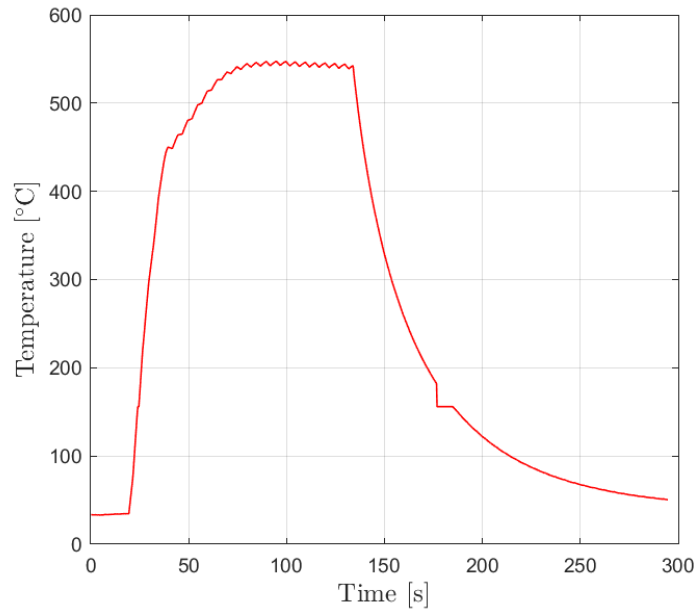


Fig. B.9 Sample temperature during microwave excitation.

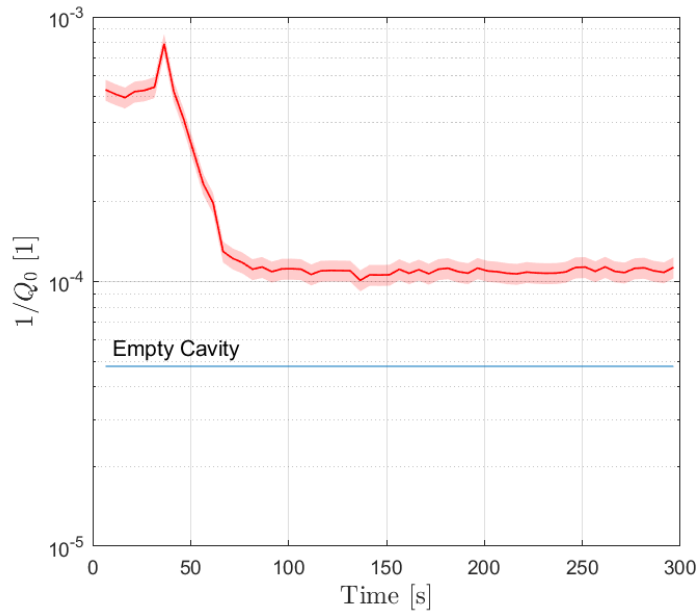


Fig. B.10 Q_0 during microwave excitation.

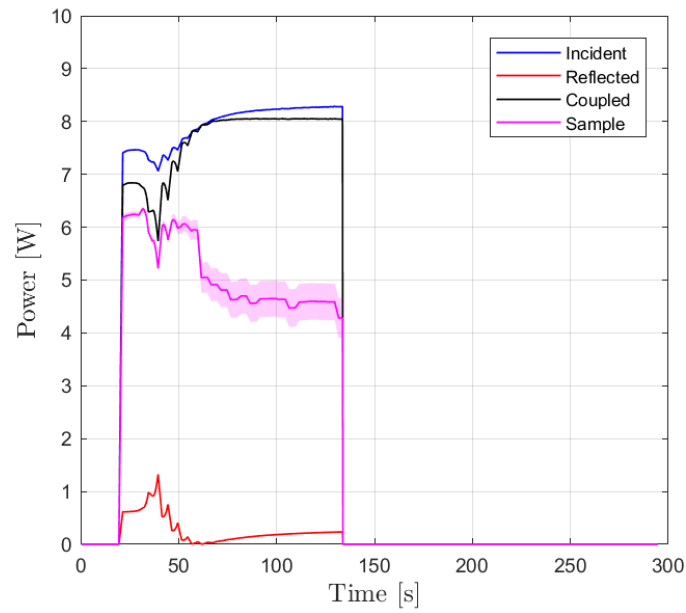
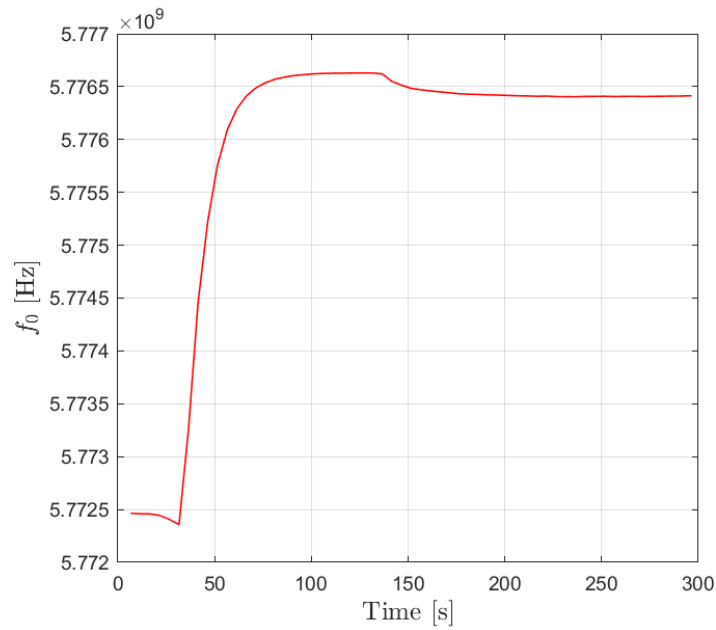


Fig. B.11 Power absorbed by sample during microwave excitation.

Fig. B.12 Change in resonant frequency, f_0 during microwave excitation.

Results for Sample A4

Ti6Al4V powder sealed in quartz capillary tubing in argon. Heating cycle was interrupted due to an unexpected error.

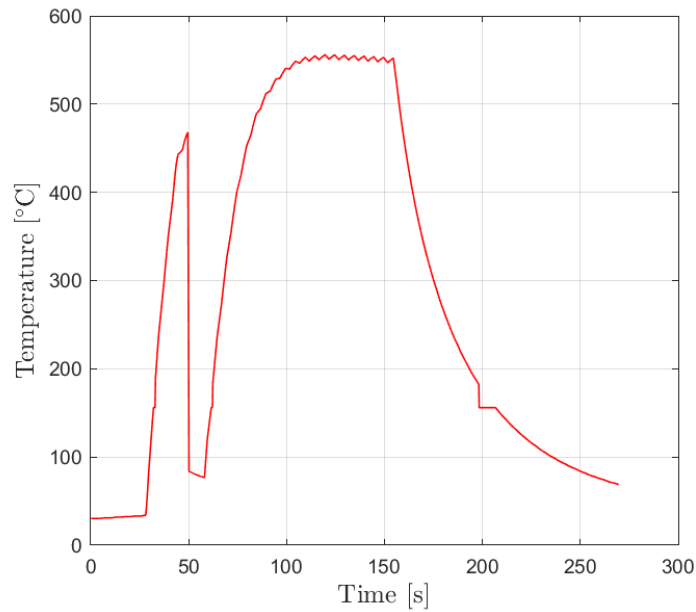


Fig. B.13 Sample temperature during microwave excitation.

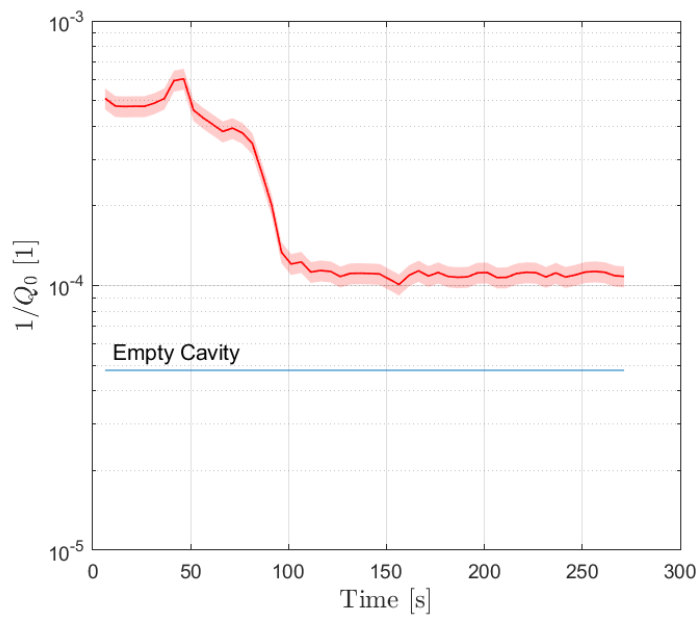


Fig. B.14 Q_0 during microwave excitation.

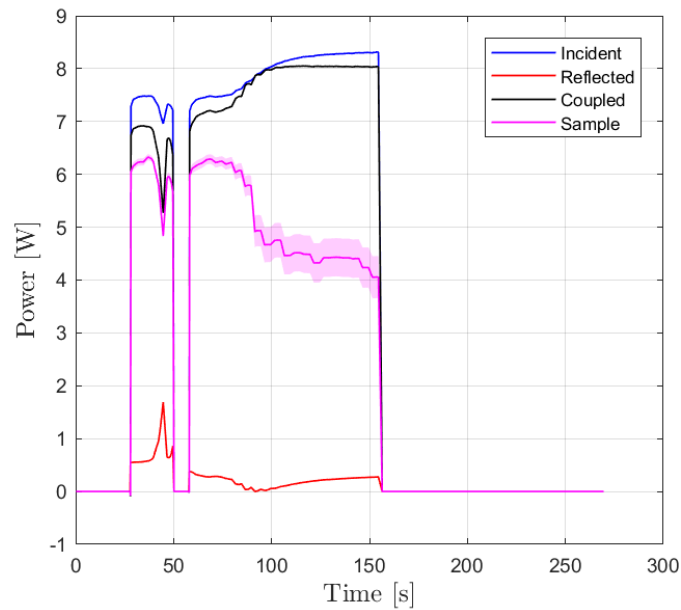


Fig. B.15 Power absorbed by sample during microwave excitation.

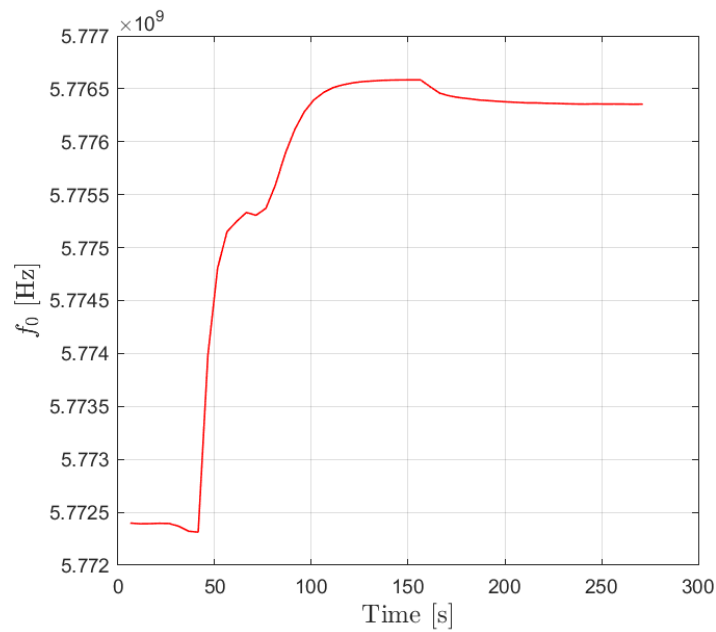


Fig. B.16 Change in resonant frequency, f_0 during microwave excitation.

Results for Sample A5

Ti6Al4V powder sealed in quartz capillary tubing in argon.

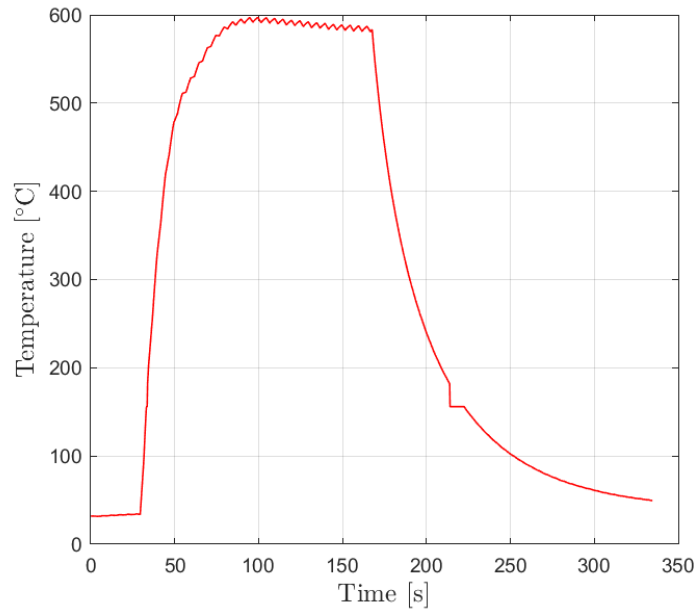


Fig. B.17 Sample temperature during microwave excitation.

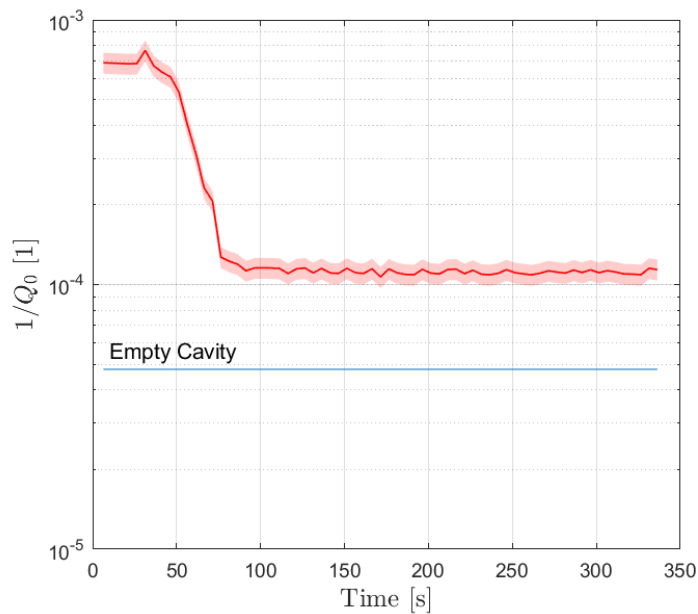


Fig. B.18 Q_0 during microwave excitation.

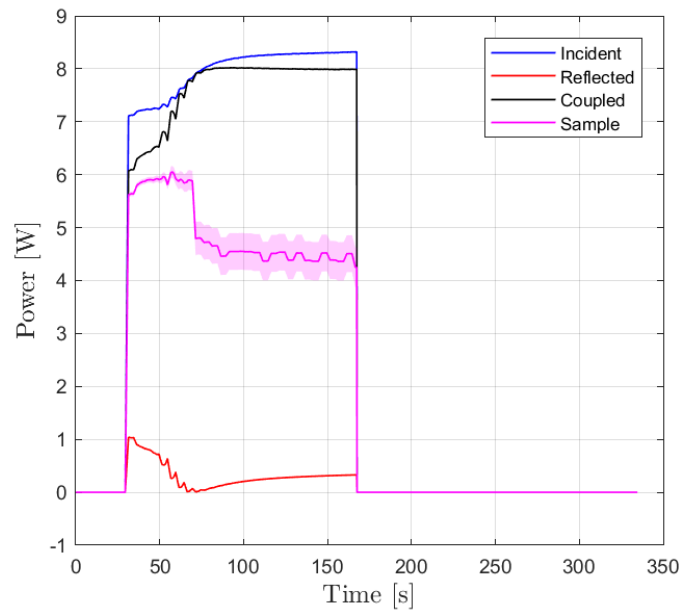


Fig. B.19 Power absorbed by sample during microwave excitation.

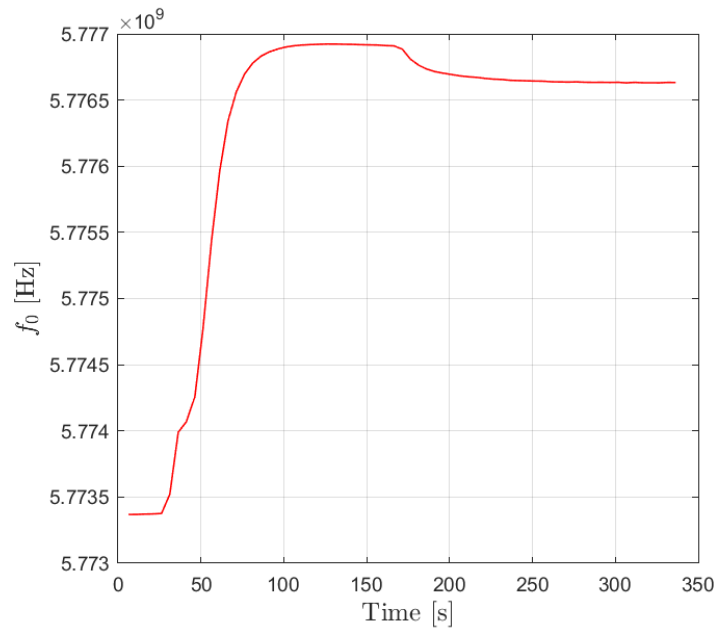


Fig. B.20 Change in resonant frequency, f_0 during microwave excitation.

B.2 High Temperature Observations

Results for Ti6Al4V - 1

Ti6Al4V powder sealed in quartz capillary tubing in argon.

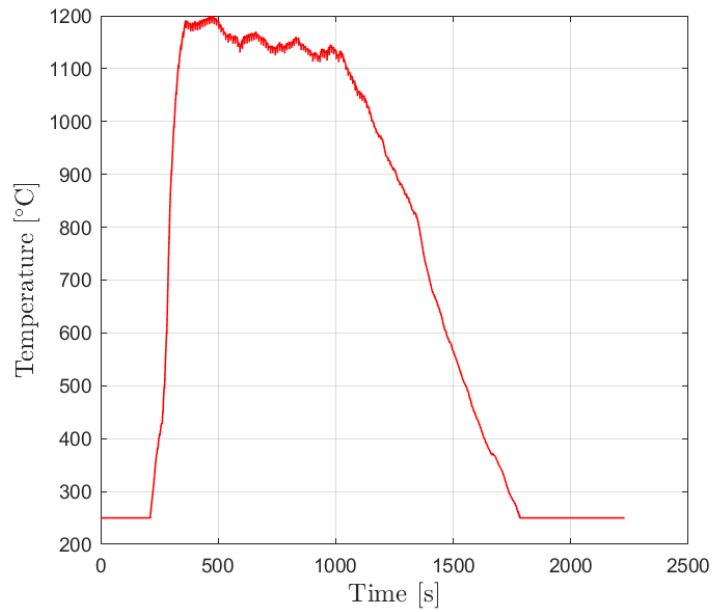


Fig. B.21 Change in sample temperature during microwave sintering of Ti6Al4V. Data shown is for sample 1

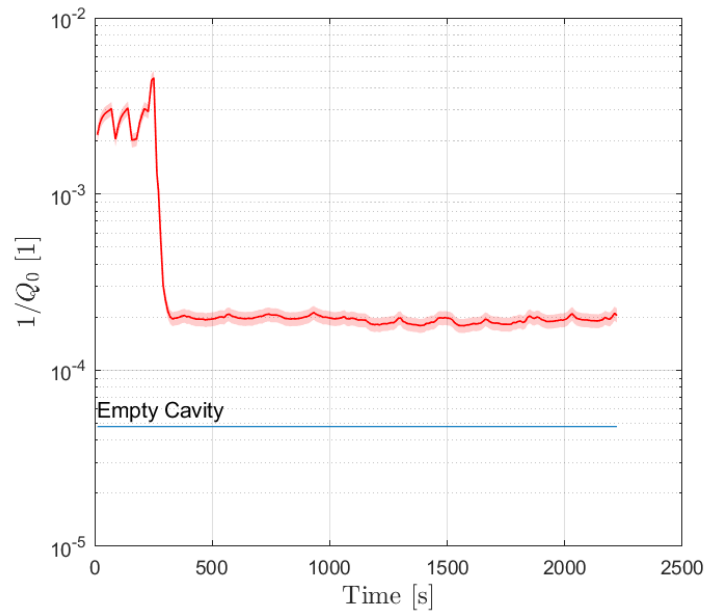


Fig. B.22 Change in system loss during microwave sintering of Ti6Al4V. Data shown is for sample 1.

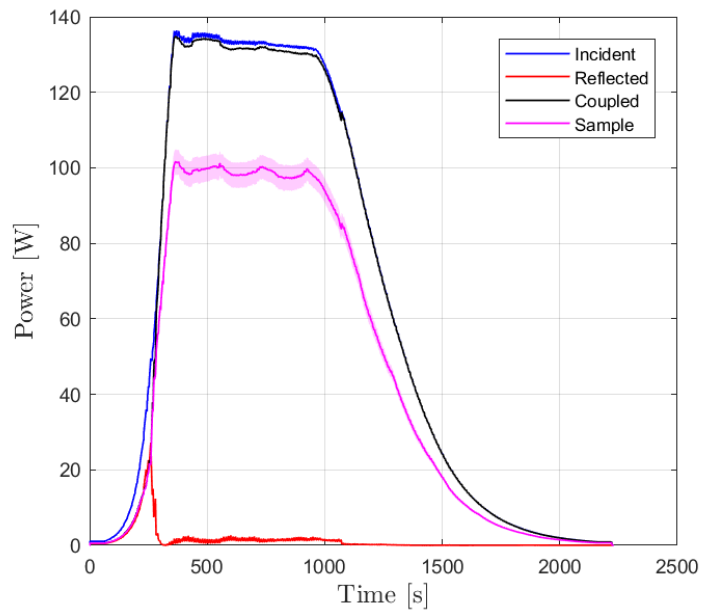


Fig. B.23 Change in delivered power during microwave sintering of Ti6Al4V. Data show is for sample 1.

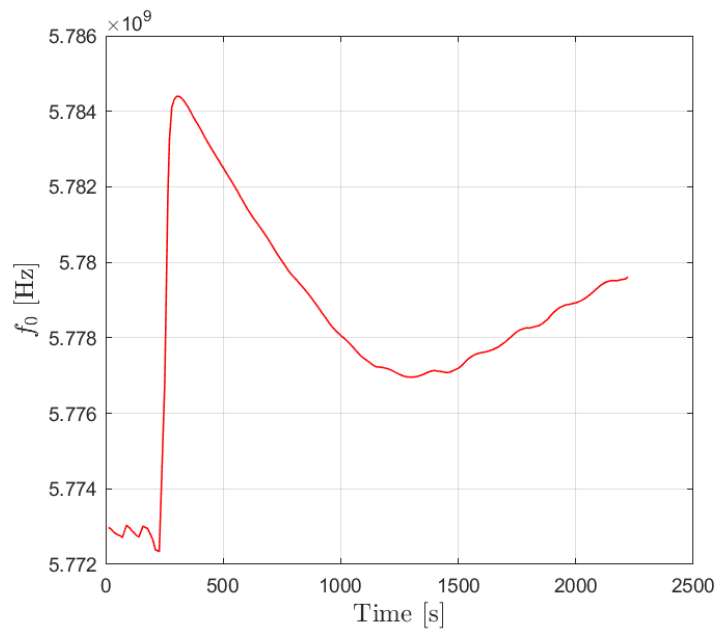


Fig. B.24 Change in resonant frequency during microwave sintering of Ti6Al4V. Data show is for sample 1.

Results for Ti6Al4V - 2

Ti6Al4V powder sealed in quartz capillary tubing in argon.

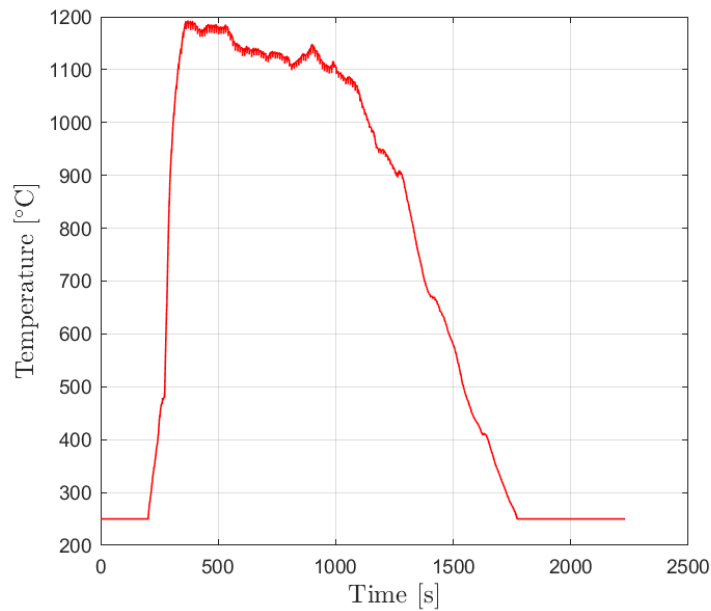


Fig. B.25 Change in sample temperature during microwave sintering of Ti6Al4V. Data shown is for sample 2

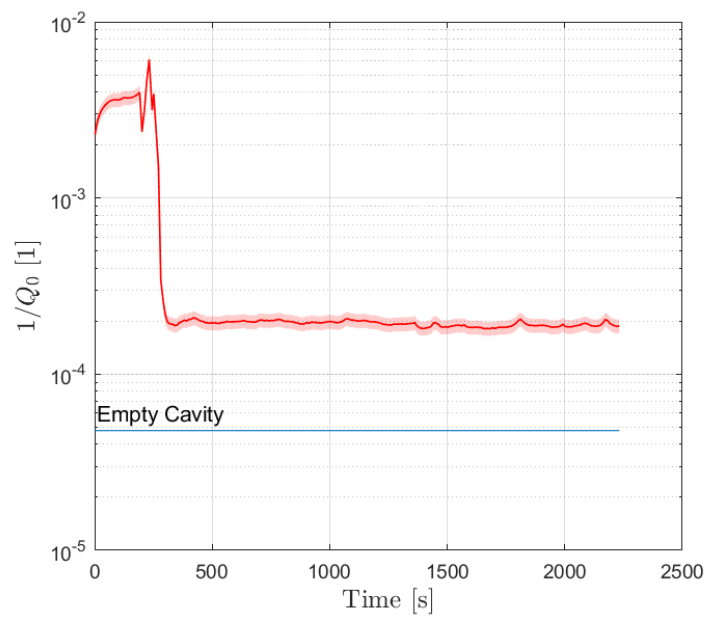


Fig. B.26 Change in system loss during microwave sintering of Ti6Al4V. Data shown is for sample 2.

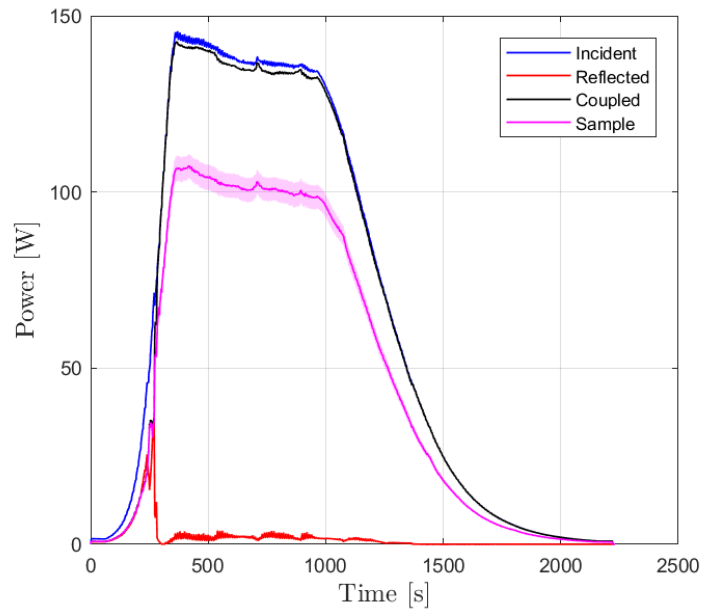


Fig. B.27 Change in delivered power during microwave sintering of Ti6Al4V. Data show is for sample 2.

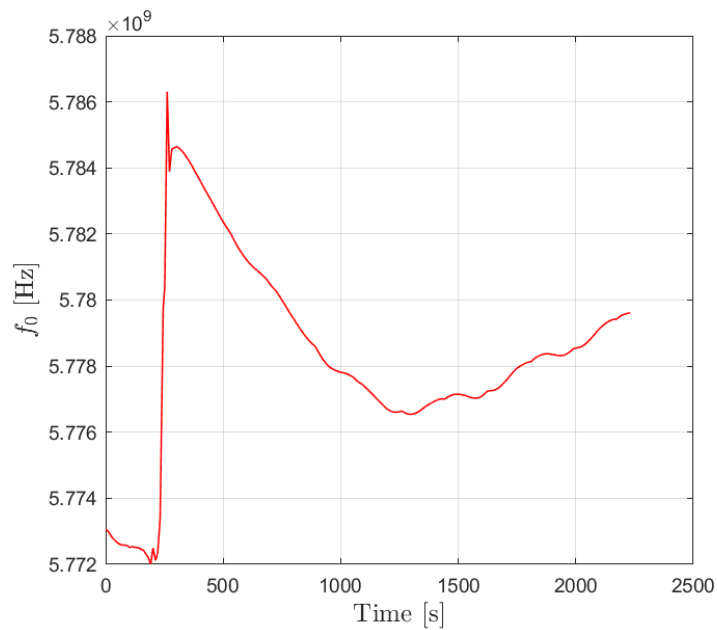


Fig. B.28 Change in resonant frequency during microwave sintering of Ti6Al4V. Data show is for sample 2.

Results for Ti6Al4V - 3

Ti6Al4V powder sealed in quartz capillary tubing in argon.

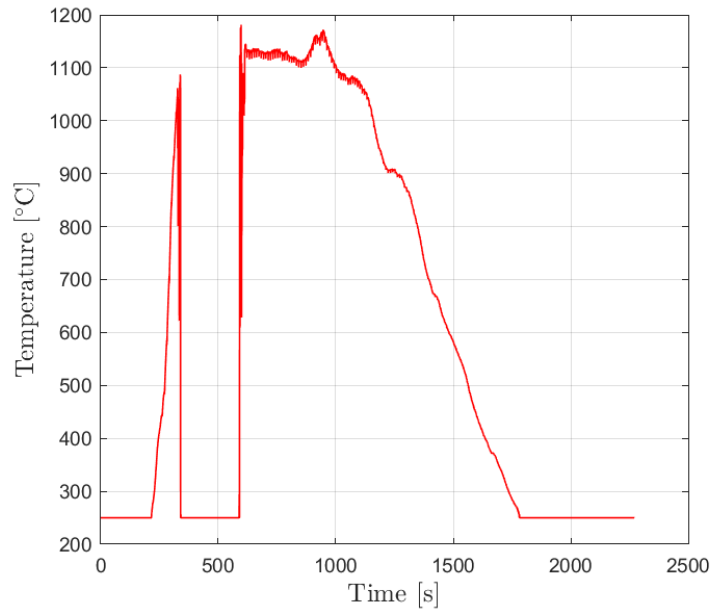


Fig. B.29 Change in sample temperature during microwave sintering of Ti6Al4V. Data shown is for sample 3

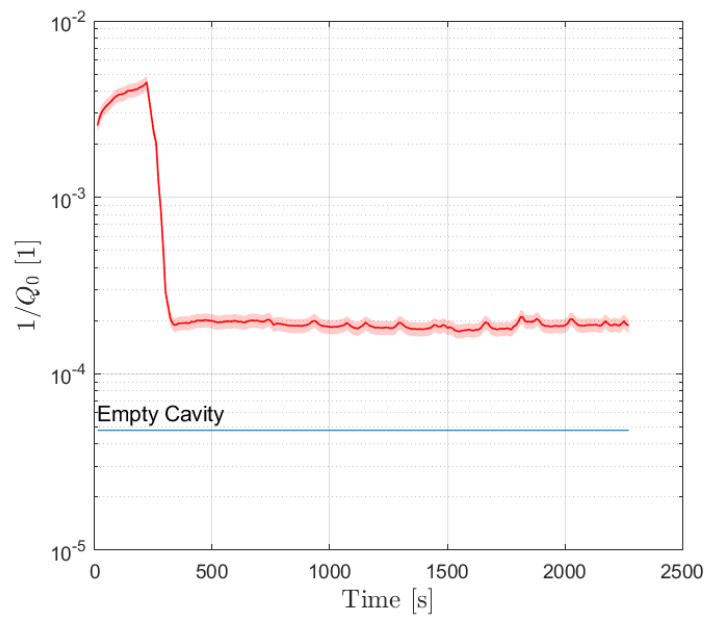


Fig. B.30 Change in system loss during microwave sintering of Ti6Al4V. Data shown is for sample 3.

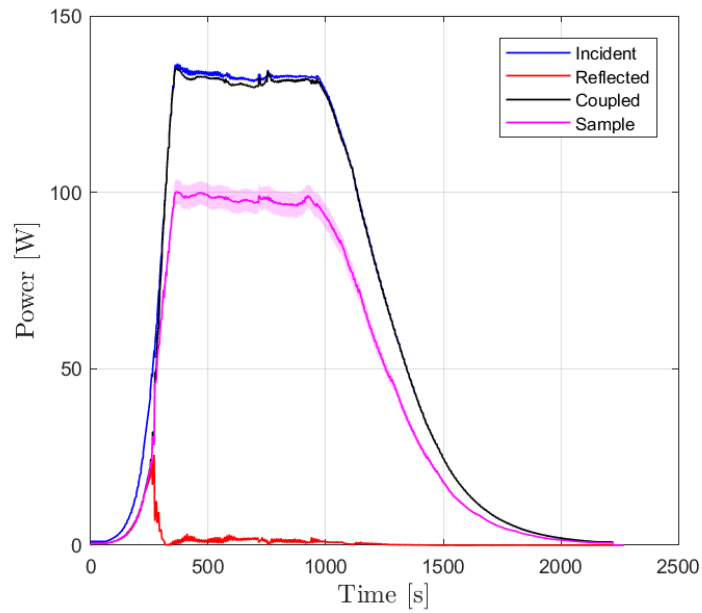


Fig. B.31 Change in delivered power during microwave sintering of Ti6Al4V. Data show is for sample 3.

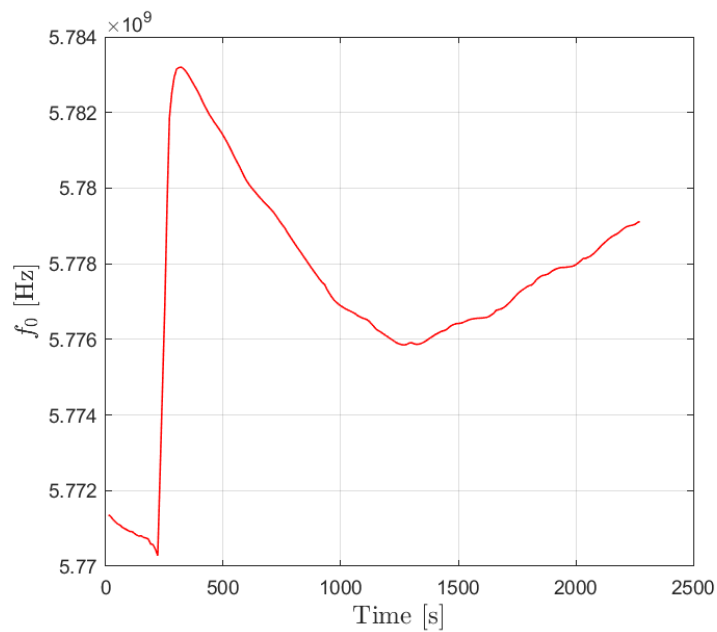


Fig. B.32 Change in resonant frequency during microwave sintering of Ti6Al4V. Data show is for sample 3.

Results for 316L - 1

316L powder sealed in quartz capillary tubing in argon.

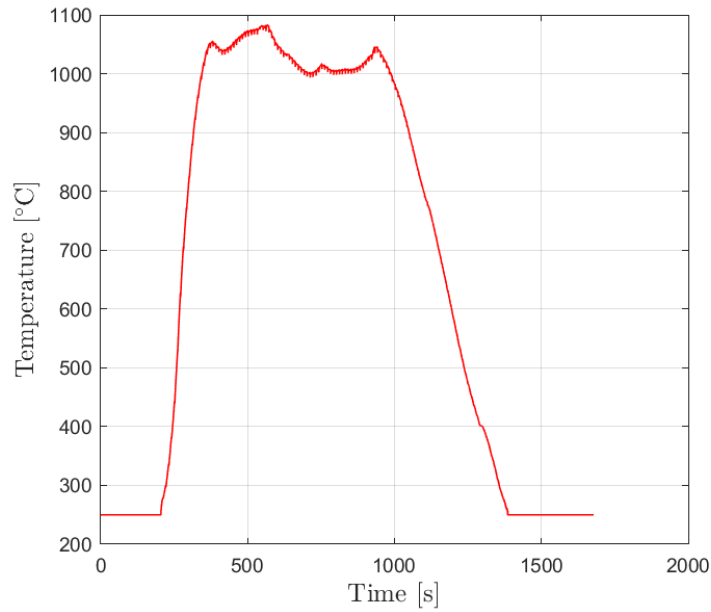


Fig. B.33 Change in sample temperature during microwave sintering of 316L. Data shown is for sample 1

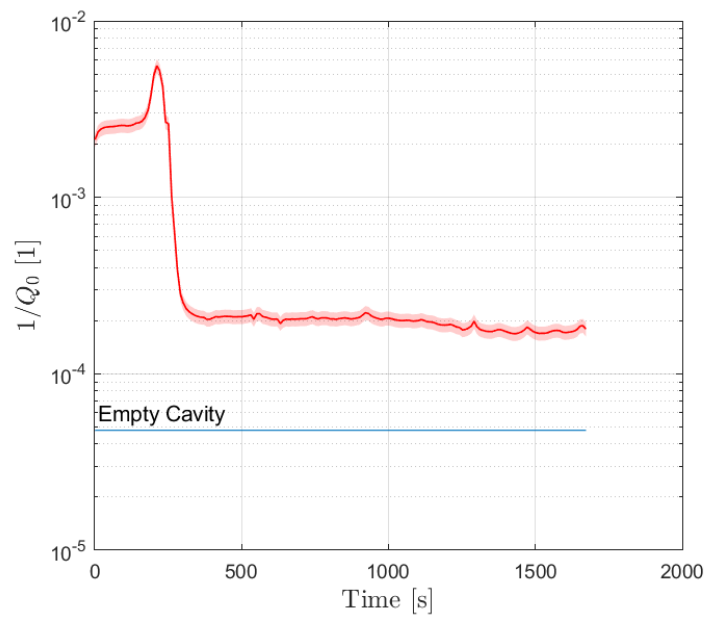


Fig. B.34 Change in system loss during microwave sintering of 316L. Data shown is for sample 1.

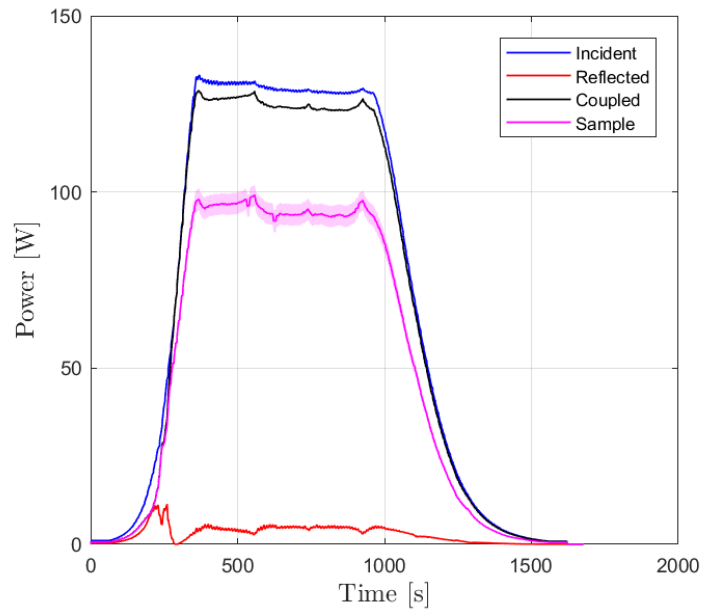


Fig. B.35 Change in delivered power during microwave sintering of 316L. Data show is for sample 1.

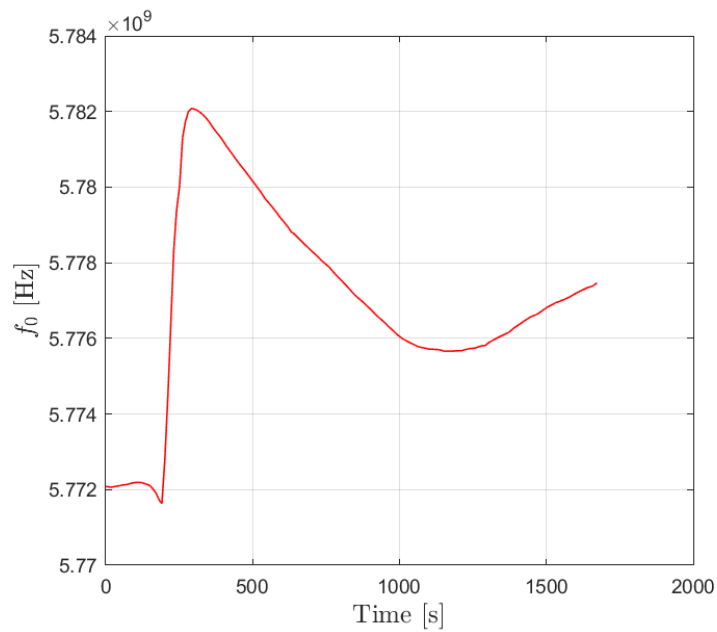


Fig. B.36 Change in resonant frequency during microwave sintering of 316L. Data show is for sample 1.

Results for 316L - 2

316L powder sealed in quartz capillary tubing in argon.

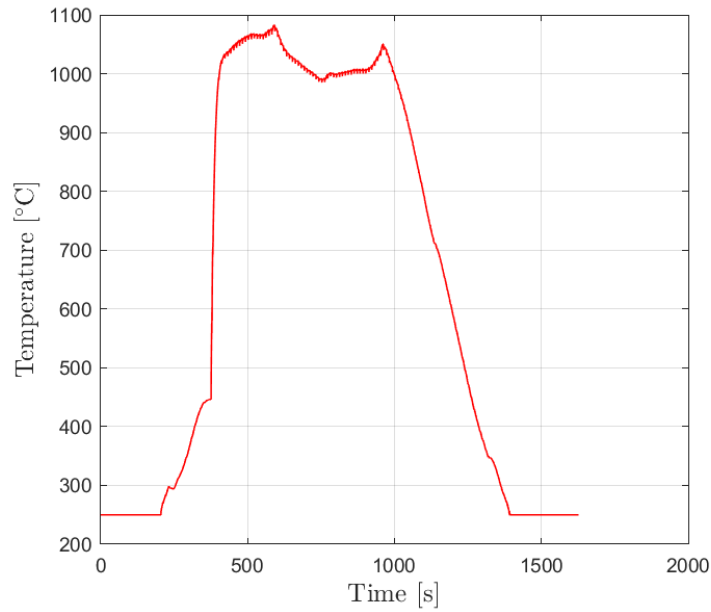


Fig. B.37 Change in sample temperature during microwave sintering of 316L. Data shown is for sample 2

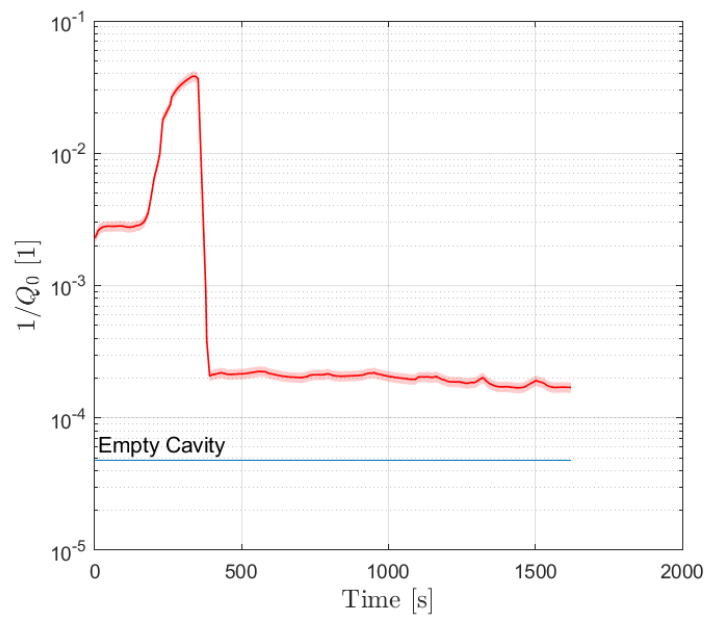


Fig. B.38 Change in system loss during microwave sintering of 316L. Data shown is for sample 2.

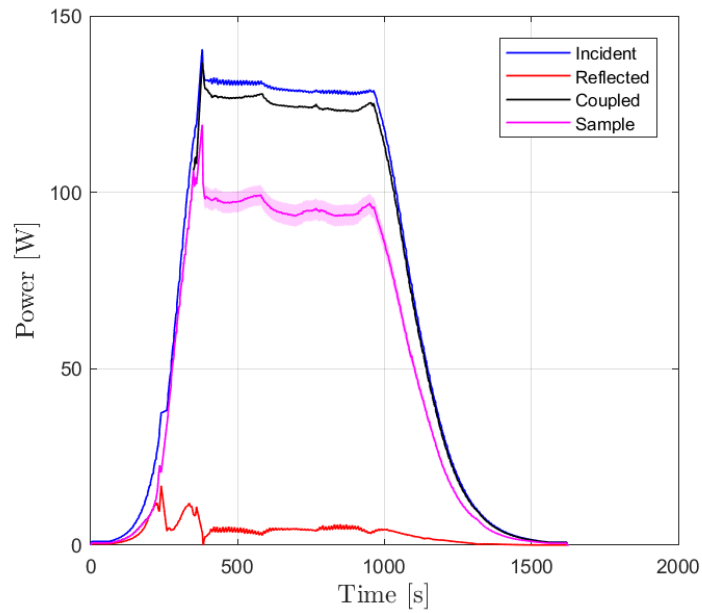


Fig. B.39 Change in delivered power during microwave sintering of 316L. Data show is for sample 2.

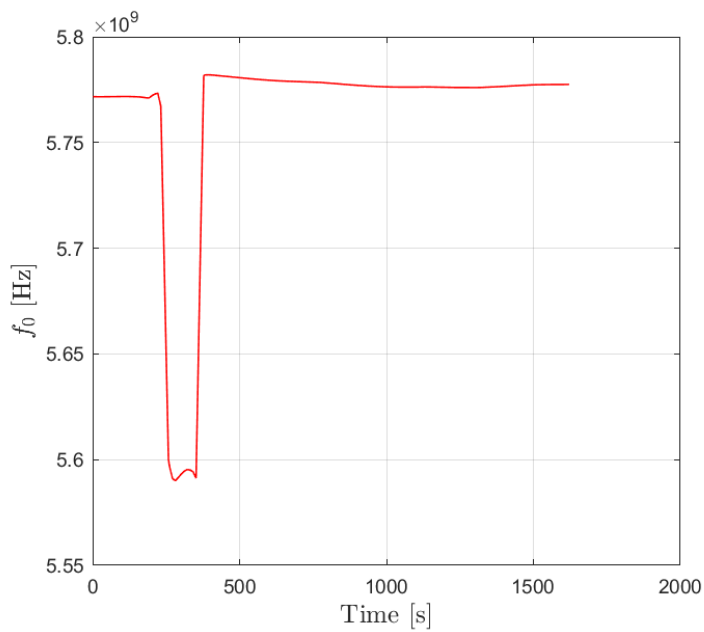


Fig. B.40 Change in resonant frequency during microwave sintering of 316L. Data show is for sample 2.

Results for 316L - 3

316L powder sealed in quartz capillary tubing in argon.

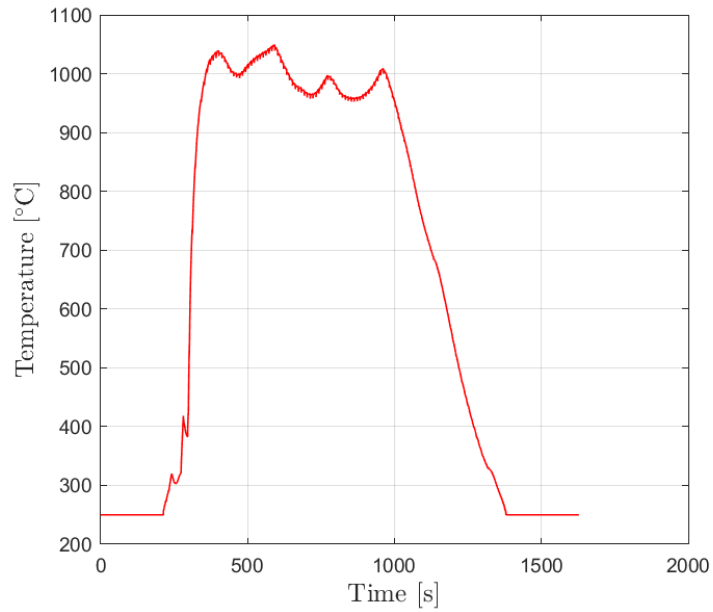


Fig. B.41 Change in sample temperature during microwave sintering of 316L. Data shown is for sample 3

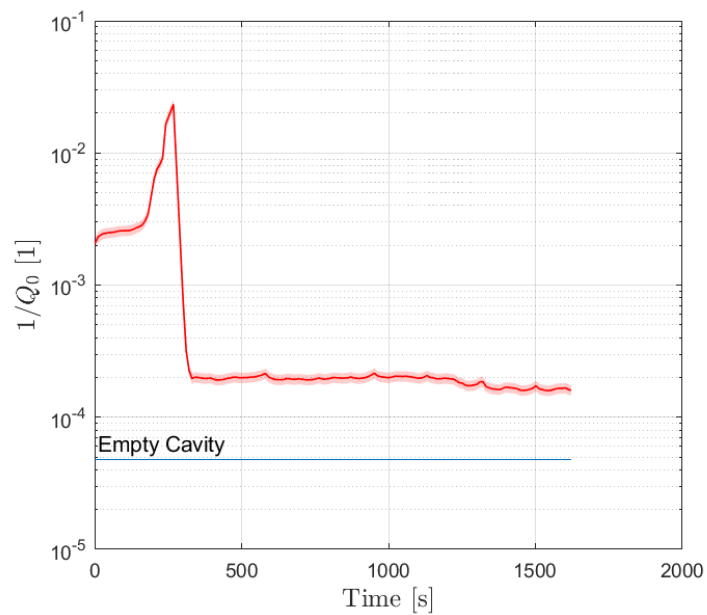


Fig. B.42 Change in system loss during microwave sintering of 316L. Data shown is for sample 3.

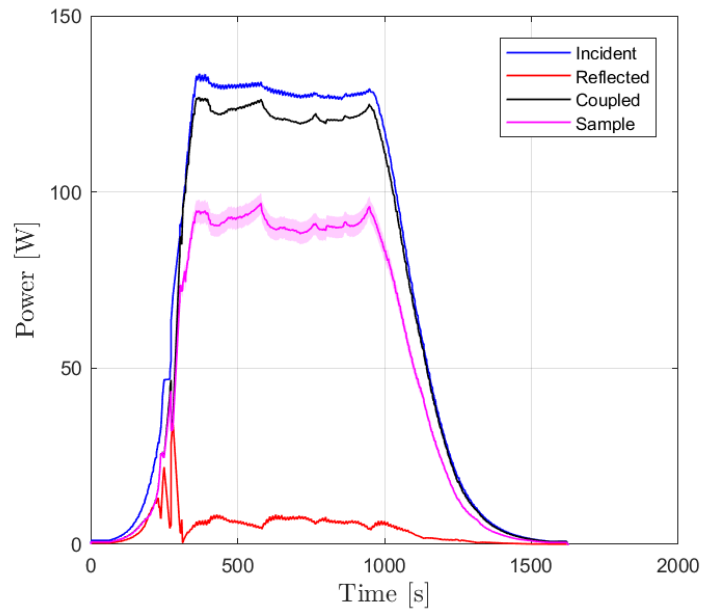


Fig. B.43 Change in delivered power during microwave sintering of 316L. Data show is for sample 3.

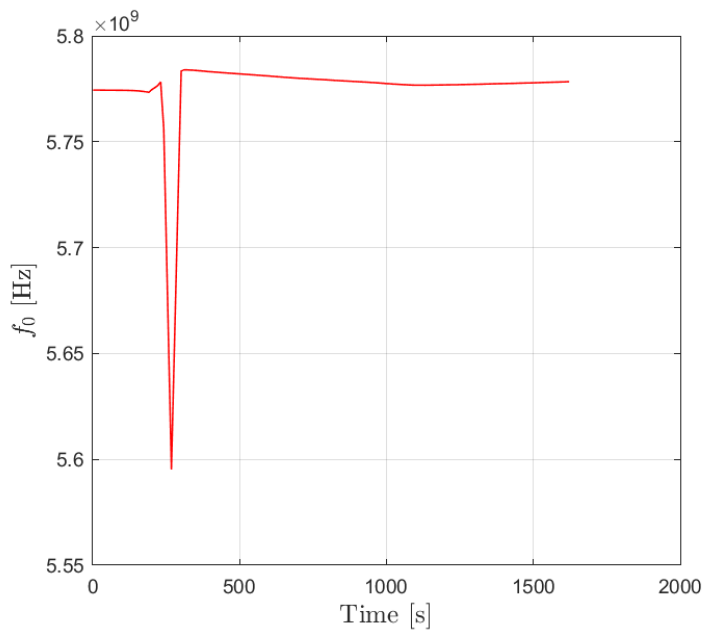


Fig. B.44 Change in resonant frequency during microwave sintering of 316L. Data show is for sample 3.

Results for 247LC - 1

247LC powder sealed in quartz capillary tubing in argon.

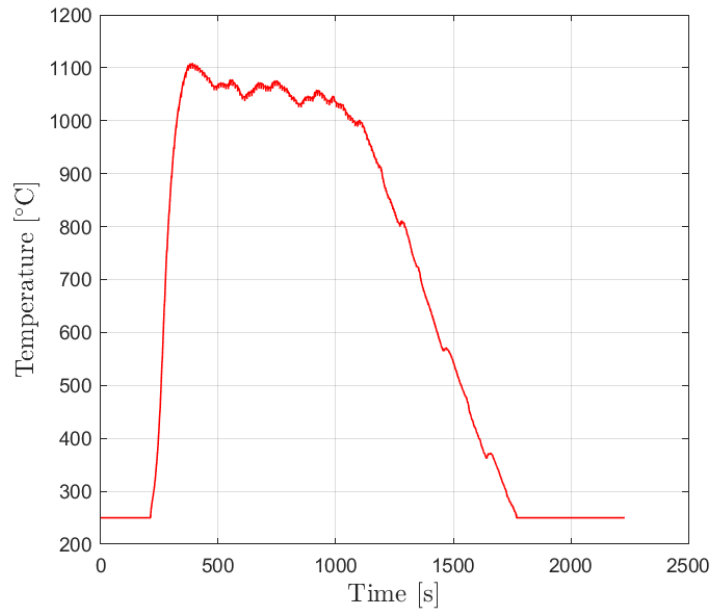


Fig. B.45 Change in sample temperature during microwave sintering of 247LC. Data shown is for sample 1

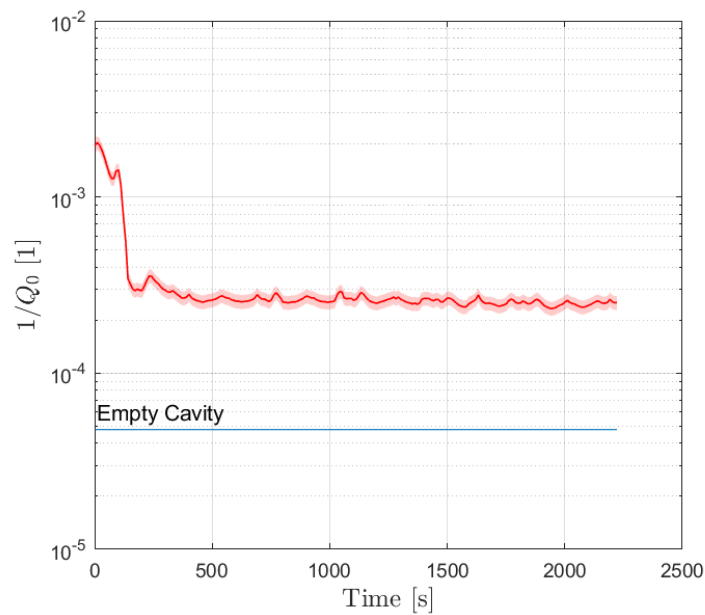


Fig. B.46 Change in system loss during microwave sintering of 247LC. Data shown is for sample 1.

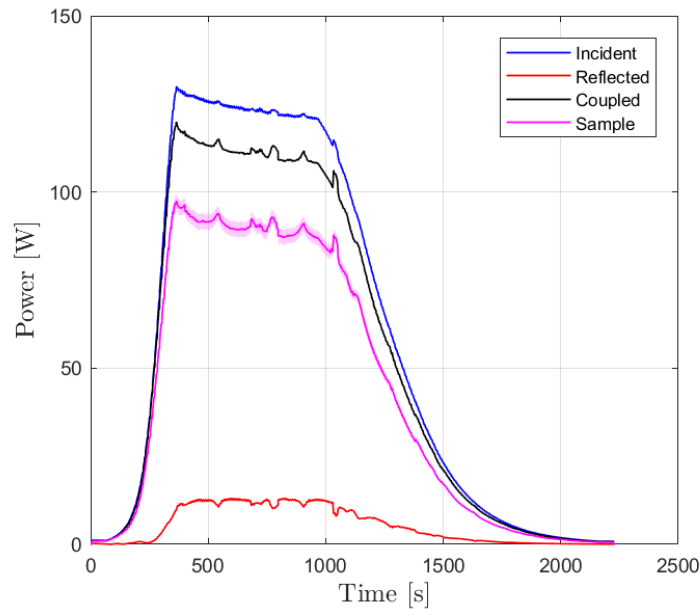


Fig. B.47 Change in delivered power during microwave sintering of 247LC. Data show is for sample 1.

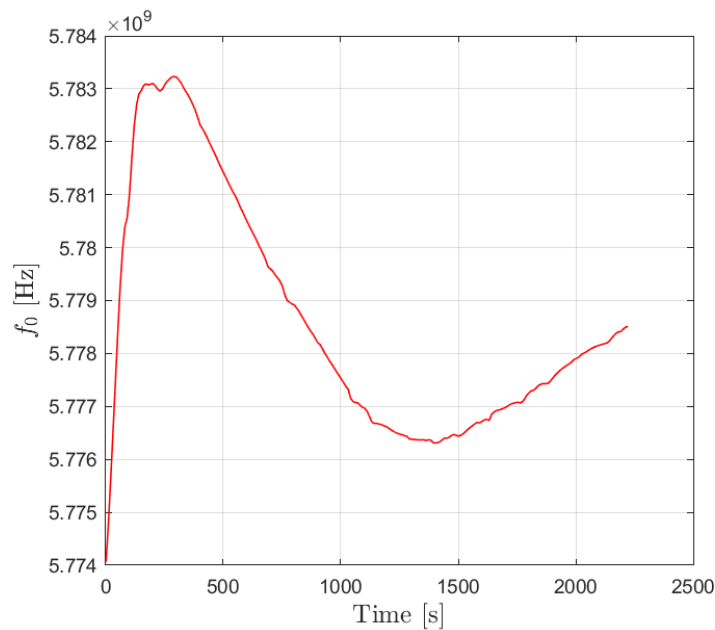


Fig. B.48 Change in resonant frequency during microwave sintering of 247LC. Data show is for sample 1.

Results for 247LC - 2

247LC powder sealed in quartz capillary tubing in argon.

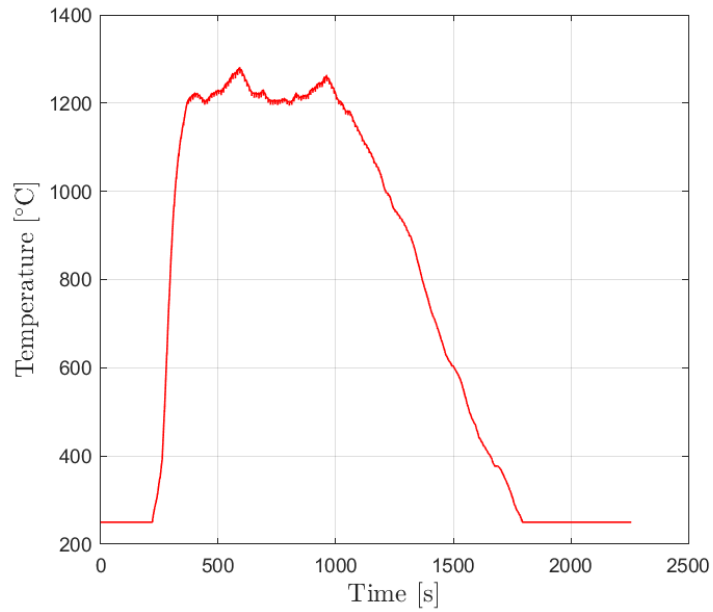


Fig. B.49 Change in sample temperature during microwave sintering of 247LC. Data shown is for sample 2

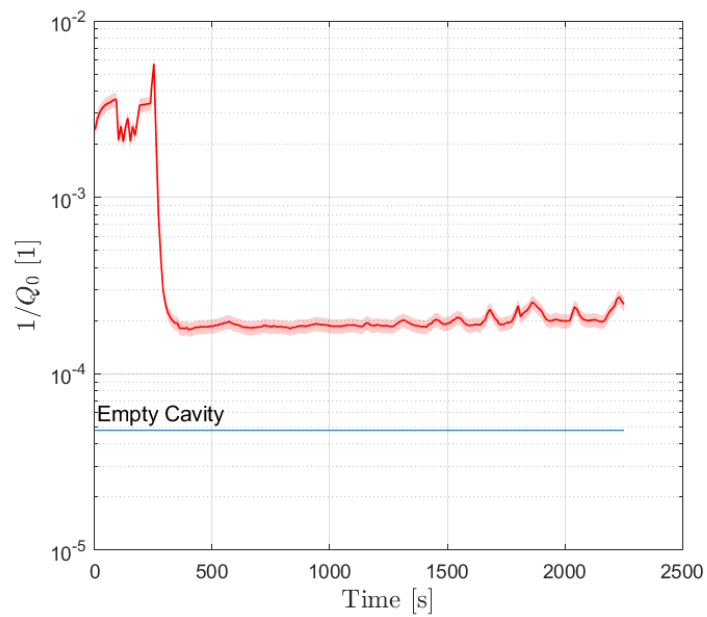


Fig. B.50 Change in system loss during microwave sintering of 247LC. Data shown is for sample 2.

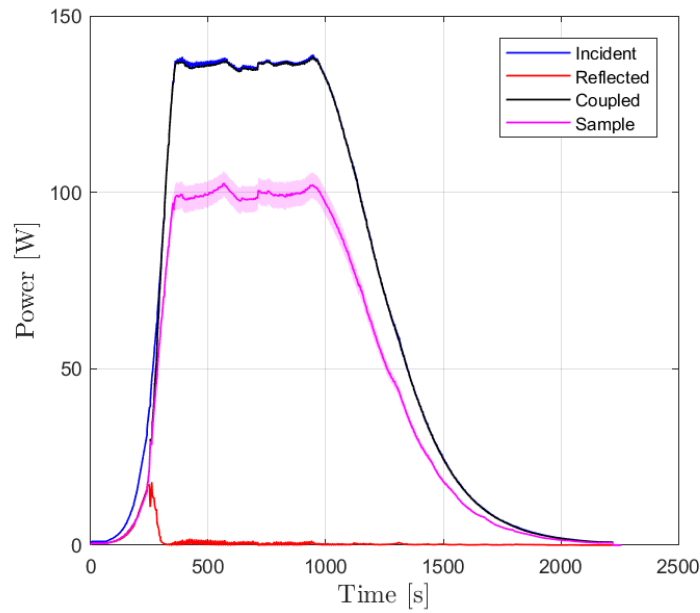


Fig. B.51 Change in delivered power during microwave sintering of 247LC. Data show is for sample 2.

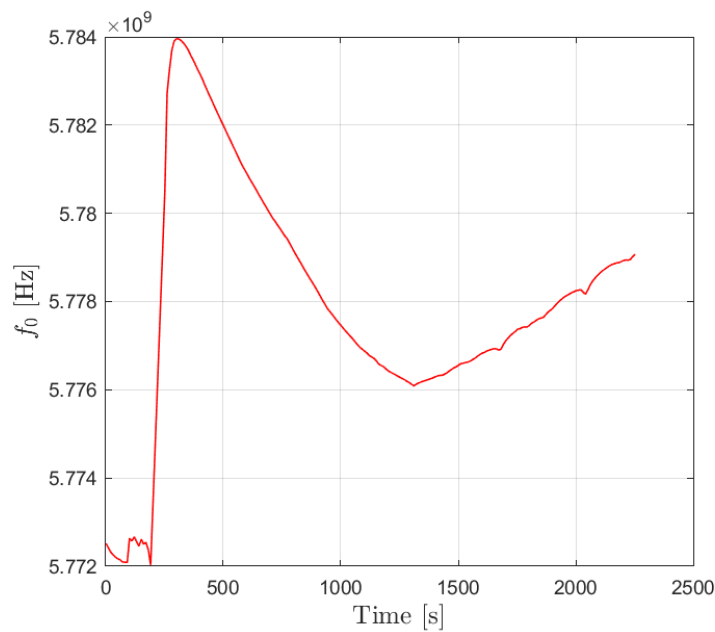


Fig. B.52 Change in resonant frequency during microwave sintering of 247LC. Data show is for sample 2.

Results for 247LC - 3

247LC powder sealed in quartz capillary tubing in argon.

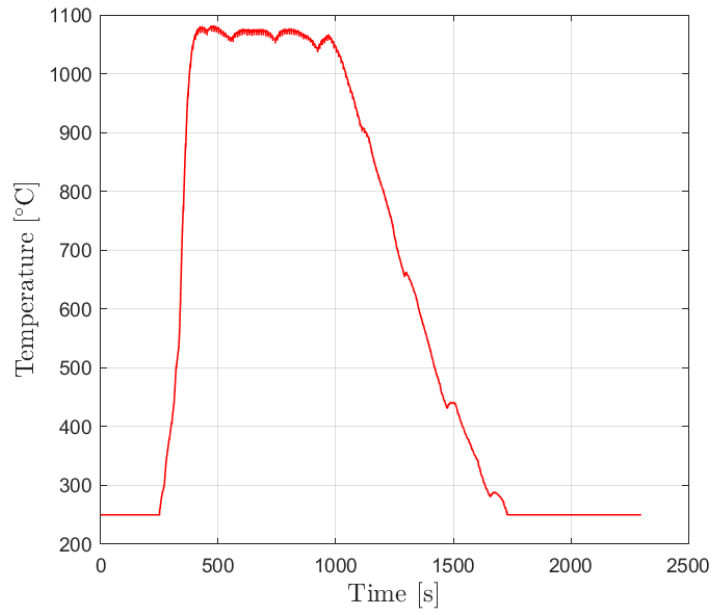


Fig. B.53 Change in sample temperature during microwave sintering of 247LC. Data shown is for sample 3

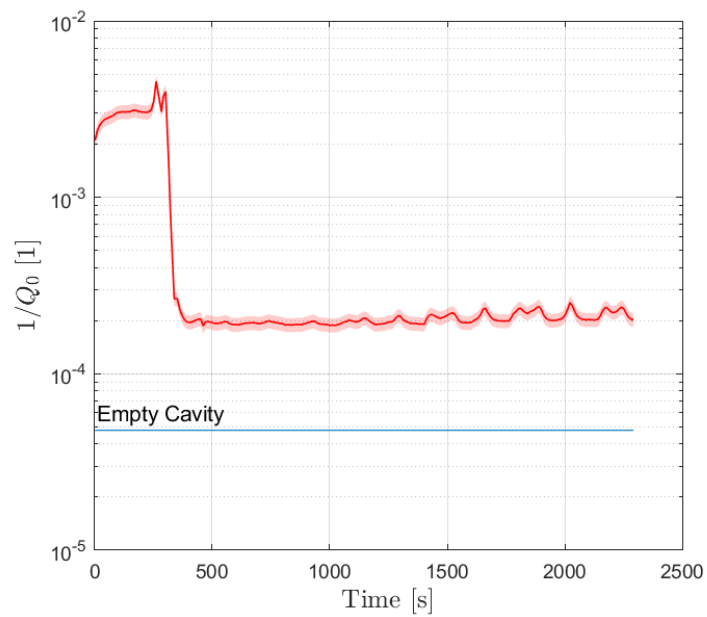


Fig. B.54 Change in system loss during microwave sintering of 247LC. Data shown is for sample 3.

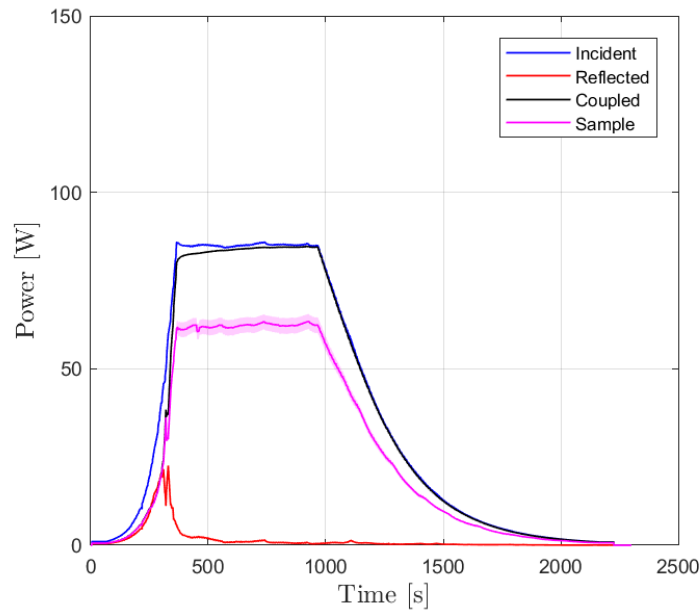


Fig. B.55 Change in delivered power during microwave sintering of 247LC. Data show is for sample 3.

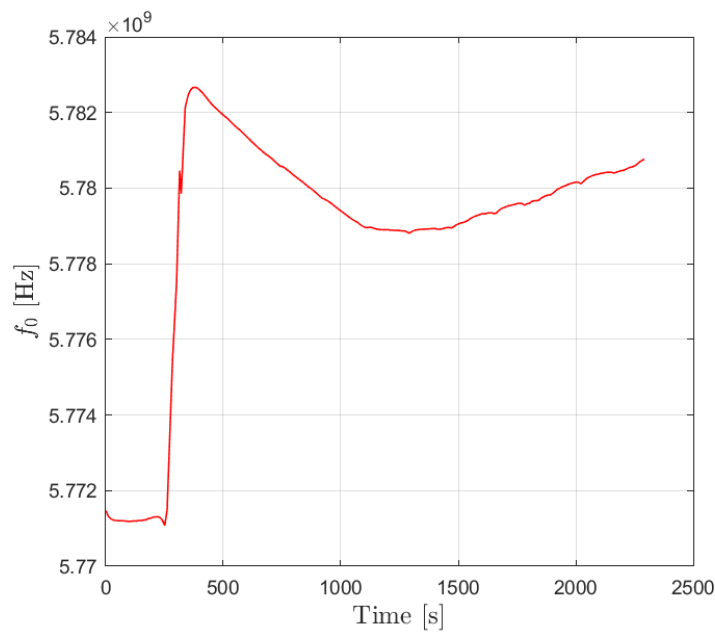


Fig. B.56 Change in resonant frequency during microwave sintering of 247LC. Data show is for sample 3.

Appendix C

Matlab Code for LODR Method

C.1 GEO.m

"GEO.m" is a storage class for the geometric and energy filling factors.

Listing C.1 "GEO.m" Class for Storing Geometric and Energy-Filling Factors for LODRs

```
1 classdef GEO < handle
2 %% CLASS DESCRIPTION
3 % Class used to store geometric and energy-filling factors
4 %% CODE
5 properties
6     x;
7     G_w;    G_b;
8     P_d;    P_r;
9 end
10 methods
11     function obj = GEO(x, G_w, G_b, P_d, P_r)
12         switch nargin
13             case(4)
14                 obj.x    = x;
15                 obj.G_w = G_w;  obj.G_b = G_b;
16                 obj.P_d = P_d;  obj.P_r = [];
17             case(5)
18                 obj.x    = x;
19                 obj.G_w = G_w;  obj.G_b = G_b;
20                 obj.P_d = P_d;  obj.P_r = P_r;
21             otherwise
22                 fprintf('\nNO DATA!\n');
23         end
24     end
25 end
26 end
```

C.2 CAL.m

"CAL.m" is used to perform the calibration function and once complete, can be used to perform R_s measurements using Q_0 measurement data.

Listing C.2 "CAL.m" Class for Performing Calibration and Measurements for LODRs

```

1  classdef CAL < handle
2  %%  CLASS DESCRIPTION
3  %   Class to perform and store results of LODR calibration.
4  %   Also can be used to perform measurements of base Rs.
5  %%  CODE
6  properties
7      x0;    f0;    GEO;
8      Rsw0;  tanDR0; tanR0;
9  end
10 methods
11     function obj = CAL(x0, x, f, Q, GEO, DoFullFit)
12         %%  FUNCTION DESCRIPTION
13         %   Finds loss factors using LSQ curve fitting.
14         %   Calibration equation is fit to Q0 data over x.
15         %   Optionally, a two parameter fit can be performed.
16         %%  CODE
17         %   Dynamic data extension
18         F      = @(X) pchip(x,f,X);
19         G_w    = @(X) pchip(GEO.x,GEO.G_w,X);
20         G_b    = @(X) pchip(GEO.x,GEO.G_b,X);
21         P_d    = @(X) pchip(GEO.x,GEO.P_d,X);
22         P_r    = @(X) pchip(GEO.x,GEO.P_r,X);
23         %   Least-squares curve fitting options
24         LSQ = optimoptions('lsqcurvefit',...
25             'MaxFunEvals',4000,'TolX',1e-5,...
26             'TolFun',1e-5,'Display','off');
27         %   Setup CAL Equation
28         switch DoFullFit
29             case{false}
30                 %   2-Parameter Calibration
31                 caleqn = @(L,X) 1./...

```

```

32         ( L(1)*(G_w(X)...
33         + G_b(X))./(sqrt(F(X)*F(x0)))...
34         + L(2)*P_d(X).*F(X)/F(x0));
35         L0 = [1,1]; L_low = [0,0]; L_upp = [];
36     otherwise
37     % Full Calibration
38         caleqn = @(L,X) 1./...
39         ( L(1)*(G_w(X)...
40         + G_b(X))./(sqrt(F(X)*F(x0)))...
41         + L(2)*P_d(X).*F(X)/F(x0)...
42         + L(3)*P_r(X).*F(X)/F(x0));
43         L0 = [1,1,1]; L_low = [0,0,0]; L_upp = [];
44     end
45     % Perform Calibration by Least-Squares Curve Fitting
46     L = lsqcurvefit(caleqn,L0,x,Q,L_low,L_upp,LSQ);
47     % Assign Values
48     obj.x0 = x0;         obj.f0 = F(x0);
49     obj.Rsw0 = L(1);     obj.tanDR0 = L(2);
50     if length(L) == 3
51         obj.tanR0 = L(3);
52     else
53         obj.tanR0 = 0;
54     end
55     obj.GEO = GEO;
56     % Plot Results of Fit and Output CAL
57     X = linspace(x(1),x(end));
58     plot(x,Q,'ko',X,caleqn(L,X),'b—');
59 end
60 function Rs = Measure(obj, Q, xm, fm)
61     %% FUNCTION DESCRIPTION
62     % Uses CAL data to measure sample Rs from Q0.
63     % Optionally xm and fm can be input to change
64     % the measurement position and give a more accurate
65     % frequency value.
66     %% CODE
67     % Dynamic Data Extension

```

```
68         G_w = @(X) pchip(obj.GEO.x, obj.GEO.G_w, X);
69         G_b = @(X) pchip(obj.GEO.x, obj.GEO.G_b, X);
70         P_d = @(X) pchip(obj.GEO.x, obj.GEO.P_d, X);
71         P_r = @(X) pchip(obj.GEO.x, obj.GEO.P_r, X);
72         % Set measure point and f0
73         if nargin == 4
74             x = xm;
75             f = fm;
76         else
77             x = obj.x0;
78             f = obj.f0;
79         end
80         % Perform Measurement
81         C1 = obj.Rsw0.*G_w(x)./sqrt(obj.f0.*f);
82         D1 = obj.tanDR0.*P_d(x).*f/obj.f0;
83         D2 = obj.tanR0.*P_r(x).*f/obj.f0;
84         Rs = sqrt(obj.f0.*f).*(1./Q-C1-D1-D2)./(G_b(x));
85     end
86 end
87 end
```


Appendix D

Geometric and Energy-Filling Factors for LODRs

D.1 Simulation-Only Models

Table D.1 Geometric and Energy-Filling Factors for Simulated LODR (No Rod)

x [mm]	G_w [A ² /J]	G_b [A ² /J]	P_d [1]	P_r [1]
0.00	1.4714×10^6	1.2938×10^7	9.2796×10^{-1}	-
0.10	1.4855×10^6	1.2585×10^7	9.2855×10^{-1}	-
0.20	1.4995×10^6	1.2248×10^7	9.2911×10^{-1}	-
0.30	1.5140×10^6	1.1887×10^7	9.2963×10^{-1}	-
0.40	1.5288×10^6	1.1496×10^7	9.3010×10^{-1}	-
0.50	1.5442×10^6	1.1118×10^7	9.3053×10^{-1}	-
0.60	1.5598×10^6	1.0700×10^7	9.3090×10^{-1}	-
0.70	1.5759×10^6	1.0293×10^7	9.3122×10^{-1}	-
0.80	1.5927×10^6	9.8795×10^6	9.3149×10^{-1}	-
0.90	1.6097×10^6	9.4765×10^6	9.3171×10^{-1}	-
1.00	1.6268×10^6	9.0768×10^6	9.3188×10^{-1}	-
1.10	1.6442×10^6	8.6850×10^6	9.3200×10^{-1}	-
1.20	1.6627×10^6	8.3269×10^6	9.3207×10^{-1}	-
1.30	1.6814×10^6	7.9896×10^6	9.3211×10^{-1}	-
1.40	1.7002×10^6	7.6674×10^6	9.3210×10^{-1}	-
1.50	1.7193×10^6	7.3265×10^6	9.3206×10^{-1}	-

Continued on next page

Table D.1 – continued from previous page

x [mm]	G_w [A ² /J]	G_b [A ² /J]	p_d [1]	p_r [1]
1.60	1.7392×10^6	6.9922×10^6	9.3198×10^{-1}	-
1.70	1.7587×10^6	6.6769×10^6	9.3187×10^{-1}	-
1.80	1.7790×10^6	6.3686×10^6	9.3174×10^{-1}	-
1.90	1.7988×10^6	6.0805×10^6	9.3157×10^{-1}	-
2.00	1.8195×10^6	5.8056×10^6	9.3139×10^{-1}	-
2.10	1.8398×10^6	5.5343×10^6	9.3118×10^{-1}	-
2.20	1.8606×10^6	5.2771×10^6	9.3096×10^{-1}	-
2.30	1.8814×10^6	5.0360×10^6	9.3072×10^{-1}	-
2.40	1.9021×10^6	4.8066×10^6	9.3046×10^{-1}	-
2.50	1.9234×10^6	4.5876×10^6	9.3019×10^{-1}	-
2.60	1.9441×10^6	4.3762×10^6	9.2992×10^{-1}	-
2.70	1.9653×10^6	4.1816×10^6	9.2963×10^{-1}	-
2.80	1.9860×10^6	3.9855×10^6	9.2934×10^{-1}	-
2.90	2.0070×10^6	3.8066×10^6	9.2904×10^{-1}	-
3.00	2.0276×10^6	3.6317×10^6	9.2874×10^{-1}	-
3.10	2.0483×10^6	3.4639×10^6	9.2843×10^{-1}	-
3.20	2.0690×10^6	3.3030×10^6	9.2812×10^{-1}	-
3.30	2.0898×10^6	3.1535×10^6	9.2781×10^{-1}	-
3.40	2.1104×10^6	3.0093×10^6	9.2750×10^{-1}	-
3.50	2.1307×10^6	2.8729×10^6	9.2720×10^{-1}	-
3.60	2.1515×10^6	2.7418×10^6	9.2689×10^{-1}	-
3.70	2.1713×10^6	2.6170×10^6	9.2658×10^{-1}	-
3.80	2.1911×10^6	2.4988×10^6	9.2628×10^{-1}	-
3.90	2.2114×10^6	2.3852×10^6	9.2599×10^{-1}	-
4.00	2.2310×10^6	2.2798×10^6	9.2569×10^{-1}	-
4.10	2.2508×10^6	2.1731×10^6	9.2540×10^{-1}	-
4.20	2.2701×10^6	2.0782×10^6	9.2512×10^{-1}	-
4.30	2.2895×10^6	1.9844×10^6	9.2484×10^{-1}	-
4.40	2.3084×10^6	1.8954×10^6	9.2457×10^{-1}	-
4.50	2.3277×10^6	1.8129×10^6	9.2431×10^{-1}	-
4.60	2.3465×10^6	1.7323×10^6	9.2405×10^{-1}	-
4.70	2.3652×10^6	1.6553×10^6	9.2380×10^{-1}	-

Continued on next page

Table D.1 – continued from previous page

x [mm]	G_w [A ² /J]	G_b [A ² /J]	p_d [1]	p_r [1]
4.80	2.3838×10^6	1.5808×10^6	9.2356×10^{-1}	-
4.90	2.4024×10^6	1.5121×10^6	9.2332×10^{-1}	-
5.00	2.4207×10^6	1.4463×10^6	9.2309×10^{-1}	-

Table D.2 Geometric and Energy-Filling Factors for Simulated LODR (PTFE Rod)

x [mm]	G_w [A ² /J]	G_b [A ² /J]	P_d [1]	P_r [1]
0.00	1.4908×10^6	1.2881×10^7	9.2408×10^{-1}	4.3703×10^{-3}
0.10	1.5022×10^6	1.2516×10^7	9.2482×10^{-1}	4.2690×10^{-3}
0.20	1.5166×10^6	1.2165×10^7	9.2546×10^{-1}	4.1620×10^{-3}
0.30	1.5314×10^6	1.1826×10^7	9.2605×10^{-1}	4.0594×10^{-3}
0.40	1.5460×10^6	1.1451×10^7	9.2659×10^{-1}	3.9617×10^{-3}
0.50	1.5616×10^6	1.1049×10^7	9.2707×10^{-1}	3.8687×10^{-3}
0.60	1.5770×10^6	1.0659×10^7	9.2751×10^{-1}	3.7806×10^{-3}
0.70	1.5931×10^6	1.0247×10^7	9.2788×10^{-1}	3.6972×10^{-3}
0.80	1.6096×10^6	9.8787×10^6	9.2821×10^{-1}	3.6183×10^{-3}
0.90	1.6267×10^6	9.4643×10^6	9.2848×10^{-1}	3.5436×10^{-3}
1.00	1.6443×10^6	9.0606×10^6	9.2869×10^{-1}	3.4732×10^{-3}
1.10	1.6621×10^6	8.6860×10^6	9.2886×10^{-1}	3.4067×10^{-3}
1.20	1.6801×10^6	8.3364×10^6	9.2898×10^{-1}	3.3440×10^{-3}
1.30	1.6987×10^6	7.9798×10^6	9.2905×10^{-1}	3.2848×10^{-3}
1.40	1.7179×10^6	7.6281×10^6	9.2909×10^{-1}	3.2290×10^{-3}
1.50	1.7369×10^6	7.2967×10^6	9.2908×10^{-1}	3.1763×10^{-3}
1.60	1.7565×10^6	6.9671×10^6	9.2904×10^{-1}	3.1267×10^{-3}
1.70	1.7763×10^6	6.6511×10^6	9.2896×10^{-1}	3.0797×10^{-3}
1.80	1.7964×10^6	6.3473×10^6	9.2885×10^{-1}	3.0356×10^{-3}
1.90	1.8170×10^6	6.0564×10^6	9.2872×10^{-1}	2.9936×10^{-3}
2.00	1.8371×10^6	5.7819×10^6	9.2856×10^{-1}	2.9540×10^{-3}
2.10	1.8579×10^6	5.5140×10^6	9.2838×10^{-1}	2.9165×10^{-3}
2.20	1.8787×10^6	5.2588×10^6	9.2818×10^{-1}	2.8810×10^{-3}
2.30	1.8991×10^6	5.0264×10^6	9.2796×10^{-1}	2.8473×10^{-3}
2.40	1.9201×10^6	4.7967×10^6	9.2773×10^{-1}	2.8153×10^{-3}
2.50	1.9412×10^6	4.5742×10^6	9.2748×10^{-1}	2.7849×10^{-3}
2.60	1.9620×10^6	4.3648×10^6	9.2723×10^{-1}	2.7562×10^{-3}
2.70	1.9833×10^6	4.1657×10^6	9.2696×10^{-1}	2.7285×10^{-3}
2.80	2.0042×10^6	3.9788×10^6	9.2668×10^{-1}	2.7022×10^{-3}
2.90	2.0249×10^6	3.7990×10^6	9.2640×10^{-1}	2.6771×10^{-3}
3.00	2.0457×10^6	3.6206×10^6	9.2612×10^{-1}	2.6531×10^{-3}

Continued on next page

Table D.2 – continued from previous page

x [mm]	G_w [A ² /J]	G_b [A ² /J]	p_d [1]	p_r [1]
3.10	2.0672×10^6	3.4587×10^6	9.2583×10^{-1}	2.6301×10^{-3}
3.20	2.0874×10^6	3.3002×10^6	9.2554×10^{-1}	2.6083×10^{-3}
3.30	2.1087×10^6	3.1468×10^6	9.2524×10^{-1}	2.5870×10^{-3}
3.40	2.1292×10^6	3.0044×10^6	9.2495×10^{-1}	2.5667×10^{-3}
3.50	2.1496×10^6	2.8683×10^6	9.2466×10^{-1}	2.5472×10^{-3}
3.60	2.1698×10^6	2.7400×10^6	9.2436×10^{-1}	2.5284×10^{-3}
3.70	2.1902×10^6	2.6137×10^6	9.2407×10^{-1}	2.5103×10^{-3}
3.80	2.2103×10^6	2.4967×10^6	9.2379×10^{-1}	2.4928×10^{-3}
3.90	2.2298×10^6	2.3840×10^6	9.2350×10^{-1}	2.4758×10^{-3}
4.00	2.2501×10^6	2.2749×10^6	9.2322×10^{-1}	2.4593×10^{-3}
4.10	2.2696×10^6	2.1737×10^6	9.2295×10^{-1}	2.4434×10^{-3}
4.20	2.2894×10^6	2.0752×10^6	9.2268×10^{-1}	2.4279×10^{-3}
4.30	2.3086×10^6	1.9833×10^6	9.2241×10^{-1}	2.4128×10^{-3}
4.40	2.3279×10^6	1.8964×10^6	9.2215×10^{-1}	2.3979×10^{-3}
4.50	2.3469×10^6	1.8121×10^6	9.2190×10^{-1}	2.3836×10^{-3}
4.60	2.3661×10^6	1.7319×10^6	9.2165×10^{-1}	2.3695×10^{-3}
4.70	2.3846×10^6	1.6549×10^6	9.2141×10^{-1}	2.3557×10^{-3}
4.80	2.4037×10^6	1.5824×10^6	9.2118×10^{-1}	2.3420×10^{-3}
4.90	2.4221×10^6	1.5123×10^6	9.2096×10^{-1}	2.3286×10^{-3}
5.00	2.4404×10^6	1.4456×10^6	9.2074×10^{-1}	2.3155×10^{-3}

Table D.3 Geometric and Energy-Filling Factors for Simulated LODR (Nylon Rod)

x [mm]	G_w [A ² /J]	G_b [A ² /J]	P_d [1]	P_r [1]
0.00	1.4925×10^6	1.2816×10^7	9.2123×10^{-1}	7.4937×10^{-3}
0.10	1.5057×10^6	1.2460×10^7	9.2197×10^{-1}	7.3185×10^{-3}
0.20	1.5199×10^6	1.2111×10^7	9.2267×10^{-1}	7.1495×10^{-3}
0.30	1.5347×10^6	1.1774×10^7	9.2332×10^{-1}	6.9871×10^{-3}
0.40	1.5492×10^6	1.1401×10^7	9.2392×10^{-1}	6.8323×10^{-3}
0.50	1.5647×10^6	1.1002×10^7	9.2447×10^{-1}	6.6844×10^{-3}
0.60	1.5801×10^6	1.0615×10^7	9.2496×10^{-1}	6.5440×10^{-3}
0.70	1.5961×10^6	1.0205×10^7	9.2539×10^{-1}	6.4108×10^{-3}
0.80	1.6125×10^6	9.8390×10^6	9.2576×10^{-1}	6.2845×10^{-3}
0.90	1.6295×10^6	9.4270×10^6	9.2608×10^{-1}	6.1648×10^{-3}
1.00	1.6470×10^6	9.0254×10^6	9.2634×10^{-1}	6.0516×10^{-3}
1.10	1.6647×10^6	8.6528×10^6	9.2656×10^{-1}	5.9447×10^{-3}
1.20	1.6826×10^6	8.3051×10^6	9.2672×10^{-1}	5.8434×10^{-3}
1.30	1.7012×10^6	7.9502×10^6	9.2683×10^{-1}	5.7480×10^{-3}
1.40	1.7203×10^6	7.6003×10^6	9.2690×10^{-1}	5.6575×10^{-3}
1.50	1.7393×10^6	7.2705×10^6	9.2693×10^{-1}	5.5722×10^{-3}
1.60	1.7588×10^6	6.9424×10^6	9.2693×10^{-1}	5.4916×10^{-3}
1.70	1.7785×10^6	6.6278×10^6	9.2689×10^{-1}	5.4154×10^{-3}
1.80	1.7985×10^6	6.3254×10^6	9.2681×10^{-1}	5.3435×10^{-3}
1.90	1.8191×10^6	6.0356×10^6	9.2671×10^{-1}	5.2752×10^{-3}
2.00	1.8391×10^6	5.7623×10^6	9.2658×10^{-1}	5.2106×10^{-3}
2.10	1.8598×10^6	5.4955×10^6	9.2643×10^{-1}	5.1494×10^{-3}
2.20	1.8806×10^6	5.2413×10^6	9.2625×10^{-1}	5.0915×10^{-3}
2.30	1.9009×10^6	5.0098×10^6	9.2606×10^{-1}	5.0366×10^{-3}
2.40	1.9219×10^6	4.7810×10^6	9.2585×10^{-1}	4.9843×10^{-3}
2.50	1.9429×10^6	4.5593×10^6	9.2563×10^{-1}	4.9347×10^{-3}
2.60	1.9637×10^6	4.3507×10^6	9.2540×10^{-1}	4.8876×10^{-3}
2.70	1.9849×10^6	4.1523×10^6	9.2515×10^{-1}	4.8423×10^{-3}
2.80	2.0058×10^6	3.9660×10^6	9.2490×10^{-1}	4.7994×10^{-3}
2.90	2.0264×10^6	3.7869×10^6	9.2464×10^{-1}	4.7584×10^{-3}
3.00	2.0472×10^6	3.6091×10^6	9.2437×10^{-1}	4.7193×10^{-3}

Continued on next page

Table D.3 – continued from previous page

x [mm]	G_w [A ² /J]	G_b [A ² /J]	p_d [1]	p_r [1]
3.10	2.0687×10^6	3.4477×10^6	9.2410×10^{-1}	4.6818×10^{-3}
3.20	2.0889×10^6	3.2898×10^6	9.2382×10^{-1}	4.6461×10^{-3}
3.30	2.1101×10^6	3.1369×10^6	9.2355×10^{-1}	4.6114×10^{-3}
3.40	2.1306×10^6	2.9949×10^6	9.2327×10^{-1}	4.5783×10^{-3}
3.50	2.1509×10^6	2.8593×10^6	9.2299×10^{-1}	4.5467×10^{-3}
3.60	2.1711×10^6	2.7314×10^6	9.2271×10^{-1}	4.5160×10^{-3}
3.70	2.1916×10^6	2.6055×10^6	9.2244×10^{-1}	4.4867×10^{-3}
3.80	2.2116×10^6	2.4889×10^6	9.2216×10^{-1}	4.4583×10^{-3}
3.90	2.2311×10^6	2.3766×10^6	9.2189×10^{-1}	4.4308×10^{-3}
4.00	2.2514×10^6	2.2678×10^6	9.2162×10^{-1}	4.4041×10^{-3}
4.10	2.2709×10^6	2.1670×10^6	9.2136×10^{-1}	4.3786×10^{-3}
4.20	2.2907×10^6	2.0688×10^6	9.2110×10^{-1}	4.3535×10^{-3}
4.30	2.3100×10^6	1.9771×10^6	9.2085×10^{-1}	4.3292×10^{-3}
4.40	2.3292×10^6	1.8905×10^6	9.2060×10^{-1}	4.3054×10^{-3}
4.50	2.3482×10^6	1.8065×10^6	9.2035×10^{-1}	4.2824×10^{-3}
4.60	2.3675×10^6	1.7265×10^6	9.2012×10^{-1}	4.2599×10^{-3}
4.70	2.3860×10^6	1.6498×10^6	9.1989×10^{-1}	4.2379×10^{-3}
4.80	2.4051×10^6	1.5774×10^6	9.1967×10^{-1}	4.2161×10^{-3}
4.90	2.4235×10^6	1.5076×10^6	9.1945×10^{-1}	4.1948×10^{-3}
5.00	2.4419×10^6	1.4411×10^6	9.1924×10^{-1}	4.1740×10^{-3}

D.2 First Prototype Design "Boromir"

Table D.4 Geometric and Energy-Filling Factors for Prototype LODR "Boromir"

x [mm]	G_w [A ² /J]	G_b [A ² /J]	p_d [1]	p_r [1]
0.00	1.6186×10^6	9.4769×10^6	9.4127×10^{-1}	1.3742×10^{-3}
0.10	1.6300×10^6	9.2815×10^6	9.4166×10^{-1}	1.3572×10^{-3}
0.20	1.6430×10^6	9.0942×10^6	9.4205×10^{-1}	1.3404×10^{-3}
0.30	1.6580×10^6	8.8968×10^6	9.4244×10^{-1}	1.3237×10^{-3}
0.40	1.6686×10^6	8.6895×10^6	9.4279×10^{-1}	1.3078×10^{-3}
0.50	1.6868×10^6	8.4724×10^6	9.4312×10^{-1}	1.2923×10^{-3}
0.60	1.6963×10^6	8.2556×10^6	9.4340×10^{-1}	1.2775×10^{-3}
0.70	1.7106×10^6	8.0332×10^6	9.4368×10^{-1}	1.2630×10^{-3}
0.80	1.7273×10^6	7.8110×10^6	9.4396×10^{-1}	1.2485×10^{-3}
0.90	1.7386×10^6	7.5656×10^6	9.4417×10^{-1}	1.2353×10^{-3}
1.00	1.7535×10^6	7.3310×10^6	9.4440×10^{-1}	1.2218×10^{-3}
1.10	1.7665×10^6	7.1049×10^6	9.4458×10^{-1}	1.2091×10^{-3}
1.20	1.7836×10^6	6.8906×10^6	9.4470×10^{-1}	1.1974×10^{-3}
1.30	1.7961×10^6	6.6687×10^6	9.4487×10^{-1}	1.1851×10^{-3}
1.40	1.8125×10^6	6.4615×10^6	9.4494×10^{-1}	1.1743×10^{-3}
1.50	1.8256×10^6	6.2487×10^6	9.4506×10^{-1}	1.1629×10^{-3}
1.60	1.8410×10^6	6.0363×10^6	9.4512×10^{-1}	1.1524×10^{-3}
1.70	1.8546×10^6	5.8339×10^6	9.4512×10^{-1}	1.1428×10^{-3}
1.80	1.8752×10^6	5.6253×10^6	9.4519×10^{-1}	1.1326×10^{-3}
1.90	1.8884×10^6	5.4293×10^6	9.4514×10^{-1}	1.1238×10^{-3}
2.00	1.9036×10^6	5.2353×10^6	9.4518×10^{-1}	1.1142×10^{-3}
2.10	1.9192×10^6	5.0477×10^6	9.4515×10^{-1}	1.1056×10^{-3}
2.20	1.9348×10^6	4.8660×10^6	9.4505×10^{-1}	1.0979×10^{-3}
2.30	1.9507×10^6	4.6864×10^6	9.4505×10^{-1}	1.0893×10^{-3}
2.40	1.9658×10^6	4.5166×10^6	9.4492×10^{-1}	1.0822×10^{-3}
2.50	1.9843×10^6	4.3502×10^6	9.4489×10^{-1}	1.0742×10^{-3}
2.60	2.0003×10^6	4.1904×10^6	9.4480×10^{-1}	1.0670×10^{-3}
2.70	2.0182×10^6	4.0429×10^6	9.4463×10^{-1}	1.0608×10^{-3}
2.80	2.0314×10^6	3.8991×10^6	9.4451×10^{-1}	1.0542×10^{-3}
2.90	2.0462×10^6	3.7521×10^6	9.4439×10^{-1}	1.0478×10^{-3}

Continued on next page

Table D.4 – continued from previous page

x [mm]	G_w [A ² /J]	G_b [A ² /J]	p_d [1]	p_r [1]
3.00	2.0651×10^6	3.6119×10^6	9.4432×10^{-1}	1.0410×10^{-3}
3.10	2.0821×10^6	3.4772×10^6	9.4419×10^{-1}	1.0350×10^{-3}
3.20	2.0985×10^6	3.3476×10^6	9.4404×10^{-1}	1.0293×10^{-3}
3.30	2.1127×10^6	3.2237×10^6	9.4382×10^{-1}	1.0244×10^{-3}
3.40	2.1298×10^6	3.1041×10^6	9.4367×10^{-1}	1.0191×10^{-3}
3.50	2.1446×10^6	2.9860×10^6	9.4359×10^{-1}	1.0132×10^{-3}
3.60	2.1621×10^6	2.8735×10^6	9.4343×10^{-1}	1.0082×10^{-3}
3.70	2.1802×10^6	2.7656×10^6	9.4326×10^{-1}	1.0033×10^{-3}
3.80	2.1910×10^6	2.6610×10^6	9.4302×10^{-1}	9.9936×10^{-4}
3.90	2.2042×10^6	2.5642×10^6	9.4285×10^{-1}	9.9481×10^{-4}
4.00	2.2244×10^6	2.4660×10^6	9.4277×10^{-1}	9.8966×10^{-4}
4.10	2.2365×10^6	2.3726×10^6	9.4260×10^{-1}	9.8537×10^{-4}
4.20	2.2552×10^6	2.2850×10^6	9.4243×10^{-1}	9.8121×10^{-4}
4.30	2.2683×10^6	2.1999×10^6	9.4217×10^{-1}	9.7790×10^{-4}
4.40	2.2832×10^6	2.1177×10^6	9.4201×10^{-1}	9.7396×10^{-4}
4.50	2.3040×10^6	2.0364×10^6	9.4193×10^{-1}	9.6938×10^{-4}
4.60	2.3150×10^6	1.9618×10^6	9.4176×10^{-1}	9.6564×10^{-4}
4.70	2.3330×10^6	1.8877×10^6	9.4160×10^{-1}	9.6200×10^{-4}
4.80	2.3447×10^6	1.8184×10^6	9.4135×10^{-1}	9.5921×10^{-4}
4.90	2.3612×10^6	1.7510×10^6	9.4118×10^{-1}	9.5574×10^{-4}
5.00	2.3756×10^6	1.6846×10^6	9.4112×10^{-1}	9.5160×10^{-4}

D.3 Second Prototype Design "Faramir"

Table D.5 Geometric and Energy-Filling Factors for Prototype LODR "Faramir"

x [mm]	G_w [A ² /J]	G_b [A ² /J]	p_d [1]	p_r [1]
0.00	1.4739×10^6	1.2885×10^7	9.2490×10^{-1}	5.1083×10^{-3}
0.10	1.4872×10^6	1.2524×10^7	9.2556×10^{-1}	4.9914×10^{-3}
0.20	1.4990×10^6	1.2213×10^7	9.2585×10^{-1}	4.8780×10^{-3}
0.30	1.5175×10^6	1.1834×10^7	9.2676×10^{-1}	4.7703×10^{-3}
0.40	1.5287×10^6	1.1491×10^7	9.2691×10^{-1}	4.6657×10^{-3}
0.50	1.5492×10^6	1.1058×10^7	9.2777×10^{-1}	4.5678×10^{-3}
0.60	1.5630×10^6	1.0669×10^7	9.2820×10^{-1}	4.4739×10^{-3}
0.70	1.5751×10^6	1.0289×10^7	9.2812×10^{-1}	4.3831×10^{-3}
0.80	1.5934×10^6	9.8842×10^6	9.2889×10^{-1}	4.3000×10^{-3}
0.90	1.6076×10^6	9.4964×10^6	9.2867×10^{-1}	4.2179×10^{-3}
1.00	1.6315×10^6	9.0668×10^6	9.2937×10^{-1}	4.1438×10^{-3}
1.10	1.6482×10^6	8.6802×10^6	9.2954×10^{-1}	4.0720×10^{-3}
1.20	1.6619×10^6	8.3511×10^6	9.2911×10^{-1}	4.0020×10^{-3}
1.30	1.6839×10^6	7.9772×10^6	9.2973×10^{-1}	3.9399×10^{-3}
1.40	1.7007×10^6	7.6459×10^6	9.2918×10^{-1}	3.8770×10^{-3}
1.50	1.7226×10^6	7.2971×10^6	9.2976×10^{-1}	3.8219×10^{-3}
1.60	1.7404×10^6	6.9651×10^6	9.2971×10^{-1}	3.7677×10^{-3}
1.70	1.7608×10^6	6.6504×10^6	9.2964×10^{-1}	3.7165×10^{-3}
1.80	1.7769×10^6	6.3640×10^6	9.2889×10^{-1}	3.6656×10^{-3}
1.90	1.7958×10^6	6.0685×10^6	9.2875×10^{-1}	3.6196×10^{-3}
2.00	1.8215×10^6	5.7730×10^6	9.2925×10^{-1}	3.5788×10^{-3}
2.10	1.8396×10^6	5.5032×10^6	9.2907×10^{-1}	3.5377×10^{-3}
2.20	1.8623×10^6	5.2566×10^6	9.2887×10^{-1}	3.4987×10^{-3}
2.30	1.8741×10^6	5.0369×10^6	9.2796×10^{-1}	3.4591×10^{-3}
2.40	1.8974×10^6	4.8015×10^6	9.2772×10^{-1}	3.4239×10^{-3}
2.50	1.9237×10^6	4.5768×10^6	9.2819×10^{-1}	3.3931×10^{-3}
2.60	1.9444×10^6	4.3639×10^6	9.2793×10^{-1}	3.3613×10^{-3}
2.70	1.9642×10^6	4.1604×10^6	9.2767×10^{-1}	3.3309×10^{-3}
2.80	1.9817×10^6	3.9854×10^6	9.2666×10^{-1}	3.2994×10^{-3}
2.90	2.0059×10^6	3.8023×10^6	9.2638×10^{-1}	3.2718×10^{-3}

Continued on next page

Table D.5 – continued from previous page

x [mm]	G_w [A ² /J]	G_b [A ² /J]	p_d [1]	p_r [1]
3.00	2.0258×10^6	3.6176×10^6	9.2684×10^{-1}	3.2482×10^{-3}
3.10	2.0450×10^6	3.4528×10^6	9.2655×10^{-1}	3.2231×10^{-3}
3.20	2.0689×10^6	3.2928×10^6	9.2626×10^{-1}	3.1989×10^{-3}
3.30	2.0922×10^6	3.1500×10^6	9.2520×10^{-1}	3.1730×10^{-3}
3.40	2.1048×10^6	3.0057×10^6	9.2491×10^{-1}	3.1508×10^{-3}
3.50	2.1302×10^6	2.8621×10^6	9.2539×10^{-1}	3.1321×10^{-3}
3.60	2.1488×10^6	2.7349×10^6	9.2510×10^{-1}	3.1116×10^{-3}
3.70	2.1785×10^6	2.6081×10^6	9.2481×10^{-1}	3.0918×10^{-3}
3.80	2.1890×10^6	2.4926×10^6	9.2374×10^{-1}	3.0701×10^{-3}
3.90	2.2111×10^6	2.3802×10^6	9.2345×10^{-1}	3.0516×10^{-3}
4.00	2.2248×10^6	2.2706×10^6	9.2397×10^{-1}	3.0363×10^{-3}
4.10	2.2511×10^6	2.1674×10^6	9.2369×10^{-1}	3.0191×10^{-3}
4.20	2.2652×10^6	2.0733×10^6	9.2342×10^{-1}	3.0022×10^{-3}
4.30	2.2814×10^6	1.9831×10^6	9.2235×10^{-1}	2.9834×10^{-3}
4.40	2.2984×10^6	1.8947×10^6	9.2209×10^{-1}	2.9676×10^{-3}
4.50	2.3316×10^6	1.8071×10^6	9.2265×10^{-1}	2.9546×10^{-3}
4.60	2.3464×10^6	1.7262×10^6	9.2240×10^{-1}	2.9395×10^{-3}
4.70	2.3614×10^6	1.6483×10^6	9.2217×10^{-1}	2.9247×10^{-3}
4.80	2.3787×10^6	1.5788×10^6	9.2111×10^{-1}	2.9077×10^{-3}
4.90	2.3951×10^6	1.5090×10^6	9.2089×10^{-1}	2.8936×10^{-3}
5.00	2.4157×10^6	1.4418×10^6	9.2149×10^{-1}	2.8819×10^{-3}

